University of California
Los Angeles

Reduced order modeling of soil structure interaction problems

A dissertation submitted in partial satisfaction
of the requirements for the degree
Doctor of Philosophy in Civil Engineering

by

Elnaz Esmaeilzadeh Seylabi

2016

Abstract of the Dissertation

Reduced order modeling of soil structure interaction problems

by

Elnaz Esmaeilzadeh Seylabi

Doctor of Philosophy in Civil Engineering

University of California, Los Angeles, 2016

Professor Ertugrul Taciroglu, Chair

This dissertation is focused on creating the key ingredients of a numerical platform for reduced order modeling of soil structure interaction (SSI) problems. Specifically, a computer code is developed for forward simulation of wave propagation in the two-dimensional (plane-strain and axisymmetric) semi-infinite heterogeneous solid media. Perfectly matched layers (PMLs) are used for absorbing the outgoing waves. The computationally efficient symmetric hybrid PML formulation available for the plane-strain setting is extended to axisymmetric problems. The domain reduction method (DRM) is used for translation of the remote excitation within a PML-truncated medium. The methodologies are devised for using this finite element (FE) solver to (i) compute the soil impedance functions and (ii) the modified input motions (a.k.a. foundation input motion) of rigid and flexible interfaces embedded in heterogeneous half-spaces numerically. Existing semi-analytical solutions are used to verify these methods comprehensively. The verified framework is validated using data from a large-scale field test as well as centrifuge experiments. In order to demonstrate the framework's application: (i) the impedance functions and kinematic interaction transfer functions (KITFs) of a number of SSI problems—for which existing analytical solutions are limited—are computed; and (ii) the reduced order model of a buried structure in an elastic half-space is constructed. In order to avoid integro-differential equations, stable discrete-time filters are used for de-

vising time-domain representations of the computed soil impedance matrix. The dynamic response of the resulting spatio-temporal reduced order model is compared against those obtained from solving the same problem using the direct modeling approach, and excellent agreement is observed.

The dissertation of Elnaz Esmaeilzadeh Seylabi is approved.

Jian Zhang

Joseph M. Teran

Jonathan P. Stewart

Ertugrul Taciroglu, Committee Chair

University of California, Los Angeles

2016

To my loving parents, Raheleh and Mosleh

Table of Contents

List of Figures

List of Tables

Acknowledgments

I would like to express my sincere gratitude to my advisor, Professor Ertugrul Taciroglu, for his guidance, encouragement, and ingenuity. This dissertation would not have been possible without his persistent support. I would like to thank Professors Jian Zhang, Joseph M. Teran, and Jonathan P. Stewart for serving on my dissertation committee, and for their insightful comments. I am also grateful to Professor Chanseok Jeong for his assistance in developing the backbone of the numerical solver, and to Professors Shideh Dashti and Asli Kurtulus for providing the centrifuge experiment and field test data, respectively.

Vita

2007 **B.Sc.** in Civil Engineering, Sharif University of Technology, Tehran, Iran.

2009 **M.Sc.** in Earthquake Engineering, Sharif University of Technology, Tehran, Iran.

Publications

R. Gash, E. Esmaeilzadeh Seylabi, E. Taciroglu (2016), Frequency dependent effects of soil-structure interaction on inelastic behavior of superstructures, *ACI Special Publication*, accepted.

E. Esmaeilzadeh Seylabi, C. Jeong, E. Taciroglu (2016), On numerical computation of impedance functions for rigid soil-structure interfaces embedded in heterogeneous half-spaces, *Computers & Geotechnics*, Vol. 72, 15-27.

C. Jeong, E. Esmaeilzadeh Seylabi, E. Taciroglu (2013), A time-domain sub-structuring method for dynamic soil-structure interaction analysis of arbitrarily shaped foundation systems on heterogeneous media, *Computing in Civil Engineering*, 346-353.

E. Esmaeilzadeh Seylabi, H. Jahankhah, M. A. Ghannad (2012), Equivalent linearization of nonlinear soil-structure systems, *Earthquake Engineering & Structural Dynamics*, Vol. 41, 1775-1792.

CHAPTER 1

Introduction

1.1 What is soil structure interaction (SSI)?

Almost all civil structures have foundations and other support elements that either rest on, or are embedded in, soil. Because of complexities in modeling the mechanical behavior of soils, and the high degree of uncertainty and variability in their properties, it is not uncommon among structural engineers to completely ignore their effects on the structural system. This simplistic approach, wherein the soil structure interaction (SSI) effects are unaccounted for, might yield acceptable designs for certain cases—for example, for lightweight aboveground structures resting on, or stiff underground structures buried in, rock and stiff soils. Nevertheless, SSI effects can also bear perilous consequences under strong earthquakes.

Different types of agents—e.g., rotating machinery, earthquakes, traffic, etc.—excite a structure. Depending on the nature of the loading, the ensuing structural vibrations result in time-harmonic or time-varying tractions at the soil-structure interface. These tractions will cause further deformations within the structure due to the soil's flexibility, which may reach significant levels under certain combinations of soil and structural properties—for example, for a massive structure resting on soft soil (Mylonakis and Gazetas, 2000). On the positive side, the surrounding/supporting soil transmits energy away from the structure in the form of outgoing waves. The amount of this radiated energy depends, to a large extent, on the soil profile and properties (Wolf, 1985). For buried structures, although these inertially induced tractions may become negligible, the nominal incapability of their foundation systems to conform to the soil deformations may significantly alter their responses.

1.2 How to model the SSI effects?

One approach to take the effects of SSI into account is to use the finite element method (FEM) to model a portion of the supporting/surrounding soil media along with the structure. This approach is known as the *direct modeling* (Wolf, 1985; Bielak and Christiano, 1984) method. Apparently, it is not possible to discretize the semi-infinite soil domain with a finite number of elements; and thus, it is necessary to truncate it by introducing appropriate boundary conditions. For an exact representation of the omitted domain—dubbed the *far-field*—, the introduced boundaries on the computational domain (the *near-field*) must have the ability to transmit the energy of the outgoing and incoming waves perfectly[1].

In problems where the source of excitation is inside the near-field, all waves impinging upon the imposed boundaries are outgoing; and the inserted boundary condition must absorb the energy of these outgoing waves through the, so-called, absorbing-boundary-conditions (ABCs). On the other hand, for problems where the source of excitation is outside the near-field, the forged boundary conditions must not only absorb the energy of the outgoing waves but also be transparent to all incoming waves. The latter device is usually referred to as an open-boundary-condition (OBC).

Although domain truncation, together with the insertion of an appropriate boundary condition, reduces the order of the original problem, it is still computationally expensive and is rarely used in engineering practice. Therefore, it is desirable to entirely avoid the discretization of the soil domain by defining the near-field boundaries at the soil-structure interface. In this approach, which is known as the *substructure* method, special treatments are required for taking into account the possible soil nonlinearities in the near-field.

For problems where the soil-structure interface is fairly rigid, the substructure modeling approach reduces the order of the model significantly, by restricting the degrees-of-freedom (DOFs) of the soil domain to those of the rigid interface[2]. However, it requires defining

[1] In this text, the terms "outgoing" and "incoming" refer to wave-fields within the near-field.

[2] These are typically the rigid body modes of the foundation—e.g., the lateral, vertical, and rocking DOFs of the foundation for two-dimensional problems.

an appropriate Dirichlet-to-Neumann (DtN) mapping function, which relates the interacting force and displacement components. Moreover, in cases where the source of excitation is within the soil medium—e.g., seismic excitations—the input motion at the soil-structure interface—a.k.a. the foundation input motion, or FIM—may be different from the so-called free-field motion. This is mainly because of the so-called "incoherency" effects, and requires the free-field motion to somehow be transformed into an approximation of the (true) FIM (Veletsos et al., 1997). Starting as early as 1960s, a fairly large number of studies focused on deriving appropriate DtN-maps in the frequency domain (Kausel, 2010). These DtN-maps are better known as "soil impedance functions," which are frequency-dependent and complex-valued functions that represents the stiffness and radiation damping at the soil-structure interface. A number of studies were also focused on deriving transfer functions for appropriate modification of the free-field motion to take the effects of incoherency into account.

For linear SSI analysis, it is convenient to solve the problem in the frequency domain, using the soil impedance functions and the modified input motion, together with dynamic characteristic of the structure. While the use of impedance functions in linear SSI analyses are quite straightforward, they cannot be used—at least, directly—in nonlinear SSI analysis, even for cases where *only* the structural components are behaving nonlinearly. This is because it is not nominally possible to solve nonlinear problems in the frequency domain. Therefore, soil impedance functions must be transformed into the time domain.

The use of inverse Fourier transform techniques results in integro-differential equations, which, in turn, leads to exact representations of the impedance functions in the time domain. However, it is typically more appealing to deal with differential equations in time. This is mainly because these equations can be solved using standard numerical schemes, such as the finite element or finite difference methods. An alternative is to approximate the original impedance function with another function using rational approximations. The resulting DtN-map has the advantage of being represented in the time domain as differential (or difference) equations (e.g. Wolf, 1994; Safak, 2006), and for certain simple cases, as discrete mechanical

models (e.g. Wolf, 1994; Wu and Lee, 2002, 2004; Saitoh, 2007; Du and Zhao, 2010).

In engineering practice, common approaches for taking the effects of SSI into account are typically based on modifying the dynamic properties of the structure by attaching representative soil springs and dashpots at the interface of the soil and structure, and by modifying the input motion (e.g. NIST, 2012; NCHRP Report 611, 2008; Pitilakis and Tsinidis, 2014; Brandenberg et al., 2015). The major drawbacks of these methods for above-ground or partially embedded structures are their inability to include the frequency-dependency of the soil impedance functions in time domain analyses and their limitations to represent the actual dynamic characteristics of flexible soil-foundation interfaces. For underground structures, the situation is even worse as the exact impedance functions and FIMs are not adequately explored in open literature, even for rigid interfaces (e.g., Pitilakis and Tsinidis, 2014).

1.3 Objectives and the approach

Direct modeling of SSI problems usually suffer from defining inappropriate ABCs and input ground motions (Jeremic et al., 2004; Zhang et al., 2008; Carbonari et al., 2011). In order to increase the modeling accuracy, a large extent of the soil domain has to be discretized, and this is usually fatal—from a practicing engineer's point of view—because of the high level of computational effort required (Solberg et al., 2013). On the other hand, to date, impedance functions and FIMs have been devised only for simple foundation shapes and soil profiles, which limits their usefulness in substructure modeling of SSI problems. The objective of this work, therefore, is to devise an adequately general framework for reduced order modeling of SSI problems in a two-dimensional setting. The main steps toward achieving this goal, along with the tools developed in that process, are listed below:

- *Direct modeling of SSI problems with high fidelity:* A finite element code is developed in Fortran that features perfectly matched layers (PMLs) to absorb the radiation energy thoroughly, and the domain reduction method (DRM) to consistently prescribe the input motions within the PML-truncated domain.

- *Computing the impedance functions for arbitrarily complex foundation geometry and stiffness and soil heterogeneity:* The direct modeling code discussed above is used to devise methodologies for numerically computing the impedance functions for rigid and flexible interfaces, using either time or frequency domain solvers.

- *Computing the input motion modification factors (a.k.a. kinematic interaction transfer functions or KITFs) for different types of soil-structure interfaces:* Methods are developed to deduce the KITFs under vertically propagating shear waves, given the soil-structure interface geometry and stiffness.

1.4 Organization of the text

The remainder of this dissertation—i.e., Chapter 2—begins with a more detailed overview of the direct and substructure modeling approaches, as well as existing methodologies for time domain representations of impedance functions.

In Chapter 3, the finite element formulations used for the simulation of wave propagation in a heterogeneous half-space are provided. In Chapter 4, the methodologies devised for computing the impedance functions of rigid and flexible soil-structure interfaces are explained. In Chapter 5, the approach used for computing the modified input motions (KITFs) of a soil-structure interface is demonstrated.

The application of the developed framework is demonstrated in Chapter 6 with a specific focus on the dynamic behavior of buried structures. First, the impedance functions and KITFs of a number of buried rigid soil-structure interfaces are provided. Second, a reduced order model for a rectangular structure buried in a homogeneous half-space is developed by computing the soil impedance matrix and modified input motions for a flexible soil-structure interface and by using a discrete-time filter method for time-domain representation of the said impedance matrix.

Chapters 7 and 8 demonstrate the attempts made to validate different aspects of the

developed numerical platform. Chapter 7 focuses on numerical simulations of a series of centrifuge experiments conducted on underground reservoir structures. The capability of the equivalent linear soil model in capturing the dynamic responses of the buried specimen structures is explored. Moreover, the effects centrifuge container are studied by modeling and simulating the same soil deposit using the developed FE solver to rest on an elastic bedrock and to have an infinite lateral extent Chapter 8, on the other hand, is focused on numerical simulations of a large-scale field test on a vertically vibrated drilled shaft. The vertical impedance of the shaft is computed numerically and is compared against those obtained from the test data. Furthermore, the potential of back-calculating small-strain dynamic soil properties using the measured in-depth velocity data is explored.

The concluding remarks are provided in Chapter 9.

CHAPTER 2

Background

2.1 Direct modeling of SSI problems

Problems involving unbounded domains—i.e., domains with infinite length, area, or volume—frequently occur in different fields of engineering. In the field of earthquake engineering, a pertinent example is the SSI problem where the semi-infinite domain (far-field) is the earth, and the finite domain (near-field) is the structure and its surrounding soil as shown schematically in Figure 2.1.

One approach to solve this problem is the direct modeling approach. In direct modeling, standard numerical (e.g., finite element and finite difference) methods are typically used to discretize the problem domain in space and time. However, it is not possible to model the semi-infinite domain directly by using finite elements, and only the near-field subdomain, which usually encloses domain irregularities and/or nonlinearities, is discretized; the effects of the truncated far-field subdomain mimicked by defining appropriate conditions at the truncation boundary. For exact representation of the truncated far-field, the boundary condition must be transparent to both outgoing and incoming waves in order to transmit the energy of waves traveling from the inside and outside sources of excitation completely (Wolf, 1985).

In the past, extensive studies had been devoted for developing appropriate boundary conditions for the far-field. While a review of the entire related literature will not be undertaken here—which extends into physics, electromagnetics, acoustics, etc.—, the properties of two important classes of local (approximate) ABCs in the context of forward wave propagation

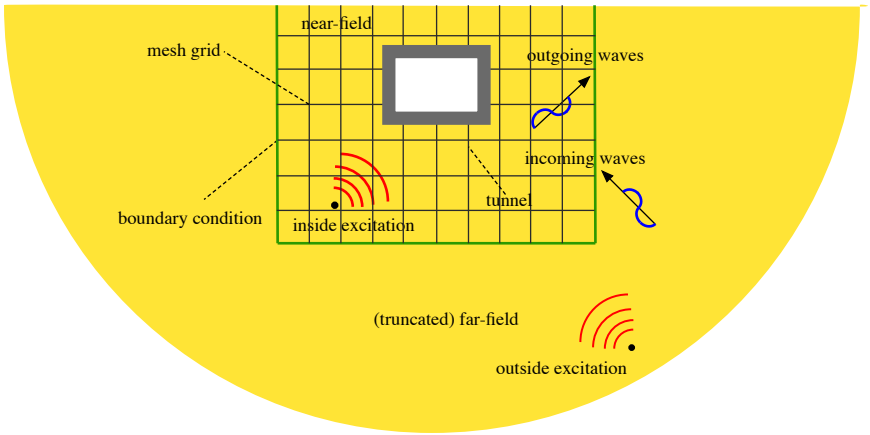

Figure 2.1: Schematic direct modeling of the SSI problem.

simulation will be discussed. Moreover, existing methods for considering the effects of remote excitations will be reviewed—a topic that is also highly relevant to SSI problems.

2.1.1 Absorbing boundary conditions (ABCs)

ABCs may be classified as *nonlocal* and *local*. Nonlocal ABCs are derived by using analytical solutions of waves propagating in the far-field, and are represented as a DtN-map, which is nonlocal in both time and space. However, it is not always possible to derive the exact DtN-maps for infinite domain problems and these maps are usually computationally expensive. Therefore, different types of local ABCs were developed in an attempt to solve more complex infinite domain problems with sufficient accuracy, using less computational effort. In the subsequent sections, two major classes of local ABCs are introduced.

2.1.1.1 High-order local ABCs

Lysmer and Kuhlemeyer (1969) proposed the first local ABC, which could only absorb waves traveling along a prescribed direction. Higdon (1990) proposed the m-th order multi-directional boundary condition that can absorb traveling waves with m different angles of incidence perfectly. Although the accuracy of this boundary condition increases by m, its usage in application is limited to $m \leq 2$. This is because it is very difficult to define high-order

derivatives in standard numerical schemes, such as the finite element method. High-order local ABCs must have the following properties (Givoli, 2004):

- Increasing accuracy as a function of the order of the local ABC,
- Ability to be implemented in numerical applications regardless of the order of the local ABC.

The local ABC devised by Collino (1993) can be considered as the first high-order local ABC satisfying the above properties. Since then, different high-order ABCs are proposed (Givoli, 2004). Almost all these boundary conditions are limited to scalar problems such as electrodynamics and acoustic problems. Though many infinite domain problems involve vectorial elastic waves, only a few high-order ABCs have been developed for elastodynamics problems thus far (Baffet et al., 2012). High-order local ABCs proposed by Joly and Tsogka (2010) and Rabinovich et al. (2011) are, respectively, the extensions of Collino ABC and Hagstrom-Warburton (HW) ABC (Hagstrom and Warburton, 2004) to elastodynamics problems. However, both ABCs suffer from long-time instability issues (Baffet et al., 2012).

Recently, Baffet et al. (2012) proposed the first long-time stable high-order local ABC. Thus far, this high-order ABC is only available for the relatively simple case of 2D elastodynamics with a single artificial boundary and two physical boundaries . Extensions to more involved cases, such as problems in SSI analysis, which consist of a single physical boundary and three artificial boundaries (see Figure 2.1), do not yet exist.

2.1.1.2 Perfectly matched layer (PML)

Another class of local ABCs is PMLs, which were originally introduced by Berenger (1994) for absorbing electromagnetic waves, and extended to elastodynamic problems by Basu and Chopra (2003). In short, a PML is an absorbing layer adjacent to the finite computational domain–i.e., near-field—with two main properties (Rabinovich et al., 2010):

- It results in no reflections at the truncated near-field boundary (i.e., "perfect matches"

it) for all non-zero-frequency impinging waves, irrespective of their angles of incidence.

- It attenuates the wave energy within itself.

Though only a few studies are devoted to comparing the advantages and disadvantages of PMLs with respect to high-order ABCs, PMLs have become more popular than high-order ABCs in dealing with infinite domain problems, which may be due to the easier implementation of PMLs in comparison to high-order ABCs (Rabinovich et al., 2010) and their applicability for heterogeneous media (Kucukcoban and Kallivokas, 2011). However, one noticeable advantage of high-order ABCs over PMLs may be their capability to be extended to OBCs in order to take the effects of exterior sources of excitation into account (Rabinovich et al., 2011).

Literature on different types of PMLs is extensive and a detailed review of the subject is beyond the scope of this work and can be found elsewhere (e.g. Kucukcoban and Kallivokas, 2011, 2013). In this work, we employ the symmetric hybrid PML formulation proposed by Kucukcoban and Kallivokas (2013) for simulation of wave propagation in heterogeneous half-spaces. Detailed description of this formulation will be provided in Chapter 3.

2.1.2 Open boundary conditions (OBCs)

In problems with source of excitation outside the domain of interest, both outgoing and incoming waves exist. One approach for solving infinite domain problems with exterior source is introducing ABC with capability of handling both outgoing and incoming waves, i.e., OBCs. Carpenter (1982) proposed a simple OBC, which was in fact the extension of LK ABC, considering rational assumptions. Since LK ABC is in fact 0-th order ABC, the resulting OBC has low-order of accuracy. Later, Mar-Or and Givoli (2009) modified Carpenter scheme for scalar wave equation, replacing LK ABC with HW ABC, which has high-order accuracy. The Carpenter OBC is more applicable to numerical weather prediction. For SSI analysis, Zhang et al. (2003) proposed another OBC which was based on simulation of wave propagation in semi-infinite soil column. In this approach, the far-field soil is replaced

with LK ABC while the input motion is defined as an equivalent force on the imposed boundary (Joyner, 1975). This approach again is susceptible to low-order accuracy of LK ABC.

2.1.3 Domain reduction method (DRM)

Bielak and Christiano (1984); Bielak et al. (2003) proposed a two-step finite element method for modeling a semi-infinite domain under remote excitations. The most appealing advantage of their method is that the problem at hand is inverted to an equivalent problem in which the effects of incoming waves due to remote excitations are translated inside the domain truncated by ABCs. Therefore there is no need to define OBCs and robust ABCs can be used with no difficulty. This method, which is employed in this work for quantification of kinematic SSI effects, will be discussed in details in Chapter 3.

2.2 Substructure modeling of SSI problems

The method of dynamic substructuring involves (i) dividing the whole structure into its components, (ii) modeling behavior of each substructure and (iii) coupling the sub-structural models to evaluate the behavior of the whole structure (Craig and Kurdila, 2006). Dynamic substructuring has some advantages over modeling the whole structure (de Klerk et al., 2008). First, it allows analysis of too large or complex structures within reasonable amount of time and memory. Second, local dynamic behavior of each components can be identified, which in turn, may be used to disregard local dynamic properties that do not have appreciable effects on behavior of the whole structure. Finally, it allows combining components that are modeled from different approaches, i.e, numerical, analytical, and experimental.

In the context of SSI, dynamic substructuring is known as the substructure modeling (Wolf, 1985) or three-step modeling (Kausel, 2010) approach and is usually the method of choice in common practice. This is because design procedures usually involve too many analyses. First, material and geometric properties of structural components must be ad-

justed at the end of each analysis, and second, response analysis should be repeated for a suite of strong ground motions, specially in the framework of performance-based earthquake engineering (PBEE).

2.2.1 General formulation

A generic soil-structure system is shown schematically in Figure 2.2a and the uncoupled components are shown in Figure 2.2b. Using the FEM to model the structure, the semi-

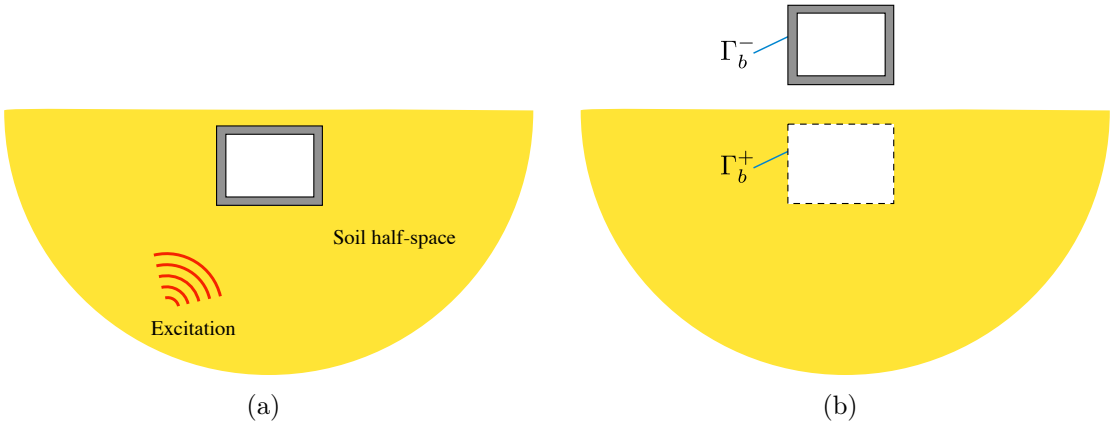

Figure 2.2: A (a) generic soil-structure system and (b) its uncoupled components.

discrete equations of motion for the structure shown in Figure 2.2b—when partitioned to non-interfacial (s) and interfacial (b) DOFs—are

$$\begin{bmatrix} \mathbf{M}_{\mathrm{ss}} & \mathbf{M}_{\mathrm{sb}} \\ \mathbf{M}_{\mathrm{bs}} & \mathbf{M}_{\mathrm{bb}} \end{bmatrix} \begin{bmatrix} \ddot{\mathbf{u}}_{\mathrm{s}}(t) \\ \ddot{\mathbf{u}}_{\mathrm{b}}^{-}(t) \end{bmatrix} + \begin{bmatrix} \mathbf{f}_{\mathrm{s}}(t) \\ \mathbf{f}_{\mathrm{b}}^{-}(t) \end{bmatrix} = \begin{bmatrix} \mathbf{f}_{\mathrm{ext}}(t) \\ \mathbf{f}_{\mathrm{int}}(t) \end{bmatrix} \tag{2.1}$$

where $\mathbf{M}_{\mathrm{ss}}$, $\mathbf{M}_{\mathrm{bs}} = \mathbf{M}_{\mathrm{sb}}^T$, and $\mathbf{M}_{\mathrm{bb}}$ are the non-interfacial, coupling, and interfacial mass sub-matrices, respectively; $\mathbf{u}^T = \begin{bmatrix} \mathbf{u}_{\mathrm{s}}^T & \mathbf{u}_{\mathrm{b}}^{-T} \end{bmatrix}$ is the displacement response vector, and $\begin{bmatrix} \mathbf{f}_{\mathrm{s}}^T & \mathbf{f}_{\mathrm{b}}^{-T} \end{bmatrix}$ is the transpose of a (nonlinear) restoring force vector within the main structure; $\ddot{(\,)}$ denotes the second differentiation of the subtended variable with respect to time; $\mathbf{f}_{\mathrm{ext}}(t)$ is the external force vector applied to the non-interfacial DOFs of the structure; and $\mathbf{f}_{\mathrm{int}}(t)$ is the force vector applied to the interfacial DOFs as a result of its coupling with the surrounding soil

domain.

On the other hand, the soil behavior is replicated by the soil impedance matrix—i.e. a DtN-map relating force and displacement vectors $\mathbf{f}_{\mathrm{b}}^{+}(t)$ and $\mathbf{u}_{\mathrm{b}}^{+}(t)$ (see Figure 2.2b). It is well-known that the soil impedance function is frequency dependent and complex-valued. The real part corresponds to the stiffness and inertial effects, and the imaginary part accounts for radiation damping (Gazetas, 1983). The discrete form of this DtN-map in frequency domain is

$$\hat{\mathbf{S}}(\omega)\hat{\mathbf{u}}_{\mathrm{b}}^{+}(\omega) = \hat{\mathbf{f}}_{\mathrm{b}}^{+}(\omega), \tag{2.2}$$

and in time domain is

$$\int_0^t \mathbf{S}(t-\tau)\mathbf{u}_{\mathrm{b}}^{+}(\tau)\mathrm{d}\tau = \mathbf{S}(t) * \mathbf{u}_{\mathrm{b}}^{+}(t) = \mathbf{f}_{\mathrm{b}}^{+}(t) \tag{2.3}$$

where $\hat{\mathbf{S}}(\omega)$ and $\mathbf{S}(t)$ are the soil impedance matrices in frequency and time, respectively; $\hat{\ }$ and $(*)$ stand for the Fourier transform and the convolution operators, respectively.

The compatibility and equilibrium conditions along the interface of the structure and the surrounding soil should be satisfied setting

$$\mathbf{u}_{\mathrm{b}}^{-}(t) = \mathbf{u}_{\mathrm{b}}^{+}(t), \quad \mathbf{f}_{\mathrm{int}}(t) + \mathbf{f}_{\mathrm{b}}^{+}(t) = \mathbf{0}\,. \tag{2.4}$$

By substituting Eq. (2.4) into Eq. (2.3), and by enforcing the compatibility and equilibrium conditions in Eq. (2.1), we get

$$\begin{bmatrix} \mathbf{M}_{\mathrm{ss}} & \mathbf{M}_{\mathrm{sb}} \\ \mathbf{M}_{\mathrm{bs}} & \mathbf{M}_{\mathrm{bb}} \end{bmatrix} \begin{bmatrix} \ddot{\mathbf{u}}_{\mathrm{s}}(t) \\ \ddot{\mathbf{u}}_{\mathrm{b}}^{-}(t) \end{bmatrix} + \begin{bmatrix} \mathbf{f}_{\mathrm{s}}(t) \\ \mathbf{f}_{\mathrm{b}}^{-}(t) + \mathbf{S}(t) * \mathbf{u}_{\mathrm{b}}^{-}(t) \end{bmatrix} = \begin{bmatrix} \mathbf{f}_{\mathrm{ext}}(t) \\ \mathbf{0} \end{bmatrix}. \tag{2.5}$$

Finally, Eq. (2.5) should be modified as follows to incorporate the effects of seismic

excitation (Wolf, 1985):

$$\begin{bmatrix} \mathbf{M}_{\mathrm{ss}} & \mathbf{M}_{\mathrm{sb}} \\ \mathbf{M}_{\mathrm{bs}} & \mathbf{M}_{\mathrm{bb}} \end{bmatrix} \begin{bmatrix} \ddot{\mathbf{u}}_{\mathrm{s}}(t) \\ \ddot{\mathbf{u}}_{\mathrm{b}}^{-}(t) \end{bmatrix} + \begin{bmatrix} \mathbf{f}_{\mathrm{s}}(t) \\ \mathbf{f}_{\mathrm{b}}^{-}(t) + \mathbf{S}(t) * \mathbf{u}_{\mathrm{b}}^{-}(t) \end{bmatrix} = \begin{bmatrix} \mathbf{f}_{\mathrm{ext}}(t) \\ \mathbf{S}(\mathbf{t}) * \mathbf{u}_{\mathrm{g}}(\mathbf{t}) \end{bmatrix} \tag{2.6}$$

where $\mathbf{u}_{\mathrm{g}}(t)$ is the modified input motion or the FIM to be determined along the interface Γ_{b}^{+}. For a structure with linear behavior, Eq. (2.6) can be reformulated in the frequency domain as:

$$\begin{bmatrix} \hat{\mathbf{S}}_{\mathrm{ss}}(\omega) & \hat{\mathbf{S}}_{\mathrm{sb}}(\omega) \\ \hat{\mathbf{S}}_{\mathrm{bs}}(\omega) & \hat{\mathbf{S}}_{\mathrm{bb}}(\omega) + \hat{\mathbf{S}}(\omega) \end{bmatrix} \begin{bmatrix} \hat{\mathbf{u}}_{\mathrm{s}}(\omega) \\ \hat{\mathbf{u}}_{\mathrm{b}}^{-}(\omega) \end{bmatrix} = \begin{bmatrix} \hat{\mathbf{f}}_{\mathrm{ext}}(\omega) \\ \hat{\mathbf{S}}(\omega)\hat{\mathbf{u}}_{\mathrm{g}}(\omega) \end{bmatrix} \tag{2.7}$$

where

$$\begin{bmatrix} \hat{\mathbf{S}}_{\mathrm{ss}}(\omega) & \hat{\mathbf{S}}_{\mathrm{sb}}(\omega) \\ \hat{\mathbf{S}}_{\mathrm{bs}}(\omega) & \hat{\mathbf{S}}_{\mathrm{bb}}(\omega) \end{bmatrix} = -\omega^2 \begin{bmatrix} \mathbf{M}_{\mathrm{ss}} & \mathbf{M}_{\mathrm{sb}} \\ \mathbf{M}_{\mathrm{bs}} & \mathbf{M}_{\mathrm{bb}} \end{bmatrix} + i\omega \begin{bmatrix} \mathbf{C}_{\mathrm{ss}} & \mathbf{C}_{\mathrm{sb}} \\ \mathbf{C}_{\mathrm{bs}} & \mathbf{C}_{\mathrm{bb}} \end{bmatrix} + \begin{bmatrix} \mathbf{K}_{\mathrm{ss}} & \mathbf{K}_{\mathrm{sb}} \\ \mathbf{K}_{\mathrm{bs}} & \mathbf{K}_{\mathrm{bb}} \end{bmatrix}. \tag{2.8}$$

In Eq. (2.8) $\mathbf{C}_{\mathrm{ss}}$, $\mathbf{C}_{\mathrm{bs}} = \mathbf{C}_{\mathrm{sb}}^{T}$, and $\mathbf{C}_{\mathrm{bb}}$ are the non-interfacial, coupling, and interfacial damping matrices, respectively (assuming, without loosing generality, viscous damping behavior within the main structure) and $\mathbf{K}_{\mathrm{ss}}$, $\mathbf{K}_{\mathrm{bs}} = \mathbf{K}_{\mathrm{sb}}^{T}$, and $\mathbf{K}_{\mathrm{bb}}$ are the corresponding stiffness matrices.

As a result, for the analysis of a soil-structure system using the substructure modeling approach, one needs to determine the dynamic properties of the structure and the soil medium, as well as the appropriate input motions to construct the reduced order model. Detailed description of these ingredients and the methodologies to compute them are provided in Chapters 4 and 5.

2.2.2 Time domain representation of the impedance function

Time domain analysis is an indispensable part of nonlinear SSI problems. Nonlinearities may be confined to the structure or extended to the surrounding soil. As discussed above,

the exact representation of the soil impedance matrices in time results in integro-differential equations. This hinders the use of standard numerical scheme, which is commonly used for time domain analysis of structures.

A simple approach for taking the advantages of substructure modeling, while avoiding the complexities associated with the inherent frequency dependency property of impedance functions, is modeling the effects of surrounding soil through defining a set of springs and dashpots with constant coefficients at the soil-structure interface. For more simplicity, usually the coupling of the interfacial DOFs is ignored as well. Figure 2.3 shows schematically two examples of commonly used models in practice (e.g. Stewart and Tileylioglu, 2007; NIST, 2012). Coefficients of springs and dashpots are usually determined based on either static properties of the surrounding soil or its dynamic properties at a specific frequency, using engineering judgement. These simplifications, though acceptable for time-harmonic analysis, e.g., vibrations of machinery foundations, may lead to unreliable results for seismic response analysis of structures.

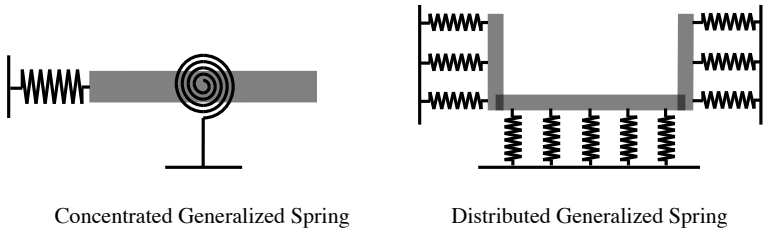

Figure 2.3: Generalized spring (spring-dashpot) with constant coefficients.

2.2.2.1 Rational approximation method

As shown in Eqs. (2.2) and (2.3), the general form of the DtN-map equation that relates the force at the i-th DOF due to the displacement at the j-th DOF along the interface Γ_{b}^{+} is

$$\hat{f}_{\mathrm{b},i}^{j+}(\omega) = \hat{S}_{ij}(\omega)\hat{u}_{\mathrm{b},j}^{+}(\omega) \tag{2.9}$$

in the frequency domain and is

$$f_{\mathrm{b},i}^{j+}(t) = \int_0^t S_{ij}(t-\tau) u_{\mathrm{b},j}^{+}(\tau) d\tau = S_{ij}(t) * u_{\mathrm{b},j}^{+}(t) \tag{2.10}$$

in the time domain. In open literature, several attempts are made to avoid these integral equations in time domain analyses (e.g. Wolf and Motosaka, 1989; Wolf, 1991; Wu and Lee, 2002, 2004; Saitoh, 2007; Du and Zhao, 2010; Safak, 2006; Xiuli and Zhao, 2010; Ruge et al., 2001; Cazzani and Ruge, 2012; Gash, 2015). The underlying idea is to approximate the original DtN-map equation with another function, which is in fact a DtN-map of another dynamic system. This approximate transfer function must have two properties:

- to be transformed into the time domain as a continuous-time differential or discrete-time difference equation; and
- to be a DtN-map of a stable dynamic system.

Rational functions, which are the ratio of two polynomials, satisfy the first property. However, the identified rational transfer function may not satisfy the second property. In continuous-time systems, the poles, i.e., the roots of the denominator of the system transfer function, must have negative real values in order to guarantee stability, which in turn calls for adding more constraints on identification of the coefficients of the polynomials used for rational approximation. In discrete-time systems, the poles of the system transfer function must lie within a complex unit circle (Oppenheim et al., 1996). A number of studies has investigated the global stability of the approximate transfer functions in combination with the structure and in combination with the utilized numerical integration scheme (e.g. Lesgidis et al., 2015; Laudon et al., 2015; Gash, 2015).

In this work, we use the stable discrete-time filter method implemented by Gash (2015) for time domain representation of the soil impedance functions to construct a reduced order model for a buried structure in an elastic half-space. More details are provided in Chapter 6.

CHAPTER 3

Simulation of wave propagation in a PML-truncated heterogeneous half-space

As mentioned in §1.3, the first objective of this work is developing a numerical platform for high-fidelity simulation of wave propagation in heterogeneous half-spaces. To achieve this, we use PMLs to truncate the semi-infinite extent of soil. The DRM is used for translation of the seismic excitation inside the truncated computational domain. Details of these ingredients are provided in the following sections.

3.1 Complex coordinate stretching

The central idea in the PML formulation is to use a finite-sized layer that surrounds the near-field and stretched internal spatial coordinates in order to mimic the effects of the semi-infinite domain it replaces. This is shown schematically in Figure 3.1.

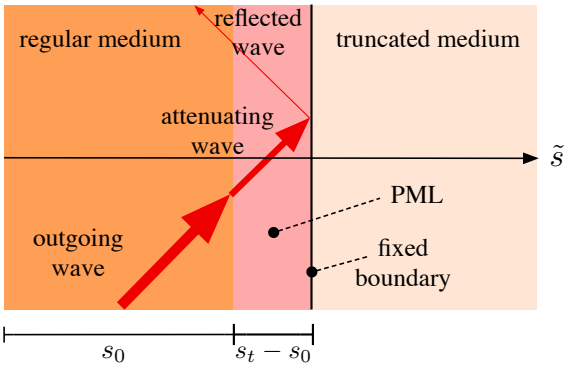

Figure 3.1: Schematic geometry of a PML-truncated extent.

Different complex stretching functions were proposed in past research. Using a frequency-

independent complex stretching function produces the standard PML formulation. An alternative is the frequency-shifted stretching function proposed by Kuzuoglu and Mittra (1996). The resulting complex-frequency-shifted (CFS) PML outperforms the standard PML in presence of the evanescent waves, but has degrading performance in absorbing low frequency propagating waves (Roden and Gedney, 2000; Berenger, 2002a,b). Consequently a second-order PML was devised by Correia and Jin (2005), which combines the capability of the standard PML in absorbing the low frequency propagating waves with the capability of CFS PML in absorbing the evanescent waves.

Since we are interested in exploring the behavior of SSI problems under seismic excitations where the frequency content of the input motions are in general predominant in low frequencies, we employ the standard PML formulation (Fathi, 2015). The frequency-independent complex coordinate stretching function is defined as:

$$\tilde{s} = \int_0^s (\alpha_s(s') + \frac{\beta_s(s')}{i\omega})ds' = \bar{\alpha}_s(s) + \frac{\bar{\beta}_s(s)}{i\omega} \tag{3.1}$$

where α_s and β_s control the stretching behavior; $i = \sqrt{-1}$, ω is the angular frequency; and s is the original coordinate to be stretched. The following second-order polynomials are used to define α_s and β_s as suggested in Kucukcoban (2010):

$$\alpha_s(s) = \begin{cases} 1 & 0 \le s \le s_0 \\ 1 + \frac{3b}{2L_{\mathrm{PML}}} \log(\frac{1}{|R|})(\frac{(s-s_0)n_s}{L_{\mathrm{PML}}})^2 & s_0 \le s \le s_t \end{cases} \tag{3.2}$$

$$\beta_s(s) = \begin{cases} 0 & 0 \le s \le s_0 \\ \frac{3c_p^{ref}}{2L_{\mathrm{PML}}} \log(\frac{1}{|R|})(\frac{(s-s_0)n_s}{L_{\mathrm{PML}}})^2 & s_0 \le s \le s_t \end{cases} \tag{3.3}$$

where s denotes either x_1 or x_2; n_s is the normal direction; R, L_{PML}, and c_p^{ref} are tuning parameters controlling the performance of the PML in attenuating the outgoing waves; s_0 is the distance from the origin to the interface of the regular domain and PML and s_t is the distance from the origin to the fixed boundary; b is the characteristic length.

Using Eq. (3.3) to define α_s and β_s, parameters $\bar{\alpha}_s$ and $\bar{\beta}_s$, as defined in Eq. (3.1), are:

$$\bar{\alpha}_s(s) = \begin{cases} s & 0 \leq s \leq s_0 \\ s + \frac{bn_s^2}{2L_{\mathrm{PML}}^3} \log(\frac{1}{|R|})(s - s_0)^3 & s_0 \leq s \leq s_t \end{cases} \tag{3.4}$$

$$\bar{\beta}_s(s) = \begin{cases} 0 & 0 \leq s \leq s_0 \\ \frac{c_p^{ref} n_s^2}{2L_{\mathrm{PML}}^3} \log(\frac{1}{|R|})(s - s_0)^3 & s_0 \leq s \leq s_t \end{cases}. \tag{3.5}$$

The wave physics within the standard PML can be clarified by studying the behavior of a time-harmonic wave in the stretched coordinate system as follows (detailed mathematical descriptions can be found in Kucukcoban and Kallivokas (2013, 2011); Kucukcoban (2010)):

$$e^{-ik\tilde{s}} e^{i\omega t} = \left[e^{-ik \int_0^s \alpha(s')ds'} \underbrace{e^{-\frac{1}{c} \int_0^s \beta(s')ds'}}_{\text{attenuating}} \right] e^{i\omega t}, \tag{3.6}$$

where $k = \omega/c$ denotes the wavenumber, and c the wave speed. As shown in Eq. (3.6), the propagating waves in the PML are subject to amplitude attenuation in their propagation direction due to the elongated coordinate. Here, the order of the magnitude of the attenuation—i.e., $1/c \int_0^s \beta(s')ds'$—is frequency-independent, and is controlled by the parameters used to define β_s.

3.2 Formulation of a PML-truncated domain

Kucukcoban and Kallivokas (2011, 2010) proposed a fully-mixed *unsymmetric* PML formulation for both plane-strain and axisymmetric problems. Displacement and stress fields were considered as primary fields in both the regular domain and PMLs. Kucukcoban and Kallivokas (2013) improved their work for plane-strain problems through providing a *symmetric* hybrid approach in which a mixed-field formulation in the PML was coupled with non-mixed displacement-based formulation in the regular domain. In this work, we are concerned with both plane-strain and axisymmetric problems. For plane-strain problems, we employ the

existing hybrid formulation as will be discussed in §3.2.1. For axisymmetric problems, we extend the existing mixed formulation (Kucukcoban, 2010) to the hybrid one using the same approach proposed by Kucukcoban and Kallivokas (2013) for plane-strain problems. This will be discussed in §3.2.2.

3.2.1 Hybrid formulation of PML-truncated domain in a plane-strain setting

3.2.1.1 The governing equations

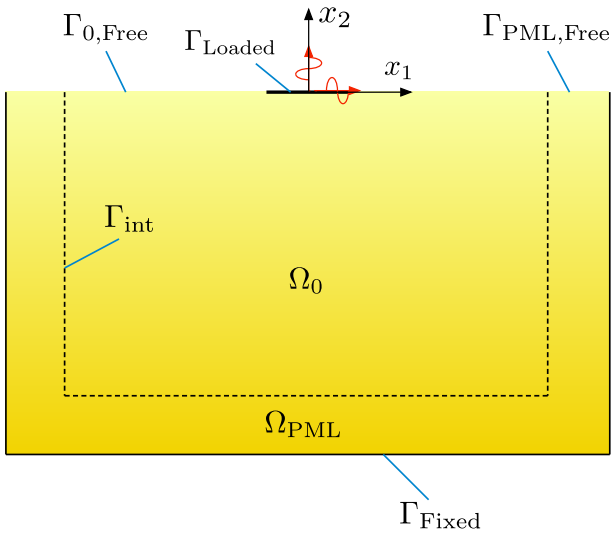

Figure 3.2: The problem geometry and boundary conditions of a PML-truncated domain in a plane-strain setting.

Considering a linear elastic solid medium in the plane-strain setting as shown in Figure 3.2, the elastic wave equation in the regular domain (Ω_0) is:

$$\text{div}(\boldsymbol{\sigma}) = \rho \ddot{\mathbf{u}}_{\text{a}}, \quad \boldsymbol{x} \in \Omega_0, (0, T], \tag{3.7}$$

where $\boldsymbol{x} = (x_1, x_2)$ and $(0, T]$ is the defined time interval; $\boldsymbol{\sigma} = \left[\mu \left(\nabla \mathbf{u}_{\text{a}} + (\nabla \mathbf{u}_{\text{a}})^T\right) + \lambda \, \text{div}(\mathbf{u}_{\text{a}})\mathbf{I}\right]$ is the stress tensor; and λ and μ are the Lamé constants for an elastic solid, and both can have arbitrary spatial variations. Their relationships with the Young's modulus (E) and the Poisson's ratio (ν) are given as $\lambda = \nu E/[(1+\nu)(1-2\nu)]$ and $\mu = E/[2(1+\nu)]$; ρ is the

mass density. The subscript 'a', in Eq. (3.7), denotes the variable of the equation satisfied in Ω_0; $\dot{(\,)}$ denotes the partial derivative of the subtended variable with respect to time.

In the PML domain $(\Omega \setminus \Omega_0)$ where the wave is attenuated, wave motion is governed by the following partial differential equations[1]:

$$\operatorname{div}\left(\dot{\boldsymbol{\mathcal{S}}}^T\tilde{\Lambda}_e + \boldsymbol{\mathcal{S}}^T\tilde{\Lambda}_p\right) - \rho\left(a\ddot{\mathbf{u}}_{\mathrm{b}} + b\dot{\mathbf{u}}_{\mathrm{b}} + c\mathbf{u}_{\mathrm{b}}\right) = \mathbf{0}, \quad \boldsymbol{x} \in \Omega \setminus \Omega_0, (0,T], \tag{3.8a}$$

$$\begin{aligned}&\Lambda_e^T(\mathcal{D} : \ddot{\boldsymbol{\mathcal{S}}})\Lambda_e + \Lambda_e^T(\mathcal{D} : \dot{\boldsymbol{\mathcal{S}}})\Lambda_p + \Lambda_p^T(\mathcal{D} : \dot{\boldsymbol{\mathcal{S}}})\Lambda_e + \Lambda_p^T(\mathcal{D} : \boldsymbol{\mathcal{S}})\Lambda_p \\ &-\frac{1}{2}\left[\Lambda_p^T\nabla\mathbf{u}_{\mathrm{b}} + (\nabla\mathbf{u}_{\mathrm{b}})^T\Lambda_p\right] - \frac{1}{2}\left[\Lambda_e^T\nabla\dot{\mathbf{u}}_{\mathrm{b}} + (\nabla\dot{\mathbf{u}}_{\mathrm{b}})^T\Lambda_e\right] = \mathbf{0}, \quad \boldsymbol{x} \in \Omega \setminus \Omega_0, (0,T],\end{aligned} \tag{3.8b}$$

where the subscript 'b' corresponds to the solution variables in the PML wave equation in $\Omega \setminus \Omega_0$; $\boldsymbol{\mathcal{S}}(\boldsymbol{x}, t)$ denotes the, so-called, stress-history tensor, defined as:

$$\boldsymbol{\mathcal{S}}(\boldsymbol{x}, t) = \begin{bmatrix} \mathcal{S}_{11}(\boldsymbol{x}, t) & \mathcal{S}_{12}(\boldsymbol{x}, t) \\ \mathcal{S}_{21}(\boldsymbol{x}, t) & \mathcal{S}_{22}(\boldsymbol{x}, t) \end{bmatrix} = \int_0^t \boldsymbol{\sigma}(\boldsymbol{x}, \tau)d\tau; \tag{3.9}$$

$\mathcal{D}(\boldsymbol{x})$ denotes the fourth-order compliance tensor; and (:) that follows $\mathcal{D}$ denotes the tensor operation such that the strain tensor can be obtained as:

$$\boldsymbol{\varepsilon}(\boldsymbol{x}, t) = \mathcal{D} : \dot{\boldsymbol{\mathcal{S}}}(\boldsymbol{x}, t), \tag{3.10}$$

or

$$\begin{bmatrix} \frac{\partial u_1}{\partial x_1}, & \frac{1}{2}\left(\frac{\partial u_1}{\partial x_2} + \frac{\partial u_2}{\partial x_1}\right) \\ \frac{1}{2}\left(\frac{\partial u_2}{\partial x_1} + \frac{\partial u_1}{\partial x_2}\right), & \frac{\partial u_2}{\partial x_2} \end{bmatrix} = \frac{1+\nu}{E}\begin{bmatrix} (1-\nu)\sigma_{11} - \nu\sigma_{22}, & \sigma_{12} \\ \sigma_{21}, & (1-\nu)\sigma_{22} - \nu\sigma_{11} \end{bmatrix}. \tag{3.11}$$

[1]As mentioned before, we adopt the PMLs suggested in Kucukcoban and Kallivokas (2013, 2011); Kucukcoban (2010), and its governing equations are recalled from Kucukcoban and Kallivokas (2013, 2011); Kucukcoban (2010) to the following Eqs. (3.8-3.11) in this work.

Coordinate stretching tensors Λ_e, Λ_p, $\tilde{\Lambda}_e$ and $\tilde{\Lambda}_p$ in Eq. (3.8) are defined as:

$$\Lambda_e = \begin{bmatrix} \alpha_1 & 0 \\ 0 & \alpha_2 \end{bmatrix}, \quad \Lambda_p = \begin{bmatrix} \beta_1 & 0 \\ 0 & \beta_2 \end{bmatrix}, \quad \tilde{\Lambda}_e = \begin{bmatrix} \alpha_2 & 0 \\ 0 & \alpha_1 \end{bmatrix}, \quad \tilde{\Lambda}_p = \begin{bmatrix} \beta_2 & 0 \\ 0 & \beta_1 \end{bmatrix}. \tag{3.12}$$

The following interface conditions are used to couple the two governing PDEs of Eqs. (3.7) and (3.8):

$$\mathbf{u}_{\mathrm{a}}(\boldsymbol{x}, t) = \mathbf{u}_{\mathrm{b}}(\boldsymbol{x}, t), \quad \boldsymbol{x} \in \Gamma_{\mathrm{int}}, (0, T], \tag{3.13}$$

$$\boldsymbol{\sigma}_{\mathrm{a}}(\boldsymbol{x}, t)\mathbf{n}_{\mathrm{a}} = -\left(\dot{\mathbf{S}}\tilde{\Lambda}_e + \mathbf{S}\tilde{\Lambda}_p\right)\mathbf{n}_{\mathrm{b}}, \quad \boldsymbol{x} \in \Gamma_{\mathrm{int}}, (0, T], \tag{3.14}$$

where $\mathbf{n}_a$ and $\mathbf{n}_b$ denote the normal vectors, on Γ_{int}, pointing from the regular domain to the PML domain and vice versa, respectively. The governing wave equations are also subject to the following boundary conditions:

$$\mathbf{u}_{\mathrm{b}}(\boldsymbol{x}, t) = \mathbf{0}, \quad \boldsymbol{x} \in \Gamma_{\mathrm{Fixed}}, (0, T], \tag{3.15a}$$

$$\mathbf{u}_{\mathrm{a}}(\boldsymbol{x}, t) = \mathbf{g}, \quad \boldsymbol{x} \in \Gamma_{\mathrm{Loaded}}, (0, T], \tag{3.15b}$$

$$\boldsymbol{\sigma}_{\mathrm{a}}(\boldsymbol{x}, t)\mathbf{n}_{\mathrm{a}} = \mathbf{0}, \quad \boldsymbol{x} \in \Gamma_{0,\mathrm{Free}}, (0, T], \tag{3.15c}$$

$$\left(\dot{\mathbf{S}}^T\tilde{\Lambda}_e + \mathbf{S}^T\tilde{\Lambda}_p\right)\mathbf{n}_{\mathrm{b}} = \mathbf{0}, \quad \boldsymbol{x} \in \Gamma_{\mathrm{PML,Free}}, (0, T], \tag{3.15d}$$

where the known displacement boundary condition $\mathbf{g}$ is imposed on Γ_{Loaded}; $\Gamma_{0,\mathrm{Free}}$ denotes the traction-free top surface that is attached to the regular domain only; $\Gamma_{\mathrm{PML,Free}}$ denotes the traction-free top surface that is attached to the PML domain.

3.2.1.2 The semi-discrete forms

The field variables of the two governing equations—i.e., Eqs. (3.7) and (3.8)—are approximated as follows:

$$\mathbf{u}(\boldsymbol{x},t) = \begin{bmatrix} u_1(\boldsymbol{x},t) \\ u_2(\boldsymbol{x},t) \end{bmatrix} \approx \begin{bmatrix} \boldsymbol{\Phi}(\boldsymbol{x})^T \mathbf{u}_1(t) \\ \boldsymbol{\Phi}(\boldsymbol{x})^T \mathbf{u}_2(t) \end{bmatrix},$$
$$\boldsymbol{\mathcal{S}}(\boldsymbol{x},t) = \begin{bmatrix} \mathcal{S}_{11}(\boldsymbol{x},t) & \mathcal{S}_{12}(\boldsymbol{x},t) \\ \mathcal{S}_{21}(\boldsymbol{x},t) & \mathcal{S}_{22}(\boldsymbol{x},t) \end{bmatrix} \approx \begin{bmatrix} \boldsymbol{\Psi}(\boldsymbol{x})^T \boldsymbol{\mathcal{S}}_{11}(t) & \boldsymbol{\Psi}(\boldsymbol{x})^T \boldsymbol{\mathcal{S}}_{12}(t) \\ \boldsymbol{\Psi}(\boldsymbol{x})^T \boldsymbol{\mathcal{S}}_{21}(t) & \boldsymbol{\Psi}(\boldsymbol{x})^T \boldsymbol{\mathcal{S}}_{22}(t) \end{bmatrix}, \tag{3.16}$$

where $\mathbf{u}_1(t)$, $\mathbf{u}_2(t)$, $\boldsymbol{\mathcal{S}}_{11}(t)$, $\boldsymbol{\mathcal{S}}_{22}(t)$, and $\boldsymbol{\mathcal{S}}_{12}(t)$ are the vectors of nodal solutions of $u_1(\boldsymbol{x},t)$, $u_2(\boldsymbol{x},t)$, $\mathcal{S}_{11}(\boldsymbol{x},t)$, $\mathcal{S}_{22}(\boldsymbol{x},t)$, and $\mathcal{S}_{12}(\boldsymbol{x},t)$. Then, the wave response of the soil model in Figure 3.2 can be obtained by solving the following semi-discrete system of equations:

$$\mathbf{M}\,\ddot{\mathbf{d}}(t) + \mathbf{C}\,\dot{\mathbf{d}}(t) + \mathbf{K}\,\mathbf{d}(t) = \mathbf{f}(t), \tag{3.17}$$

where $\mathbf{M}$, $\mathbf{C}$, and $\mathbf{K}$ denote the mass, damping, and stiffness matrices; $\mathbf{d}$ denotes the solution vector, i.e., $\mathbf{d}(t) = [\mathbf{u}_1^T(t), \mathbf{u}_2^T(t), \boldsymbol{\mathcal{S}}_{11}^T(t), \boldsymbol{\mathcal{S}}_{22}^T(t), \boldsymbol{\mathcal{S}}_{12}^T(t)]^T$; $\mathbf{f}$ denotes the force vector that corresponds to the known traction on the free surface. We note that soil heterogeneity is incorporated into the $\mathbf{M}$, $\mathbf{C}$, and $\mathbf{K}$ matrices when the element matrices are built through numerical integration. Detailed description of $\mathbf{M}$, $\mathbf{C}$, $\mathbf{K}$, and $\mathbf{f}$ can be found in Kucukcoban and Kallivokas (2013).

3.2.2 Hybrid formulation of PML-truncated domain in an axisymmetric setting

3.2.2.1 The governing equations

Considering a linear elastic solid medium in the axisymmetric setting as shown in Figure 3.3, the elastic wave equation in the regular domain (Ω_0) is:

$$\mathrm{div}\{\mu[\nabla\dot{\mathbf{u}}_\mathrm{a} + (\nabla\dot{\mathbf{u}}_\mathrm{a})^T] + \lambda\mathrm{div}(\dot{\mathbf{u}}_\mathrm{a})\mathbf{I}\} = \rho\ddot{\mathbf{u}}_\mathrm{a} \quad \boldsymbol{x} \in \Omega_0, (0,T] \tag{3.18}$$

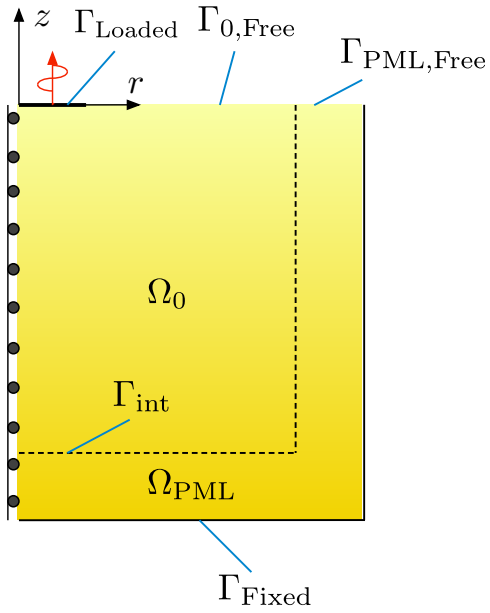

Figure 3.3: The problem geometry and boundary conditions of a PML-truncated domain in an axisymmetric setting.

where $\boldsymbol{x} = (r, z)$, and $\dddot{(\,)}$ denotes the third-order time derivative of the subtended variable. Other parameters are defined in the previous sections. In the PML domain $(\Omega \setminus \Omega_0)$, the wave motion is governed by (Kucukcoban, 2010):

$$
\begin{aligned}
&\operatorname{div}[\ddot{\boldsymbol{\mathcal{S}}}^T \tilde{\Lambda}_e + \dot{\boldsymbol{\mathcal{S}}}^T \tilde{\Lambda}_p + \boldsymbol{\mathcal{S}}^T \tilde{\Lambda}_w] = \rho(a\dddot{\mathbf{u}}_\mathrm{b} + b\ddot{\mathbf{u}}_\mathrm{b} + c\dot{\mathbf{u}}_\mathrm{b} + d\mathbf{u}_\mathrm{b}) \quad \boldsymbol{x} \in \Omega \setminus \Omega_0, (0, T] \\
&\mathcal{D} : [a\dddot{\boldsymbol{\mathcal{S}}} + b\ddot{\boldsymbol{\mathcal{S}}} + c\dot{\boldsymbol{\mathcal{S}}} + d\boldsymbol{\mathcal{S}}] = \\
&\frac{1}{2}[\nabla\ddot{\mathbf{u}}_\mathrm{b}\tilde{\Lambda}_e + \tilde{\Lambda}_e(\nabla\ddot{\mathbf{u}}_\mathrm{b})^T] + \frac{1}{2}[\nabla\dot{\mathbf{u}}_\mathrm{b}\tilde{\Lambda}_p + \tilde{\Lambda}_p(\nabla\dot{\mathbf{u}}_\mathrm{b})^T] + \frac{1}{2}[\nabla\mathbf{u}_\mathrm{b}\tilde{\Lambda}_w + \tilde{\Lambda}_w(\nabla\mathbf{u}_\mathrm{b})^T] \quad \boldsymbol{x} \in \Omega \setminus \Omega_0, (0, T]
\end{aligned}
\tag{3.19}
$$

where $\boldsymbol{\mathcal{S}}$ denotes the so-called stress-history tensor defined as:

$$
\boldsymbol{\mathcal{S}}(\boldsymbol{x}, t) = \int_0^t \begin{bmatrix} \sigma_{rr}(\boldsymbol{x}, \tau) & 0 & \sigma_{rz}(\boldsymbol{x}, \tau) \\ 0 & \sigma_{\theta\theta}(\boldsymbol{x}, \tau) & 0 \\ \sigma_{zr}(\boldsymbol{x}, \tau) & 0 & \sigma_{zz}(\boldsymbol{x}, \tau) \end{bmatrix} \mathrm{d}\tau \tag{3.20}
$$

and $\mathcal{D}$ is the fourth-order compliance tensor, relating the first time derivative of stress-history and strain tensors as in Eq. (3.21).

$$\boldsymbol{\varepsilon}(\boldsymbol{x},t) = \mathcal{D} : \dot{\boldsymbol{S}}(\boldsymbol{x},t) \tag{3.21}$$

or

$$\begin{bmatrix} \epsilon_{rr} & 0 & \epsilon_{rz} \\ 0 & \epsilon_{\theta\theta} & 0 \\ \epsilon_{zr} & 0 & \epsilon_{zz} \end{bmatrix} = \begin{bmatrix} D_1\sigma_{rr} - D_2(\sigma_{\theta\theta}+\sigma_{zz}) & 0 & \frac{1}{2\mu}\sigma_{rz} \\ 0 & D_1\sigma_{\theta\theta} - D_2(\sigma_{rr}+\sigma_{zz}) & 0 \\ \frac{1}{2\mu}\sigma_{zr} & 0 & D_1\sigma_{zz} - D_2(\sigma_{rr}+\sigma_{\theta\theta}) \end{bmatrix} \tag{3.22}$$

where

$$D_1 = \frac{\lambda+\mu}{\mu(3\lambda+2\mu)}, \quad D_2 = \frac{\lambda}{2\mu(3\lambda+2\mu)}. \tag{3.23}$$

Coordinate stretching tensors $\tilde{\Lambda}_e$, $\tilde{\Lambda}_p$ and $\tilde{\Lambda}_w$ in Eq. (3.19) are defined as (Kucukcoban, 2010):

$$\tilde{\Lambda}_e = \mathrm{diag}(\frac{\alpha_z\bar{\alpha}_r}{r}, \alpha_r\alpha_z, \frac{\alpha_r\bar{\alpha}_r}{r}), \tag{3.24}$$

$$\tilde{\Lambda}_p = \mathrm{diag}(\frac{\alpha_z\bar{\beta}_r + \bar{\alpha}_r\beta_z}{r}, \alpha_r\beta_z + \beta_r\alpha_z, \frac{\alpha_r\bar{\beta}_r + \bar{\alpha}_r\beta_r}{r}), \tag{3.25}$$

$$\tilde{\Lambda}_w = \mathrm{diag}(\frac{\beta_z\bar{\beta}_r}{r}, \beta_r\beta_z, \frac{\beta_r\bar{\beta}_r}{r}). \tag{3.26}$$

In regular domain $\tilde{\Lambda}_e$ reduces to Identity tensor, and $\tilde{\Lambda}_p$, and $\tilde{\Lambda}_w$ vanish. Parameters a, b, c and d in Eq. (3.19) are defined as:

$$a = \frac{\alpha_r\alpha_z\bar{\alpha}_r}{r}, \tag{3.27}$$

$$b = \frac{\alpha_r\alpha_z\bar{\beta}_r + \alpha_r\bar{\alpha}_r\beta_z + \bar{\alpha}_r\alpha_z\beta_r}{r}, \tag{3.28}$$

$$c = \frac{\alpha_r\beta_z\bar{\beta}_r + \alpha_z\beta_r\bar{\beta}_r + \bar{\alpha}_r\beta_r\beta_z}{r}, \tag{3.29}$$

$$d = \frac{\beta_r \beta_z \bar{\beta}_r}{r}. \tag{3.30}$$

The following interface conditions are used to couple the two governing PDEs of Eqs. (3.18) and (3.19):

$$\mathbf{u}_{\mathrm{a}} = \mathbf{u}_{\mathrm{b}} \quad \boldsymbol{x} \in \Gamma_{\mathrm{int}}, (0, T] \tag{3.31}$$

$$\mathrm{div}\{\mu[\nabla \dot{\mathbf{u}}_{\mathrm{a}} + (\nabla \dot{\mathbf{u}}_{\mathrm{a}})^T] + \lambda \mathrm{div}(\dot{\mathbf{u}}_{\mathrm{a}})\mathbf{I}\}\mathbf{n}_{\mathrm{a}} = -(\ddot{\boldsymbol{\mathcal{S}}}^T \tilde{\Lambda}_e + \dot{\boldsymbol{\mathcal{S}}}^T \tilde{\Lambda}_p + \boldsymbol{\mathcal{S}}^T \tilde{\Lambda}_w)\mathbf{n}_{\mathrm{b}} \quad \boldsymbol{x} \in \Gamma_{\mathrm{int}}, (0, T]. \tag{3.32}$$

The governing wave equations are also subject to the following boundary conditions:

$$\mathbf{u}_{\mathrm{b}} = 0 \quad \boldsymbol{x} \in \Gamma_{\mathrm{Fixed}}, (0, T] \tag{3.33}$$

$$(\ddot{\boldsymbol{\mathcal{S}}}^T \tilde{\Lambda}_e + \dot{\boldsymbol{\mathcal{S}}}^T \tilde{\Lambda}_p + \boldsymbol{\mathcal{S}}^T \tilde{\Lambda}_w)\mathbf{n}_{\mathrm{b}} = 0 \quad \boldsymbol{x} \in \Gamma_{\mathrm{PML,Free}}, (0, T] \tag{3.34}$$

$$\{\mu[\nabla \dot{\mathbf{u}}_{\mathrm{a}} + (\nabla \dot{\mathbf{u}}_{\mathrm{a}})^T] + \lambda \mathrm{div}(\dot{\mathbf{u}}_{\mathrm{a}})\mathbf{I}\}\mathbf{n}_{\mathrm{a}} = \dot{\mathbf{g}} \quad \boldsymbol{x} \in \Gamma_{\mathrm{Loaded}}, (0, T] \tag{3.35}$$

$$\{\mu[\nabla \dot{\mathbf{u}}_{\mathrm{a}} + (\nabla \dot{\mathbf{u}}_{\mathrm{a}})^T] + \lambda \mathrm{div}(\dot{\mathbf{u}}_{\mathrm{a}})\mathbf{I}\}\mathbf{n}_{\mathrm{a}} = 0 \quad \boldsymbol{x} \in \Gamma_{\mathrm{0,Free}}, (0, T] \tag{3.36}$$

where $\mathbf{g}$ is the known imposed traction on Γ_{Loaded}.

3.2.2.2 The semi-discrete forms

In order to solve the problem using the standard FEM, the field variables are approximated as:

$$\mathbf{u}(\boldsymbol{x}, t) \approx \begin{bmatrix} \boldsymbol{\Phi}^T \mathbf{u}_r(t) \\ \boldsymbol{\Phi}^T \mathbf{u}_z(t) \end{bmatrix}, \quad \boldsymbol{\mathcal{S}}(\boldsymbol{x}, t) \approx \begin{bmatrix} \boldsymbol{\Psi}^T \boldsymbol{\mathcal{S}}_{rr}(t) & 0 & \boldsymbol{\Psi}^T \boldsymbol{\mathcal{S}}_{rz}(t) \\ 0 & \boldsymbol{\Psi}^T \boldsymbol{\mathcal{S}}_{\theta\theta}(t) & 0 \\ \boldsymbol{\Psi}^T \boldsymbol{\mathcal{S}}_{zr}(t) & 0 & \boldsymbol{\Psi}^T \boldsymbol{\mathcal{S}}_{zz}(t) \end{bmatrix} \tag{3.37}$$

where $\mathbf{u}_r$, $\mathbf{u}_z$, $\boldsymbol{\mathcal{S}}_{rr}$, $\boldsymbol{\mathcal{S}}_{rz}$, $\boldsymbol{\mathcal{S}}_{zz}$, $\boldsymbol{\mathcal{S}}_{\theta\theta}$ are vectors of nodal solutions for the introduced field variables. $\boldsymbol{\Phi}$ and $\boldsymbol{\Psi}$ are the defined shape function vectors for displacement and stress-history fields, respectively. Using the introduced approximations in Eq. (3.37), the resulting semi-discrete

form of the system of equations in time for wave propagation within a PML-truncated domain can be written as:

$$\mathbf{M}\dddot{\mathbf{d}}(t) + \mathbf{C}\ddot{\mathbf{d}}(t) + \mathbf{K}\dot{\mathbf{d}}(t) + \mathbf{G}\mathbf{d}(t) = \dot{\mathbf{f}}(t) \tag{3.38}$$

where the symmetric matrices $\mathbf{M}$, $\mathbf{C}$, $\mathbf{K}$ and $\mathbf{G}$, and the force vector $\mathbf{f}$ are defined in Appendix A; $\mathbf{d}$ denotes the solution vector—i.e. $\mathbf{d}(t) = \left[\mathbf{u}_r^T(t), \mathbf{u}_z^T(t), \mathbf{s}_{rr}^T(t), \mathbf{s}_{\theta\theta}^T(t), \mathbf{s}_{zz}^T(t), \mathbf{s}_{rz}^T(t)\right]^T$.

3.3 DRM formulation in a PML-truncated domain

In order to compute the modified input motions and KITFs, we extend the hybrid PML formulation in plane-strain setting such that the effective forces associated with the seismic excitations can be incorporated. Considering a semi-infinite domain with localized near-field features under remote seismic excitation (as shown in Figure 3.4a) and the same semi-infinite domain with no localized features (as shown in Figure 3.4b), the total-field and free-field elastic wave equations are:

$$\mathrm{div}\left\{\mu\left[\nabla\mathbf{u}_{\mathrm{free}} + (\nabla\mathbf{u}_{\mathrm{free}})^T\right] + \lambda\mathrm{div}(\mathbf{u}_{\mathrm{free}})\mathbf{I}\right\} = \rho\ddot{\mathbf{u}}_{\mathrm{free}}, \quad \boldsymbol{x} \in \Omega, (0, T], \tag{3.39}$$

$$\mathrm{div}\left\{\mu\left[\nabla\mathbf{u}_{\mathrm{total}} + (\nabla\mathbf{u}_{\mathrm{total}})^T\right] + \lambda\mathrm{div}(\mathbf{u}_{\mathrm{total}})\mathbf{I}\right\} = \rho\ddot{\mathbf{u}}_{\mathrm{total}}, \quad \boldsymbol{x} \in \Omega, (0, T]. \tag{3.40}$$

As discussed in Chapter 2, when the semi-infinite domain is truncated by ABCs, it is not straightforward to use the remote excitation input that is embarked from the outside of the ABC for modeling of wave response $\mathbf{u}_{\mathrm{total}}$ within a truncated domain. To address this challenge, the DRM proposed by Bielak et al. (2003) can be used, which is shown schematically in Figure 3.4c. The governing wave equation is:

$$\mathrm{div}\left\{\mu\left[\nabla\mathbf{u} + (\nabla\mathbf{u})^T\right] + \lambda\mathrm{div}(\mathbf{u})\mathbf{I}\right\} = \rho\ddot{\mathbf{u}} \quad \boldsymbol{x} \in \Omega_{\mathrm{N}} \cup \Omega_{\mathrm{L}}, (0, T], \tag{3.41}$$

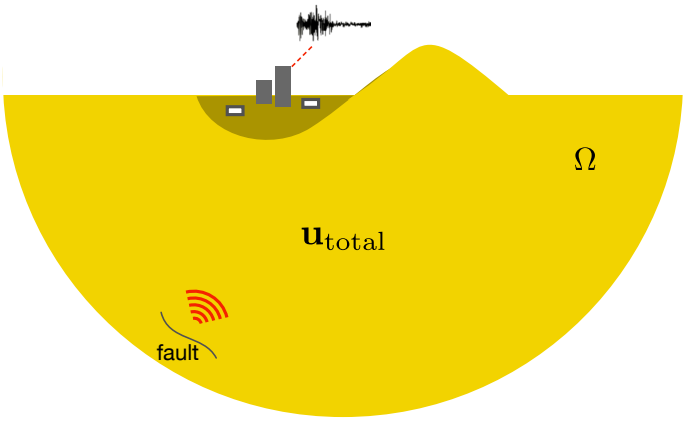

(a) Semi-infinite domain with a localized feature

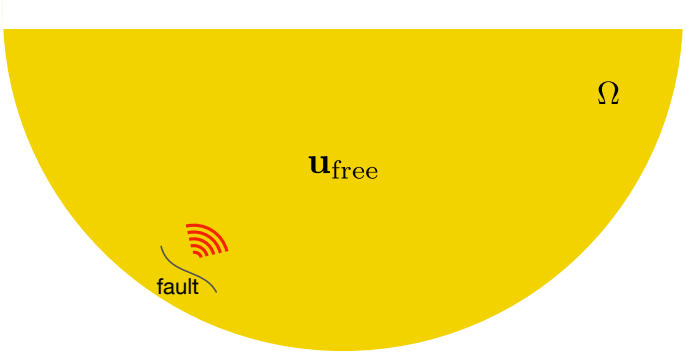

(b) Semi-infinite domain without localized feature

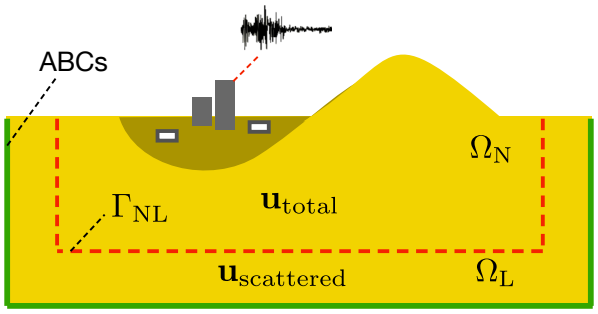

(c) Truncated domain with a localized feature enclosed by ABCs

Figure 3.4: (a) The total-field displacement $\mathbf{u}_{\text{total}} = \mathbf{u}_{\text{free}} + \mathbf{u}_{\text{scattered}}$ around structures due to the soil-structure interaction induced by the remote seismic excitation in a semi-infinite domain; (b) the free-field displacement $\mathbf{u}_{\text{free}}$ due to remote seismic excitation in a semi-infinite domain; (c) the DRM modeling approach for a domain truncated by ABCs (adopted from Bielak et al. (2003)).

with the response field $\mathbf{u}$ defined as follows:

$$\mathbf{u} := \mathbf{u}_{\text{total}} \quad \boldsymbol{x} \in \Omega_{\text{N}}, (0, T], \tag{3.42a}$$

$$\mathbf{u} := \mathbf{u}_{\text{total}} - \mathbf{u}_{\text{free}} \quad \boldsymbol{x} \in \Omega_{\text{L}}, (0, T]. \tag{3.42b}$$

$\mathbf{u}$, defined in Eqs. (3.42a) and (3.42b), is discontinuous on Γ_{NL}, the interface between Ω_{N} and Ω_{L}, which denote, respectively, the domain near the localized feature and the domain surrounding the Ω_{N}. Moreover, the scattered motion $\mathbf{u}_{\text{scattered}} = \mathbf{u}_{\text{total}} - \mathbf{u}_{\text{free}}$, satisfies the radiation condition. Therefore, the equation in terms of $\mathbf{u}$, defined in Eq. (3.42), can be solved in a domain of the semi-infinite extent, truncated by ABCs. As will be shown later, the aforementioned discontinuity (a.k.a. the jump condition (Bielak and Christiano, 1984)) serves as a driving or effective force vector.

3.3.1 Governing equations of the scattered field in a PML-truncated domain

To address the scattered wave field that includes the jump condition and uses PML as ABC (as shown schematically in Figure 3.5), the following wave equations are considered:

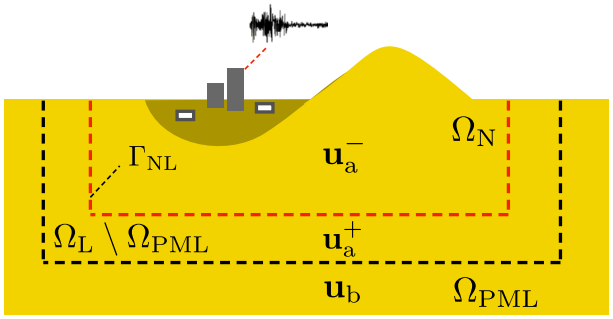

Figure 3.5: Schematic scattering problem modeled in a PML-truncated domain.

$$\text{div}\left\{\mu\left[\nabla\mathbf{u}_{\text{a}}^{-} + (\nabla\mathbf{u}_{\text{a}}^{-})^{T}\right] + \lambda\text{div}(\mathbf{u}_{\text{a}}^{-})\mathbf{I}\right\} = \rho\ddot{\mathbf{u}}_{\text{a}}^{-} \quad \boldsymbol{x} \in \Omega_{\text{N}}, (0, T], \tag{3.43a}$$

$$\text{div}\left\{\mu\left[\nabla\mathbf{u}_{\text{a}}^{+} + (\nabla\mathbf{u}_{\text{a}}^{+})^{T}\right] + \lambda\text{div}(\mathbf{u}_{\text{a}}^{+})\mathbf{I}\right\} = \rho\ddot{\mathbf{u}}_{\text{a}}^{+} \quad \boldsymbol{x} \in \Omega_{\text{L}} \setminus \Omega_{\text{PML}}, (0, T], \tag{3.43b}$$

$$\text{div}\left(\dot{\mathbf{S}}^{T}\tilde{\Lambda}_{e} + \mathbf{S}^{T}\tilde{\Lambda}_{p}\right) - \rho\left(a\ddot{\mathbf{u}}_{\text{b}} + b\dot{\mathbf{u}}_{\text{b}} + c\mathbf{u}_{\text{b}}\right) = \mathbf{0} \quad \boldsymbol{x} \in \Omega_{\text{PML}}, (0, T], \tag{3.43c}$$

$$
\begin{aligned}
&\Lambda_e^T(\mathcal{D}:\ddot{\boldsymbol{\mathcal{S}}})\Lambda_e + \Lambda_e^T(\mathcal{D}:\dot{\boldsymbol{\mathcal{S}}})\Lambda_p + \Lambda_p^T(\mathcal{D}:\dot{\boldsymbol{\mathcal{S}}})\Lambda_e + \Lambda_p^T(\mathcal{D}:\boldsymbol{\mathcal{S}})\Lambda_p \\
=&\frac{1}{2}\left[\Lambda_p^T\nabla\mathbf{u}_{\mathrm{b}} + (\nabla\mathbf{u}_{\mathrm{b}})^T\Lambda_p\right] + \frac{1}{2}\left[\Lambda_e^T\nabla\dot{\mathbf{u}}_{\mathrm{b}} + (\nabla\dot{\mathbf{u}}_{\mathrm{b}})^T\Lambda_e\right] \quad \boldsymbol{x}\in\Omega_{\mathrm{PML}}, (0,T], \qquad (3.43\mathrm{d})
\end{aligned}
$$

where the subscripts 'a' and 'b', in Eq. (3.43), denote the variables of the equations satisfied in $\Omega\setminus\Omega_{\mathrm{PML}}$ and Ω_{PML}, respectively. The superscripts '–' and '+' denote the total and scattered fields in Ω_{N} (per Eq. (3.43a)) and $\Omega_{\mathrm{L}}\setminus\Omega_{\mathrm{PML}}$ (per Eq. (3.43b)), respectively. $\boldsymbol{\mathcal{S}} = \int_0^t \boldsymbol{\sigma}_b(\tau)d\tau$ is the stress-history tensor corresponding to the scattered fields $\mathbf{u}_{\mathrm{b}}$ and $\boldsymbol{\sigma}_b$.

3.3.2 The semi-discrete form

Again, we introduce the Galerkin approximation of the solution variables as:

$$
\begin{aligned}
\mathbf{u}_{\mathrm{a}}^-(\boldsymbol{x},t) &= \begin{bmatrix} u_{a_1}^-(\boldsymbol{x},t) \\ u_{a_2}^-(\boldsymbol{x},t) \end{bmatrix} \approx \begin{bmatrix} \boldsymbol{\Phi}^-(\boldsymbol{x})^T\mathbf{u}_{a_1}^-(t) \\ \boldsymbol{\Phi}^-(\boldsymbol{x})^T\mathbf{u}_{a_2}^-(t) \end{bmatrix}, \\
\mathbf{u}_{\mathrm{a}}^+(\boldsymbol{x},t) &= \begin{bmatrix} u_{a_1}^+(\boldsymbol{x},t) \\ u_{a_2}^+(\boldsymbol{x},t) \end{bmatrix} \approx \begin{bmatrix} \boldsymbol{\Phi}^+(\boldsymbol{x})^T\mathbf{u}_{a_1}^+(t) \\ \boldsymbol{\Phi}^+(\boldsymbol{x})^T\mathbf{u}_{a_2}^+(t) \end{bmatrix}, \\
\mathbf{u}_{\mathrm{b}}(\boldsymbol{x},t) &= \begin{bmatrix} u_{b_1}(\boldsymbol{x},t) \\ u_{b_2}(\boldsymbol{x},t) \end{bmatrix} \approx \begin{bmatrix} \boldsymbol{\Phi}^+(\boldsymbol{x})^T\mathbf{u}_{b_1}(t) \\ \boldsymbol{\Phi}^+(\boldsymbol{x})^T\mathbf{u}_{b_2}(t) \end{bmatrix}, \\
\boldsymbol{\mathcal{S}}(\boldsymbol{x},t) &= \begin{bmatrix} \mathcal{S}_{11}(\boldsymbol{x},t) & \mathcal{S}_{12}(\boldsymbol{x},t) \\ \mathcal{S}_{21}(\boldsymbol{x},t) & \mathcal{S}_{22}(\boldsymbol{x},t) \end{bmatrix} \approx \begin{bmatrix} \boldsymbol{\Psi}(\boldsymbol{x})^T\boldsymbol{\mathcal{S}}_{11}(t) & \boldsymbol{\Psi}(\boldsymbol{x})^T\boldsymbol{\mathcal{S}}_{12}(t) \\ \boldsymbol{\Psi}(\boldsymbol{x})^T\boldsymbol{\mathcal{S}}_{21}(t) & \boldsymbol{\Psi}(\boldsymbol{x})^T\boldsymbol{\mathcal{S}}_{22}(t) \end{bmatrix}, \qquad (3.44)
\end{aligned}
$$

where $\boldsymbol{\Phi}^-$, $\boldsymbol{\Phi}^+$, and $\boldsymbol{\Psi}$ denote the shape function vectors to approximate the solutions. The semi-discrete form of Eq. (3.43a) is:

$$
\begin{bmatrix} \mathbf{M}_{u_1u_1}^- & 0 \\ 0 & \mathbf{M}_{u_2u_2}^- \end{bmatrix} \begin{bmatrix} \ddot{\mathbf{u}}_{\mathrm{a}_1}^- \\ \ddot{\mathbf{u}}_{\mathrm{a}_2}^- \end{bmatrix} + \begin{bmatrix} \mathbf{K}_{u_1u_1}^- & \mathbf{K}_{u_1u_2}^- \\ \mathbf{K}_{u_2u_1}^- & \mathbf{K}_{u_2u_2}^- \end{bmatrix} \begin{bmatrix} \mathbf{u}_{\mathrm{a}_1}^- \\ \mathbf{u}_{\mathrm{a}_2}^- \end{bmatrix} = \begin{bmatrix} \int_{\Gamma_{\mathrm{NL}}} \boldsymbol{\Phi}^- T_1^- d\Gamma \\ \int_{\Gamma_{\mathrm{NL}}} \boldsymbol{\Phi}^- T_2^- d\Gamma \end{bmatrix} \qquad (3.45)
$$

where T_1^- (or T_2^-) denotes the x_1 (or x_2) component of a traction $\mathbf{T}^- = \sigma^-\mathbf{n}^-$ on the boundary Γ_{NL}; $\mathbf{n}^-$ is an outward unit normal vector from Ω_{N} on Γ_{NL}.

The semi-discrete form of Eqs. (3.43b), (3.43c), and (3.43d) is:

$$
\begin{bmatrix}
\mathbf{M}^+_{u_1u_1} & 0 & 0 & 0 & 0 \\
0 & \mathbf{M}^+_{u_2u_2} & 0 & 0 & 0 \\
0 & 0 & \mathbf{M}^+_{\mathcal{S}_{11}\mathcal{S}_{11}} & \mathbf{M}^+_{\mathcal{S}_{11}\mathcal{S}_{22}} & 0 \\
0 & 0 & \mathbf{M}^+_{\mathcal{S}_{22}\mathcal{S}_{11}} & \mathbf{M}^+_{\mathcal{S}_{22}\mathcal{S}_{22}} & 0 \\
0 & 0 & 0 & 0 & \mathbf{M}^+_{\mathcal{S}_{12}\mathcal{S}_{12}}
\end{bmatrix}
\begin{bmatrix}
\ddot{\mathbf{u}}^+_1 \\ \ddot{\mathbf{u}}^+_2 \\ \ddot{\boldsymbol{\mathcal{S}}}_{11} \\ \ddot{\boldsymbol{\mathcal{S}}}_{22} \\ \ddot{\boldsymbol{\mathcal{S}}}_{12}
\end{bmatrix}
$$

$$
+
\begin{bmatrix}
\mathbf{C}^+_{u_1u_1} & 0 & \mathbf{C}^+_{u_1\mathcal{S}_{11}} & 0 & \mathbf{C}^+_{u_1\mathcal{S}_{21}} \\
0 & \mathbf{C}^+_{u_2u_2} & 0 & \mathbf{C}^+_{u_2\mathcal{S}_{22}} & \mathbf{C}^+_{u_2\mathcal{S}_{12}} \\
\mathbf{C}^+_{\mathcal{S}_{11}u_1} & 0 & \mathbf{C}^+_{\mathcal{S}_{11}\mathcal{S}_{11}} & \mathbf{C}^+_{\mathcal{S}_{11}\mathcal{S}_{22}} & 0 \\
0 & \mathbf{C}^+_{\mathcal{S}_{22}u_2} & \mathbf{C}^+_{\mathcal{S}_{22}\mathcal{S}_{11}} & \mathbf{C}^+_{\mathcal{S}_{22}\mathcal{S}_{22}} & 0 \\
\mathbf{C}^+_{\mathcal{S}_{12}u_1} & \mathbf{C}^+_{\mathcal{S}_{12}u_2} & 0 & 0 & \mathbf{C}^+_{\mathcal{S}_{12}\mathcal{S}_{12}}
\end{bmatrix}
\begin{bmatrix}
\dot{\mathbf{u}}^+_1 \\ \dot{\mathbf{u}}^+_2 \\ \dot{\boldsymbol{\mathcal{S}}}_{11} \\ \dot{\boldsymbol{\mathcal{S}}}_{22} \\ \dot{\boldsymbol{\mathcal{S}}}_{12}
\end{bmatrix}
$$

$$
+
\begin{bmatrix}
\mathbf{K}^+_{u_1u_1} & \mathbf{K}^+_{u_1u_2} & \mathbf{K}^+_{u_1\mathcal{S}_{11}} & 0 & \mathbf{K}^+_{u_1\mathcal{S}_{21}} \\
\mathbf{K}^+_{u_2u_1} & \mathbf{K}^+_{u_2u_2} & 0 & \mathbf{K}^+_{u_2\mathcal{S}_{22}} & \mathbf{K}^+_{u_2\mathcal{S}_{12}} \\
\mathbf{K}^+_{\mathcal{S}_{11}u_1} & 0 & \mathbf{K}^+_{\mathcal{S}_{11}\mathcal{S}_{11}} & \mathbf{K}^+_{\mathcal{S}_{11}\mathcal{S}_{22}} & 0 \\
0 & \mathbf{K}^+_{\mathcal{S}_{22}u_2} & \mathbf{K}^+_{\mathcal{S}_{22}\mathcal{S}_{11}} & \mathbf{K}^+_{\mathcal{S}_{22}\mathcal{S}_{22}} & 0 \\
\mathbf{K}^+_{\mathcal{S}_{12}u_1} & \mathbf{K}^+_{\mathcal{S}_{12}u_2} & 0 & 0 & \mathbf{K}^+_{\mathcal{S}_{12}\mathcal{S}_{12}}
\end{bmatrix}
\begin{bmatrix}
\mathbf{u}^+_1 \\ \mathbf{u}^+_2 \\ \boldsymbol{\mathcal{S}}_{11} \\ \boldsymbol{\mathcal{S}}_{22} \\ \boldsymbol{\mathcal{S}}_{12}
\end{bmatrix}
=
\begin{bmatrix}
\int_{\Gamma_{\mathrm{NL}}} \boldsymbol{\Phi}^+ T^+_1 d\Gamma \\
\int_{\Gamma_{\mathrm{NL}}} \boldsymbol{\Phi}^+ T^+_2 d\Gamma \\
0 \\ 0 \\ 0
\end{bmatrix}
\tag{3.46}
$$

where $\mathbf{u}^+_1$ and $\mathbf{u}^+_2$ denote the following vectors:

$$
\mathbf{u}^+_1 = \begin{bmatrix} \mathbf{u}^+_{\mathrm{a}_1} \\ \mathbf{u}_{\mathrm{b}_1} \end{bmatrix}, \quad \mathbf{u}^+_2 = \begin{bmatrix} \mathbf{u}^+_{\mathrm{a}_2} \\ \mathbf{u}_{\mathrm{b}_2} \end{bmatrix}, \tag{3.47}
$$

and T^+_1 (or T^+_2) denotes the x_1 (or x_2) component of a traction $\mathbf{T}^+ = \sigma^+ \mathbf{n}^+$ on the boundary Γ_{NL}; $\mathbf{n}^+$ is an outward unit normal vector from Ω_{L} on Γ_{NL}.

Now, we repartition Eqs. (3.45) and (3.46) by separating DOFs on Γ_{NL} from the other

DOFs, which results in:

$$\begin{bmatrix} \mathbf{M}^{-}_{\Omega_{\mathrm{N}}\setminus\Gamma_{\mathrm{NL}}} & \mathbf{M}^{-}_{(\Omega_{\mathrm{N}}\setminus\Gamma_{\mathrm{NL}}),\Gamma_{\mathrm{NL}}} \\ \mathbf{M}^{-}_{\Gamma_{\mathrm{NL}},(\Omega_{\mathrm{N}}\setminus\Gamma_{\mathrm{NL}})} & \mathbf{M}^{-}_{\Gamma_{\mathrm{NL}}} \end{bmatrix} \begin{bmatrix} \ddot{\mathbf{u}}^{-}_{\mathrm{a}}(\Omega_{\mathrm{N}}\setminus\Gamma_{\mathrm{NL}}) \\ \ddot{\mathbf{u}}^{-}_{\mathrm{a}}(\Gamma_{\mathrm{NL}}) \end{bmatrix}$$
$$+ \begin{bmatrix} \mathbf{K}^{-}_{\Omega_{\mathrm{N}}\setminus\Gamma_{\mathrm{NL}}} & \mathbf{K}^{-}_{(\Omega_{\mathrm{N}}\setminus\Gamma_{\mathrm{NL}}),\Gamma_{\mathrm{NL}}} \\ \mathbf{K}^{-}_{\Gamma_{\mathrm{NL}},(\Omega_{\mathrm{N}}\setminus\Gamma_{\mathrm{NL}})} & \mathbf{K}^{-}_{\Gamma_{\mathrm{NL}}} \end{bmatrix} \begin{bmatrix} \mathbf{u}^{-}_{\mathrm{a}}(\Omega_{\mathrm{N}}\setminus\Gamma_{\mathrm{NL}}) \\ \mathbf{u}^{-}_{\mathrm{a}}(\Gamma_{\mathrm{NL}}) \end{bmatrix} = \begin{bmatrix} \mathbf{0} \\ \mathbf{f}^{-}_{\Gamma_{\mathrm{NL}}} \end{bmatrix}, \tag{3.48}$$

and

$$\begin{bmatrix} \mathbf{M}^{+}_{\Gamma_{\mathrm{NL}}} & \mathbf{M}^{+}_{\Gamma_{\mathrm{NL}},(\Omega_{\mathrm{L}}\setminus\Gamma_{\mathrm{NL}})} \\ \mathbf{M}^{+}_{(\Omega_{\mathrm{L}}\setminus\Gamma_{\mathrm{NL}}),\Gamma_{\mathrm{NL}}} & \mathbf{M}^{+}_{(\Omega_{\mathrm{L}}\setminus\Gamma_{\mathrm{NL}})} \end{bmatrix} \begin{bmatrix} \ddot{\mathbf{u}}^{+}_{\mathrm{a}}(\Gamma_{\mathrm{NL}}) \\ \ddot{\mathbf{sv}}^{+}(\Omega_{\mathrm{L}}\setminus\Gamma_{\mathrm{NL}}) \end{bmatrix}$$
$$+ \begin{bmatrix} \mathbf{C}^{+}_{\Gamma_{\mathrm{NL}}} & \mathbf{C}^{+}_{\Gamma_{\mathrm{NL}},(\Omega_{\mathrm{L}}\setminus\Gamma_{\mathrm{NL}})} \\ \mathbf{C}^{+}_{(\Omega_{\mathrm{L}}\setminus\Gamma_{\mathrm{NL}}),\Gamma_{\mathrm{NL}}} & \mathbf{C}^{+}_{(\Omega_{\mathrm{L}}\setminus\Gamma_{\mathrm{NL}})} \end{bmatrix} \begin{bmatrix} \dot{\mathbf{u}}^{+}_{\mathrm{a}}(\Gamma_{\mathrm{NL}}) \\ \dot{\mathbf{sv}}^{+}(\Omega_{\mathrm{L}}\setminus\Gamma_{\mathrm{NL}}) \end{bmatrix}$$
$$+ \begin{bmatrix} \mathbf{K}^{+}_{\Gamma_{\mathrm{NL}}} & \mathbf{K}^{+}_{\Gamma_{\mathrm{NL}},(\Omega_{\mathrm{L}}\setminus\Gamma_{\mathrm{NL}})} \\ \mathbf{K}^{+}_{(\Omega_{\mathrm{L}}\setminus\Gamma_{\mathrm{NL}}),\Gamma_{\mathrm{NL}}} & \mathbf{K}^{+}_{(\Omega_{\mathrm{L}}\setminus\Gamma_{\mathrm{NL}})} \end{bmatrix} \begin{bmatrix} \mathbf{u}^{+}_{\mathrm{a}}(\Gamma_{\mathrm{NL}}) \\ \mathbf{sv}^{+}(\Omega_{\mathrm{L}}\setminus\Gamma_{\mathrm{NL}}) \end{bmatrix} = \begin{bmatrix} \mathbf{f}^{+}_{\Gamma_{\mathrm{NL}}} \\ 0 \end{bmatrix}. \tag{3.49}$$

$\mathbf{u}^{-}_{\mathrm{a}}(\Gamma_{\mathrm{NL}})$ denotes a vector of the total field displacement only at the nodes on Γ_{NL}; $\mathbf{u}^{+}_{\mathrm{a}}(\Gamma_{\mathrm{NL}})$ denotes vector of the scattered field displacement only at the nodes on Γ_{NL}; $\mathbf{sv}^{+}(\Omega_{\mathrm{L}}\setminus\Gamma_{\mathrm{NL}})$ denotes a vector of the components of $\mathbf{sv}^{+}$ except for $\mathbf{u}^{+}_{\mathrm{a}}$ at the nodes on Γ_{NL}. $\mathbf{f}^{+}_{\Gamma_{\mathrm{NL}}}$ and $\mathbf{f}^{-}_{\Gamma_{\mathrm{NL}}}$ are, respectively, parts of the following vectors:

$$\begin{bmatrix} \int_{\Gamma_{\mathrm{NL}}} \mathbf{\Phi}^{+} T_1^{+} d\Gamma \\ \int_{\Gamma_{\mathrm{NL}}} \mathbf{\Phi}^{+} T_2^{+} d\Gamma \end{bmatrix}, \quad \begin{bmatrix} \int_{\Gamma_{\mathrm{NL}}} \mathbf{\Phi}^{-} T_1^{-} d\Gamma \\ \int_{\Gamma_{\mathrm{NL}}} \mathbf{\Phi}^{-} T_2^{-} d\Gamma \end{bmatrix}. \tag{3.50}$$

Considering $\mathbf{u}^{-}_{\mathrm{a}}(\Gamma_{\mathrm{NL}}) = \mathbf{u}^{+}_{\mathrm{a}}(\Gamma_{\mathrm{NL}}) + \mathbf{u}_{\mathrm{free}}(\Gamma_{\mathrm{NL}})$, the terms associated with *known* free field motions—i.e. $\mathbf{u}_{\mathrm{free}}(\Gamma_{\mathrm{NL}})$—can be moved from the left hand side of Eq. (3.49) to the right hand side, which results in:

$$\begin{bmatrix} \mathbf{M}^{+}_{\Gamma_{\mathrm{NL}}} & \mathbf{M}^{+}_{\Gamma_{\mathrm{NL}},(\Omega_{\mathrm{L}}\setminus\Gamma_{\mathrm{NL}})} \\ \mathbf{M}^{+}_{(\Omega_{\mathrm{L}}\setminus\Gamma_{\mathrm{NL}}),\Gamma_{\mathrm{NL}}} & \mathbf{M}^{+}_{(\Omega_{\mathrm{L}}\setminus\Gamma_{\mathrm{NL}})} \end{bmatrix} \begin{bmatrix} \ddot{\mathbf{u}}^{-}_{\mathrm{a}}(\Gamma_{\mathrm{NL}}) \\ \ddot{\mathbf{sv}}^{+}(\Omega_{\mathrm{L}}\setminus\Gamma_{\mathrm{NL}}) \end{bmatrix}$$

$$
+\begin{bmatrix} \mathbf{C}^{+}_{\Gamma_{\mathrm{NL}}} & \mathbf{C}^{+}_{\Gamma_{\mathrm{NL}},(\Omega_{\mathrm{L}}\setminus\Gamma_{\mathrm{NL}})} \\ \mathbf{C}^{+}_{(\Omega_{\mathrm{L}}\setminus\Gamma_{\mathrm{NL}}),\Gamma_{\mathrm{NL}}} & \mathbf{C}^{+}_{(\Omega_{\mathrm{L}}\setminus\Gamma_{\mathrm{NL}})} \end{bmatrix} \begin{bmatrix} \dot{\mathbf{u}}^{-}_{\mathrm{a}}(\Gamma_{\mathrm{NL}}) \\ \dot{\mathbf{sv}}^{+}(\Omega_{\mathrm{L}}\setminus\Gamma_{\mathrm{NL}}) \end{bmatrix}
$$

$$
+\begin{bmatrix} \mathbf{K}^{+}_{\Gamma_{\mathrm{NL}}} & \mathbf{K}^{+}_{\Gamma_{\mathrm{NL}},(\Omega_{\mathrm{L}}\setminus\Gamma_{\mathrm{NL}})} \\ \mathbf{K}^{+}_{(\Omega_{\mathrm{L}}\setminus\Gamma_{\mathrm{NL}}),\Gamma_{\mathrm{NL}}} & \mathbf{K}^{+}_{(\Omega_{\mathrm{L}}\setminus\Gamma_{\mathrm{NL}})} \end{bmatrix} \begin{bmatrix} \mathbf{u}^{-}_{\mathrm{a}}(\Gamma_{\mathrm{NL}}) \\ \mathbf{sv}^{+}(\Omega_{\mathrm{L}}\setminus\Gamma_{\mathrm{NL}}) \end{bmatrix}
$$

$$
=\begin{bmatrix} \mathbf{f}^{+}_{\Gamma_{\mathrm{NL}}} + \mathbf{M}^{+}_{\Gamma_{\mathrm{NL}}}\ddot{\mathbf{u}}_{\mathrm{free}}(\Gamma_{\mathrm{NL}}) + \mathbf{C}^{+}_{\Gamma_{\mathrm{NL}}}\dot{\mathbf{u}}_{\mathrm{free}}(\Gamma_{\mathrm{NL}}) + \mathbf{K}^{+}_{\Gamma_{\mathrm{NL}}}\mathbf{u}_{\mathrm{free}}(\Gamma_{\mathrm{NL}}) \\ \mathbf{M}^{+}_{(\Omega_{\mathrm{L}}\setminus\Gamma_{\mathrm{NL}}),\Gamma_{\mathrm{NL}}}\ddot{\mathbf{u}}_{\mathrm{free}}(\Gamma_{\mathrm{NL}}) + \mathbf{C}^{+}_{(\Omega_{\mathrm{L}}\setminus\Gamma_{\mathrm{NL}}),\Gamma_{\mathrm{NL}}}\dot{\mathbf{u}}_{\mathrm{free}}(\Gamma_{\mathrm{NL}}) + \mathbf{K}^{+}_{(\Omega_{\mathrm{L}}\setminus\Gamma_{\mathrm{NL}}),\Gamma_{\mathrm{NL}}}\mathbf{u}_{\mathrm{free}}(\Gamma_{\mathrm{NL}}) \end{bmatrix}. \quad (3.51)
$$

Since the solution vectors in Eqs. (3.48) and (3.51) share $\mathbf{u}^{-}_{\mathrm{a}}(\Gamma_{\mathrm{NL}})$, Eqs. (3.48) and (3.51) can be coupled to the following form:

$$
\begin{bmatrix} \mathbf{M}^{-}_{\Omega_{\mathrm{N}}\setminus\Gamma_{\mathrm{NL}}} & \mathbf{M}^{-}_{(\Omega_{\mathrm{N}}\setminus\Gamma_{\mathrm{NL}}),\Gamma_{\mathrm{NL}}} & 0 \\ \mathbf{M}^{-}_{\Gamma_{\mathrm{NL}},(\Omega_{\mathrm{N}}\setminus\Gamma_{\mathrm{NL}})} & \mathbf{M}^{-}_{\Gamma_{\mathrm{NL}}} + \mathbf{M}^{+}_{\Gamma_{\mathrm{NL}}} & \mathbf{M}^{+}_{\Gamma_{\mathrm{NL}},(\Omega_{\mathrm{L}}\setminus\Gamma_{\mathrm{NL}})} \\ 0 & \mathbf{M}^{+}_{(\Omega_{\mathrm{L}}\setminus\Gamma_{\mathrm{NL}}),\Gamma_{\mathrm{NL}}} & \mathbf{M}^{+}_{(\Omega_{\mathrm{L}}\setminus\Gamma_{\mathrm{NL}})} \end{bmatrix} \begin{bmatrix} \ddot{\mathbf{u}}^{-}_{\mathrm{a}}(\Omega_{\mathrm{N}}\setminus\Gamma_{\mathrm{NL}}) \\ \ddot{\mathbf{u}}^{-}_{\mathrm{a}}(\Gamma_{\mathrm{NL}}) \\ \ddot{\mathbf{sv}}^{+}(\Omega_{\mathrm{L}}\setminus\Gamma_{\mathrm{NL}}) \end{bmatrix}
$$

$$
+\begin{bmatrix} \mathbf{0} & \mathbf{0} & \mathbf{0} \\ \mathbf{0} & \mathbf{C}^{+}_{\Gamma_{\mathrm{NL}}} & \mathbf{C}^{+}_{\Gamma_{\mathrm{NL}},(\Omega_{\mathrm{L}}\setminus\Gamma_{\mathrm{NL}})} \\ \mathbf{0} & \mathbf{C}^{+}_{(\Omega_{\mathrm{L}}\setminus\Gamma_{\mathrm{NL}}),\Gamma_{\mathrm{NL}}} & \mathbf{C}^{+}_{(\Omega_{\mathrm{L}}\setminus\Gamma_{\mathrm{NL}})} \end{bmatrix} \begin{bmatrix} \dot{\mathbf{u}}^{-}_{\mathrm{a}}(\Omega_{\mathrm{N}}\setminus\Gamma_{\mathrm{NL}}) \\ \dot{\mathbf{u}}^{-}_{\mathrm{a}}(\Gamma_{\mathrm{NL}}) \\ \dot{\mathbf{sv}}^{+}(\Omega_{\mathrm{L}}\setminus\Gamma_{\mathrm{NL}}) \end{bmatrix}
$$

$$
+\begin{bmatrix} \mathbf{K}^{-}_{\Omega_{\mathrm{N}}\setminus\Gamma_{\mathrm{NL}}} & \mathbf{K}^{-}_{(\Omega_{\mathrm{N}}\setminus\Gamma_{\mathrm{NL}}),\Gamma_{\mathrm{NL}}} & \mathbf{0} \\ \mathbf{K}^{-}_{\Gamma_{\mathrm{NL}},(\Omega_{\mathrm{N}}\setminus\Gamma_{\mathrm{NL}})} & \mathbf{K}^{-}_{\Gamma_{\mathrm{NL}}} + \mathbf{K}^{+}_{\Gamma_{\mathrm{NL}}} & \mathbf{K}^{+}_{\Gamma_{\mathrm{NL}},(\Omega_{\mathrm{L}}\setminus\Gamma_{\mathrm{NL}})} \\ \mathbf{0} & \mathbf{K}^{+}_{(\Omega_{\mathrm{L}}\setminus\Gamma_{\mathrm{NL}}),\Gamma_{\mathrm{NL}}} & \mathbf{K}^{+}_{(\Omega_{\mathrm{L}}\setminus\Gamma_{\mathrm{NL}})} \end{bmatrix} \begin{bmatrix} \mathbf{u}^{-}_{\mathrm{a}}(\Omega_{\mathrm{N}}\setminus\Gamma_{\mathrm{NL}}) \\ \mathbf{u}^{-}_{\mathrm{a}}(\Gamma_{\mathrm{NL}}) \\ \mathbf{sv}^{+}(\Omega_{\mathrm{L}}\setminus\Gamma_{\mathrm{NL}}) \end{bmatrix}
$$

$$
=\begin{bmatrix} \mathbf{0} \\ \mathbf{f}^{-}_{\Gamma_{\mathrm{NL}}} + \mathbf{f}^{+}_{\Gamma_{\mathrm{NL}}} + \mathbf{M}^{+}_{\Gamma_{\mathrm{NL}}}\ddot{\mathbf{u}}_{\mathrm{free}}(\Gamma_{\mathrm{NL}}) + \mathbf{C}^{+}_{\Gamma_{\mathrm{NL}}}\dot{\mathbf{u}}_{\mathrm{free}}(\Gamma_{\mathrm{NL}}) + \mathbf{K}^{+}_{\Gamma_{\mathrm{NL}}}\mathbf{u}_{\mathrm{free}}(\Gamma_{\mathrm{NL}}) \\ \mathbf{M}^{+}_{(\Omega_{\mathrm{L}}\setminus\Gamma_{\mathrm{NL}}),\Gamma_{\mathrm{NL}}}\ddot{\mathbf{u}}_{\mathrm{free}}(\Gamma_{\mathrm{NL}}) + \mathbf{C}^{+}_{(\Omega_{\mathrm{L}}\setminus\Gamma_{\mathrm{NL}}),\Gamma_{\mathrm{NL}}}\dot{\mathbf{u}}_{\mathrm{free}}(\Gamma_{\mathrm{NL}}) + \mathbf{K}^{+}_{(\Omega_{\mathrm{L}}\setminus\Gamma_{\mathrm{NL}}),\Gamma_{\mathrm{NL}}}\mathbf{u}_{\mathrm{free}}(\Gamma_{\mathrm{NL}}) \end{bmatrix}. \quad (3.52)
$$

In Eq. (3.52), $\mathbf{f}^{-}_{\Gamma_{\mathrm{NL}}} + \mathbf{f}^{+}_{\Gamma_{\mathrm{NL}}}$ can be rewritten as a function of the free field stress. To wit:

$$
\mathbf{f}^{-}_{\Gamma_{\mathrm{NL}}} + \mathbf{f}^{+}_{\Gamma_{\mathrm{NL}}} = -\begin{bmatrix} \int_{\Gamma_{\mathrm{NL}}} (\mathbf{\Phi}^{+}(\boldsymbol{\sigma}_{\mathrm{free}}\boldsymbol{n}^{+})_1) d\Gamma \\ \int_{\Gamma_{\mathrm{NL}}} (\mathbf{\Phi}^{+}(\boldsymbol{\sigma}_{\mathrm{free}}\boldsymbol{n}^{+})_2) d\Gamma \end{bmatrix}. \quad (3.53)
$$

As shown in Eqs. (3.52) and (3.53), only the free field displacement and stress—i.e. $\mathbf{u}_{\mathrm{free}}$ and

$\boldsymbol{\sigma}_{\text{free}}$—are needed to compute the effective force vector that translates the effects of remote excitation along the introduced fictitious interface Γ_{NL}. Moreover, it is useful to note here that, as shown in Bielak et al. (2003), the effective force vector can also be formulated such that only a free-field displacement information over a one-layer element thickness surrounding the interface Γ_{NL} within the domain $\Omega_{\text{L}} \setminus \Omega_{\text{NL}}$ will be required. This is because (i) the mass, damping and stiffness matrices in the region $\Omega_{\text{L}} \setminus \Omega_{\text{PML}}$ are the same for both scattered- and free-field problems and (ii) nonzero terms in matrices $\mathbf{M}^{+}_{\Gamma_{\text{NL}},(\Omega_{\text{L}}\setminus\Gamma_{\text{NL}})}$, $\mathbf{C}^{+}_{\Gamma_{\text{NL}},(\Omega_{\text{L}}\setminus\Gamma_{\text{NL}})}$, and $\mathbf{K}^{+}_{\Gamma_{\text{NL}},(\Omega_{\text{L}}\setminus\Gamma_{\text{NL}})}$ are only confined to elements sharing the nodes along the interface Γ_{NL}.

In general, one needs to solve an auxiliary problem to obtain the free-field wave response. Bielak et al. (2003) used the method provided by Hisada (1994) to compute the Green's functions of the layered half-space. Jeong (2013) also explored the accuracy of different methods (e.g. Wang and Herrmann, 1980; Haskell, 1964; Zhu and Rivera, 2002) to compute the input needed for the DRM. In this work, we assume that the incoming waves are vertically propagating shear waves. Considering this assumption, the effective force vector can be efficiently computed using a solution of a soil column as an auxiliary problem. Details of the approach used is provided in Chapter 5.

CHAPTER 4

Computing the soil impedance functions

The second objective of this work is to compute the impedance functions for complex interface geometries and soil heterogeneity. Quite a number of studies have been carried out since the late 1960s to compute the impedance functions for different types of soil-foundation systems. In these efforts, various modeling techniques were employed including analytical and semi-analytical approaches, the boundary element method (BEM), and the coupled boundary and finite element method (BEM-FEM). As a result, most of the available impedance functions are for relatively simple soil profiles and interface geometries. A non-exhaustive list of these studies for plane-strain problems are summarized in Table 4.1.

In this work, we devise a fully discrete approach for computing the impedance functions of a general soil-structure interface. Using the PML formulation (as explained in Chapter 3) allows us to model wave propagation in heterogenous semi-infinite domains robustly and efficiently. Moreover, using the FEM allows us to model any soil-structure interface geometry and soil profile.

4.1 Impedance matrix of a rigid interface

Kinematics of a rigid foundation in a plane-strain setting (Figure 4.1) can be described by three degrees of freedom—namely, the vertical, horizontal, and rotational motions, respectively denoted here by Δ_1, Δ_2, and θ. The subscripts 1 and 2 denote the x_1 and x_2 directions in the 2D Cartesian coordinate system. The displacement-reaction relationships

Table 4.1: A list of theoretically-obtained impedance functions available in open literature.

Authors	Analysis method	Soil profile	Foundation type	Motion
Karasudhi et al. (1968)	Analytic	Homogenous elastic halfspace	Rigid, surface	V, H, R
Luco and Westmann (1972)	Analytic	Homogeneous elastic halfspace	Rigid, surface	V, H, R
Gazetas (1980)	Semi-Analytic	Non-homogenous elastic halfspace	Rigid, surface	V, H, R
Hryniewicz (1981)	Analytic	Homogeneous elastic halfspace	Rigid, surface	V, H, R
Rajapakse and Shah (1988)	BEM	Homogeneous elastic halfspace	Rigid, embedded	V, H, R
Israil and Ahmad (1989)	BEM	viscoelastic layer on a viscoelastic halfspace	Rigid, embedded	V
Ahmad and Bharadwaj (1991)	BEM	viscoelastic layered halfspace	Rigid, embedded	H
Bharadwaj and Ahmad (1992)	BEM	viscoelastic layered halfspace	Rigid, embedded	R
Spyrakos and Xu (2004)	BEM-FEM	Elastic layered halfspace	Flexible, embedded	V, H

In the 5-th column, V, H, and R stand for, respectively, vertical, horizontal, and rotational movements.

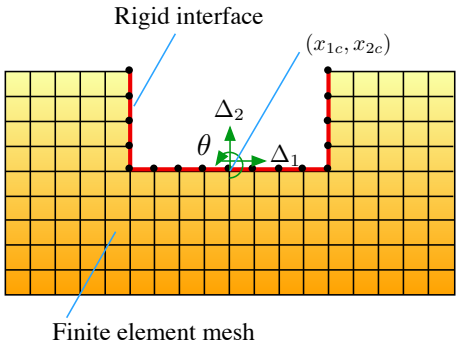

Figure 4.1: Rigid foundation kinematics: the grids indicate the finite element meshes, and the dots indicate the nodes along the soil-structure interface.

in the frequency domain can be described by an impedance matrix, as in

$$\begin{bmatrix} \hat{R}_2 \\ \hat{R}_1 \\ \hat{M}/b \end{bmatrix} = \pi\mu \begin{bmatrix} \hat{K}_V & 0 & 0 \\ 0 & \hat{K}_{HH} & \hat{K}_{HM} \\ 0 & \hat{K}_{MH} & \hat{K}_{MM} \end{bmatrix} \begin{bmatrix} \hat{\Delta}_2 \\ \hat{\Delta}_1 \\ b\hat{\theta} \end{bmatrix}, \tag{4.1}$$

where $\hat{R}_1$ and $\hat{R}_2$ are resultant reaction forces in x_1 and x_2 directions, respectively. The characteristic length b is used for normalizing $\hat{M}$ and $\hat{\theta}$, which denote, respectively, the moment and the rotation angle with respect to the point (x_{1c}, x_{2c}) (see Figure 4.1). It is expedient to note here that the horizontal and rotational degrees of freedom—i.e., $\hat{\Delta}_1$ and $\hat{\theta}$—are coupled, and that the impedance function matrix in Eq. (4.1) is symmetric.

4.2 FE Solver for computing the nodal reaction forces in time and frequency

In Chapter 3, we described the procedure to obtain the semi-discrete form of wave equations in a PML-truncated domain in time, which is repeated here as:

$$\mathbf{M}\,\ddot{\mathbf{d}}(t) + \mathbf{C}\,\dot{\mathbf{d}}(t) + \mathbf{K}\,\mathbf{d}(t) = \mathbf{f}(t). \tag{4.2}$$

Eq. (4.2) can be solved using Newmark's time-stepping method (Newmark, 1959). To treat the Dirichlet boundary condition ($\mathbf{u}_{\mathrm{a}} = \mathbf{g}$ on $\Gamma_{\mathrm{Loaded}} \cup \Gamma_{\mathrm{Fixed}}$), we partition the solution vector and the matrices as follows:

$$\mathbf{d} = \left[\begin{array}{c} \mathbf{d}^{\mathrm{unkn}} \\ \hdashline \mathbf{d}^{\mathrm{kn}} \end{array}\right], \quad \mathbf{M}(\text{ or } \mathbf{C}, \mathbf{K}) = \left[\begin{array}{c:c} \mathbf{M}^{\mathrm{unkn,unkn}} & \mathbf{M}^{\mathrm{unkn,kn}} \\ \hdashline \mathbf{M}^{\mathrm{kn,unkn}} & \mathbf{M}^{\mathrm{kn,kn}} \end{array}\right], \tag{4.3}$$

where $\mathbf{d}^{\mathrm{unkn}}$ and $\mathbf{d}^{\mathrm{kn}}$ denote the unknown and known nodal solution vectors, respectively. Because of the partitioning, a new force vector needs to be constructed as well. Once we obtain the unknown part of the solution vector ($\mathbf{d}^{\mathrm{unkn}}$), we can compute the reaction force

vector through the equation

$$\mathbf{M}^{\mathrm{kn,unkn}}\ddot{\mathbf{d}}_j^{\mathrm{unkn}} + \mathbf{M}^{\mathrm{kn,kn}}\ddot{\mathbf{d}}_j^{\mathrm{kn}} + \mathbf{C}^{\mathrm{kn,unkn}}\dot{\mathbf{d}}_j^{\mathrm{unkn}} + \mathbf{C}^{\mathrm{kn,kn}}\dot{\mathbf{d}}_j^{\mathrm{kn}} + \mathbf{K}^{\mathrm{kn,unkn}}\mathbf{d}_j^{\mathrm{unkn}} + \mathbf{K}^{\mathrm{kn,kn}}\mathbf{d}_j^{\mathrm{kn}} = \mathbf{r}_j, \tag{4.4}$$

where $\mathbf{r}_j$ corresponds to the nodal reaction force vector at the nodes on $\Gamma_{\mathrm{Loaded}} \cup \Gamma_{\mathrm{Fixed}}$ at the j-th time step. Finally, we integrate the nodal reaction force values along the boundary Γ_{Loaded} into the vertical and horizontal forces, as well as the moment.

The wave governing equations can also be solved in the frequency domain. In this case, at each frequency ω, a complex-valued algebraic system of equations needs to be solved. The resulting frequency-domain semi-discrete form is

$$(-\omega^2\mathbf{M} + i\omega\mathbf{C} + \mathbf{K})\hat{\mathbf{d}}(\omega) = \hat{\mathbf{f}}(\omega), \tag{4.5}$$

where $(\hat{})$ denotes the Fourier transform of the subtended variable. Again, we use the partitioning described in Eq. (4.3) to compute the unknown portion of the solution vector ($\hat{\mathbf{d}}^{\mathrm{unkn}}$). We then compute the complex-valued reaction force vector $\hat{\mathbf{r}}_j$ at each frequency ω_j and, subsequently, the resultant forces and the moment.

4.2.1 Computing the impedance functions through time-domain forward analyses

In order to compute each component of the impedance matrix using the time domain FE solver, we first prescribe judiciously chosen displacement time-histories—i.e., $\Delta_1(t)$, $\Delta_2(t)$, and $\theta(t)$—, and subsequently compute reaction forces $R_1(t)$ and $R_2(t)$ and the moment $M(t)$ as described in §4.2. Then, we carry out the following procedure by considering that the soil-structure interface is "welded"[1]:

[1]For "relaxed" soil-foundation interface assumption, the same procedure can be used by considering that the displacement time-history is prescribed only at one degree of freedom (i.e., Δ_1, Δ_2 or θ).

(i) Use Fourier transform to compute the vertical reaction $\hat{R}_2$ for a given vertical motion ($\hat{\Delta}_1 = 0, \hat{\Delta}_2 \neq 0, \hat{\theta} = 0$), and then compute $\hat{K}_V = \hat{R}_2/\pi\mu\hat{\Delta}_2$.

(ii) Use Fourier transform to compute reactions $\hat{R}_1$ and $\hat{M}$ for a given horizontal motion ($\hat{\Delta}_1 \neq 0, \hat{\Delta}_2 = 0, \hat{\theta} = 0$), and then compute $\hat{K}_{HH} = \hat{R}_1/\pi\mu\hat{\Delta}_1$ and $\hat{K}_{MH} = \hat{M}/\pi\mu b\hat{\Delta}_1$.

(iii) Use Fourier transform to compute reactions $\hat{R}_1$ and $\hat{M}$ for a given rotational motion ($\hat{\Delta}_1 = 0, \hat{\Delta}_2 = 0, \hat{\theta} \neq 0$), and then compute $\hat{K}_{HM} = \hat{R}_1/\pi\mu b\hat{\theta}$ and $\hat{K}_{MM} = \hat{M}/\pi\mu b^2\hat{\theta}$.

These steps will thus yield the impedance matrix components for the frequency spectrum excited through the prescribed loading time-history.

4.2.2 Computing the impedance functions through frequency-domain forward analyses

In order to use the frequency domain FE solver to obtain the impedance matrix for the welded condition, constant-valued displacements and rotation must be prescribed—i.e., $\hat{\Delta}_1$, $\hat{\Delta}_2$, and $\hat{\theta}$—as enumerated in §4.2.1, and the resulting reaction forces and moment—i.e., $\hat{R}_1$, $\hat{R}_2$, and $\hat{M}$—must be computed. Then, obtaining the ratio of reactions with respect to the prescribed displacements will directly yield the components of the impedance matrix. This procedure must be repeated for different frequencies in order to obtain the impedance matrix spectra.

4.2.3 Choosing the temporal variation of the input signal for time domain analyses

A straightforward approach to obtain the steady-state response of the system is to prescribe a harmonic displacement $A\sin(\omega t)$ on the foundation boundary. Then, by fitting a sinusoidal function to the resultant reaction histories, we can obtain their amplitude (F) and phase shift (ϕ) with respect to the imposed displacement. Once these data are available, the impedance

functions at frequency ω can be computed as,

$$\hat{K}(\omega) = \frac{F}{A}(\cos\phi + i\sin\phi). \tag{4.6}$$

However, this procedure requires repeating the forward time-domain analyses for different values of ω to cover the frequency range of interest. In order to avoid such time-consuming frequency sweeps, we investigate here the feasibility of prescribing displacement time histories with a wide-band frequency spectra instead, and consider the Ricker wavelet (Eq. (4.7)) and the linear Chirp (Eq. (4.8)) loadings. With a Ricker wavelet, all frequencies are excited simultaneously, whereas with the chirp, the excitation frequency increases linearly (and continuously) with time.

$$\Upsilon_{\text{Ricker}}(t) = \begin{cases} \frac{13.0e^{-13.5} - (0.25\eta^2 - 0.5)e^{(-0.25\eta^2)}}{0.5 + 13.0e^{-13.5}} & t \le \bar{t} \\ 0 & t > \bar{t} \end{cases},$$
$$\eta = 2\pi f_{\text{ctr}} t - 3\sqrt{6}, \quad \bar{t} = \frac{6\sqrt{6}}{2\pi f_{\text{ctr}}}. \tag{4.7}$$

$$\Upsilon_{\text{Chirp}}(t) = \sin\left(\frac{\pi f_1}{t_1} t^2\right). \tag{4.8}$$

The parameter f_{ctr} in Eq. (4.7) denotes the central frequency of the Ricker pulse signal, and f_1 in Eq. (4.8) is the instantaneous frequency of the linear Chirp at time t_1. Given the time-history, the motions can be prescribed through,

$$\{\Delta_1(t),\, \Delta_2(t),\, \theta(t)\} = A \times \Upsilon_{\text{Ricker/Chirp}}(t) \tag{4.9}$$

where A is a chosen amplitude.

To examine the effectiveness of different input excitation types—namely, sinusoidal, Ricker pulse and linear Chirp—, we use them to compute the horizontal impedance of a strip foundation resting on the surface of an elastic half space for a wide range of frequencies

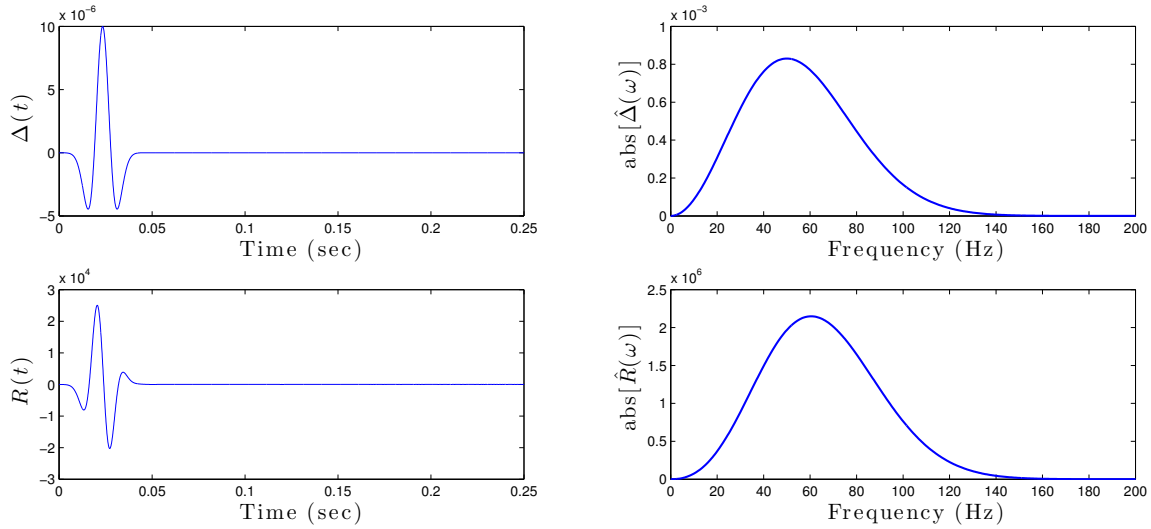

(a) Ricker pulse

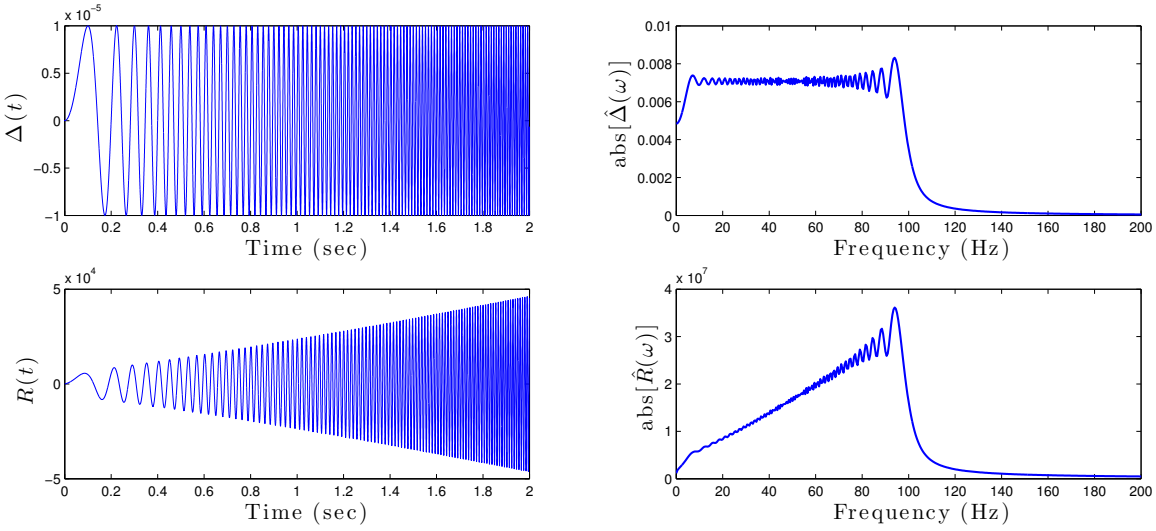

(b) Linear Chirp

Figure 4.2: Time history and Fourier amplitude of the prescribed (a) Ricker wavelet and (b) linear chirp displacements, $\Delta(t)$, $\hat{\Delta}(\omega)$, and the resulting reactions, $R(t)$, $\hat{R}(\omega)$.

and compare them to impedances obtained using frequency domain data. The width of the foundation is 8 m. Young's modulus, Poisson's ratio, and density of the soil are $E = 1$ GPa, $\nu = 0.4$, and $\rho = 2200$ kg/m^3, respectively. Figure 4.2 shows prescribed displacements and the resulting reactions in both time- and frequency domains. The Ricker and linear chirp parameters are $f_{\text{ctr}} = 50$ Hz, $f_1 = 100$ Hz and $t_1 = 1$ sec. The reference solution is obtained using the frequency-domain FE solver for frequencies ranging from 1 to 100 Hz. Figure 4.3 displays the real and imaginary parts of the dynamic stiffnesses resulting from each method. As seen in Figure 4.3, all results are in an excellent agreement.

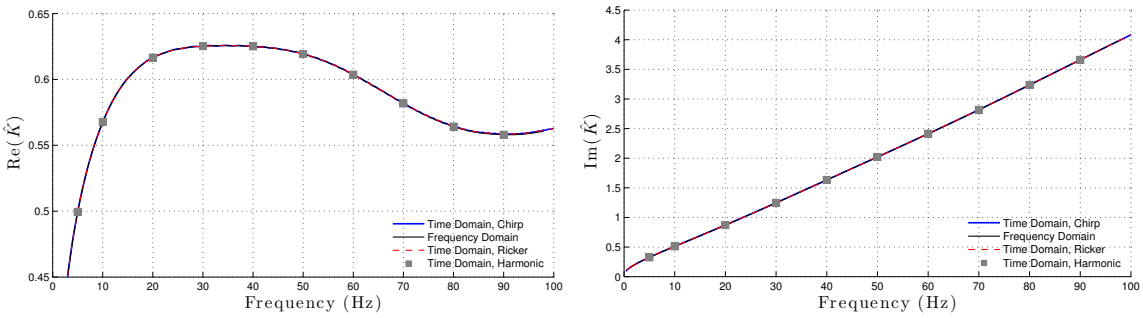

(a) Real part (b) Imaginary part

Figure 4.3: The (a) real and (b) imaginary parts of the horizontal impedance function of a strip foundation on the surface of elastic half space with $\nu = 0.4$.

It is important to note here that one may consider prescribing tractions (instead of displacements and rotations) on Γ_{Loaded} to compute the compliance matrix, and subsequently the impedance matrix. This procedure, in general, would need longer analysis times, because the responses need to reach the steady-state (or at-rest) condition in the case of harmonic (or broadband) input forces (Day and Frazier, 1979). Furthermore, the foundation boundary should still be constrained as a rigid boundary using kinematic boundary conditions. Both issues are circumvented by prescribing kinematic boundary conditions (displacements and/or rotations) at the foundation-soil interface completely. It should be noted, however, that in the case of *very* short-duration kinematic excitations, it may be necessary to apply zero-padding at the ends of the time-domain input and output signals prior to their Fourier transformation in order to increase the resolution of the computed impedance functions in

the frequency domain while preserving the time resolution.

4.2.4 Computational costs of time and frequency domain solutions

Since both the frequency- and the time-domain (with broadband input) approaches produce accurate results, the choice between the two should be based on computational cost. Here, we offer a quantified assessment in this regard by applying both approaches on problems with different domain sizes and by counting the floating point operations (*flops*) needed to solve the resulting sparse systems of linear equations. The primary portion of the said computations consist of LU factorizations and forward/backward substitutions[2]. We have developed the FE solver using Portable, Extensible Toolkit for Scientific Computation (PETSc) (Balay et al., 2016a,b, 1997) for matrix algebra and Supernodal LU package (SuperLU) (Li and Demmel, 2003; Grigori et al., 2007) for solving the system of linear equations.

The model problem used in the computational cost study is the strip foundation resting on homogenous half space shown in Figure 4.6(a). The smallest domain considered had the dimensions $L_{\mathrm{D}} = L_{\mathrm{PML}} = 0.5L_{\mathrm{H}} = 5$ m, and the largest had $L_{\mathrm{D}} = L_{\mathrm{PML}} = 0.5L_{\mathrm{H}} = 20$ m. The other problems' domain sizes varied from the smallest to the largest in 1m increments. In all of the calculations, the finite element sizes were uniform within the domains, and were kept constant at 1 m $\times$ 1 m. Thus, increasing domain sizes meant increasing number of DOFs—smallest problem had 661 nodes, 200 elements; largest problem had 9841 nodes, 3200 elements. For all domain sizes considered, the factored matrices $\mathbf{L}$ had nearly identical sparsity patterns and percentages of nonzero matrix elements in both time and frequency domain analyses.

Figure 4.4 displays the variation of *flops* with the number of nonzero terms (n_{nz}) in the sparse matrix $\mathbf{L}$ for both approaches, along with least-squares fits to data from the computational experiments. Using these results, the computational cost ratio for obtaining

[2]The main computational cost of obtaining the impedances is due to solving the resulting systems of linear equations and time-stepping. Other calculations and operations are either negligible (e.g., stiffness assembly) or almost equal between the two approaches (e.g., mesh generation).

the impedance functions between the frequency and the time domain approaches can be approximated as,

$$\text{Cost Ratio} = \frac{[39.86\,(n_{nz})^{1.27} + 16.13\,n_{nz}]n_f}{8.073\,(n_{nz})^{1.27} + (4.042\,n_{nz}) \times N} \tag{4.10}$$

where N and n_f denote the number of time steps and number of frequencies used for time and frequency domain simulations, respectively. It is useful to note here that in order to attain the same frequency resolution for the computed impedance functions from the time- and the frequency-domain approaches, N and n_f need to be selected based on the duration of the input signal, allowable Δt, and Δf. Once these choices are made/known, then Eq. (4.10) can be used to compute the cost ratio for different problem sizes. To explore and visualize the possible values of the Cost Ratio, we plot its values for the smallest and the largest domain sizes in Figure 4.5. As seen, the time-domain approach is usually cheaper than the frequency domain approach (i.e., Cost Ratio is greater than 1 for most combinations of N and n_f).

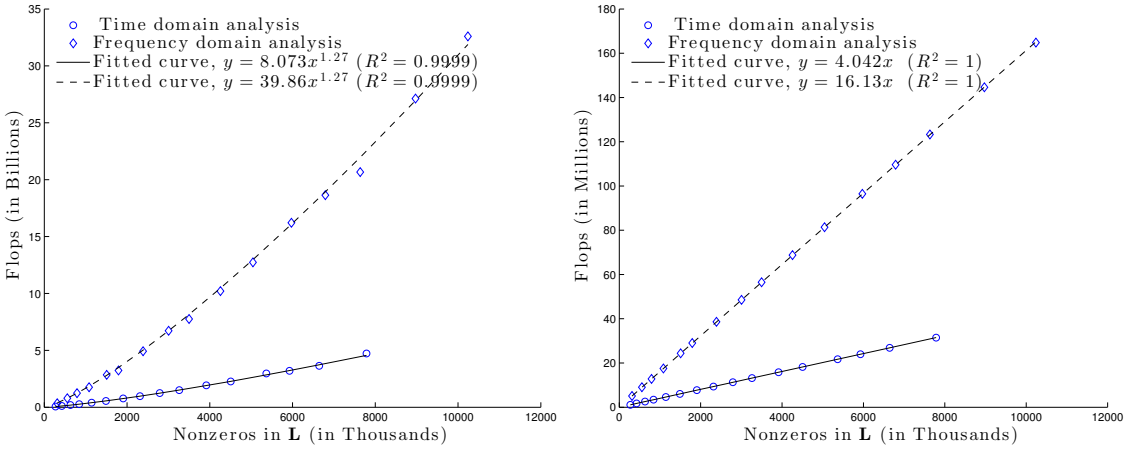

(a) LU Factorization (b) Forward/Backward Substitutions

Figure 4.4: Floating point operations of (a) LU factorization and (b) forward/backward substitutions to solve $\mathbf{Ax} = \mathbf{b}$ in time and frequency domains.

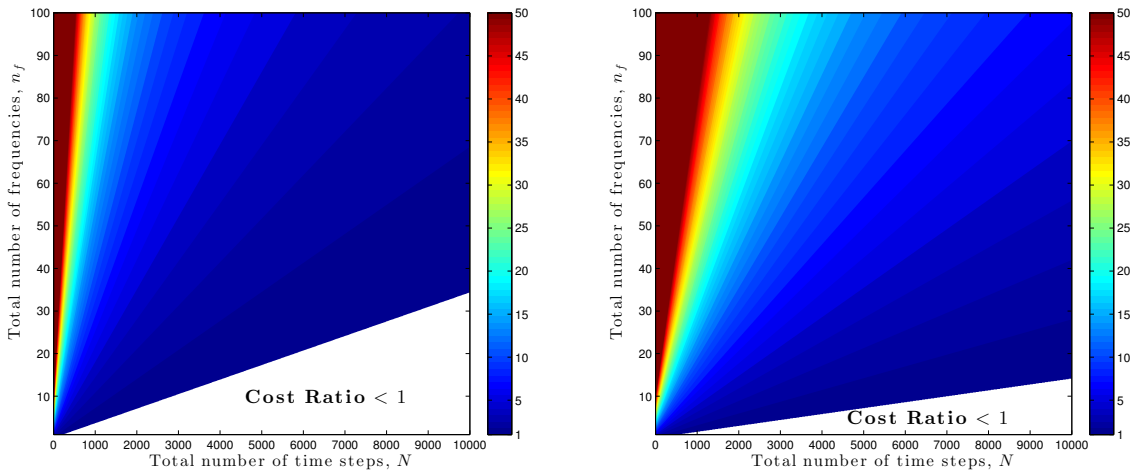

(a) Small Size Problem ($n_{nz} = 271,238$) (b) Large Size Problem ($n_{nz} = 7,787,634$)

Figure 4.5: The contour of the cost ratio for (a) small and (b) large size problems.

4.3 Verification Problems

The proposed time and frequency domain approaches are verified using (semi-)analytic solutions available in open literature for surface and embedded strip foundations (Figure 4.6). Eight-noded quadratic elements are used for discretizing both the regular and the PML portions of the computational domain. To ensure accuracy, both the spatial and temporal discretizations should be judiciously chosen. An element size is determined such that at least 20 nodes are enclosed within the smallest wavelength $V_s/f_{\max}$ (Bao et al., 1998), where V_s denotes the smallest shear wave speed and $f_{\max}$ denotes the maximum discernible frequency. The size of the time step should be sufficiently small such that $\Delta t \leq h/(3V_p)$, where h denotes the size of the quadratic elements, and V_p denotes the largest P-wave speed considered in the numerical model (Wang et al., 1992; Tokmashev et al., 2013).

4.3.1 Impedance functions of an elastic homogeneous half-space

The proposed time-domain FE solver is used to compute the impedance function of the strip foundation shown in Figure 4.6a, resting on the surface of an elastic homogeneous half-space. The reference solution for this problem is due to Luco and Westmann (1972).

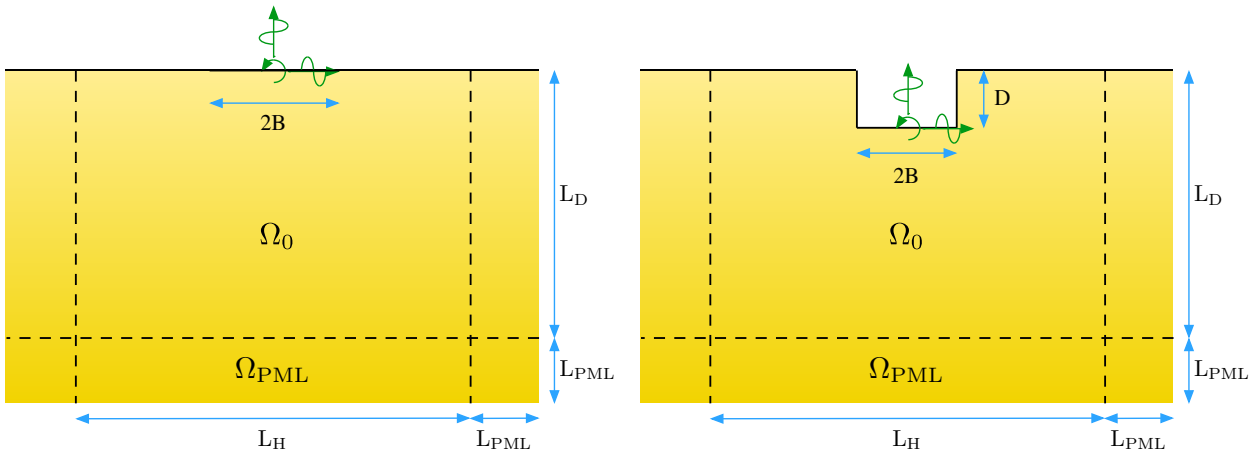

(a) Strip surface foundation (b) Strip embedded foundation

Figure 4.6: Rigid foundations of different types in a two-dimensional setting.

B denotes the half-width of the foundation, and V_s is the shear wave velocity of the soil. The soil Poisson's ratio is 0.25. The impedance components $\hat{K}_V$, $\hat{K}_{HH}$, $\hat{K}_{MM}$, and $\hat{K}_{HM}$ are obtained by considering the "welded" interface condition. Ricker pulse with the dimensionless central frequency $a_{0_{\text{ctr}}} = \omega_{\text{ctr}} B/V_s = 1.18$ and a total wave response observation time of approximately $10\, L_{\text{D}}/V_s$ is used. The total observation time is set to be ten times L_{D}/V_s — i.e., arrival time of shear waves, departing from the excitation source, to the interfaces between the regular domain and the PML areas. A verification study using such a long observation time allows the detection of errors due to wave reflections of the PML areas (i.e., possible failure of the PMLs).

As shown in Figure 4.7a, the numerically-evaluated impedance functions show an excellent agreement with the reference solutions. We note that, as discussed in Luco and Westmann (1972); Muskhelishvili (1963), the compliances (real parts) of the strip foundation for horizontal and vertical directions exhibit singular behaviors as the frequency approaches to zero. That is, the real parts of the impedance functions of a strip foundation along the horizontal and vertical directions vanish at zero frequency. On the other hand, the real part of the rocking component is nonzero, hence its compliance is finite. However, it should be noted that the zero frequency component of the rocking mode can only be retrieved asymptotically

by using the FE solver proposed in the present study, as it cannot accommodate perfectly static loads (Kucukcoban, 2010).

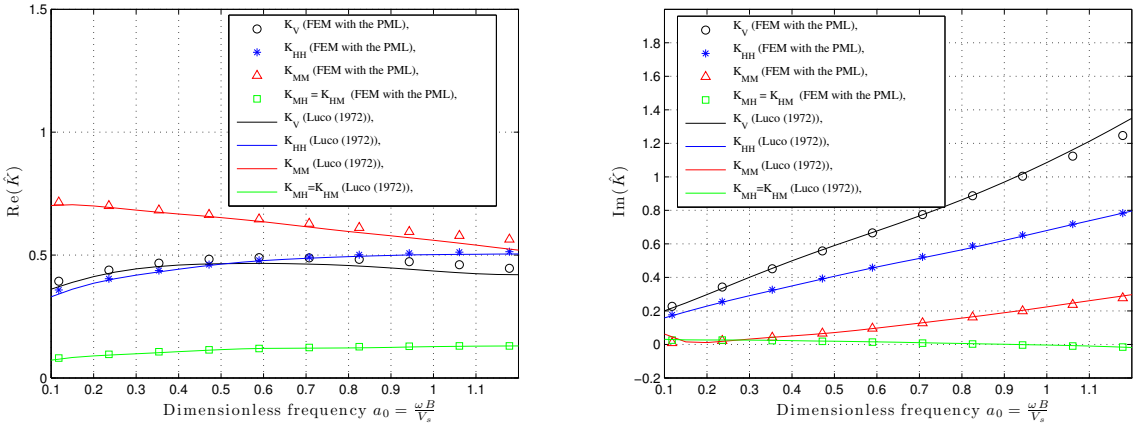

(a) Real Part

(b) Imaginary Part

Figure 4.7: Impedance function of a rigid strip surface foundation computed using a Ricker pulse versus the reference solution by Luco and Westmann (1972).

Next, the impedance function for a rigid foundation embedded in a homogenous soil (see Figure 4.6b) is considered. Here B denotes the half-width of the foundation, and D the depth of the excavated boundary. The rotational centroid is located at $x_{1c} = 0$ and $x_{2c} = -D$. The embedment ratio is $D/B = 1$. The side wall and bottom boundary of the embedded foundation are considered to be completely attached to the surrounding soil. The reference solution for this problem is due to Wang and Rajapakse (1991). Other parameters are set identical to those for the previous verification case. As seen in Figure 4.8, numerically computed impedances are in very good agreement with their analytic counterparts.

4.3.2 Impedance functions of a viscoelastic two-layered half-space

In frequency domain analyses, soil viscoelasticity can be easily incorporated into the model by modifying the Lamè parameters as in $\lambda^* = \lambda(1 + 2i\xi)$ and $\mu^* = \mu(1 + 2i\xi)$ where ξ is the soil material damping. For verifying our frequency-domain FE solver, the horizontal and rocking impedances of a strip foundation embedded in a two-layered viscoelastic soil are

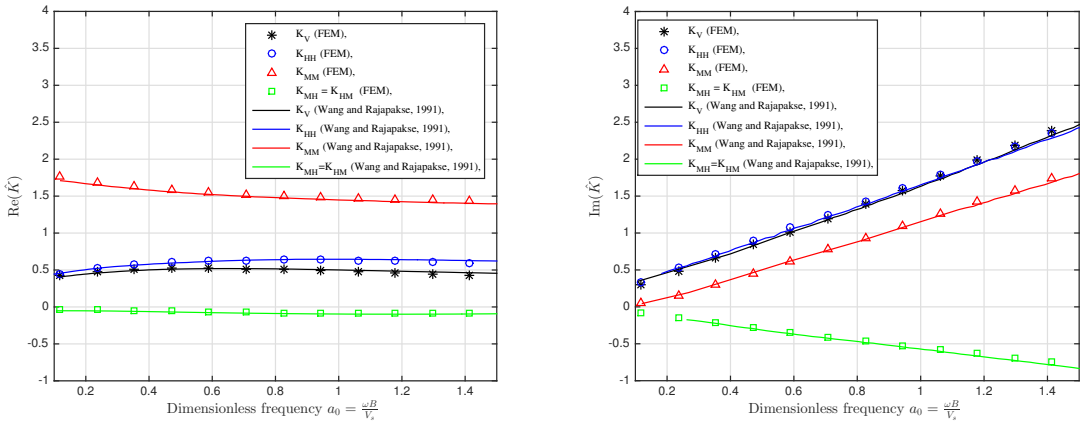

(a) Real part

(b) Imaginary part

Figure 4.8: Impedance function of a rigid strip embedded foundation computed using a Ricker pulse versus the reference solution by Wang and Rajapakse (1991).

computed. The reference BEM solutions for this problem are due to Ahmad and Bharadwaj (1991); Bharadwaj and Ahmad (1992). In all analyses, the height of the first layer over the half-space is $4B$. Three different values of $E_1/E_2 = 0.5, 1, 2$ are considered where E_1 and E_2 are Young's modulus of the first and the second layers, respectively. Two embedment ratios of $D/B = 0, 1$ are considered. The Poisson's ratio and the material damping of both layers are 0.4 and 5%, respectively. The numerically computed impedance functions $\hat{K}_{HH}$ and $\hat{K}_{MM}$ are normalized as follows to be consistent with those provided in the reference solutions:

$$\begin{aligned} \text{Horizontal:} \quad & \text{spring coefficient} = \frac{\text{Re}(\hat{K}_{HH})}{k_{0H}\mu}, \quad \text{dashpot coefficient} = \frac{\text{Im}(\hat{K}_{HH})}{2\omega B\rho V_{s1}} \\ \text{Rocking:} \quad & \text{spring coefficient} = \frac{\text{Re}(\hat{K}_{MM})}{k_{0M}\mu B^2}, \quad \text{dashpot coefficient} = \frac{\text{Im}(\hat{K}_{MM})}{\omega\rho V_{La} I_{bz}} \end{aligned} \tag{4.11}$$

where k_{0H} and k_{0M} are constant values defined in Table 4.2; V_{s1} is the shear wave speed of the first layer; $V_{La} = 3.4V_{s1}/[\pi(1-\nu)]$ and $I_{bz} = 2B^3/3$. Figures 4.9 and 4.10 display the resulting spring and dashpot coefficients along with the reference solutions, which again are in excellent agreement.

Table 4.2: Values of parameters k_{0H} and k_{0M} in Eq. (4.11).

	k_{0H}			k_{0M}		
D/B	$E_1/E_2 = 0.5$	$E_1/E_2 = 1$	$E_1/E_2 = 2$	$E_1/E_2 = 0.5$	$E_1/E_2 = 1$	$E_1/E_2 = 2$
0	1.39	1.21	1.02	2.82	2.76	2.62
1	1.95	1.55	1.19	6.76	6.6	5.94

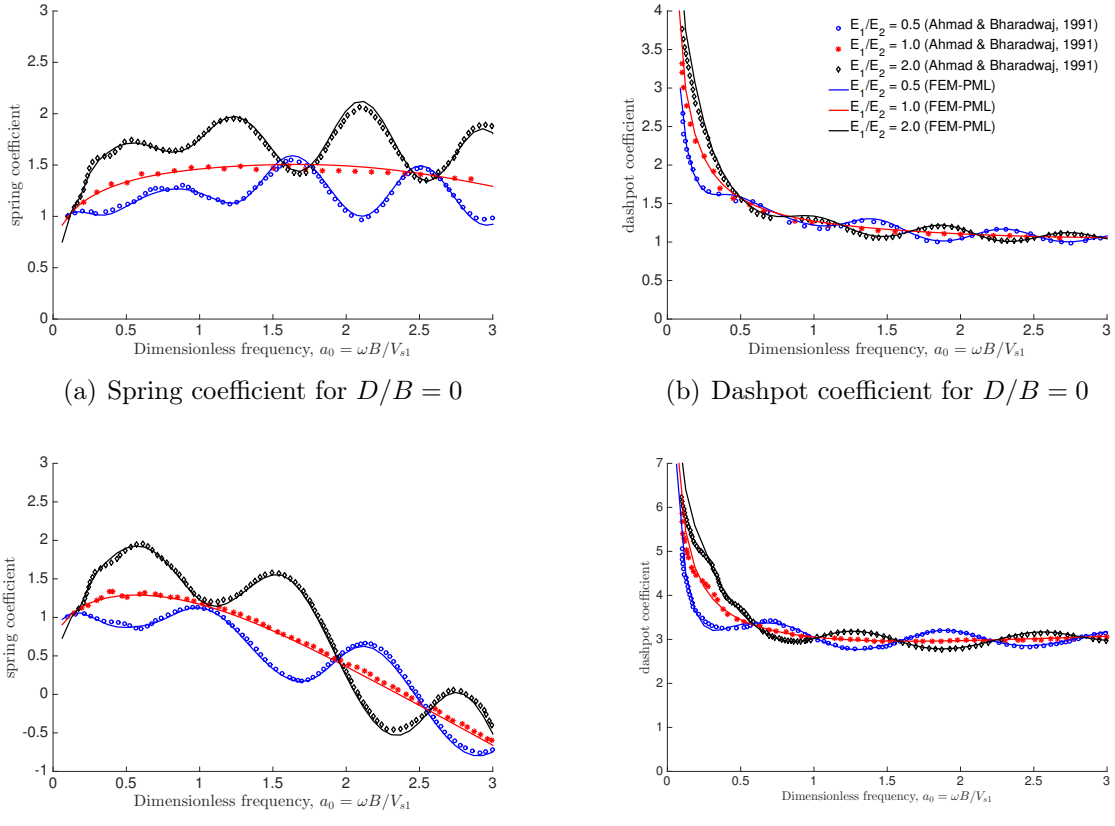

(a) Spring coefficient for $D/B = 0$

(b) Dashpot coefficient for $D/B = 0$

(c) Spring coefficient for $D/B = 1$

(d) Dashpot coefficient for $D/B = 1$

Figure 4.9: Horizontal impedance function of a rigid strip foundation embedded in viscoelastic two-layered half-space computed using frequency domain FE solver versus the reference solution by Ahmad and Bharadwaj (1991).

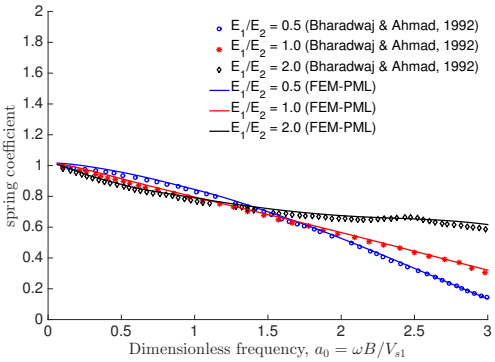

(a) Spring coefficient for $D/B = 0$

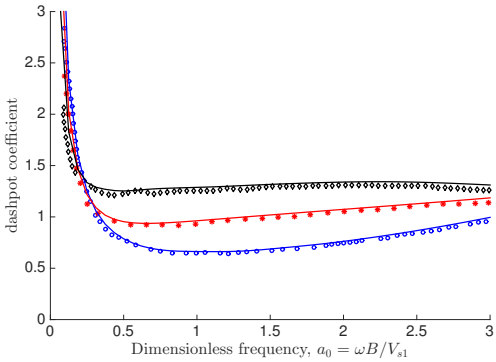

(b) Dashpot coefficient for $D/B = 0$

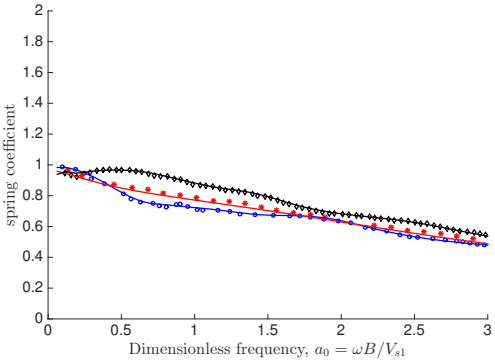

(c) Spring coefficient for $D/B = 1$

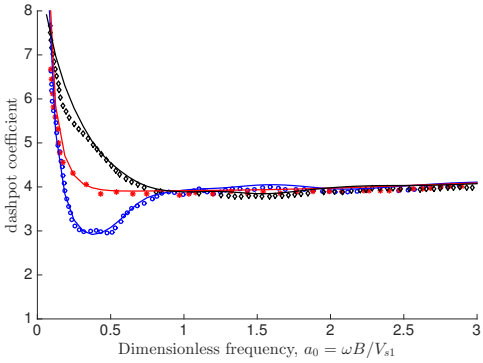

(d) Dashpot coefficient for $D/B = 1$

Figure 4.10: Rocking impedance function of a rigid strip foundation embedded in viscoelastic two-layered half-space computed using frequency domain FE solver versus the reference solution by Bharadwaj and Ahmad (1992).

4.3.3 Impedance functions of a viscoelastic incompressible soil on a rigid bedrock

In order to explore the capability of the developed FE solver for computing the impedance functions for a viscoelastic incompressible soil layer on a rigid bedrock, we compute the complex-valued compliance functions, as defined in Eq. (4.12) (Gazetas, 1981), of a surface rigid foundation with the geometry shown in Figure 4.11. The material damping of the soil layer is 5% and the interface condition is "welded". Three cases of $H/B = \infty, 1, 3$ are considered. The reference solution is due to a semi-analytical solution proposed by Gazetas (1981).

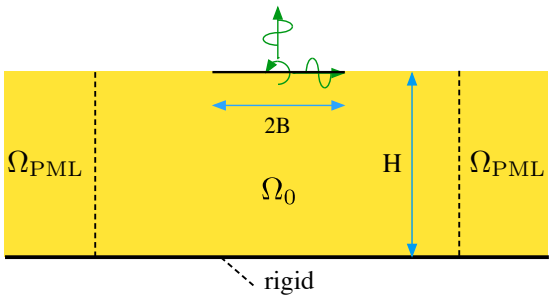

Figure 4.11: Rigid foundation on a surface of a soil layer supported by a rigid bedrock.

$$\hat{C}_V = E\frac{\hat{\Delta}_2}{\hat{R}_2}, \quad \hat{C}_{HH} = E\frac{\hat{\Delta}_1}{\hat{R}_1}, \quad \hat{C}_{MM} = EB^2\frac{\hat{\theta}}{\hat{M}}\,. \tag{4.12}$$

Frequency domain FE solver is used to compute the impedance matrix for each configuration. Then, the compliance matrix can be computed through inverting the impedance matrix. In order to handle the incompressibility of the soil layer, in all numerical simulations, the Poisson's ratio of the soil layer is $\nu = 0.49$. Figure 4.12 shows the resulting vertical, horizontal and rocking compliance functions, which are in good agreement with the reference solutions. As expected, for the case of $H/B = \infty$, the real and imaginary parts of the vertical and horizontal compliance functions tend to infinity as frequency tends to zero.

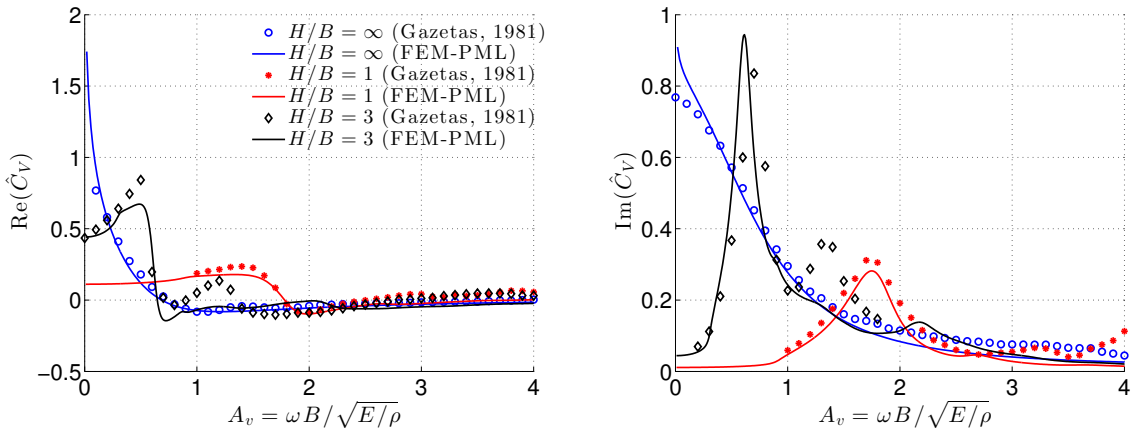

(a) Vertical

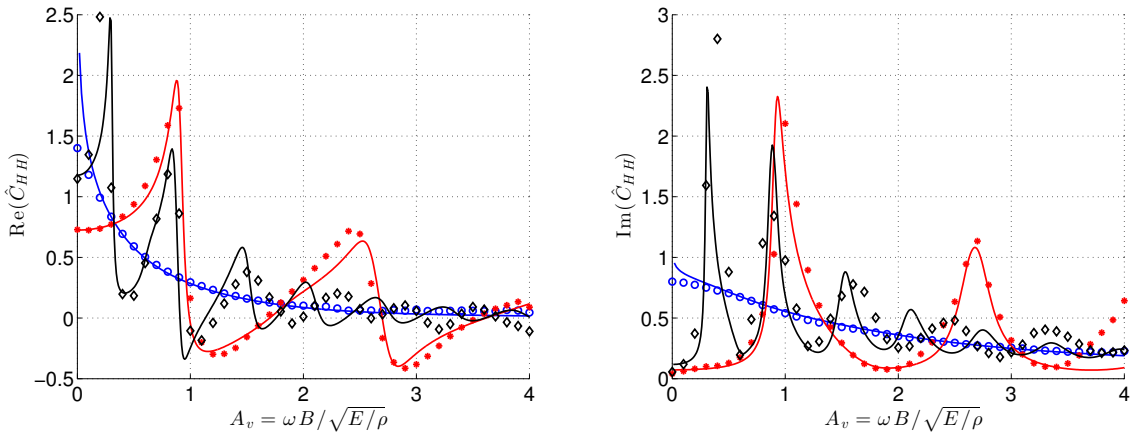

(b) Horizontal

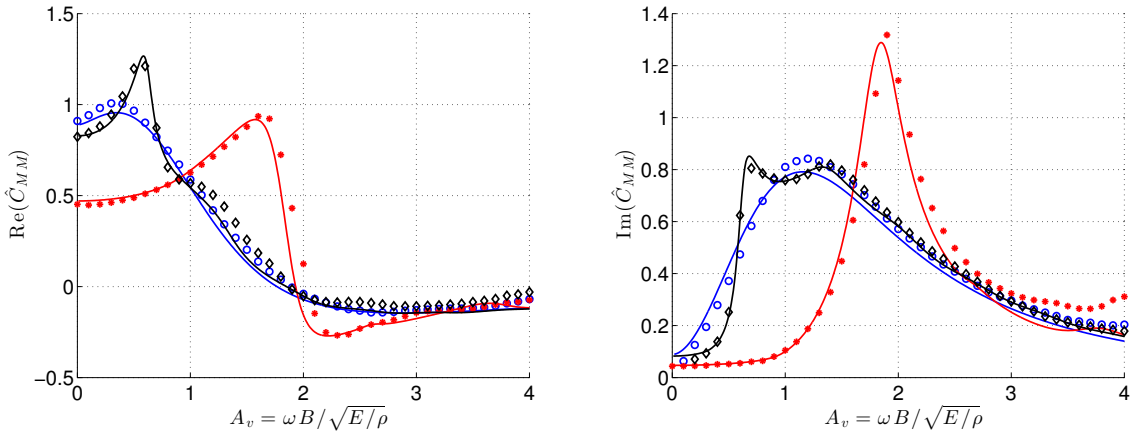

(c) Rocking

Figure 4.12: Real and imaginary parts of (a) vertical, (b) horizontal and (c) rocking compliance functions of a surface rigid foundation on a viscoelastic incompressible soil layer computed using the frequency domain FE solver versus the reference solution by Gazetas (1981).

4.4 Performance of PMLs in comparison to Lysmer-Kuhlemeyer (LK) dashpots

In order to investigate the performance of PMLs in absorbing the outgoing waves in comparison to LK dashpots (Lysmer and Kuhlemeyer, 1969)—which are widely used in time domain analyses—, we modified our time-domain FE solver such that the fixed degrees of freedom on Γ_{Fixed} (see Figure 3.2) are released and replaced with dashpots. Coefficients of these dashpots along the normal and tangent directions to the new boundary—i.e., Γ_{LK}—are set at $\rho V_p/\ell$ and $\rho V_s/\ell$, respectively, where V_p and V_s are the longitudinal and shear wave velocities—which can be computed based on the soil properties along Γ_{LK}—and ℓ is the length of the corresponding edge of Γ_{LK}.

4.4.1 A strip foundation on the surface of an elastic half-space

Again, the reference solution is chosen as the horizontal impedance function of a strip foundation resting on an elastic half-space (as discussed in §4.3.1). A Ricker pulse with $f_{\text{ctr}} = 10$ Hz is used as the input signal. Soil properties are selected such that $V_s = 150$ m/s and $V_p = 259.81$ m/s. The total observation time considered is $T = 10$ sec. The half-width of the foundation is $B = 4$ m. Figure 4.13 displays the resulting impedance functions obtained by prescribing Γ_{LK} at different distances around the regular domain, and by using the PML at the original distance considered earlier for the same problem. As expected, increasing the size of the regular domain improves the accuracy of the impedances obtained using the LK dashpots. This is because the incidence angle of the outgoing waves become closer to the normal direction of Γ_{LK} as the domain size increases, which in turn, results in a better performance by the LK dashpots. Nevertheless, even as the accuracy of the LK-based impedances increase with increasing domain size, they are plagued by noise, which indicates that LK dashpots cannot absorb outgoing waves at all frequencies equally well. For larger domain sizes, incidence angles become more favorable for the LK dashpots, but at the same time, the modal space of the computational domain increases, and thus, higher modes become active

that interact with the truncated LK boundary. This is very likely the cause of the increased oscillations seen in Figure 4.13.

4.4.2 A strip foundation embedded in a two-layered elastic half-space

In order to explore the effects of soil heterogeneity and foundation embedment, horizontal impedance of a strip foundation embedded in a two-layered elastic soil is computed. The embedment ratio is $D/B = 1$, the height of the first layer is $4B$, and the stiffness ratio is $E_1/E_2 = 0.5$. Other parameters are the same as the previous example. Figure 4.14 shows the resulting impedance functions obtained by prescribing Γ_{LK} at different distances and by using PML. Again, while the performance of LK dashpots increases by enlarging the size of the domain, they exhibit more oscillatory behavior than their counterparts in the previous example. Moreover, we need to use thicker PML in this example to achieve the desired performance. This is mainly because the prescribed ABCs should absorb a larger amount of energy created due to (i) the increased length of interface at which the input motion is prescribed, and (ii) multiple reflections and refractions occur at the interface of the first and second soil layers and at the free surface of the first layer.

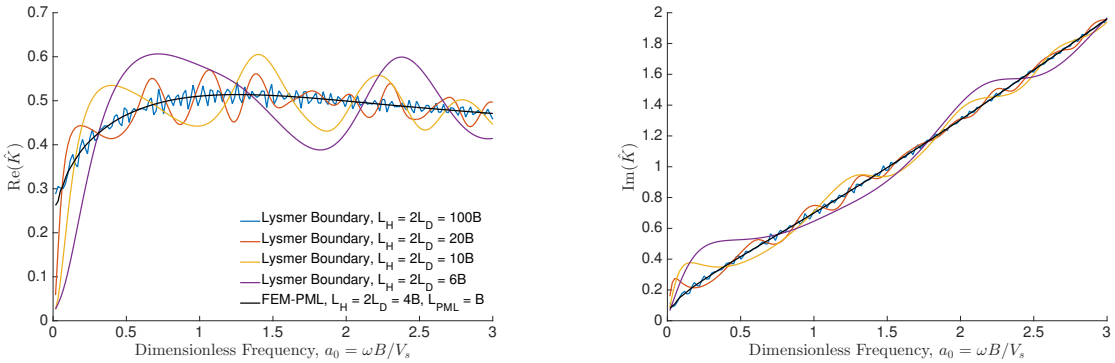

(a) Real part (b) Imaginary part

Figure 4.13: Horizontal impedance function of a strip foundation on surface of elastic half space with $\nu = 0.25$, computed by using LK dashpots and PMLs as ABC.

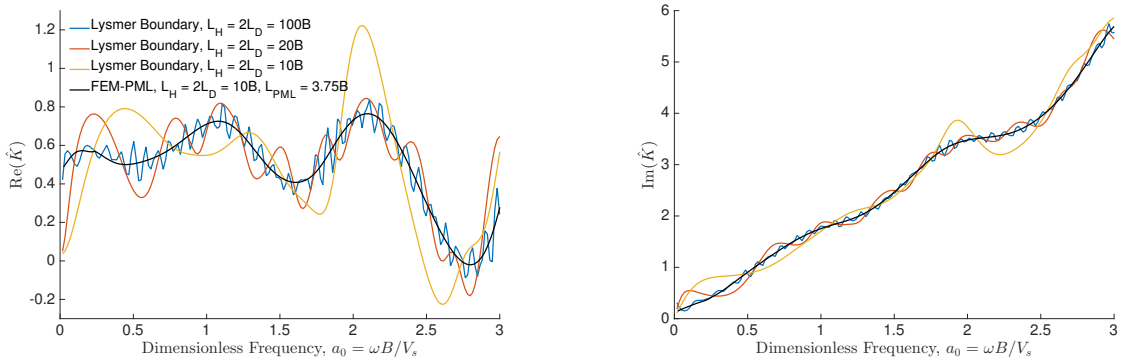

(a) Real part

(b) Imaginary part

Figure 4.14: Horizontal impedance function of a strip foundation embedded in a two-layered elastic half space with $\nu = 0.25$, computed by using LK dashpots and PMLs as ABC.

4.4.3 Computational cost

LK and PML approaches should also be compared based on their computational costs. To provide a better understating in this regard, the total number of nodes used for discretization of the computational domain for each analysis case, and the corresponding total number of DOFs are shown in Table 4.3. Accordingly, for the case of strip foundation on surface of elastic half-space, the number of DOFs for computing with LK dashpots at $L_{\mathrm{H}} = 100B$ is about 180 times that of the PML option with thickness B at $L_{\mathrm{H}} = 4B$. This is a significant increase in computational cost, considering the fact that the number of *flops* for nominal direct solvers for linear systems typically increase with order $O(\mathrm{dof}^3)$. For the case of a strip foundation embedded in two-layered soil, the computational cost of using LK dashpots at $L_{\mathrm{H}} = 100B$ is about 16 times that of the PML option with thickness of $3.75B$ at $L_{\mathrm{H}} = 10B$. The comparisons above indicate that the PML approach yields significantly more accurate impedance functions than the LK approach, and moreover, they are far more efficient computationally.

Table 4.3: Computational cost of using PMLs versus LK dashpots to compute the horizontal impedance function of a strip foundation.

ABC	L_{H}	L_{PML}	Number of Nodes	Number of DOFs	$\mathrm{DOF}_{\mathrm{LK}}/\mathrm{DOF}_{\mathrm{PML}}$ (on surface of half-space)	$\mathrm{DOF}_{\mathrm{LK}}/\mathrm{DOF}_{\mathrm{PML}}$ (embedded in two-layered half-space)
LK	6B	—	937	1874	0.7	—
LK	10B	—	2521	5042	1.9	0.2
LK	20B	—	9841	19682	7.3	0.6
LK	100B	—	241201	482402	179	15.8
PML	4B	1B	937	3581	1.0	—
PML	10B	3.75B	7473	30549	—	1.0

4.5 Impedance matrix of a flexible interface

Nearly all of the available impedance functions were obtained based on the simplifying assumption that the soil-structure interface behaves rigidly. As mentioned before, this assumption reduces the size of the problem and yields only the impedance functions for rigid modes of the interface, which are 3×3 and 6×6 matrices for two- and three dimensional problems, respectively. However, this rigid interface assumption may not always be appropriate for all foundation configurations and geometries, and for problems that require the impedance functions to be defined at an interface within the flexible soil domain—i.e., problems that involve near-field nonlinearities such as soil inelasticity (Preisig, 2005), or soil-foundation gapping/contact (Rha and Taciroglu, 2007).

The effects of interface flexibility on the impedance functions and the dynamic response of structures have been the subject of a number of studies. Table 4.4 provides a (not necessarily exhaustive) list of existing studies on response of flexible foundations from the late 70s to date. It is observed in these cited studies that the responses of flexible foundations depend on several factors—namely, the stiffness of the foundation relative to the surrounding soil, the foundation geometry, the soil stratification, the spatial variability and frequency content of the applied loading, and the spatial distribution of the foundation mass and stiffness. Recently, Maravas et al. (2013) extracted nodal impedances for a rectangular foundation using the computer program ACS SASSI (Ghi, 2010), which can only handle horizontally layered soil domains. In their approach, Maravas et al. (2013) imposed unit harmonic forces

Table 4.4: A list of existing studies on impedance functions and response analysis of flexible foundations.

Authors	Analysis method	Foundation type	Soil profile
Savidis and Richter (1979)	Analytic & FEM	Surface, Rectangular	Elastic half-space
Iguchi and Luco (1981)	Continuum approach & FEM	Surface, Rectangular (with rigid core or edge)	Elastic half-space
Riggs and Waas (1985)	Semianalytic & FEM	Surface, Circular (with concentric rigid walls)	Elastic layer over bedrock
Karabalis and Beskos (1985)	Time domain BEM & FEM	Surface, Rectangular	Elastic half-space
Spyrakos and Beskos (1986)	Time domain BEM & FEM	Surface, Strip	Elastic half-space
Kokkinos and Spyrakos (1991)	Frequency domain BEM & FEM	Surface, Strip	Elastic layered half-space
Gucunski and Peek (1993)	Stiffness matrix approach & finite difference energy method	Surface, Circular	Elastic layered half-space
Liou and Huang (1994)	Substructure technique	Surface, Circular	Visco-elastic half-space
Gucunski (1996)	Stiffness matrix approach & finite difference energy method	Surface, Circular	Elastic layered half-space
Spyrakos and Xu (2004)	Frequency domain BEM & FEM	Embedded, Massive, Strip	Elastic layered half-space
Saitoh and Watanabe (2004)	Closed-form formula based on wave propagation theory	Embedded, Cylindrical	Elastic layer over bedrock
Chen and Hou (2009)	Modal stiffness matrix approach	Surface, Circular	Elastic half-space
Maravas et al. (2013)	FEM	Surface, Rectangular	Elastic half-space

successively at different surface interaction points and used the resulting displacements at all interaction nodes to extract *compliance* functions. The resulting compliance matrix was then inverted to obtain the impedance matrix. The other pertinent study is by Chen and Hou (2009) who studied modal impedances of a surface circular foundation. Chen and Hou (2009) also opted to use a flexibility approach—that is, they applied a "unit modal load" and computed corresponding displacements at the soil-foundation interface using an analytical solution by Kausel and Roesset (1981).

In this section we describe the extension of the devised methodology to compute the impedance functions of a flexible soil-structure interface, which is again based on prescribed displacements that result in the direct extraction of nodal impedance matrices. We verify the accuracy of the numerically computed impedance functions in Chapter 6 where the substructure modeling approach will be used to compute the response of a reduced order SSI problem.

4.5.1 Computing the nodal impedance matrix

We want to obtain the impedance matrix $\hat{\mathbf{S}}(\omega)$ for a discretized interface (Figure 4.15). This can be done by obtaining the DtN-map relating the displacements to the reactions/forces

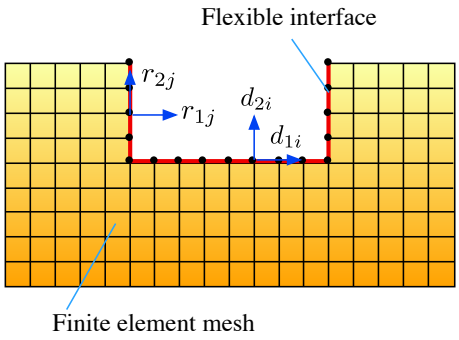

Figure 4.15: Flexible interface kinematics: the grids indicate the finite element meshes, and the dots indicate the nodes along the soil-structure interface.

along the interface. The general form of a DtN-map written in frequency domain is

$$\hat{\mathbf{S}}(\omega)\hat{\mathbf{d}}(\omega) = \hat{\mathbf{r}}(\omega) \tag{4.13}$$

where $\mathbf{d}$ and $\mathbf{r}$ are interfacial displacement and reaction force vectors, respectively. Considering N_b discretization nodes (the black points in Figure 4.15), the total number of DOFs along the interface would be $2N_\mathrm{b}$ for a two-dimensional problem, and therefore $\hat{\mathbf{d}}(\omega)$ and $\hat{\mathbf{r}}(\omega)$ would be $\in \mathbb{C}^{2N_\mathrm{b}}$, and $\hat{\mathbf{S}}(\omega) \in \mathbb{C}^{2N_\mathrm{b}\times 2N_\mathrm{b}}$. Thus, the general procedure for deriving the nodal impedance matrix in frequency domain can be described as follows:

1. Prescribe a known steady-state displacement $\hat{h}(\omega)$ in the direction of the j-th DOF while keeping all the other interface DOFs fixed—i.e., $\hat{d}_k(\omega) = 0$ for $k = 1, \ldots, j-1, j+1, \ldots, 2N_\mathrm{b}$ and $\hat{d}_k(\omega) = \hat{h}(\omega)$ for $k = j$).

2. Obtain the reaction forces $\hat{r}_k(\omega)$ for $k = 1, \ldots, 2N_\mathrm{b}$.

3. Compute the j-th column of the nodal impedance function matrix as:

$$\hat{S}_{ij}(\omega) = \frac{\hat{r}_i(\omega)}{\hat{h}(\omega)} \quad \text{for} \quad i = 1, \ldots, 2N_\mathrm{b}\,. \tag{4.14}$$

4. Repeat the above procedure for all DOFs along the interface, i.e., $j = 1, \ldots, 2N_\mathrm{b}$, which will yield the full expression of the nodal impedance matrix $\hat{\mathbf{S}}(\omega)$.

CHAPTER 5

Computing the kinematic interaction transfer functions

As outlined in Chapter 1, the third objective of this work is to compute KITFs for different types of soil-structure interfaces. Since late 1960s, a number of studies have been carried out to obtain the response of rigid embedded foundations under different types of incoming waves by solving the scattering problem (e.g., Day, 1977; Elsabee and Morray, 1977; Dominguez, 1978). Luco (1986) used the reciprocity theorem to convert the scattering problem—i.e., the problem of foundation response under seismic waves—to the radiation problem—i.e., the problem of foundation response under external forces. As a result, the *scattered* response of the foundation interface, or the so called FIM, could be evaluated if one knows the soil impedance matrix, the distribution of tractions along the excavated soil interface, and the free-field displacement and traction responses. Iguchi (1982) proposed an approximate method to compute the FIM using only the foundation geometry and impedance, and the free-field motion. The accuracy of this approximate method was investigated by Pais and Kausel (1989).

Here, we present a method that uses our developed FE solver to compute the scattered responses as well as the associated KITFs of a soil-structure interface. As discussed in Chapter 4, in order to solve the scattering problem using the DRM, we need to compute free-field tractions and displacements at the fictitious interface (Γ_{NL}) where we want to define the effective force vector. For vertically propagating shear waves, we can efficiently compute the free-field data from one-dimensional (1D) wave propagation analysis. This allows us to solve a simpler auxiliary problem instead of computing the free-field information along the soil-structure interface, as proposed by Luco (1986).

5.1 Modeling 1D wave propagation in a soil layer on elastic bedrock

5.1.1 Wave physics in an elastic homogeneous bedrock

We consider 1D wave propagation in a soil column on an elastic bedrock (see Figure 5.1a) here. The governing wave equation in the elastic bedrock is

$$\ddot{u}(z,t) = V_b^2 u_{,zz}(z,t) \tag{5.1}$$

where V_b is the shear wave velocity of the elastic bedrock; u is the horizontal displacement response as function of depth z. The wave response can be expressed as:

$$u(z,t) = u_R(t - z/V_b) + u_I(t + z/V_b) \tag{5.2}$$

where u_R and u_I are the waves traveling downward (reflected) and upward (incident), respectively. By taking the first derivative of the wave response with respect to z and by setting $z = 0$, we obtain the shear stress $\tau(t)$ on surface of the elastic bedrock. To wit,

$$\tau(t) = \rho_b V_b^2 u_{,z}(0,t) = \rho_b V_b \dot{u}_I(0,t) - \rho_b V_b \dot{u}_R(0,t) = 2\rho_b V_b \dot{u}_I(0,t) - \rho_b V_b \dot{u}(0,t). \tag{5.3}$$

Therefore, as already shown by Zhang et al. (2003), the elastic bedrock can be replaced by a dashpot with coefficient $\rho_b V_b$, while the incident wave can be replaced by an equivalent horizontal force equal to $2\rho_b V_b \dot{u}_I(0,t)$ at $z = 0$. This is shown schematically in Figure 5.1b.

5.1.2 Wave physics in a soil layer

Considering a horizontally layered soil with height H on an elastic bedrock, the governing wave equation is:

$$\mu(u_{\text{free}})_{,zz}(z,t) - \rho \ddot{u}_{\text{free}}(z,t) = 0 \tag{5.4}$$

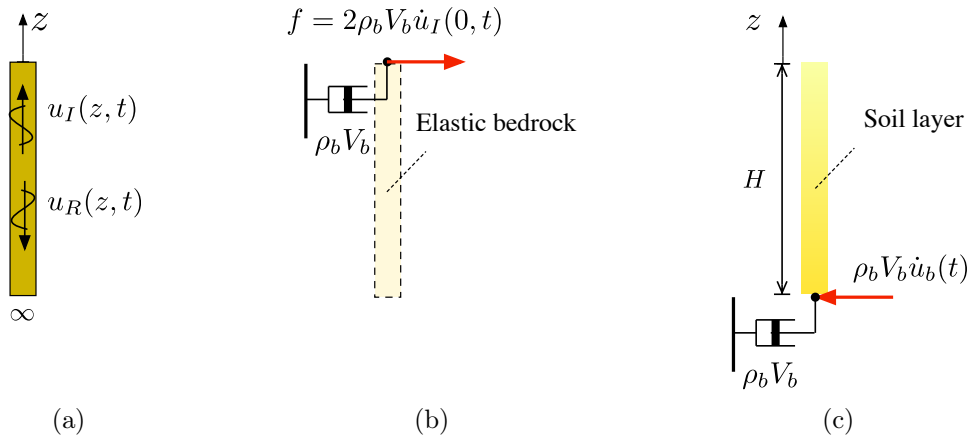

Figure 5.1: Schematic (a) semi-infinite elastic bedrock; the replaced macro-element; and (c) soil layer supported by the elastic bedrock macro-element.

and the boundary conditions at the soil surface and at its interface with the elastic bedrock are:

$$(u_{\text{free}})_{,z}(0,t) = 0\,, \tag{5.5}$$

$$\mu(u_{\text{free}})_{,z}(-H,t) = -\rho_b V_b \dot{u}_b(t) + \rho_b V_b \dot{u}_{\text{free}}(-H,t)\,, \tag{5.6}$$

where $u_b(t) = 2u_I(0,t)$; μ and ρ are the shear modulus and the density of the soil layer. Eqs. (5.4) and (5.6) can be solved numerically using the standard finite element method.

5.2 Computing the effective force vector along the interface Γ_{NL}

Here, we recall the effective force vector obtained in §3.3.2 for a PML-truncated domain to employ DRM.

$$\mathbf{f}_{\text{eff}} = \begin{bmatrix} \mathbf{0} \\ \mathbf{f}_{\text{free}}(\Gamma_{\text{NL}}) + \mathbf{M}^{+}_{\Gamma_{\text{NL}}} \ddot{\mathbf{u}}_{\text{free}}(\Gamma_{\text{NL}}) + \mathbf{C}^{+}_{\Gamma_{\text{NL}}} \dot{\mathbf{u}}_{\text{free}}(\Gamma_{\text{NL}}) + \mathbf{K}^{+}_{\Gamma_{\text{NL}}} \mathbf{u}_{\text{free}}(\Gamma_{\text{NL}}) \\ \mathbf{M}^{+}_{(\Omega_{\text{L}}\setminus\Gamma_{\text{NL}}),\Gamma_{\text{NL}}} \ddot{\mathbf{u}}_{\text{free}}(\Gamma_{\text{NL}}) + \mathbf{C}^{+}_{(\Omega_{\text{L}}\setminus\Gamma_{\text{NL}}),\Gamma_{\text{NL}}} \dot{\mathbf{u}}_{\text{free}}(\Gamma_{\text{NL}}) + \mathbf{K}^{+}_{(\Omega_{\text{L}}\setminus\Gamma_{\text{NL}}),\Gamma_{\text{NL}}} \mathbf{u}_{\text{free}}(\Gamma_{\text{NL}}) \end{bmatrix}, \tag{5.7}$$

where

$$\mathbf{f}_{\text{free}}(\Gamma_{\text{NL}}) = -\int_{\Gamma_{\text{NL}}} \mathbf{\Phi}^{+}(\boldsymbol{\sigma}_{\text{free}}\boldsymbol{n}^{+})d\Gamma. \tag{5.8}$$

As shown in Eq. (5.7), in order to compute $\mathbf{f}_{\text{eff}}$, we need to compute $\mathbf{u}_{\text{free}}(\Gamma_{\text{NL}})$ and $\mathbf{f}_{\text{free}}(\Gamma_{\text{NL}})$. We use the procedure discussed in §5.1 to characterize the free field information needed to form the effective force vector.

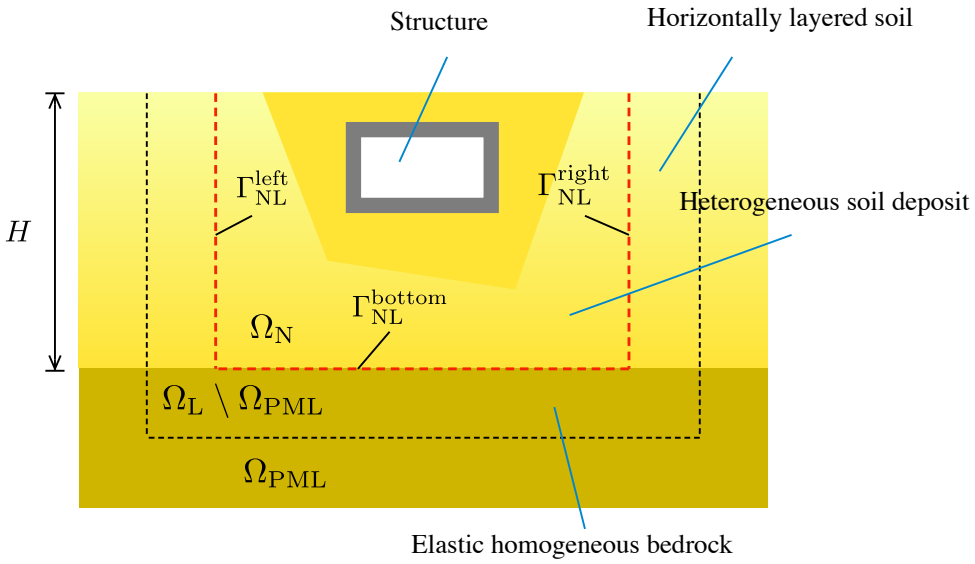

Figure 5.2: Schematic SSI problem in a PML-truncated domain for DRM analysis under vertically propagating shear waves.

Here, we assume that the soil properties in "horizontally layered soil" and "elastic homogeneous bedrock" regions shown in Figure 5.2 are, respectively, the same as those chosen for the soil layer and the elastic bedrock to obtain free field displacements and forces. The soil region in Ω_{N} may have arbitrary heterogeneity. After obtaining free field information, the results at $z = -H$ will be mapped along $\Gamma_{\text{NL}}^{\text{bottom}}$ while the results for $0 \leq z < -H$ will be mapped along the left and right interfaces $\Gamma_{\text{NL}}^{\text{left}}$ and $\Gamma_{\text{NL}}^{\text{right}}$.

5.3 Verification problems

5.3.1 Recovering the free field response in a PML-truncated domain using DRM

Here, we use the formulations presented in §3.3.2, §5.1 and §5.2 to compute the free field response for a soil layer with $H = 20$ m on an elastic bedrock (see Figure 5.3). For both

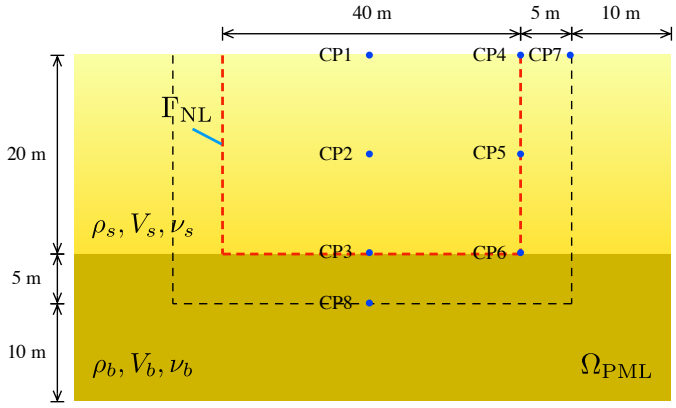

Figure 5.3: Problem configuration for recovering free field wave response in 2D wave analysis using DRM in PML-truncated domain.

soil and bedrock $\rho_b = \rho_s = 1600$ kg/m^3, $\nu_b = \nu_s = 0.3$, and $V_b = 450$ m/s. Soil layer shear wave velocity varies linearly from $V_s = 50$ m/s at surface to $V_s = 150$ m/s at depth of 20 m. The Ricker wavelet is used to compute the equivalent force. To wit,

$$u_b(t) = [1 - 2(t - t_{\mathrm{ctr}})^2 \pi^2 f_{\mathrm{ctr}}^2] \exp[-(t - t_{\mathrm{ctr}})^2 \pi^2 f_{\mathrm{ctr}}^2] \tag{5.9}$$

where t_{ctr} is the time at which the wavelet is centered and f_{ctr} is the frequency at which the Fourier amplitude of the wavelet is maximum. In our analyses, we set $f_{\mathrm{ctr}} = 10$ Hz and $t_{\mathrm{ctr}} = 0.15$ s.

In the first example, we assume that the soil layer is undamped. We consider 8 control points (CP) as shown in Figure 5.3. Figure 5.4 shows the wave response at these CPs compared against those obtained from 1D wave propagation, which are in excellent agreement. As expected the responses at CP7 and CP8 are zero. This is because, there is no scatterer within Ω_{N} to disturb the region outside Γ_{NL}.

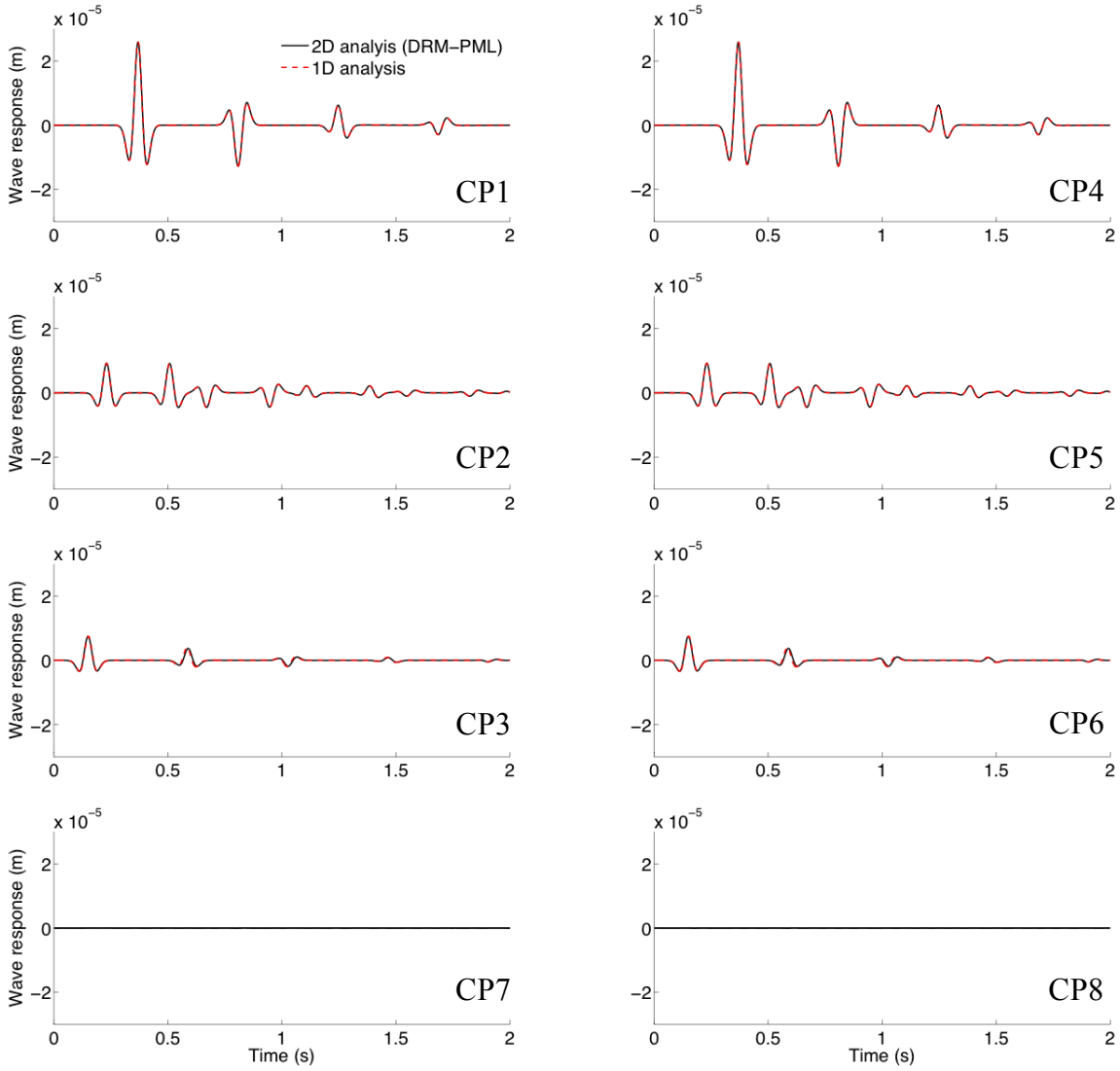

Figure 5.4: Free field wave responses for an undamped soil layer on an elastic bedrock obtained from 1D and 2D analyses.

In the second example, we obtain the wave response of a damped soil layer. For both 1D and 2D wave propagation analyses we use the Rayleigh damping model with 10% of damping ratio at control frequencies of 5 and 15 Hz. Figure 5.5 shows the wave responses at the same CPs, which are again in excellent agreement.

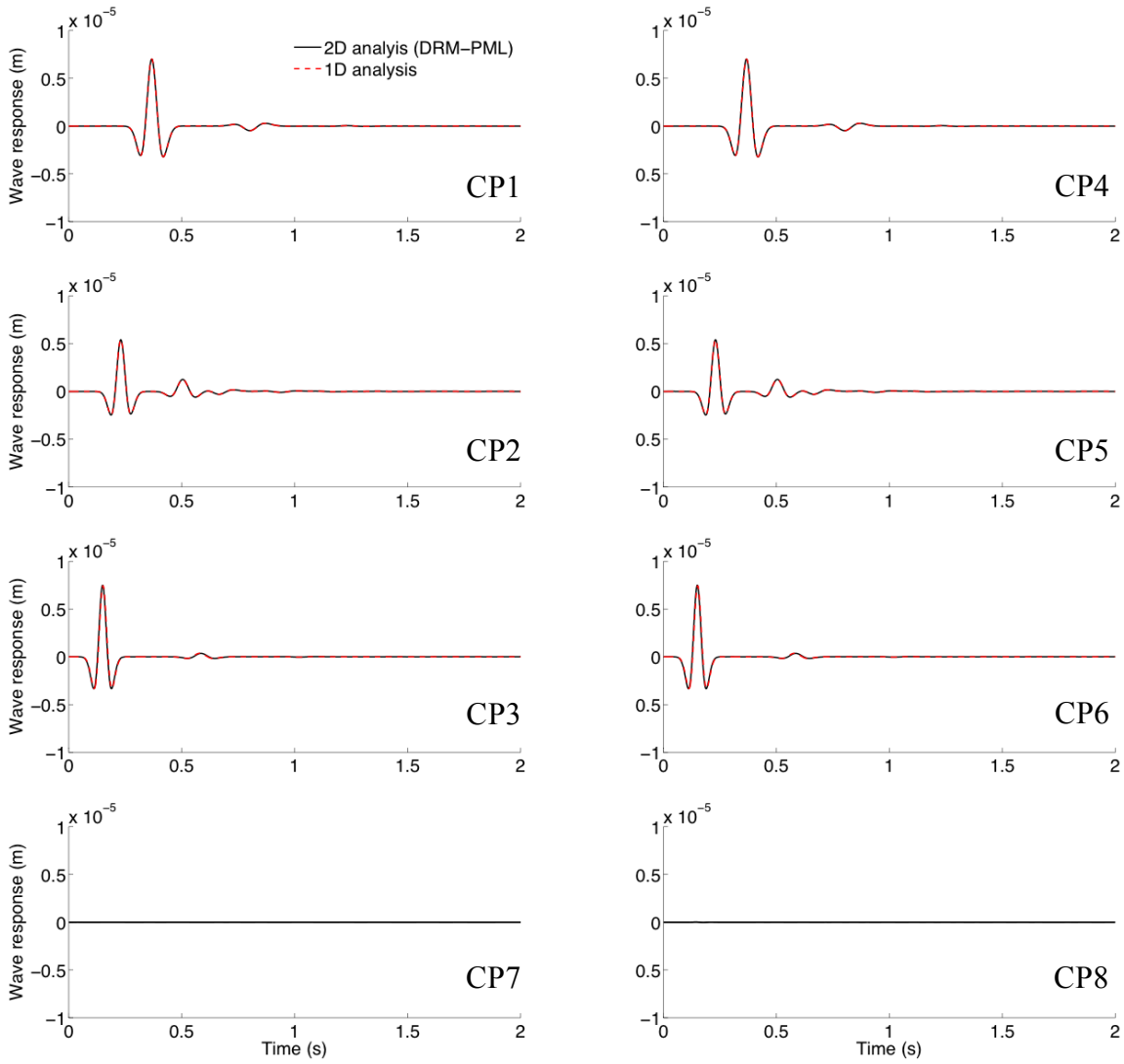

Figure 5.5: Free field wave responses for a damped soil layer on an elastic bedrock obtained from 1D and 2D wave propagation analyses.

5.3.2 Computing KITFs for a rigid semi-circular section embedded in a homogeneous half-space

Here, we consider a rigid massless semi-circular foundation embedded in an elastic half-space. The problem configuration is shown in Figure 5.6. In numerical analysis, it is assumed that

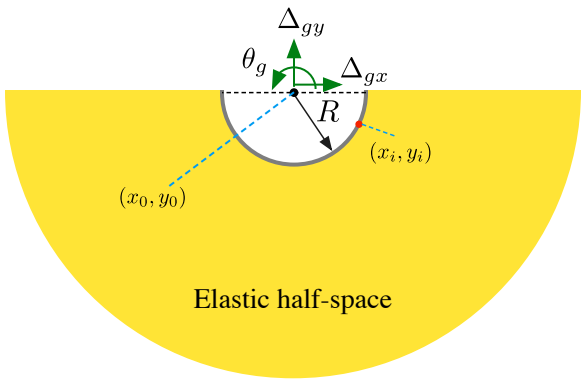

Figure 5.6: Geometry of a rigid semi-circle embedded in an elastic half-space.

the waves are embarking at depth $H = 20$ m. The properties of the homogeneous half-space is $V_s = 150$ m/s, $\rho = 1600$ kg/m^3, and $\nu = 1/3$. The radius of the foundation is $R = 5$ m. In order to impose rigidity along the interface, the Young's modulus, mass density and Poisson's ratio of the semi-circular object is set to 1000 GPa, 0.01 kg/m^3, and 1/3, respectively. Moreover, in order to capture the response of the foundation for the wide range of frequencies, Ricker wavelet with $t_{\text{ctr}} = 0.15$ s and $f_{\text{ctr}} = 20$ Hz is used. Figure 5.7 shows the amplitude of the displacement field—i.e. $|u| = \sqrt{u_x^2 + u_y^2}$—at $t = 0.2$, 0.3, 0.4, and 0.5 s.

Since the structure behaves rigidly, its motion can be defined based on the horizontal (Δ_{gx}), vertical (Δ_{gy}) and rotational (θ_g) motions at (x_0, y_0) (see Figure 5.6). These rigid body motions at each time increment can be extracted from the nodal displacements along

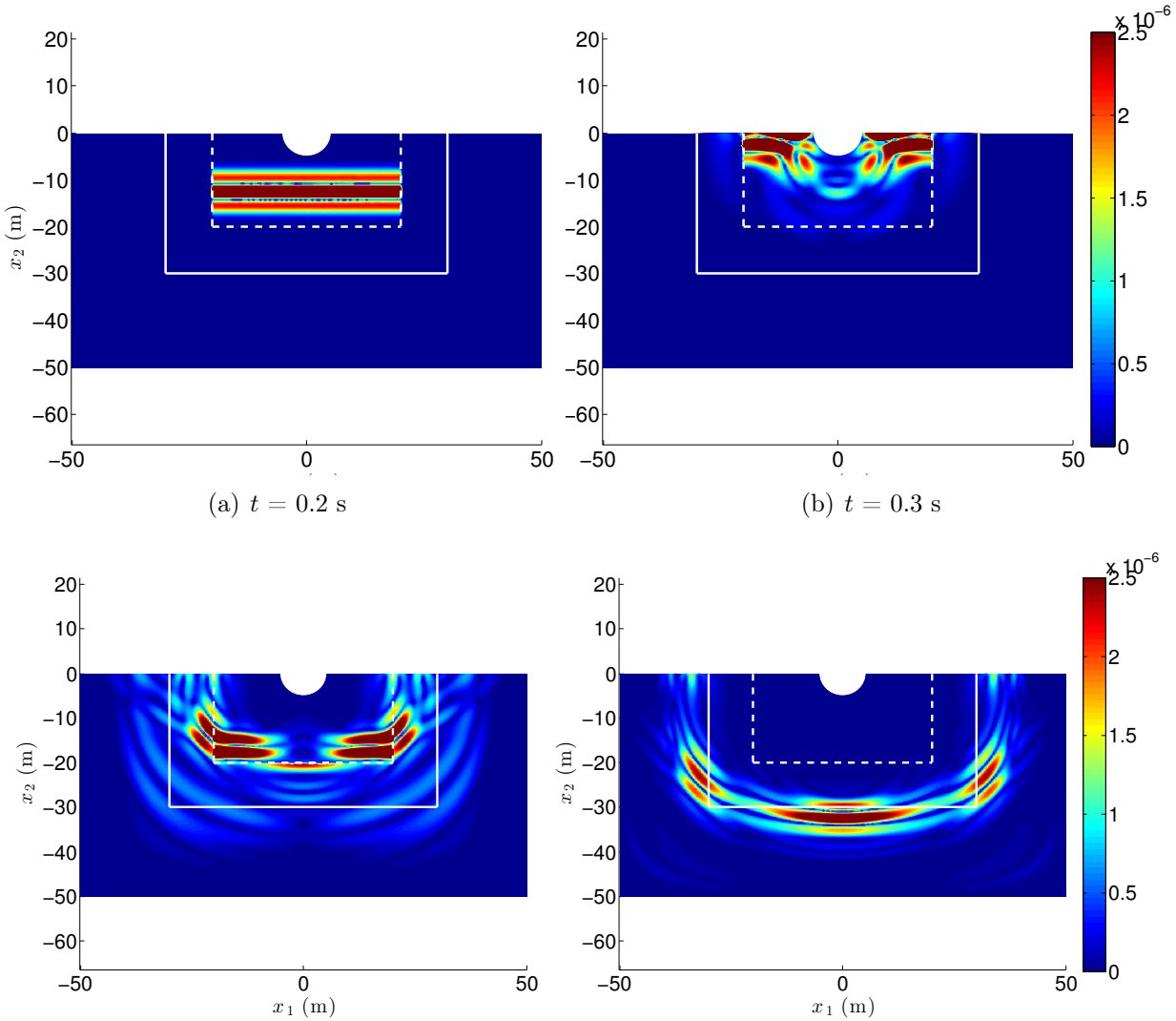

(a) $t = 0.2$ s

(b) $t = 0.3$ s

(c) $t = 0.4$ s

(d) $t = 0.5$ s

Figure 5.7: The amplitude of the displacement response for a rigid semi-circular interface embedded in a homogeneous elastic half-space with $\nu = 1/3$ and subjected to vertically propagating shear waves; The dashed white lines are the DRM interface (Γ_{NL}) and the solid white lines are the PML interface (Γ_{int}).

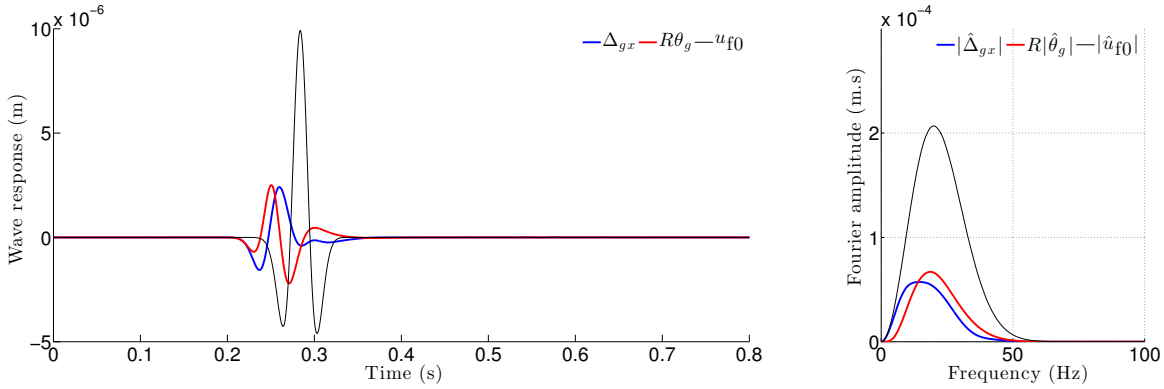

Figure 5.8: The response of the rigid semi-circular section in time and frequency.

the interface, as in:

$$\underbrace{\begin{bmatrix} 1 & 0 & -y_1+y_0 \\ 0 & 1 & x_1-x_0 \\ 1 & 0 & -y_2+y_0 \\ 0 & 1 & x_2-x_0 \\ \vdots & \vdots & \vdots \\ 1 & 0 & -y_n+y_0 \\ 0 & 1 & x_n-x_0 \end{bmatrix}}_{\mathbf{A}} \underbrace{\begin{bmatrix} \Delta_{gx}(t) \\ \Delta_{gy}(t) \\ \theta_g(t) \end{bmatrix}}_{\boldsymbol{\Delta}_g(t)} = \underbrace{\begin{bmatrix} u_{x1}(t) \\ u_{y1}(t) \\ u_{x2}(t) \\ u_{y2}(t) \\ \vdots \\ u_{xN_\mathrm{b}}(t) \\ u_{yN_\mathrm{b}}(t) \end{bmatrix}}_{\mathbf{u}(t)} \tag{5.10}$$

where (x_i, y_i) for $i \in 1, \ldots, N_\mathrm{b}$ is the position of node i along the interface Γ_b^+ (see Figure 5.6) and (u_{xi}, u_{yi}) is the node displacement. Therefore, at each time increment t, we solve:

$$\boldsymbol{\Delta}_g(t) = (\mathbf{A}^T\mathbf{A})^{-1}\mathbf{A}^T\mathbf{u}(t)\,. \tag{5.11}$$

Figure 5.8 shows the free field response as well as the rigid body motions of the interface in time and frequency. We define the KITFs for the horizontal and rotational DOFs as follows:

$$\mathrm{TF_H}(\omega) = \frac{\hat{\Delta}_{gx}(\omega)}{\hat{u}_{\mathrm{f0}}(\omega)}, \quad \mathrm{TF_R}(\omega) = \frac{R\hat{\theta}_g(\omega)}{\hat{u}_{\mathrm{f0}}(\omega)} \tag{5.12}$$

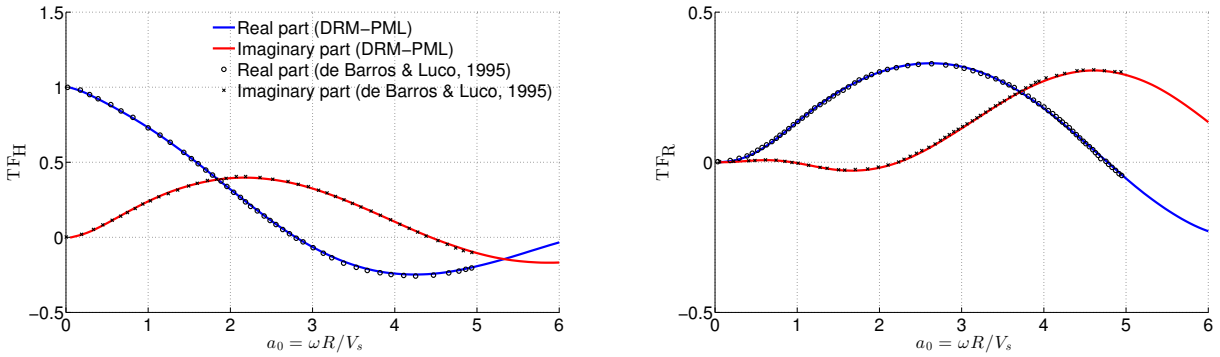

Figure 5.9: The KITFs of a rigid semi-circle embedded in elastic half-space with $\nu = 1/3$, compared against the reference solution due to de Barros and Luco (1995).

where u_{f0} is the free field motion at the surface of the elastic half-space with no excavation; $\mathrm{TF_H}$ and $\mathrm{TF_R}$ are complex-valued KITFs for horizontal and rotational DOFs. The real and imaginary parts of the resulting transfer functions are shown in Figure 5.9 as a function of dimensionless frequency $a_0 = \omega R/V_s$. The reference solution for this problem is due to de Barros and Luco (1995) who used the indirect boundary integral equation method to compute the response of the foundation to seismic waves. As shown, the numerical results are in excellent agreement with the reference solution.

CHAPTER 6

Application studies I: Reduced order modeling of buried structures

In this work, we presented detailed description of a numerical platform we used for direct modeling of linear SSI problems in a 2D setting, which took advantages of PML as the ABC and DRM as a proxy to solve the scattering problems efficiently. Moreover, we presented the methodologies we used to compute the impedance functions for rigid and flexible interfaces within the heterogeneous half-spaces as well as KITFs. We used a variety of existing theoretical solution to verify the numerically computed impedances and KITFs, which are the ingredients of constructing the representative reduced order model of the actual SSI problem.

As mentioned in Chapter 1, the existing solutions for the impedance functions and FIMs of buried structures are very limited. In this chapter, we use our numerical platform to have a closer look on the dynamic behavior of rigid and flexible buried structures through studying their impedances, KITFs, and reduced order models.

6.1 Impedance matrix of a rigid void embedded in an elastic half-space

Figure 6.1 shows two buried structures with rectangular and circular cross sections in an elastic half-space. We use the verified FE solver to explore the effects of the soil profile and interface geometry on the impedance functions. The dimensions for the rectangular and circular voids are $B = L = D/3$ and $R = 4B/\pi$, respectively, and the location of the rotational centroid is $(x_0,\, y_0) = (0,\, -D)$. The radius of the circular void is *purposely* selected

such that both voids, though their geometries are different, have the same length of contact with the surrounding soil. Two cases of $E_{1,0}/E_2 = 0.5$ and 1 are studied. The Poisson's ratio of the soil is 0.25 for both layers and $E_{1,H} = E_2$.

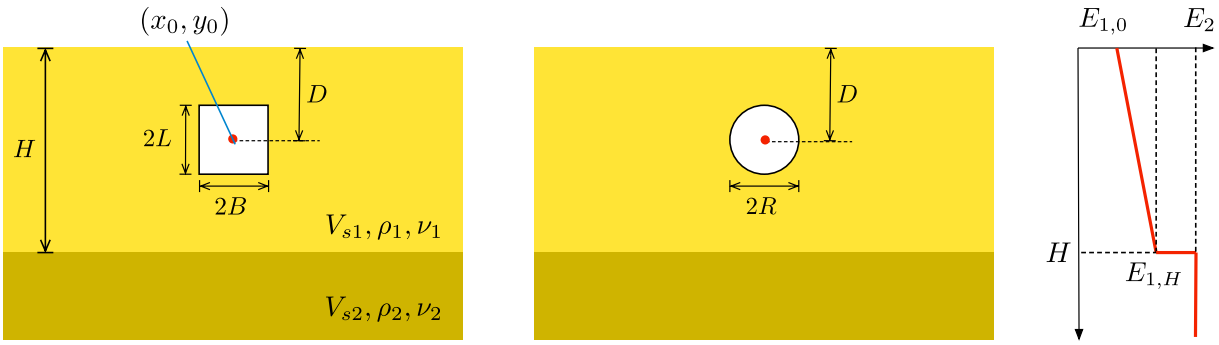

(a) Rectangular void (b) Circular void (c) Soil profile

Figure 6.1: Rigid void embedded in a heterogenous soil domain.

The computed impedances are shown in Figure 6.2. As these results indicate, both the real and imaginary parts of all impedance components—i.e., $\hat{K}_V$, $\hat{K}_{HH}$, $\hat{K}_{MM}$, and $\hat{K}_{HM}$—are highly sensitive to the modulus gradient. Moreover, the oscillatory behavior of the impedance functions—even for the homogeneous soil—is significant. This is due to constructive (or destructive) interferences of waves occur within the space between the void (tunnel) and the ground surface, so that the reaction at the tunnel boundary is amplified (or reduced).

For the vertical and horizontal DOFs, the impedance functions of rectangular and circular voids are very close to each other at frequencies with $a_0 < 1$. This is because at small frequencies the wavelength of propagating waves can become very large in comparison with dimensions of the void and therefore less sensitive to the exact shape of the soil-structure interfaces possessing same peripherality and depth of embedment. The constant shift between rocking impedances of circular and rectangular voids at small frequencies is due to the higher inertia of the circular interface. At higher frequencies, sensitivity to interface geometry increases, and therefore impedances of rectangular and circular void deviate from each other.

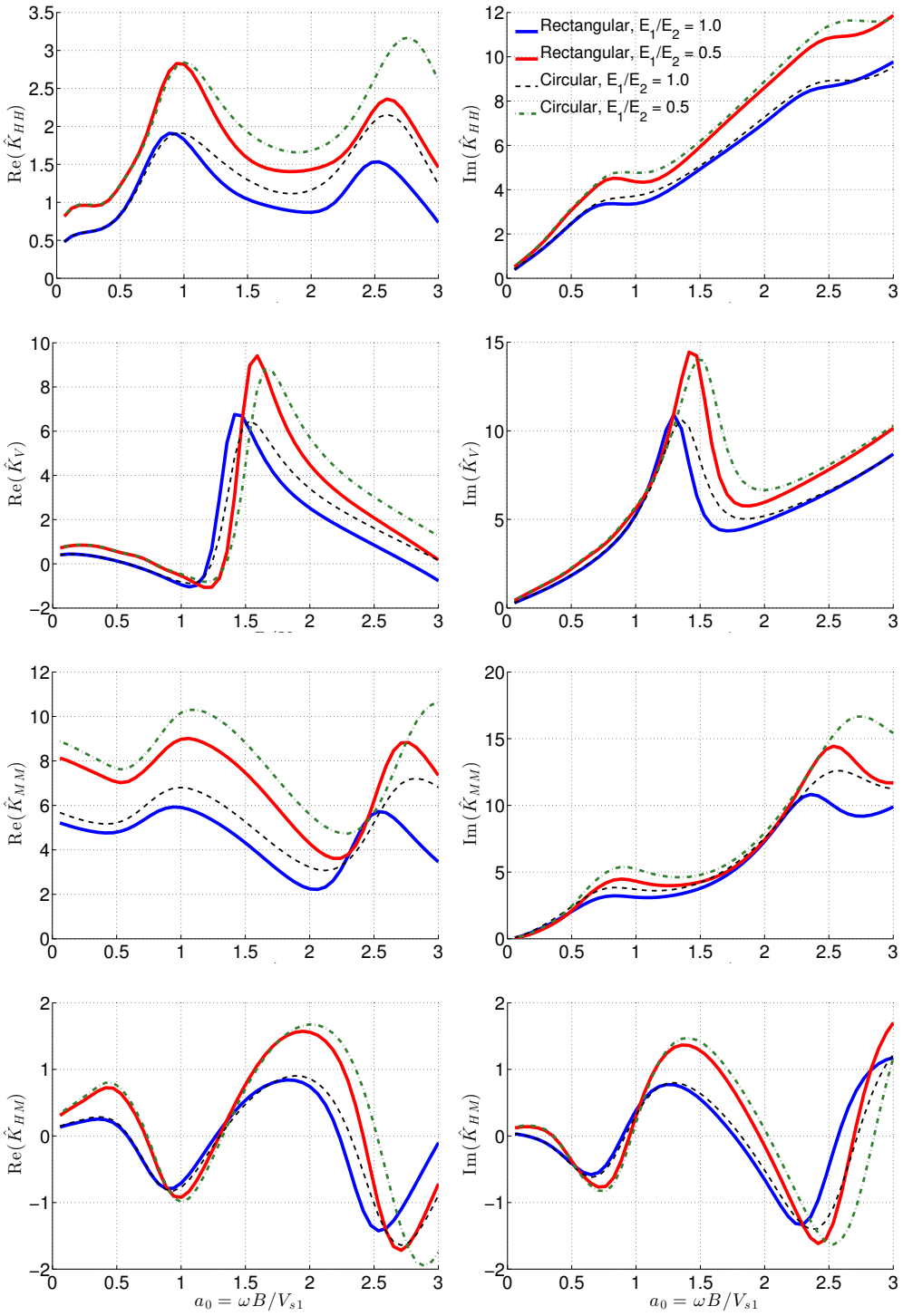

Figure 6.2: Impedance functions of a rectangular and circular voids embedded in soils with linearly-depth-dependent Young's modulus with $\nu = 0.25$; $b = B$ in Eq. (4.1).

6.2 KITFs of a rigid void embedded in an elastic half-space

Here we consider a rigid interface shown in Figure 6.1a. We set $L = 5$ m, $V_{s1,0} = V_{s1,H} = 150$ m/s, and $H = 20$ m. The soil density and Poisson's ratio for both layers are 1600 kg/m^3 and 0.3, respectively. The Ricker wavelet with central frequency of 10 Hz is used as the input motion embarking vertically at the interface of the two layers at depth H. Eight cases with $B/L = 1, 2$, $D/L = 1, 1.5$, and $E_{1,0}/E_2 = E_{1,H}/E_2 = 0.5, 1$ are considered to explore the effects of structure aspect ratio, embedment, and soil profile on the kinematic response of the structure.

Figure 6.3a,c shows the amplitude of the horizontal and rotational transfer functions computed at (x_0, y_0) for the homogeneous case and Figure 6.4a,c shows the variation of these transfer functions for the non-homogeneous case. In order to have a closer look at the effects of the wavelength of the incoming waves (λ), the horizontal axis in both figures is $\lambda/2L = \pi V_{s1,0}/\omega L$.

As shown, the amplitude of the horizontal and rotational KITFs are close to 1 and zero, respectively, for large values of λ. This is a well-known trend, and is due to the fact that the deformation of the soil particles are almost in phase with each other at small frequencies. As λ decreases, the horizontal TF decreases while the rotational TF increases due to the relative rigidity of the interface with respect to the surrounding soil.

For the homogeneous soil, with increasing the embedment and aspect ratio of the structure, the translational movement decreases and increases, respectively. This trend is reversed for the rotational movement of the structure. On the other hand, for the inhomogeneous case, we observe more oscillations in the translational and rotational KITFs, which happen around those obtained for the homogenous case.

Figures 6.3b,d and 6.4b,d show the polar plots of the computed KITFs, which show how soil heterogeneity deteriorates the smooth variation of real and imaginary parts of the KITFs.

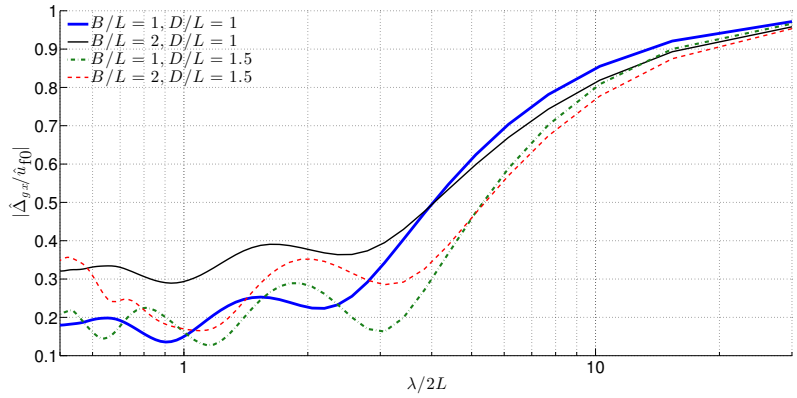

(a) Amplitude, Horizontal

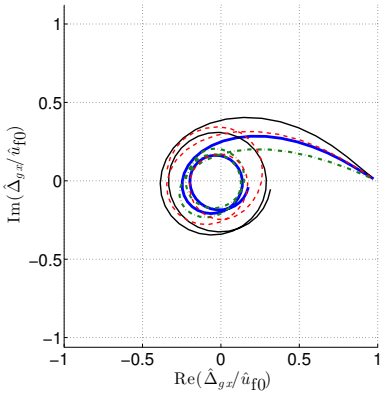

(b) Polar Plot, Horizontal

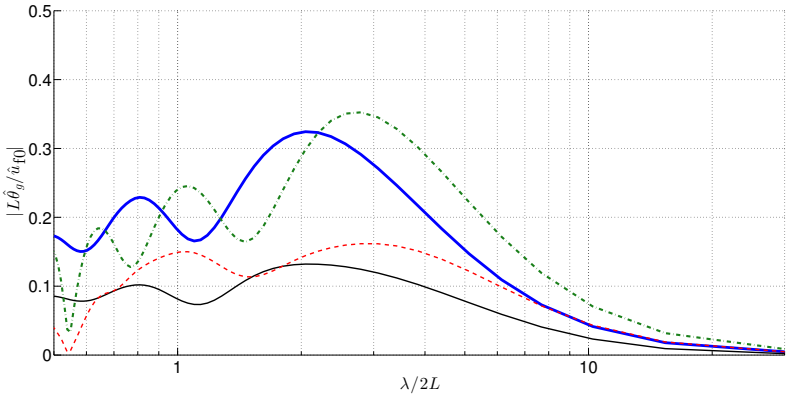

(c) Amplitude, Rotational

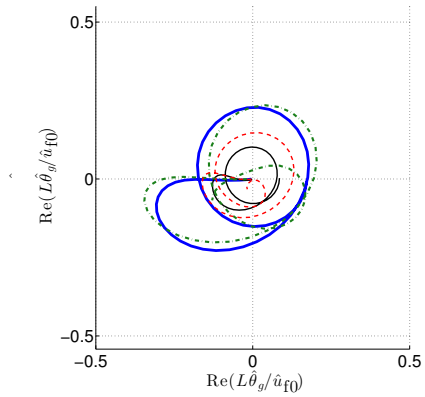

(d) Polar Plot, Rotational

Figure 6.3: The amplitude and polar plot of the KITFs for horizontal and rotational DOFs of a rectangular void embedded in a two-layered soil with $E_{1,0}/E_2 = E_{1,H}/E_2 = 1$.

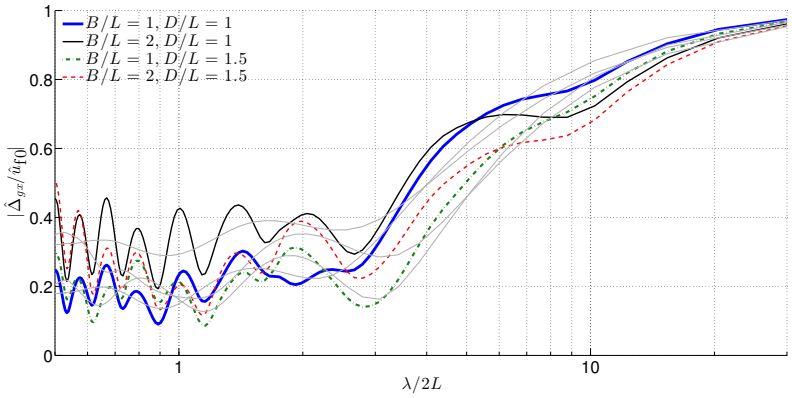

(a) Amplitude, Horizontal

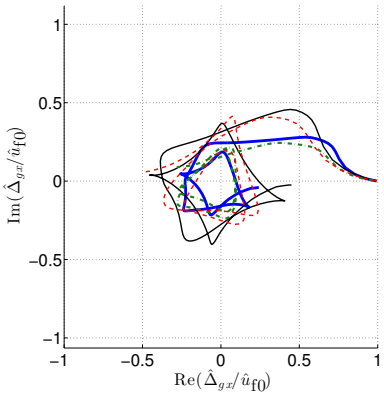

(b) Polar Plot, Horizontal

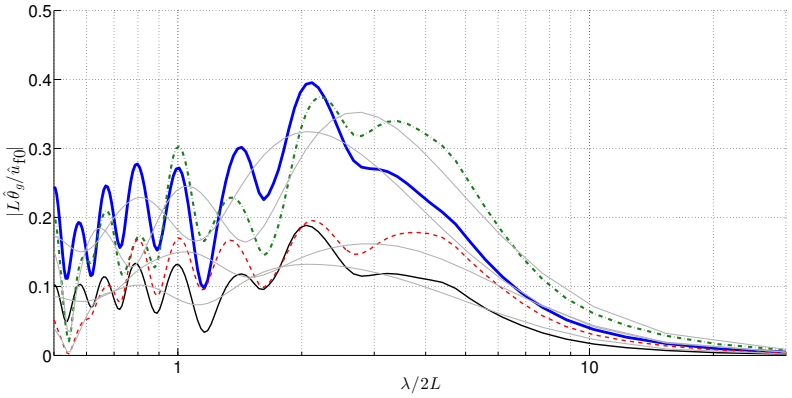

(c) Amplitude, Rotational

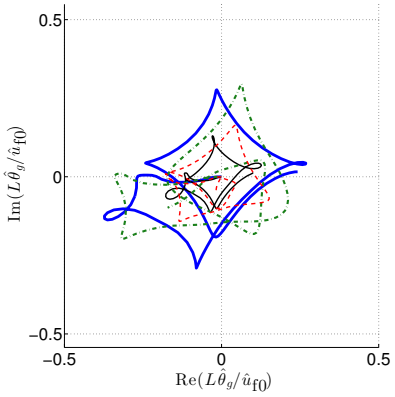

(d) Polar Plot, Rotational

Figure 6.4: The amplitude and polar plot of the KITFs for horizontal and rotational DOFs of a rectangular void embedded in a two-layered soil with $E_{1,0}/E_2 = E_{1,H}/E_2 = 0.5$; the gray solid lines are the amplitude of the KITFs for the homogeneous case in Figure 6.3.

6.3 Time domain substructure modeling of a flexible buried structure in an elastic half-space

The main objective of this work was to devise a general framework for reduced order modeling of SSI problems. Here, we show how we can use this framework to compute the response of a buried structure (see Figure 6.5) using the substructure modeling approach. As mentioned before, the main advantage of this approach is that once we construct the soil reduced order model, the response of different structural models can be investigated.

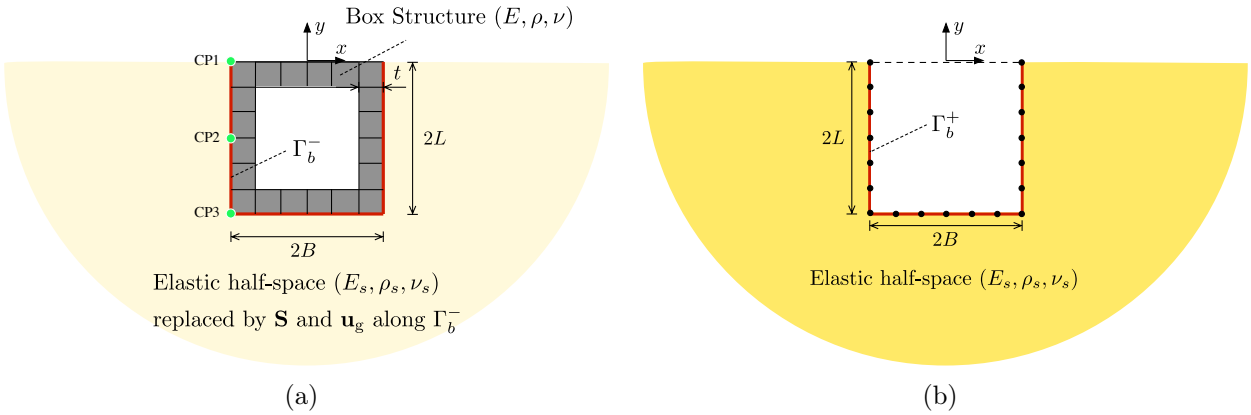

Figure 6.5: Schematic (a) box structure embedded in an elastic half-space represented by $\mathbf{S}$ and $\mathbf{u}_g$ and (b) excavated elastic half-space.

6.3.1 Step I: Computing the nodal impedance matrix $\hat{\mathbf{S}}(\omega)$ along the interface Γ_b^+

We consider an excavated half-space shown in Figure 6.5b. Soil properties are $V_s = 150$ m/s, $\nu = 0.3$, $\rho = 1600$ kg/m^3, and $\xi = 0$. Dimensions of the excavation are $L = B = 5$ m. Quadratic elements with element size of 1 m are used for discretization of the half-space, which results in $N_b = 61$ nodes, and therefore $2N_b = 122$ DOFs, on the interface Γ_b^+ . We use the procedure described in Chapter 4 to compute the nodal impedance matrix $\hat{\mathbf{S}}(\omega) \in \mathbb{C}^{122\times122}$ for $0 < \omega \leq 50\pi$. At each DOF, we prescribe a known displacement while keeping all other DOFs fixed and compute the reaction forces. We repeat this procedure for all DOFs along the interface Γ_b^+ shown in Figure 6.5b.

In order to verify the accuracy of the computed nodal impedance matrix, we use the substructure modeling formulation provided in §2.2 to recover the impedance matrix of a rigid surface foundation. We consider a soil block with dimensions $B = L = 5$ m. For computing the horizontal, vertical and rocking impedance functions, we apply known displacements Δ_1, Δ_2 an θ, respectively, on DOFs along the surface of the soil block from $x = -B$ to $x = B$. This is shown schematically in Figure 6.6. Then, for each case, we solve Eq. (2.7), which is

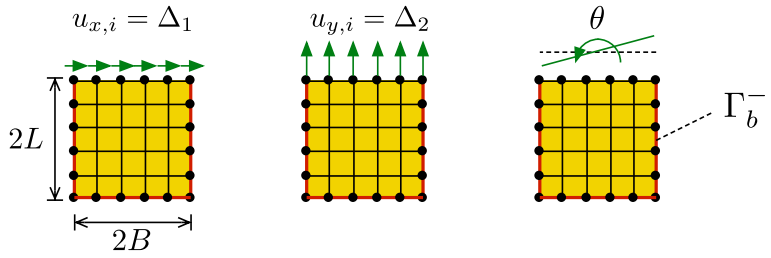

Figure 6.6: Prescribed displacements on the surface of the soil block to recover the impedance matrix of a surface rigid foundation.

repeated here as in Eq. (6.1), setting $\hat{\mathbf{f}}_{\text{ext}} = 0$ and $\hat{\mathbf{u}}_{\text{g}} = 0$.

$$\underbrace{\begin{bmatrix} \hat{\mathbf{S}}_{\text{ss}}(\omega) & \hat{\mathbf{S}}_{\text{sb}}(\omega) \\ \hat{\mathbf{S}}_{\text{bs}}(\omega) & \hat{\mathbf{S}}_{\text{bb}}(\omega) + \hat{\mathbf{S}}(\omega) \end{bmatrix}}_{\hat{\mathbf{S}}^{\text{ROM}}} \underbrace{\begin{bmatrix} \hat{\mathbf{u}}_{\text{s}}(\omega) \\ \hat{\mathbf{u}}_{\text{b}}^-(\omega) \end{bmatrix}}_{\hat{\mathbf{u}}^{\text{ROM}}} = \begin{bmatrix} \mathbf{0} \\ \mathbf{0} \end{bmatrix} . \tag{6.1}$$

We compute the reaction forces at DOFs along which the known displacements are prescribed using

$$\hat{\mathbf{r}} = [\hat{\mathbf{S}}^{\text{ROM}}_{\text{kn,kn}} - \hat{\mathbf{S}}^{\text{ROM}}_{\text{kn,unkn}} (\hat{\mathbf{S}}^{\text{ROM}}_{\text{unkn,unkn}})^{-1} \hat{\mathbf{S}}^{\text{ROM}}_{\text{unkn,kn}}] \hat{\mathbf{u}}_{\text{kn}} \tag{6.2}$$

where $\hat{\mathbf{S}}^{\text{ROM}}$ is partitioned as follows:

$$\hat{\mathbf{S}}^{\text{ROM}} = \left[\begin{array}{c|c} \hat{\mathbf{S}}^{\text{ROM}}_{\text{unkn,unkn}} & \hat{\mathbf{S}}^{\text{ROM}}_{\text{unkn,kn}} \\ \hline \hat{\mathbf{S}}^{\text{ROM}}_{\text{kn,unkn}} & \hat{\mathbf{S}}^{\text{ROM}}_{\text{kn,kn}} \end{array}\right] . \tag{6.3}$$

Then, using the similar procedure described in Chapter 4, we can compute the impedance matrix of the rigid surface foundation. The components of the resulting impedance matrix

along with those obtained from the direct modeling approach are shown in Figure 6.7. In the direct modeling, we compute the impedance functions through simulation of the PML-truncated half-space using the frequency domain FE solver. As shown, the results from both approaches are in excellent agreement.

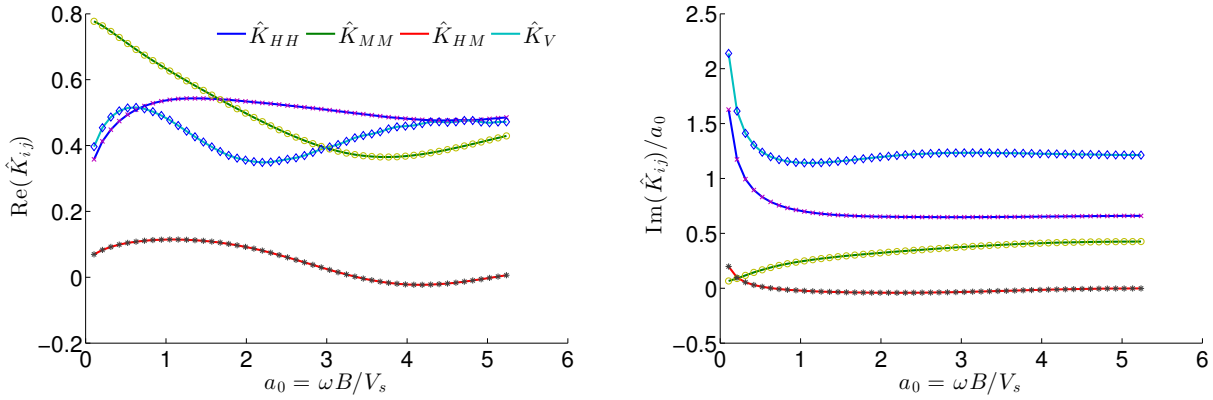

Figure 6.7: Comparison of the impedance functions of a rigid surface foundation obtained from the substructure modeling (solid lines) and direct modeling (scatter points) approaches.

6.3.2 Step II: Computing the modified input motion vector $\mathbf{u_g}(t)$ along the interface Γ_b^+

We use the procedure described in Chapter 5 to compute the displacement vector along the interface Γ_b^+ under vertically propagating shear waves. Again, in order to verify the accuracy of the procedure, we consider the same soil block as in §6.3.1. In order to compute the response of the soil surface from $x = -B$ to $x = B$, we solve Eq. (2.7) setting $\mathbf{f}_{\text{ext}} = \mathbf{0}$. Figure 6.8a shows the horizontal and vertical displacements of all DOFs on the soil block surface normalized by the free field motion $\hat{u}_{\text{f0}}$. We define the free-field motion as the motion recorded on the surface of the soil half-space with no excavation. As shown, the horizontal displacements of all DOFs are the same as the free field displacement and the vertical displacements are negligible.

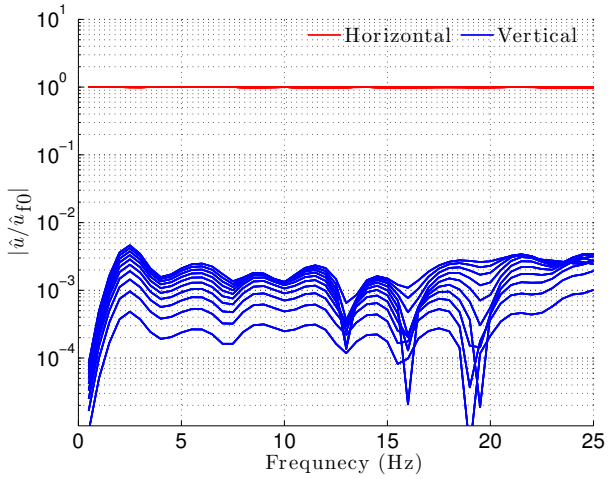

Figure 6.8: Comparison of the soil surface response obtained from the reduced order model and the direct modeling approach.

6.3.3 Step III: Computing the discrete-time filter matrix $\mathbf{S}^{\mathbf{filter}}$ along the interface Γ_b^+

As mentioned in Chapter 2, one approach for time domain representation of soil impedance functions is the rational approximation of the function. Gash (2015); Gash et al. (2016) implemented a numerically stable discrete-time filter method and studied the frequency dependent effects of soil on inelastic response of multi-degree-of-freedom structures with rigid foundation in a layered soil half-space.

Here, we use the same approach to obtain the coefficients of stable discrete-time filters for time domain representation of each components of the computed nodal impedance matrix ($\hat{S}_{ij}$). To wit,

$$S_{ij}^{\text{filter}} = \frac{b_{0,ij} + b_{1,ij}z^{-1} + \cdots + b_{M-1,ij}z^{-(M-1)}}{1 + a_{1,ij}z^{-1} + \cdots + a_{M,ij}z^{-M}} \quad \text{for} \quad i,j = 1,\ldots,2N_b \tag{6.4}$$

where M is the order of the rational function and $z = e^{i\omega_d}$; $i = \sqrt{-1}$ and ω_d is the discrete frequency. Figure 6.9 shows the map of the filter order in which indices i and j are

corresponding to the components of the computed impedance matrix partitioned as follows:

$$\hat{\mathbf{S}} = \left[\begin{array}{c:c} \hat{\mathbf{S}}_{\mathrm{xx}} & \hat{\mathbf{S}}_{\mathrm{xy}} \\ \hat{\mathbf{S}}_{\mathrm{yx}} & \hat{\mathbf{S}}_{\mathrm{yy}} \end{array}\right] . \tag{6.5}$$

In Eq. (6.5), x and y denote the horizontal and vertical DOFs along Γ_{b}^{+}, respectively.

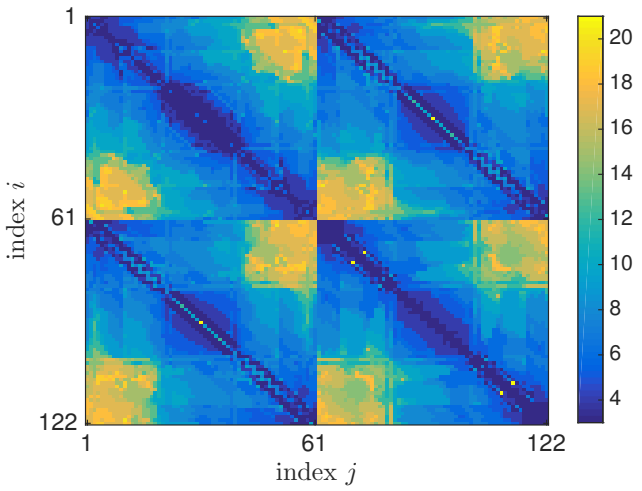

Figure 6.9: The map of the filter order for each components of the matrix $\mathbf{S}^{\mathrm{filter}}$.

Figure 6.10 shows two examples of the impedance functions. As shown, as we get farther from the diagonal terms the impedance functions become wavier and therefore higher order filters would be needed to capture the function oscillations.

6.3.4 Step IV: Constructing the reduced order model

Here, we want to use the computed modified input motions $\mathbf{u}_{\mathrm{g}}$ and the filter matrix $\mathbf{S}^{\mathrm{filter}}$ to obtain the response of the buried structure shown in Figure 6.5a. We assume that the structure behaves linearly and there is no damping in the structure. Moreover, $\rho = 1.5\rho_s$, $\nu = 0.3$, and $t = 1$ m. Two stiffness ratios of $E = 1000E_s$ and $E = 10E_s$ are considered to represent the relatively stiff and flexible structures, respectively. At each time step $t_n = n\Delta t$,

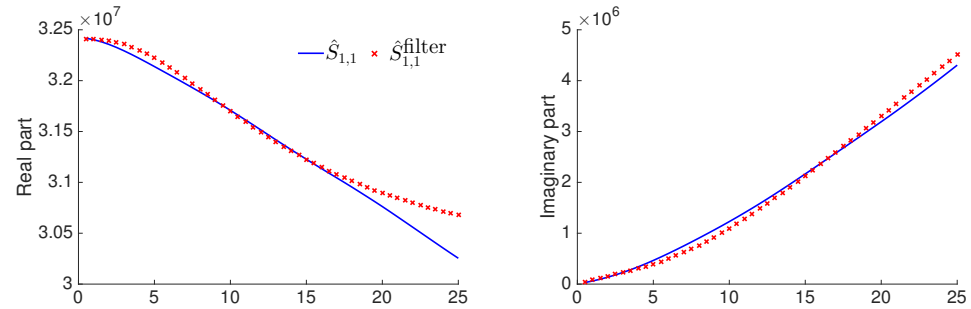

(a)

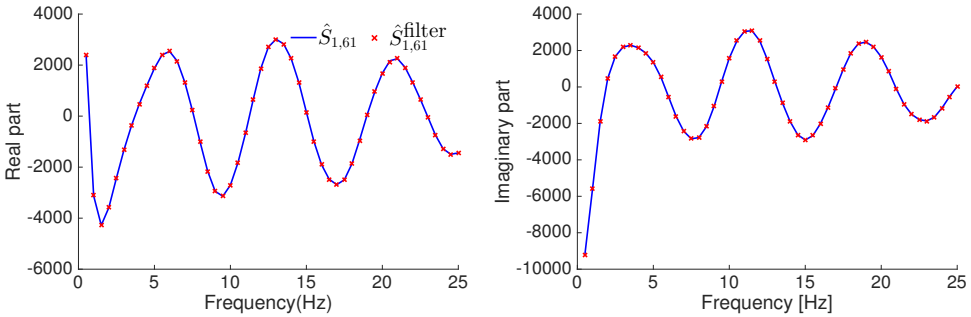

(b)

Figure 6.10: The real and imaginary parts of the impedance functions computed using the FE solver and approximated using the discrete-time filter method at two positions of (a) $i = j = 1$ and (b) $i = 1$ and $j = 61$.

we rewrite Eq. (2.6) as follows:

$$\begin{bmatrix} \mathbf{M}_{\mathrm{ss}} & \mathbf{M}_{\mathrm{sb}} \\ \mathbf{M}_{\mathrm{bs}} & \mathbf{M}_{\mathrm{bb}} \end{bmatrix} \begin{bmatrix} \ddot{\mathbf{u}}_{\mathrm{s}}[n\Delta t] \\ \ddot{\mathbf{u}}_{\mathrm{b}}^{-}[n\Delta t] \end{bmatrix} + \begin{bmatrix} \mathbf{K}_{\mathrm{ss}} & \mathbf{K}_{\mathrm{sb}} \\ \mathbf{K}_{\mathrm{bs}} & \mathbf{K}_{\mathrm{bb}} \end{bmatrix} \begin{bmatrix} \mathbf{u}_{\mathrm{s}}[n\Delta t] \\ \mathbf{u}_{\mathrm{b}}^{-}[n\Delta t] \end{bmatrix} + \begin{bmatrix} \mathbf{0} \\ \mathbf{f}_{\mathrm{b}}^{+}[n\Delta t] \end{bmatrix} = \begin{bmatrix} \mathbf{0} \\ \mathbf{f}_{\mathrm{g}}[n\Delta t] \end{bmatrix} . \quad (6.6)$$

Using the inverse z-transform (Oppenheim et al., 1996), each components of the input force vector $\mathbf{f}_{\mathrm{g}}[n\Delta t] \in \mathbb{R}^{2N_b}$ can be written as:

$$f_{\mathrm{g},i}[n\Delta t] = \sum_{j=1}^{2N_b} f_{\mathrm{g},i}^{j}[n\Delta t] \quad \text{for} \quad i = 1, \ldots, 2N_b \quad (6.7)$$

where

$$f_{\mathrm{g},i}^{j}[n\Delta t] = \sum_{k=0}^{M-1} b_{k,ij} u_{\mathrm{g},j}[(n-k)\Delta t] - \sum_{k=1}^{M} a_{k,ij} f_{\mathrm{g},i}^{j}[(n-k)\Delta t] \, . \quad (6.8)$$

At each time step, we know the value of the displacement vector $\mathbf{u}_{\mathrm{g}}$, and therefore the right hand side of Eq. (6.8) is known. On the other hand, each components of the force vector $\mathbf{f}_{\mathrm{b}}^{+}[n\Delta t]$ can be defined as follows:

$$f_{\mathrm{b},i}^{+}[n\Delta t] = \sum_{j=1}^{2N_b} f_{\mathrm{b},i}^{j+}[n\Delta t] \quad \text{for} \quad i = 1, \ldots, 2N_b \quad (6.9)$$

where

$$f_{\mathrm{b},i}^{j+}[n\Delta t] = b_{0,ij} u_{\mathrm{b},j}^{-}[n\Delta t] + \underbrace{\sum_{k=1}^{M-1} b_{k,ij} u_{\mathrm{b},j}^{-}[(n-k)\Delta t] - \sum_{k=1}^{M} a_{k,ij} f_{\mathrm{b},i}^{j+}[(n-k)\Delta t]}_{p_{\mathrm{b},i}^{j+}[n\Delta t]} \, . \quad (6.10)$$

Therefore,

$$\mathbf{f}_{\mathrm{b}}^{+}[n\Delta t] = \mathbf{B}_0 \mathbf{u}_{\mathrm{b}}^{-}[n\Delta t] + \mathbf{p}_{\mathrm{b}}^{+}[n\Delta t] \quad (6.11)$$

where

$$B_{0,ij} = b_{0,ij} \quad \text{for} \quad i,j = 1,\ldots,2N_b \tag{6.12}$$

and

$$p^{+}_{\mathrm{b},i}[n\Delta t] = \sum_{j=1}^{2N_b} p^{j+}_{\mathrm{b},i}[n\Delta t] \quad \text{for} \quad i = 1,\ldots,2N_b\,. \tag{6.13}$$

In contrary to Eq. (6.8), the first term in the right hand side of Eq. (6.10) is not known a priori and in fact is the part of the solution vector to be computed at time step $n\Delta t$. As a result, we can reformulate Eq. (6.6) as follows:

$$\begin{bmatrix} \mathbf{M}_{\mathrm{ss}} & \mathbf{M}_{\mathrm{sb}} \\ \mathbf{M}_{\mathrm{bs}} & \mathbf{M}_{\mathrm{bb}} \end{bmatrix} \begin{bmatrix} \ddot{\mathbf{u}}_{\mathrm{s}}[n\Delta t] \\ \ddot{\mathbf{u}}^{-}_{\mathrm{b}}[n\Delta t] \end{bmatrix} + \begin{bmatrix} \mathbf{K}_{\mathrm{ss}} & \mathbf{K}_{\mathrm{sb}} \\ \mathbf{K}_{\mathrm{bs}} & \mathbf{K}_{\mathrm{bb}} + \mathbf{B}_0 \end{bmatrix} \begin{bmatrix} \mathbf{u}_{\mathrm{s}}[n\Delta t] \\ \mathbf{u}^{-}_{\mathrm{b}}[n\Delta t] \end{bmatrix} = \begin{bmatrix} \mathbf{0} \\ \mathbf{f}_{\mathrm{g}}[n\Delta t] - \mathbf{p}^{+}_{\mathrm{b}}[n\Delta t] \end{bmatrix}. \tag{6.14}$$

As mentioned before, a common approach for time domain representation of a soil impedance function is to ignore the frequency dependency of the real and imaginary parts of the function. This will result in:

$$\mathbf{f}^{0}_{\mathrm{g}}[n\Delta t] = \mathbf{K}_0\mathbf{u}_{\mathrm{g}}[n\Delta t] + \mathbf{C}_0\dot{\mathbf{u}}_{\mathrm{g}}[n\Delta t] \tag{6.15}$$

$$\mathbf{f}^{0+}_{\mathrm{b}}[n\Delta t] = \mathbf{K}_0\mathbf{u}^{-}_{\mathrm{b}}[n\Delta t] + \mathbf{C}_0\dot{\mathbf{u}}^{-}_{\mathrm{b}}[n\Delta t] \tag{6.16}$$

where the instantaneous stiffness ($\mathbf{K}_0$) and damping ($\mathbf{C}_0$) matrices are defined as follows:

$$K_{0,ij} = \mathrm{Re}\{\hat{S}_{ij}(\omega = \omega_0)\} \quad \text{and} \quad C_{0,ij} = \frac{\mathrm{Im}\{\hat{S}_{ij}(\omega = \omega_0)\}}{\omega_0} \tag{6.17}$$

and ω_0 is the frequency at which the impedance functions are computed. Using this approximation, we need to solve the following system of linear equations instead:

$$\begin{bmatrix} \mathbf{M}_{\rm ss} & \mathbf{M}_{\rm sb} \\ \mathbf{M}_{\rm bs} & \mathbf{M}_{\rm bb} \end{bmatrix} \begin{bmatrix} \ddot{\mathbf{u}}_{\rm s}[n\Delta t] \\ \ddot{\mathbf{u}}_{\rm b}^{-}[n\Delta t] \end{bmatrix} + \begin{bmatrix} \mathbf{0} & \mathbf{0} \\ \mathbf{0} & \mathbf{C}_0 \end{bmatrix} \begin{bmatrix} \dot{\mathbf{u}}_{\rm s}[n\Delta t] \\ \dot{\mathbf{u}}_{\rm b}^{-}[n\Delta t] \end{bmatrix} + \begin{bmatrix} \mathbf{K}_{\rm ss} & \mathbf{K}_{\rm sb} \\ \mathbf{K}_{\rm bs} & \mathbf{K}_{\rm bb} + \mathbf{K}_0 \end{bmatrix} \begin{bmatrix} \mathbf{u}_{\rm s}[n\Delta t] \\ \mathbf{u}_{\rm b}^{-}[n\Delta t] \end{bmatrix} = \begin{bmatrix} \mathbf{0} \\ \mathbf{f}_{\rm g}^{0}[n\Delta t] \end{bmatrix} . \tag{6.18}$$

For the latter, we also consider the case that only the diagonal entries of the impedance matrix are used to create the matrices. To wit,

$$\mathbf{K}_0^{\rm diag} = {\rm diag}({\rm Re}\{{\rm diag}[\hat{\mathbf{S}}(\omega_0)]\}), \quad \mathbf{C}_0^{\rm diag} = {\rm diag}(\frac{{\rm Im}\{{\rm diag}[\hat{\mathbf{S}}(\omega_0)]\}}{\omega_0}) . \tag{6.19}$$

We use the Newmark's time stepping method to solve Eqs. (6.14) and (6.18).

We also use our time domain FE solver to model the same problem, which is considered as the reference solution. We consider the Ricker wavelet with the central frequency of 2.5 Hz as the input motion. First, we use $\omega/2\pi = 2.5$ Hz to compute the constant-valued impedances.

Figures 6.11 and 6.12 show, respectively, the time-series and Fourier amplitude of the total horizontal displacements of a relatively stiff and flexible structures at three control points CP1, CP2, and CP3 depicted in Figure 6.5a. As shown, the impedance filter results could capture those obtained from direct modeling approach for both stiff and flexible structures. On the other hand, the accuracy of the models with constant-valued springs and dashpots decreases, specially for the model that omits the off-diagonal terms of the impedance matrix.

In order to explore the effects of the chosen ω_0 on accuracy of the approximate impedance matrices, we repeat the analyses using $\omega/2\pi = 5$ Hz. Figures 6.13 and 6.14 show the displacement responses at the control points for rigid and flexible structures, respectively. As shown, using $\omega/2\pi = 5$ Hz does not affect the performance of the model that uses $\mathbf{K}_0^{\rm diag}$ and $\mathbf{C}_0^{\rm diag}$. This is mainly because the diagonal stiffness and damping values are almost

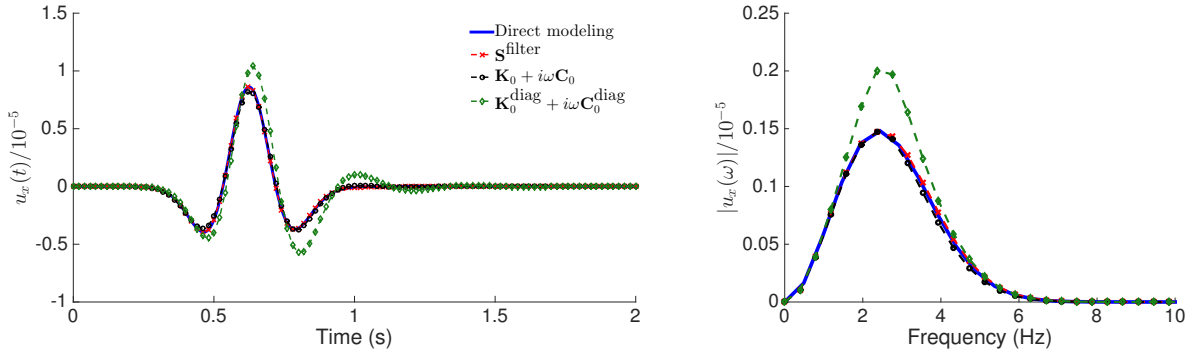

(a) Displacement response at CP1

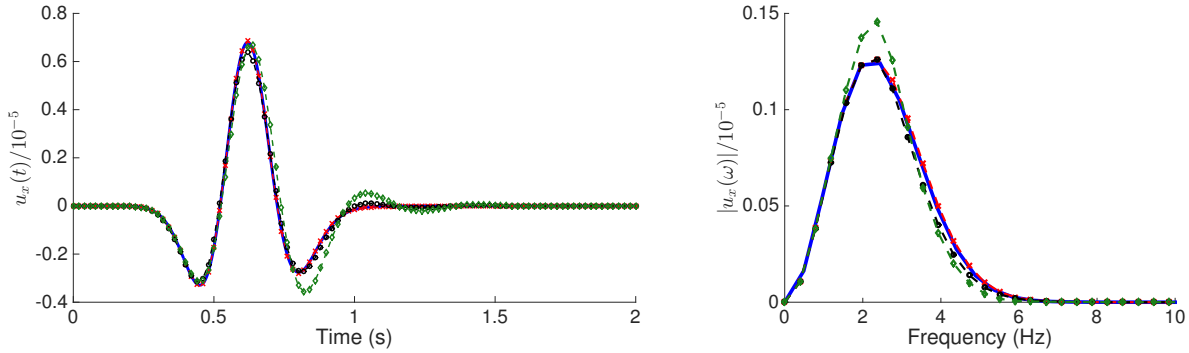

(b) Displacement response at CP2

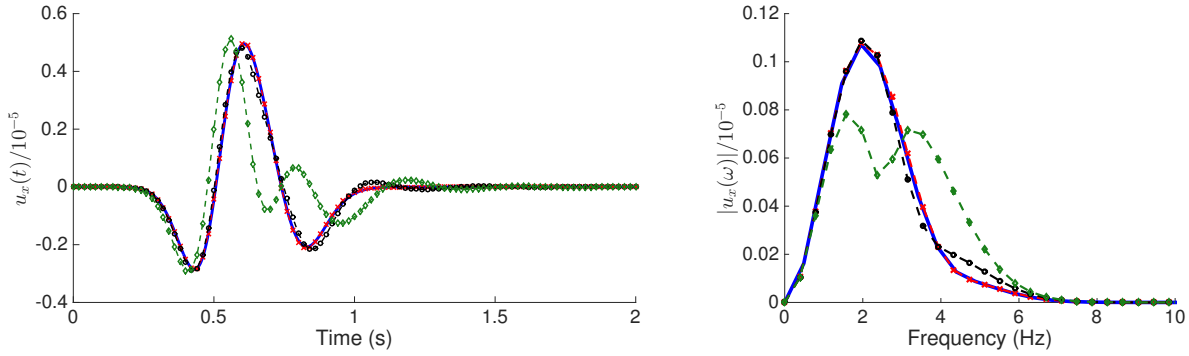

(c) Displacement response at CP3

Figure 6.11: The response of the buried structure in an elastic halfspace with $E/E_s = 1000$, $f_{\text{ctr}} = 2.5$ Hz, and $\omega_0/2\pi$=2.5 Hz.

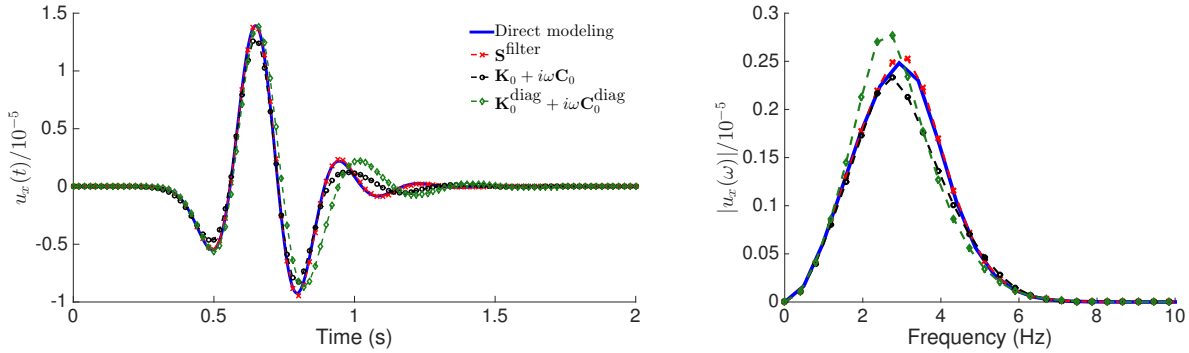

(a) Displacement response at CP1

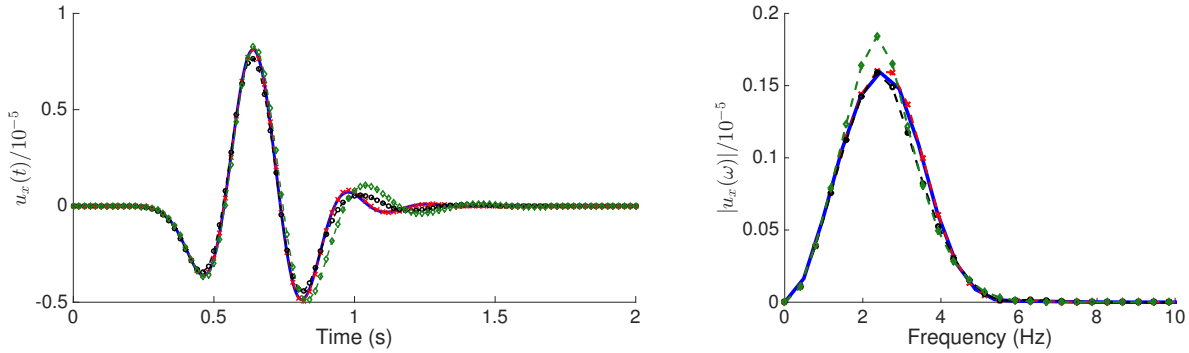

(b) Displacement response at CP2

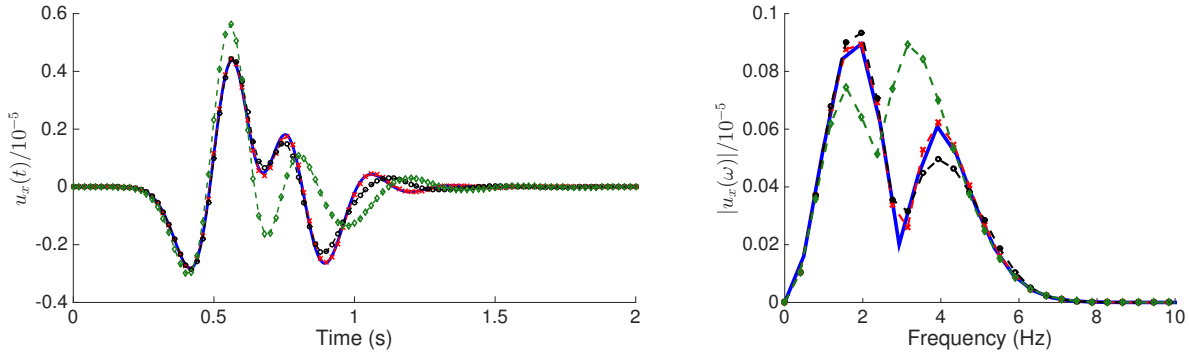

(c) Displacement response at CP3

Figure 6.12: The response of the buried structure in an elastic half-space with $E/E_s = 10$, $f_{\text{ctr}} = 2.5$ Hz, and $\omega_0/2\pi$=2.5 Hz.

constant with frequency and therefore the constructed model is not sensitive to ω_0. On the other hand, the performance of the model that uses $\mathbf{K}_0$ and $\mathbf{C}_0$ is decreased noticeably. This ascertains the importance of correct representation of the impedances that have wavier behavior—i.e. off-diagonal terms in this example—in time domain analysis.

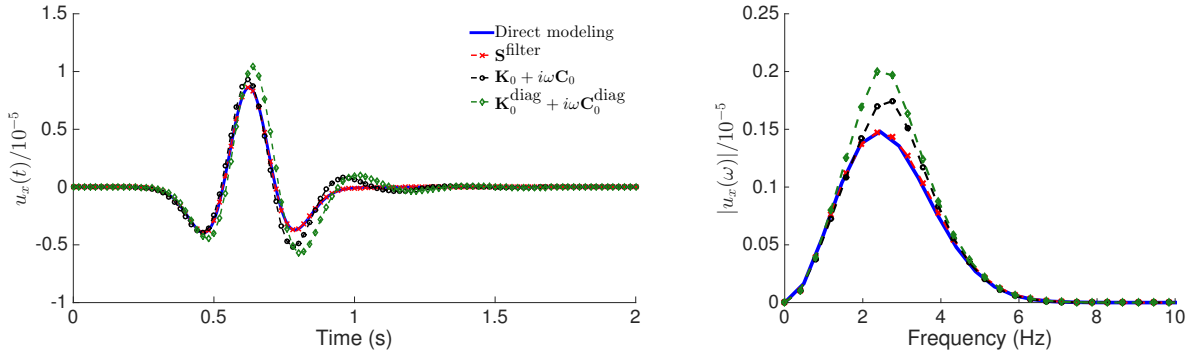

(a) Displacement response at CP1

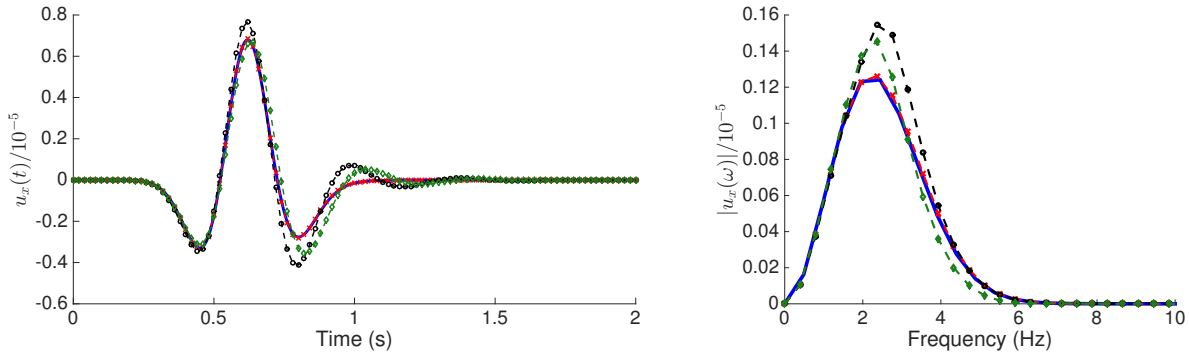

(b) Displacement response at CP2

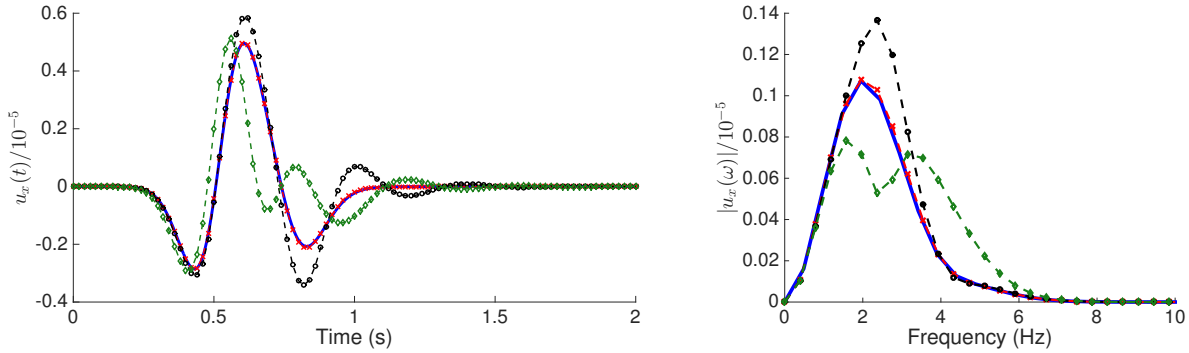

(c) Displacement response at CP3

Figure 6.13: The response of the buried structure in an elastic halfspace with $E/E_s = 1000$, $f_{\text{ctr}} = 2.5$ Hz, and $\omega_0/2\pi$=5 Hz.

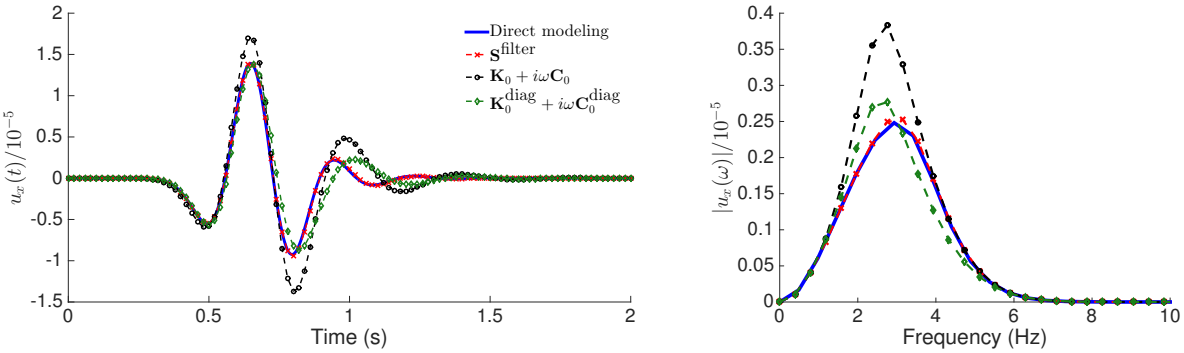

(a) Displacement response at CP1

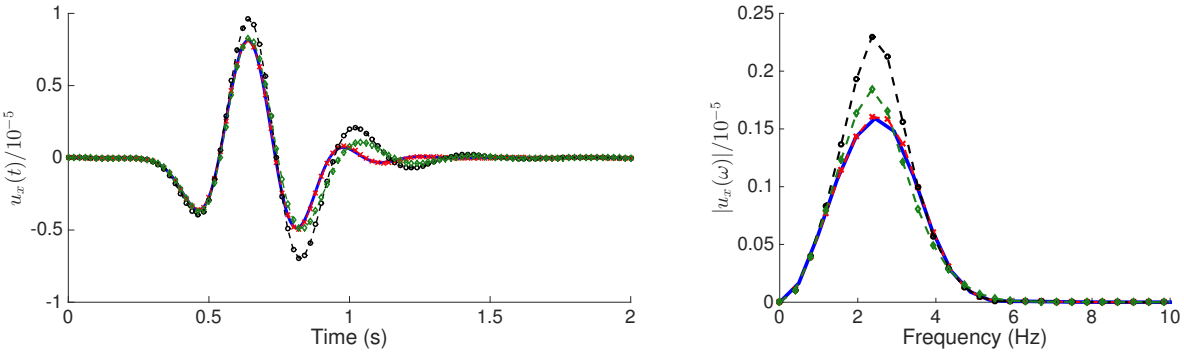

(b) Displacement response at CP2

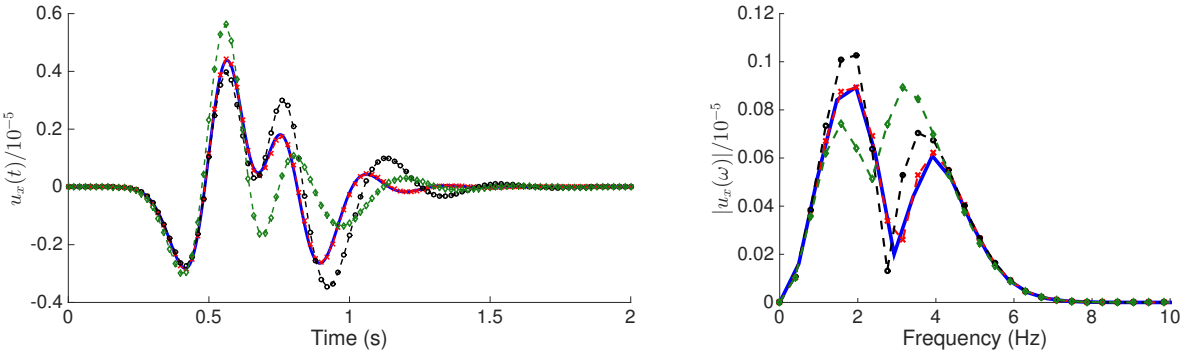

(c) Displacement response at CP3

Figure 6.14: The response of the buried structure in an elastic half-space with $E/E_s = 10$, $f_{\text{ctr}} = 2.5$ Hz, and $\omega_0/2\pi$=5 Hz.

As mentioned in Chapter 2, some global stability problems have been reported when the stable soil impedance subsystem is combined with the structure or with a numerical time integration method used to solve the resulting system of equations in time. In the example explored in this section, we do not observe any stability issue when the impedance filter is used for reduced order modeling of the buried structure. However, it is noticed that when we use constant-valued springs and dashpots for representation of the impedance matrix, the resulting reduced order model may become unstable depending on the value of ω_0 and the stiffness of the structure. To have a closer look, we compute the Eigenvalues (λ_i) of the system matrix $\mathbf{A}$ for the case $E = 10E_s$. To wit,

$$\mathbf{A} = \begin{bmatrix} \mathbf{0} & \mathbf{I} \\ -\mathbf{M}^{-1}\mathbf{K} & -\mathbf{M}^{-1}\mathbf{C} \end{bmatrix} \tag{6.20}$$

where

$$\mathbf{M} = \begin{bmatrix} \mathbf{M}_{\text{ss}} & \mathbf{M}_{\text{sb}} \\ \mathbf{M}_{\text{bs}} & \mathbf{M}_{\text{bb}} \end{bmatrix}, \quad \mathbf{C} = \begin{bmatrix} \mathbf{0} & \mathbf{0} \\ \mathbf{0} & \mathbf{C}_0(\omega_0) \end{bmatrix}, \quad \mathbf{K} = \begin{bmatrix} \mathbf{K}_{\text{ss}} & \mathbf{K}_{\text{sb}} \\ \mathbf{K}_{\text{bs}} & \mathbf{K}_{\text{bb}} + \mathbf{K}_0(\omega_0) \end{bmatrix} \tag{6.21}$$

Figure 6.15 shows the contribution of the Eigenvalues with a positive real part as a function of ω_0. As shown, for frequencies greater than 5 Hz, the dynamic system has Eigenvalues with positive real part, which will cause instability. For instance, for the case we studied, we use $\omega_0/2\pi = 7$ Hz to build the constant-valued stiffness and damping matrices. Figure 6.16 shows the response of the flexible structure at the same controlling points, which ascertain the instability of the resulting system.

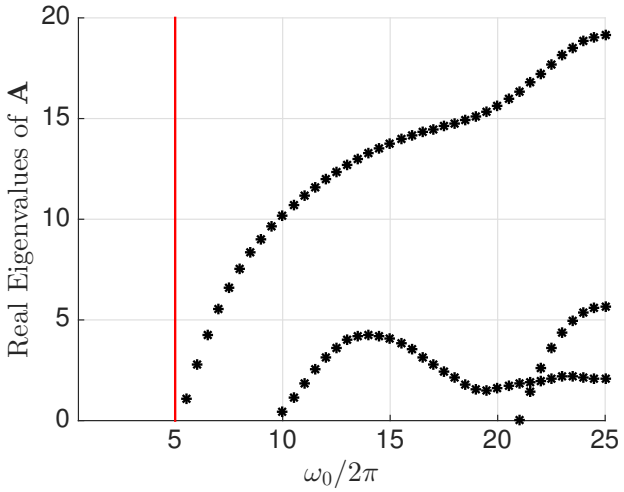

Figure 6.15: The map of the Eigenvalues of the matrix **A** with real parts greater than zero for the buried structure with $E/E_s = 10$.

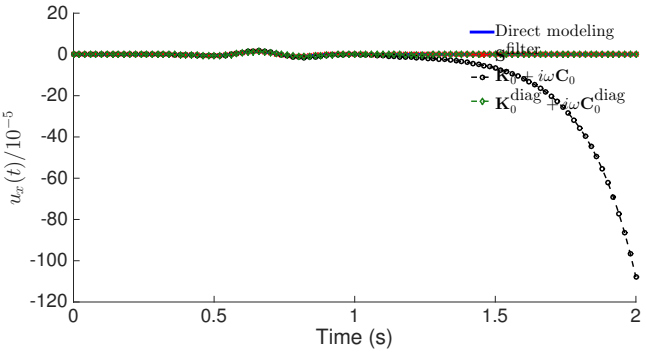

(a) Displacement response at CP1

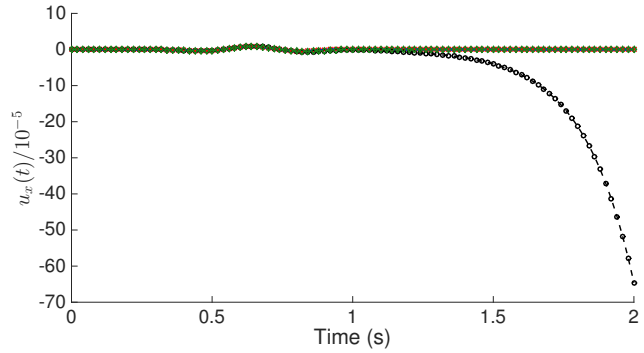

(b) Displacement response at CP2

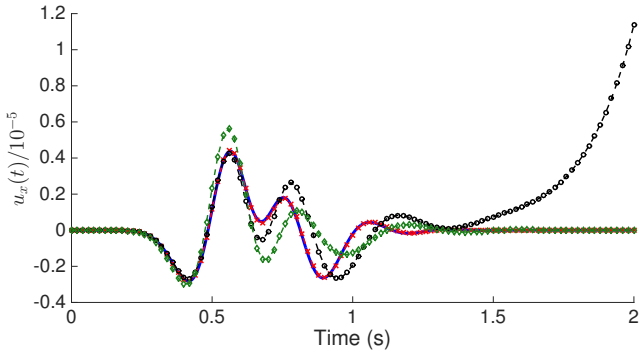

(c) Displacement response at CP3

Figure 6.16: The response of the buried structure in an elastic halfspace with $E/E_s = 10$, $f_{\text{ctr}} = 2.5$ Hz, and $\omega_0/2\pi$=7 Hz.

CHAPTER 7

Application studies II: Numerical simulation of centrifuge experiments on underground structures

Seismic response of underground structures is a complex soil-structure interaction problem influenced primarily by (i) the structure geometry, inertia, and stiffness, (ii) soil heterogeneity and nonlinearity, and (iii) input motion characteristics. The existing methods for analyzing the response of such structures are usually based on simplified analytical or numerical methodologies and their range of applicabilities are not adequately validated against physical model studies (e.g. Pitilakis and Tsinidis, 2014).

Recently, Hushmand et al. (2016) conducted a series of centrifuge experiments at the University of Colorado Boulder to investigate the seismic performance of relatively stiff structures buried in dry sand. Three different simplified box structures were designed to represent the characteristics of prototype reinforced concrete reservoir structures with varying stiffnesses. These structures were restrained from excessive rotational movements at top and bottom by their roof and floor.

Investigation of experimental results showed that the commonly used procedures could not adequately capture the loadings and deformations experienced by this class of underground structures for the range of stiffness and ground motions regularly considered in their design (Hushmand et al., 2016). This is mainly because these procedures are usually based either on the assumption of a yielding (e.g. Seed and Whitman, 1970) or a rigid-unyielding wall (e.g. Wood, 1973). A yielding wall is expected to deform enough to result in an active or yielding condition in the backfill soil, while a rigid-unyielding wall undergoes no deformation. The structures of interest in this study are expected to deform depending on their flexural

stiffness, but their deformation is restrained. Therefore, these structures do not fall in either of the commonly assumed categories.

Although soil behavior can be highly nonlinear during strong shaking, use of nonlinear soil constitutive models may not always be practical due to general complexities in calibrating their many parameters (Deng et al., 2016, e.g.). In this study, we explore the capabilities of calibrated linear soil models in capturing the seismic response of buried box structures as observed in centrifuge. Dynamic soil properties are determined such that the response of a soil column can capture the overall recorded acceleration responses of the far-field soil in centrifuge.

Moreover, we examine the effects of enforced boundary conditions in the numerical modeling of experiments on the response of buried structures. We use the developed FE solver to model the same problem in a heterogeneous soil deposit on an elastic bedrock. This is particularly important when extending the numerical simulations beyond the simplistic conditions considered in centrifuge.

7.1 An overview of the centrifuge tests

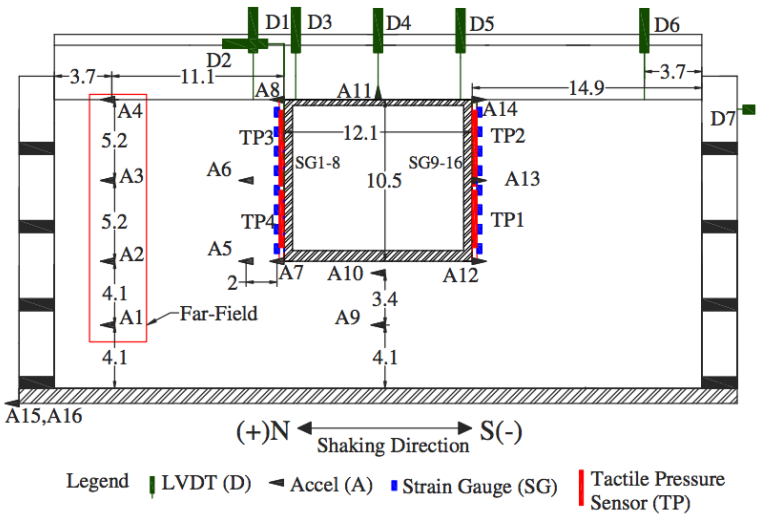

Figure 7.1: Layout of the centrifuge tests studied (dimensions in prototype scale meters).

The centrifuge test layout and instrumentation are shown in Figure 7.1. Dimensions and properties of the model structures used for the experiments are provided in Table 7.1. The density, Young's modulus and Poisson's ratio of the steel structures were 7870 kg/m^3, 200 GPa, and 0.29, respectively. The dry Nevada sand with $G_s = 2.65$, $e_{\min} = 0.56$, $e_{\max} = 0.84$, $D_{50} = 0.13$ mm, and $C_{\mathrm{u}} = 1.67$ was pluviated inside a flexible shear beam container such that an approximately uniform soil layer with dry unit weight of 15.6 kN/m^3 or a relative density (D_r) of about 60% could be achieved.

Table 7.1: Dimensions and properties of model structures in prototype scale.

	Thickness			Fundamental frequency
Structure	Base (m)	Roof (m)	Walls (m)	(Hz)
Flexible	0.5	0.28	0.28	1.9
Baseline	0.69	0.37	0.56	3.9
Stiff	1.46	1.12	1.13	9.1

Figure 7.2 shows the 5%-damped spectral accelerations and Arias intensity time histories of the base motions as recorded in centrifuge. In this study, numerical results are presented and compared with experimental recordings for four cases that cover the range of stiffness and ground motion intensities considered: the flexible and stiff buried structures when subjected to Northridge-L and Northridge-H motions (referred to as AL and AH). The experiments using the flexible and stiff structures are referred to as T-Flexible and T-Stiff, respectively. The properties of the Northridge-L and H motions as recorded during the T-Flexible-AL and AH experiments are tabulated in Table 7.2. The mean frequency is the reciprocal of the mean period defined by Rathje et al. (1998), and the predominant frequency is the frequency at which the maximum %5-damped spectral acceleration occures.

Table 7.2: Properties of the base motions as recorded in T-Flexible.

Base motion name	PGA (g)	Arias Intensity I_{A} (m/s)	Significant duration D_{5-95} (s)	Mean frequency f_{m} (Hz)	Predominant frequency f_{p} (Hz)
Northridge-L	0.22	1.13	16.18	1.19	2.70
Northridge-H	1.02	9.95	25.91	1.44	3.57

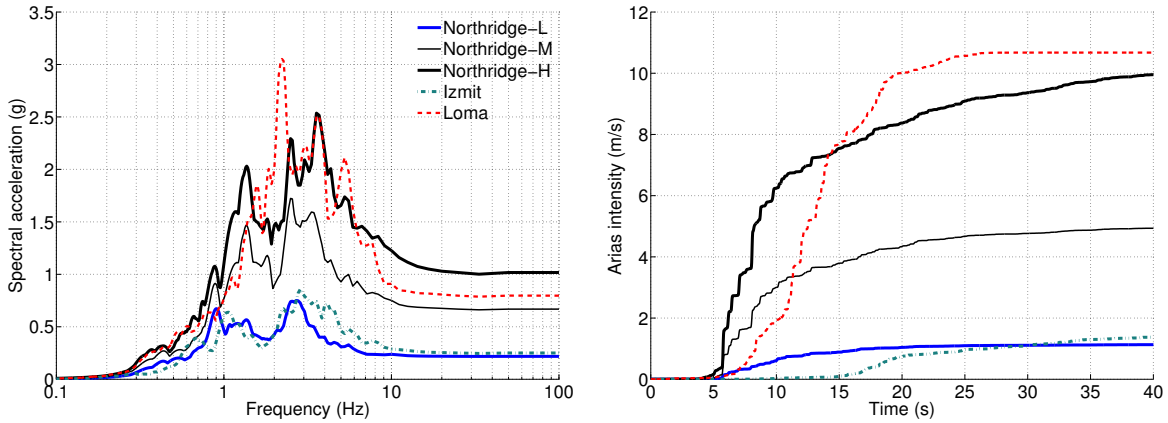

(a) %5-damped spectral acceleration

(b) Arias intensity time history

Figure 7.2: (a) 5%-damped spectral accelerations and (b) Arias intensity time histories of the container base motions recorded for the test on flexible structure.

7.2 Numerical modeling of the centrifuge experiments

In the numerical simulations, only the soil inside the container and the structure are modeled. 8-node quadratic elements are used for the discretization of both soil and structure. The element size is chosen such that approximately 12 discretized nodes exist within the minimum wavelength (Bao et al., 1998). It is assumed that the interface of the structure and soil is perfectly bonded. The FE solver is adapted such that centrifuge experiment boundary conditions can be satisfied reasonably. In this regard, since the flexible shear beam container is used for the experiments, the periodic boundary conditions are imposed on horizontal degrees of freedom at the left and right vertical edges of the domain while their vertical degrees of freedom are fixed. This numerical model is referred to as NM 1 in subsequent analyses. We assume linear behavior for the structure and equivalent linear for the soil. The properties of the structure are the same as those provided in the previous section. The soil properties are obtained through an optimization-based procedure. Details of this procedure are provided below.

7.2.1 Optimization of equivalent linear properties for the soil domain

We use the accelerations recorded by sensors A1, A2, A3, and A4 (see Figure 7.1) to optimize the shear wave velocity profile as well as the equivalent viscous damping of the soil domain. It is assumed that the soil density is constant and is equal to 15.6 kN/m^3. We use the relationship proposed by Rovithis et al. (2011) to define the general form of a shear wave velocity profile, as in:

$$V_{\mathrm{s}} = V_H[b + (1-b)\frac{z}{H}]^n \tag{7.1}$$

where $b = (V_0/V_H)^{1/n}$; n is the dimensionless inhomogeneity factor and z is the downward vertical coordinate measured from the soil surface; V_0 and V_H are shear wave velocities at $z = 0$ and $z = H$, respectively. We approximate damping of the soil domain using the Rayleigh damping model, as in:

$$\begin{bmatrix} \xi_1 \\ \xi_2 \end{bmatrix} = \begin{bmatrix} 1/4\pi f_1 & \pi f_1 \\ 1/4\pi f_2 & \pi f_2 \end{bmatrix} \begin{bmatrix} a_0 \\ a_1 \end{bmatrix} \tag{7.2}$$

where f_1 and f_2 are the control frequencies, ξ_1 and ξ_2 are the associated damping ratios, and a_0 and a_1 are the coefficients to define the viscous damping matrix as a function of mass and stiffness matrices, respectively. Although usually the first- and third-mode frequencies of the soil columns are used for determination of control frequencies in site response analyses, it has been reported that selection of controlling frequencies can influence the response of the system significantly and should be selected such that the system does not experience significant over damping in the dominant range of frequencies (Park and Hashash, 2004; Hashash et al., 2010). As a result, in this study, all four parameters (f_1, f_2, ξ_1, ξ_2) are considered as the optimization parameters.

For any given set of shear wave velocity parameters (V_0, V_H and n) and Rayleigh damping parameters (f_1, f_2, ξ_1, and ξ_2), we solve a 1D wave propagation problem of a soil column subjected to seismic input motion at its rigid base. The acceleration responses at locations

Table 7.3: Optimized shear wave velocity profile and Rayleigh damping model coefficients.

Test	V_0 (m/s)	V_H (m/s)	n	f_1 (Hz)	f_2 (Hz)	ξ_1	ξ_2
T-Flexible-AL	23.5	142.0	1.00	1.00	3.36	0.34	1
T-Stiff-AL	22.2	147.0	0.81	0.84	2.32	0.31	0.66
T-Flexible-AH	22.3	114.7	0.90	1.25	3.33	0.45	1
T-Stiff-AH	15.4	124.3	0.72	1.25	3.50	0.44	1

A1, A2, A3, and A4 in the far-field soil column are then computed to define the following minimization problem:

$$\min_{\mathbf{x}} \quad f(\mathbf{x}) = \frac{1}{2} \sum_{i=1}^{i=4} \sum_{j=1}^{j=n} E_i^*(\omega_j) E_i(\omega_j) \tag{7.3}$$

where $E_i(\omega_j) = \sqrt{|A_i^e(\omega_j)|}[A_i^e(\omega_j) - A_i(\omega_j)]$; $()^*$ is the conjugate transpose of the variable; $A_i^e(\omega_j)$ and $A_i(\omega_j)$ are the complex-valued experimental and numerical acceleration responses of the ith sensor at the frequency ω_j, respectively, in frequency domain; and $\mathbf{x} = (V_0, V_H, n, \xi_1, \xi_2, f_1, f_2)$ is the optimization variable vector. We only consider a frequency range of 0 to 10 Hz for optimization.

In total, we solve this optimization problem for four cases. The resulting optimal parameters are provided in Table 7.3. The variation of the shear wave velocity profile with depth as well as the variation of the Rayleigh damping model with frequency are shown in Figure 7.3. In general, one may use the free-field soil column to obtain dynamic soil properties as prescribed above.

Figure 7.4 shows the 5%-damped spectral accelerations for the far-field array in each test along with those obtained from the 1D wave propagation analyses using the optimized dynamic soil properties. The Rayleigh damping curve is also shown. For low amplitude motions—i.e. T-Flexible-AL and T-Stiff-AL— there are good agreements between the 1D simulations and those obtained from the far-field array experimentally. The goodness of the comparisons is slightly deteriorated during the strong motions—i.e. T-Flexible-AH and T-Stiff-AH—which is due to a higher level of soil nonlinearity and scattering effects as well

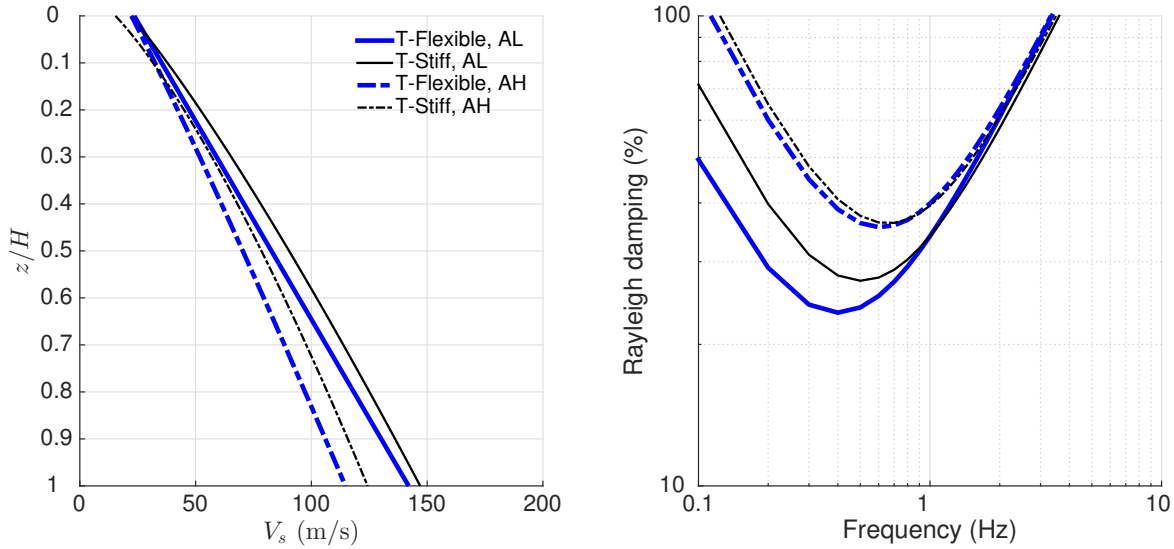

(a) Shear wave velocity profile

(b) Rayleigh damping model

Figure 7.3: The optimized (a) shear wave velocity profile and (b) Rayleigh damping model.

as spurious resonances that may happen in an equivalent linear soil model.

It is known that the first natural frequency of the uniform soil layer on rigid bedrock is $V_s/4H$ where V_s is the shear wave velocity and H is the height of the soil layer. Here, in order to obtain the natural frequencies of the nonuniform soil layer with properties shown in Table 7.3, we compute the stiffness matrix $\mathbf{K}$ and mass matrix $\mathbf{M}$ of the soil column. Then, with the assumption of classical damping behavior, we can compute the Eigenvalues of the matrix $\mathbf{M}^{-1}\mathbf{K}$. Table 7.4 shows the resulting natural frequencies for the considered cases.

Table 7.4: The first three natural frequencies of the soil column with the optimized dynamic properties.

Test	f_1 (Hz)	f_2 (Hz)	f_3 (Hz)
T-Flexible-AL	1.23	2.81	4.52
T-Stiff-AL	1.33	3.01	4.84
T-Flexible-AH	1.05	2.44	3.95
T-Stiff-AH	1.15	2.56	4.08

In order to have a closer look at the contribution of soil's damped natural frequencies as well as the predominant and mean frequencies of the base motion (see Table 7.2), we

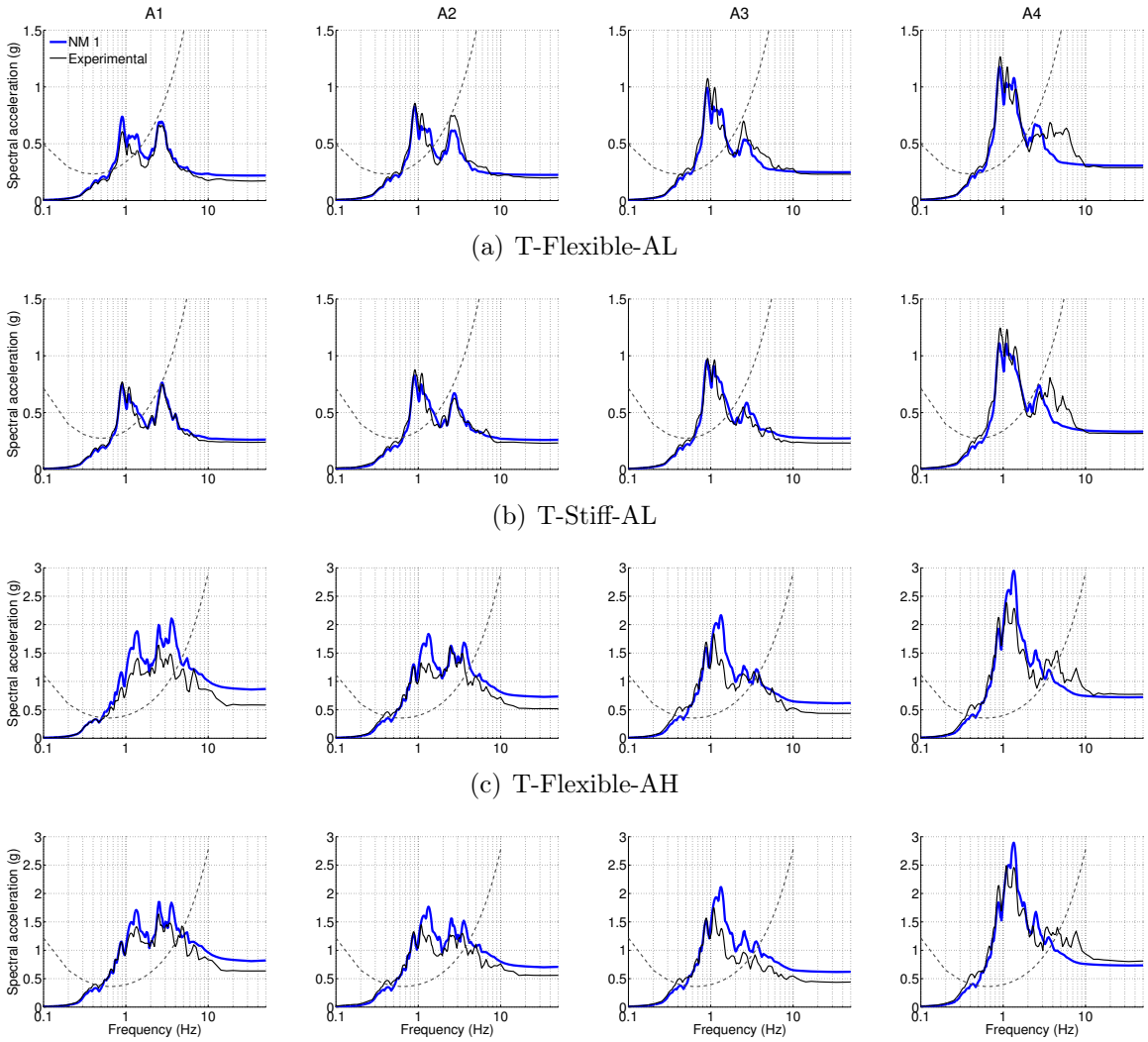

(a) T-Flexible-AL

(b) T-Stiff-AL

(c) T-Flexible-AH

(d) T-Stiff-AH

Figure 7.4: 5%-spectral acceleration obtained from far-field array in the experiment and from the 1D wave propagation analysis using optimized dynamic soil properties; the dashed curve indicates Rayleigh damping.

compute the time-frequency distribution of the energy density for acceleration time-series at locations A15 (base), A4 (far-field surface), and A14 (structure surface). Figure 7.5 shows the resulting time-frequency decomposition (TFD) for each signal in T-Flexible-AL and AH. For T-Flexible-AL, the first damped natural frequency of the far-filed soil column is very close to the mean frequency of the base motion. As shown, for both A14 and A15, the signal energy also increases around the predominant frequency of the base motion. This is while the signal energy at A4 is more influenced by the soil dynamic properties. The correlation between the first damped natural frequency of the soil layer and the mean frequency of the base motion decrease in T-Flexible-AH. This may be attributed to the fact that the measured accelerations at the base of the centrifuge container are always influenced by the dynamic properties of the container, soil, and the structure. For lower amplitude motions these effects may become more significant.

In both cases, however, we expect the system response to be more dominated by the soil deposit free vibration as we approach the end of the signal's duration. This can already be seen in T-Flexible-AH in Figure 7.5 as the signal energy is concentrated around a frequency of 1 Hz. In T-Flexible-AL, we compute the TFD of the modulated signals such that the signal amplitude remains constant with time. Figure 7.6 shows the TFD of the modulated signals for T-Flexible-AL. As shown, the signal energy becomes more significant around the fundamental frequency of the far-field soil column after $t = 25$ s, which is also in agreement with the significant duration of the base motion.

7.2.2 Quantification of scattering due to centrifuge container boundaries

In order to quantify the spurious effects of the rigid base and the periodic boundaries—which resemble a flexible shear beam container—on the response of numerically modeled buried structures, we also model the same soil deposit with depth $H = 18.6$ m and width $W = 42$ m to rest on an elastic bedrock and to extend infinitely laterally. We use the procedure prescribed in Chapter 5 to compute the free-field information, analyzing a soil column with properties the same as those in the soil deposit. In the centrifuge test, $\ddot{u}_g(t)$—

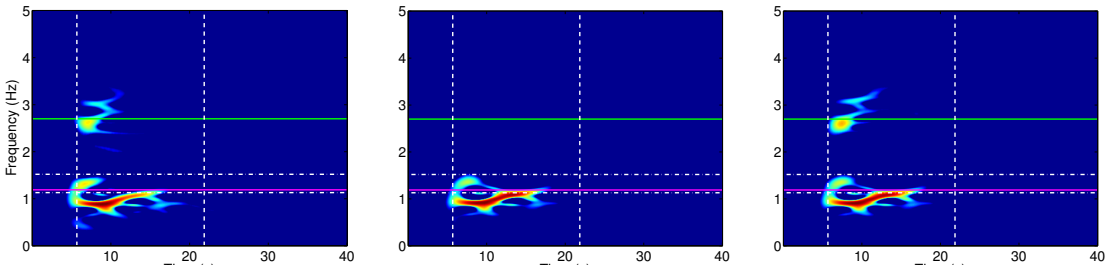

(a) T-Flexible-AL, A15 (Base) (b) T-Flexible-AL, A4 (Far-filed Surface) (c) T-Flexible-AL, A14 (Structure Surface)

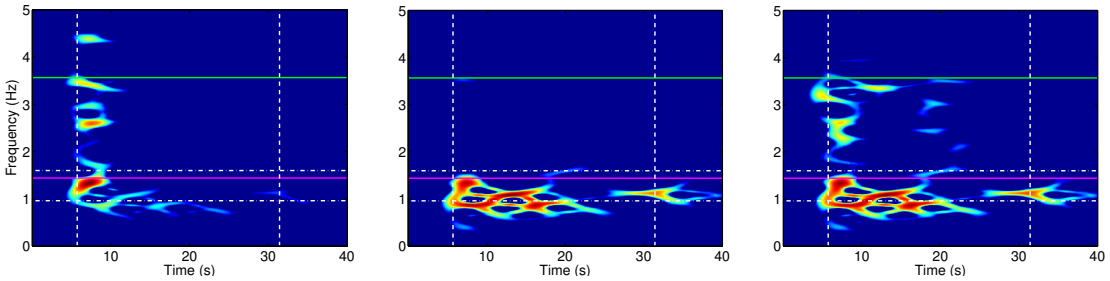

(d) T-Flexible-AH, A15 (Base) (e) T-Flexible-AH, A4 (Far-field Surface) (f) T-Flexible-AH, A14 (Structure Surface)

Figure 7.5: TFD of acceleration time-series for T-Flexible-AL and AH; horizontal white dashed lines are the first two damped natural frequencies of the far-field soil column; horizontal green solid line is the predominant frequency of the base motion; magenta horizontal solid line is the mean frequency of the base motion; vertical white dashed lines span the significant duration of the base motion.

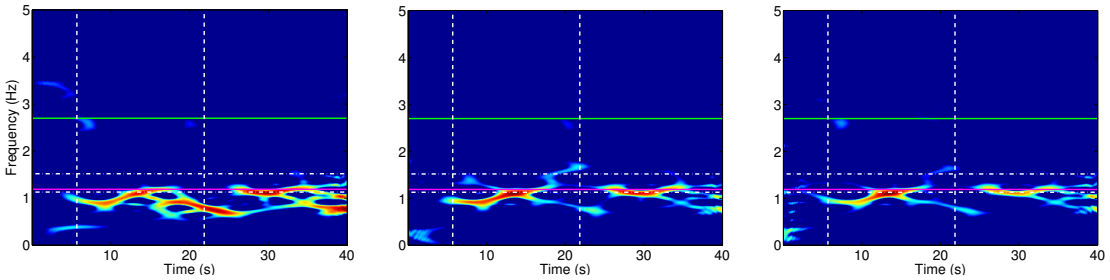

(a) T-Flexible-AL, A15 (Base) (b) T-Flexible-AL, A4 (Far-field Surface) (c) T-Flexible-AL, A14 (Structure Surface)

Figure 7.6: TFD of modulated acceleration time-series for T-Flexible-AL; horizontal white dashed lines are the first two damped natural frequencies of the far-field soil column; horizontal green solid line is the predominant frequency of the base motion; magenta horizontal solid line is the mean frequency of the base motion; vertical white dashed lines span the significant duration of the base motion.

i.e. the base motion of the container— is known and is prescribed at the rigid bedrock in NM 1 numerical simulations. In the subsequent scattering analyses, we assume that the shear modulus of the elastic bedrock is about 9 times the shear modulus of the soil layer at $z = H$, and therefore we assume that $u_g(t) = u_b(t)$[1].

7.3 Comparison of numerical and experimental results

In this section, we explore the capability of the numerical simulations in capturing the main features of the conducted centrifuge experiments in terms of acceleration, racking, bending strains, and dynamic lateral earth pressures along the walls of the structures in tests T-Flexible-AL, T-Stiff-AL, T-Flexible-AH, and T-Stiff-AH.

7.3.1 Acceleration

Figure 7.7 compares the 5%-damped spectral accelerations obtained numerically and experimentally at different locations for different tests and motions. During the low amplitude base motion, in which we expect less soil nonlinearity, the resulting spectral accelerations are in good agreement with their experimental counterparts at all locations. Discrepancies at higher frequencies are mainly due to overdamping of the numerical model which becomes significant at the location of A14 (on top of the buried structure). During high amplitude motions, as we get close to the soil surface, discrepancies between the equivalent-linear soil model and experimental accelerations increase both in the far-field and on the structure. These discrepancies are correlated with those depicted in Figure 7.4.

In order to explore the effects of the assumed boundary conditions on the responses of the far-field soil and structure, we use the NM 2 numerical modeling approach described in the previous section to compute the response of the same soil deposit and structure rested on an elastic bedrock. It is assumed that $\rho_b = 15.6$ kN/m^3 and $V_b = 450$ m/s $\approx 3V_H$.

[1] The accuracy of this assumption depends on the rigidity of the elastic bedrock. In case the bedrock is very flexible one may use the deconvolution method to obtain the within motion from those recorded at the soil surface to be used in scattering analyses.

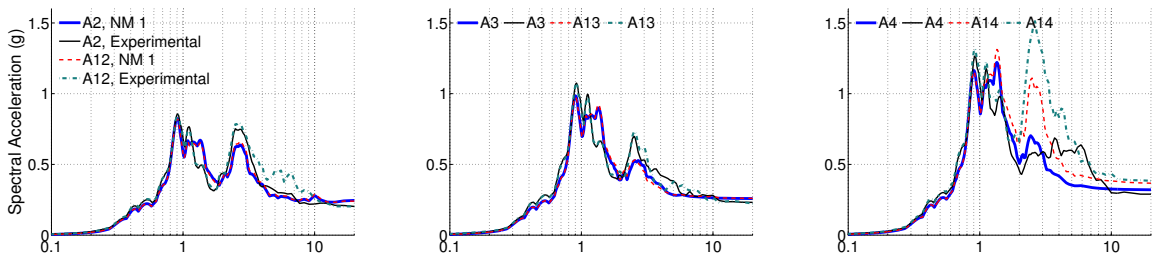

(a) T-Flexible-AL

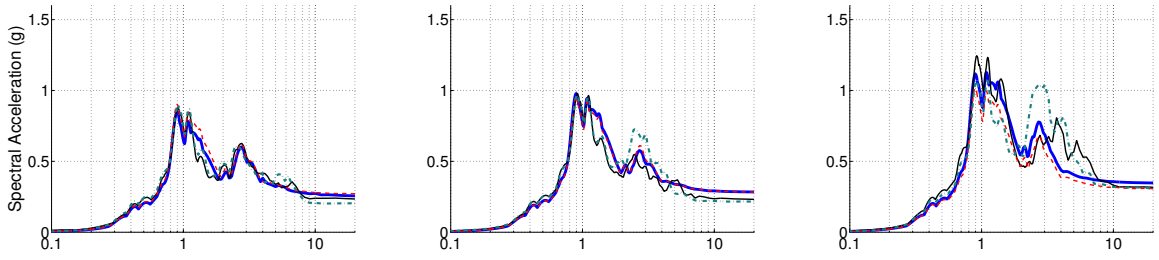

(b) T-Stiff-AL

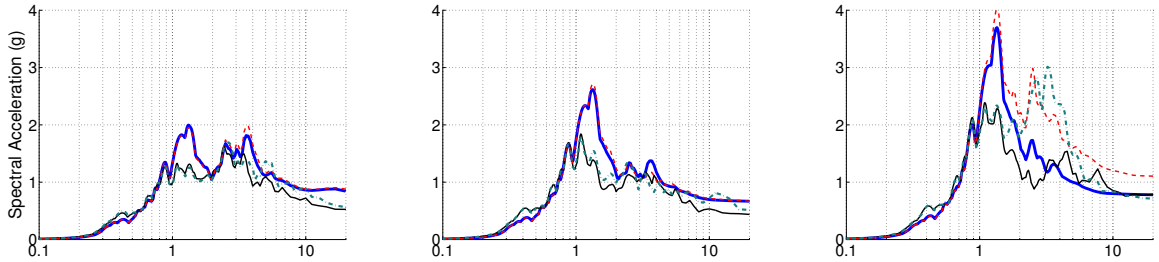

(c) T-Flexible-AH

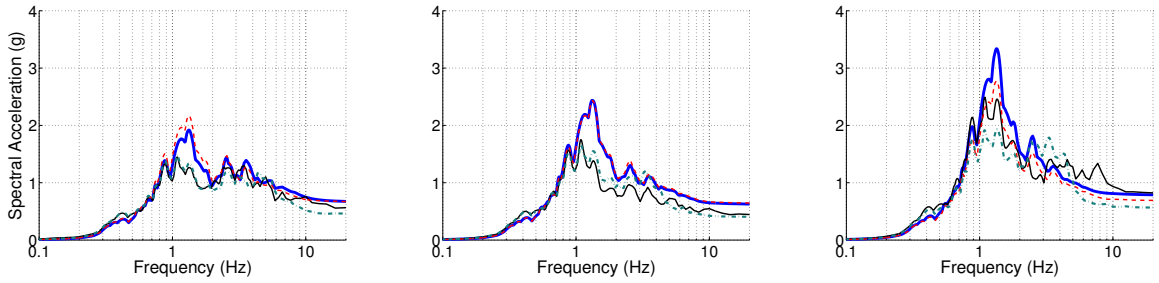

(d) T-Stiff-AH

Figure 7.7: 5% damped spectral acceleration at far-field (A2, A3, A4) and on structure (A12, A13, A14) for T-Flexible-AL, Stiff-AL, Flexible-AH, and Stiff-AH obtained numerically and experimentally.

The scattering effects in both numerical models—i.e. NM 1 and NM 2— are quantified through computing the scattering transfer function $A_i/A_{i,\text{free-field}}$. A_i is the Fourier transform of the acceleration response at location i (see Figure 7.1) and $A_{i,\text{free-field}}$ is the Fourier transform of the corresponding free-field acceleration response. The latter is computed through numerical modeling of the studied cases with no structure.

Figure 7.8 shows the amplitude of the computed transfer functions. As mentioned before, NM 1 is the numerical model with the assumption of a rigid bedrock and periodic side boundaries. On the other hand, NM 2 is the numerical model with the assumption of elastic bedrock and semi-infinite extent of the soil deposit laterally. The main observations are as

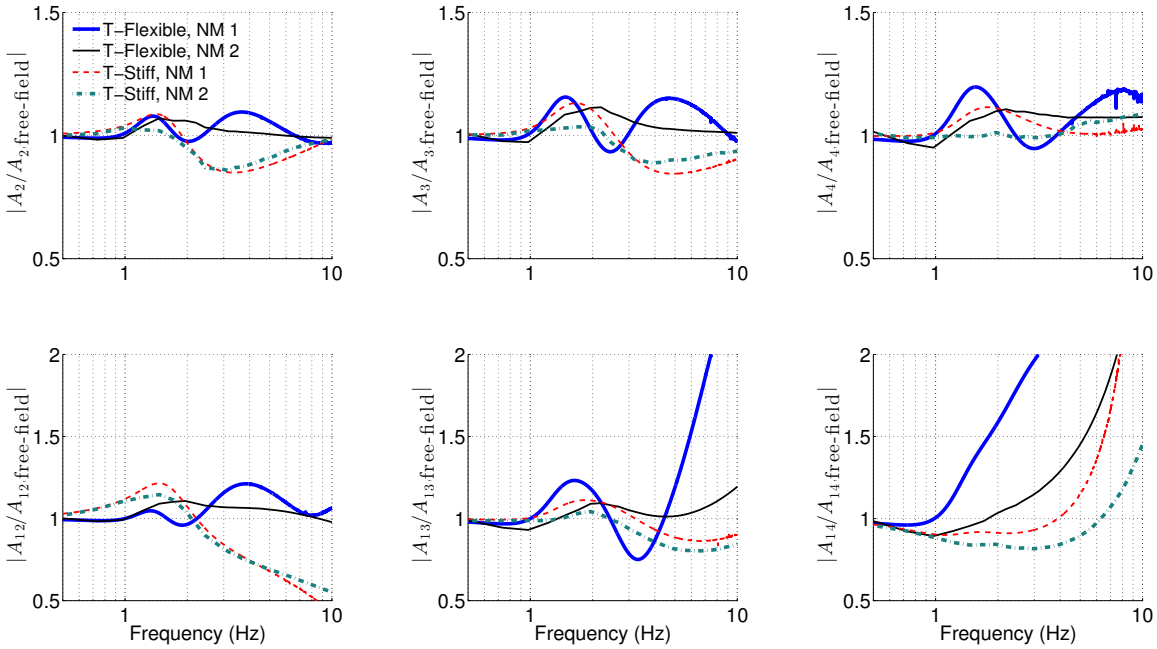

Figure 7.8: Amplitude of scattering transfer functions for NM 1 (numerical model with rigid base and periodic side boundaries) and NM 2 (numerical model with elastic bedrock and laterally infinite soil extent) for T-Flexible-AL and T-Stiff-AL.

follows:

- As the frequency increases, the scattering effects become more significant. This is mainly because at small frequencies all particles move in phase with each other and therefore the effects of scatterer diminishes. This is in agreement with trends of kinematic transfer functions observed for embedded foundations and retaining walls.

- The far-field response is influenced by scatterings, even for NM 2, due to its proximity to the buried structure. Depending on the stiffness of the structure and the input excitation frequency, it may result in amplification or de-amplification of scattering transfer functions. Existence of a rigid bedrock as well as the periodic boundaries in NM 1 can accentuate the effects of instructive and destructive interferences, especially for T-Flexible-AL.

- The scattering amplifications in T-Stiff-AL is generally smaller than those in T-Flexible-AL, which is in agreement with experimental observations on tested structures (Deng et al., 2016) and may be partly due to the higher inertial effects of the flexible structure.

In order to compare the numerical and experimental results, we also compute the ratio of the structure to far-field acceleration responses. Figure 7.9 shows the amplitude of the resulting transfer functions. For experimental data, we use the procedure suggested by Mikami et al. (2008) to reduce the noise levels in computed transfer functions. A 0.2 Hz Hamming window with 21 points is used for smoothing the power spectral densities of the acceleration time-series. Despite discrepancies at higher frequencies, the experimental transfer functions are in general agreement with numerically computed ones.

7.3.2 Racking of the structure

Racking deformation is generally defined as the relative lateral displacement of the roof of the buried structure with respect to its base, and is an important parameter in displacement-based design procedures for buried structures. In order to compute the racking deformation from the experimental data, we double integrate the acceleration responses at locations A14 and A12 and subtract the latter from the former. Numerical racking can be computed directly from subtracting the total displacements at A12 from A14. As shown in Figure 7.10, in all cases the numerical and experimental results are in a good agreement.

Figure 7.11 shows the transfer function of total displacements on the structure and in the far-field, to evaluate scattering effects in different models. For numerically computed transfer

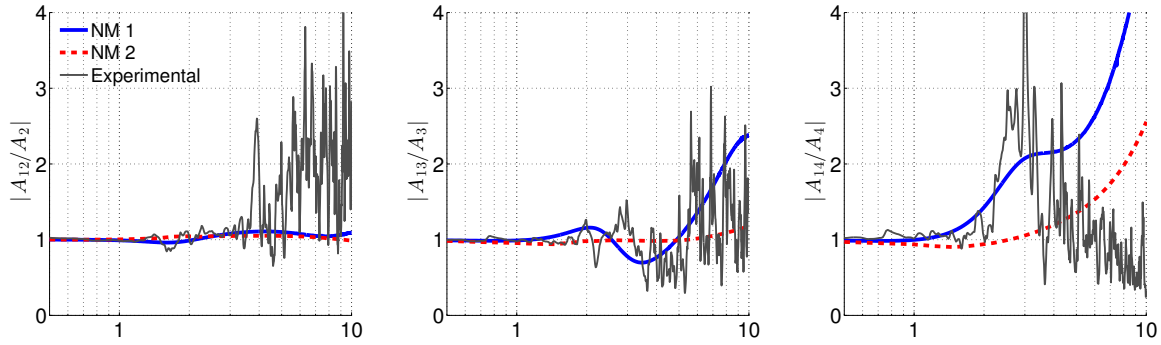

(a) T-Flexible-AL

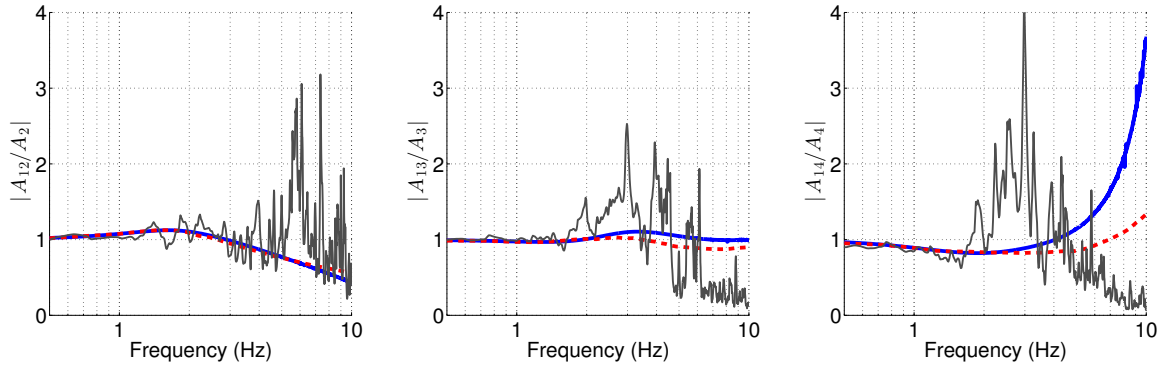

(b) T-Stiff-AL

Figure 7.9: Numerical and experimental amplitude of the structure to far-field soil transfer functions for T-Flexible-AL and T-Stiff-AL.

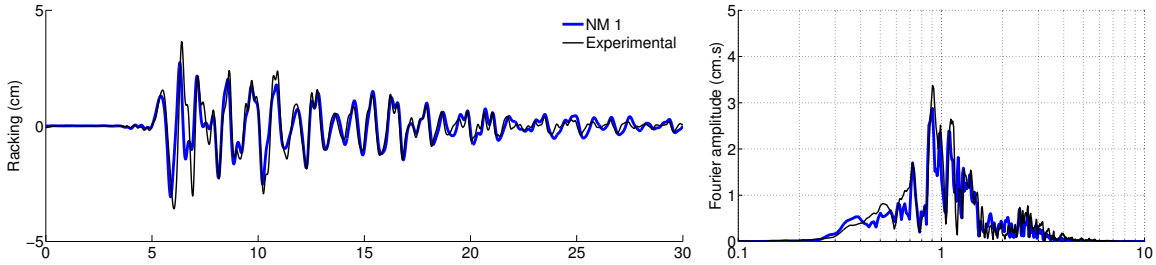

(a) T-Flexible-AL

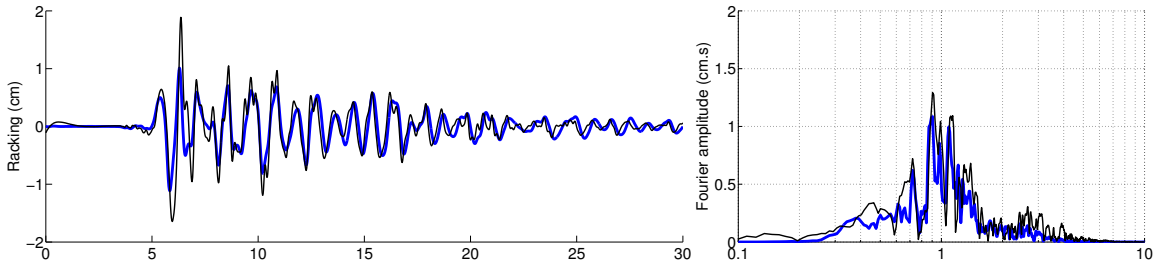

(b) T-Stiff-AL

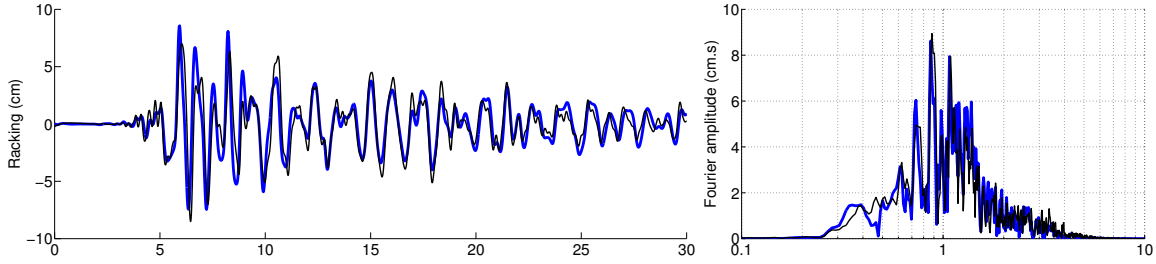

(c) T-Flexible-AH

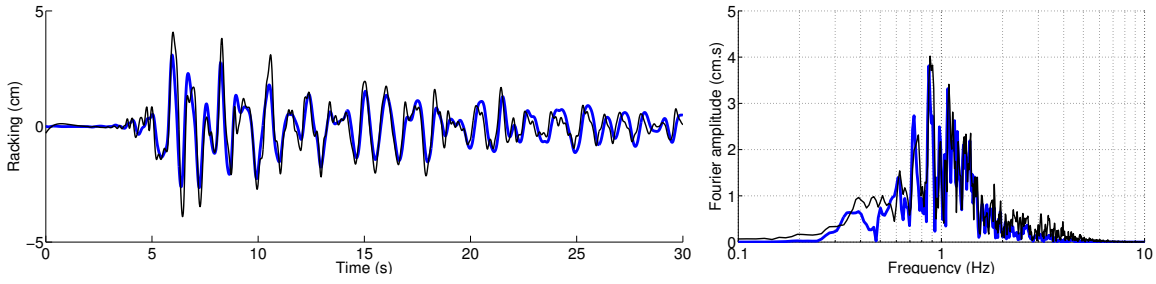

(d) T-Stiff-AH

Figure 7.10: Time-series and Fourier amplitude of the experimental and numerical racking of the south wall of the structures.

functions, the peak for the flexible structure is larger than that in the far-field. This is reverse for the stiff structure. Moreover, as the frequency increases, the far-field transfer functions obtained in T-Flexible and T-Stiff start deviating from each other, which demonstrates the different scattering effects of the flexible and stiff structures on the far-field soil. Further, it is shown that the experimental transfer functions follow the numerical ones better for the stiff structure.

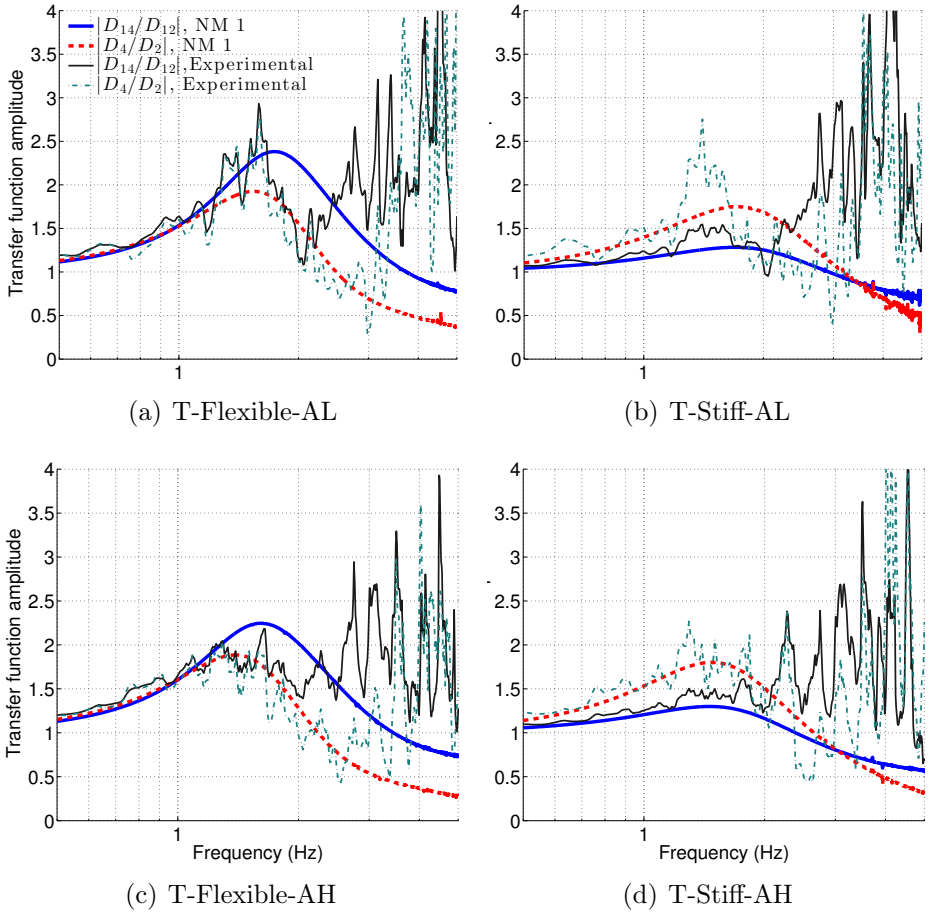

(a) T-Flexible-AL (b) T-Stiff-AL

(c) T-Flexible-AH (d) T-Stiff-AH

Figure 7.11: The total displacement transfer functions obtained from numerically computed displacements and experimentally measured accelerations in the far-field and on the structure.

7.3.3 Bending strain

Bending strains and moments are an important measure of the seismic performance of buried structures and are used regularly in design. In order to measure the bending strain along the walls of the structures in centrifuge, 8 strain gauges were installed outside of each wall. In numerical simulations, for reservoir elements with one side in contact with soil, we compute the tangential strain at the center of the element side. Figure 7.12 shows the numerically computed and experimentally measured strain values at the location of SG8 shown in Figure 7.1, at the bottom of the north wall. For both structures (flexible and stiff) the numerical and experimental results are in a good agreement. It should be mentioned that a low-pass Butterworth filter is used to reduce the noise in strain data measured for the stiff structure.

In order to have a closer look at the spatial distribution and temporal variation of bending strains along the structure wall, we use the method of proper orthogonal decomposition (Kerschen et al., 2005). We (i) create the data matrix: $\mathbf{X} = \begin{bmatrix} \mathbf{e}_1 & \mathbf{e}_2 & \dots & \mathbf{e}_n \end{bmatrix}^T$ where $\mathbf{e}_i$ for $i = 1, 2, \dots, n$ is a strain time-series at location i; (ii) compute the correlation matrix: $\mathbf{R} = \mathbf{X}\mathbf{X}^T/N$, where N is the total number of data points of the time-series; (iii) obtain the Eigen decomposition of the matrix $\mathbf{R}$, which is $\mathbf{R} = \mathbf{\Phi}\mathbf{\Lambda}^2\mathbf{\Phi}^T$. $\mathbf{\Phi} = [\boldsymbol{\phi}_1 \dots \boldsymbol{\phi}_n]$ contains the so-called mode shape vectors $\boldsymbol{\phi}_i$ and $\mathbf{\Lambda}$ is a diagonal matrix with entries λ_i to be the i-th singular value of the matrix $\mathbf{X}$; and (iv) compute the so-called modal contribution coefficients, which is $\mathbf{Q} = [\mathbf{q}_1 \dots \mathbf{q}_n]^T = \mathbf{\Phi}^T\mathbf{X}$.

Figure 7.13 shows the first and second proper orthogonal modes of the numerical results compared against those obtained from experimental data. As shown, for all cases numerical simulations can capture both spatial and temporal variations of the experimentally measured bending strains successfully. The discrepancies in the second mode of the stiff structure are due to the noise level in experimental data. In general, we expect the contribution of the second mode to be less for the stiff structure. Participation of the proper orthogonal components shown in Figure 7.13 can be quantified through the Eigenvalues of the correlation matrix, using Eq. (7.4). The resulting values for the first and second modes are provided in

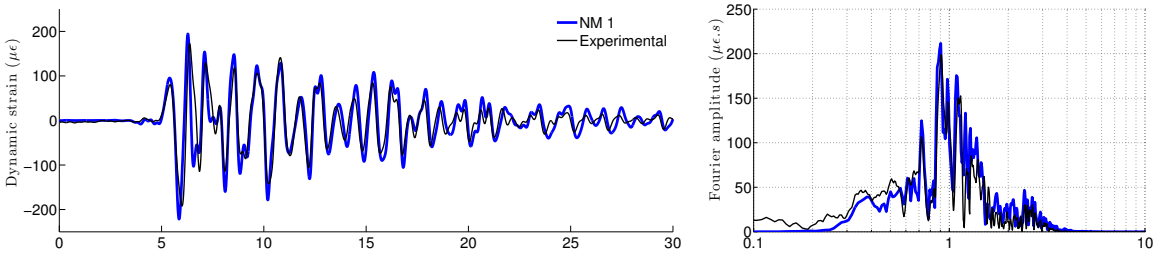

(a) T-Flexible-AL

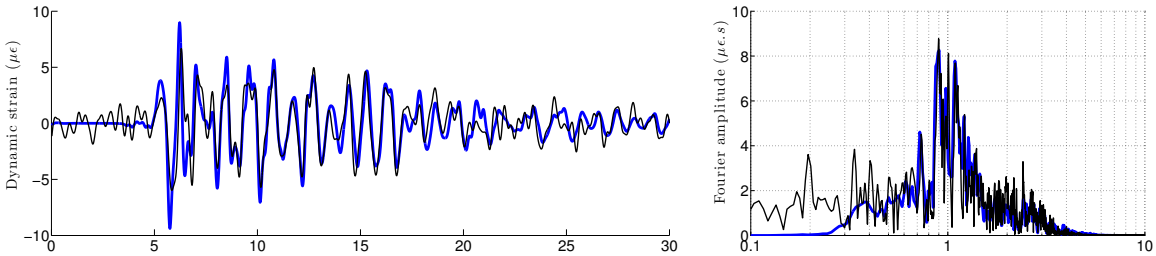

(b) T-Stiff-AL

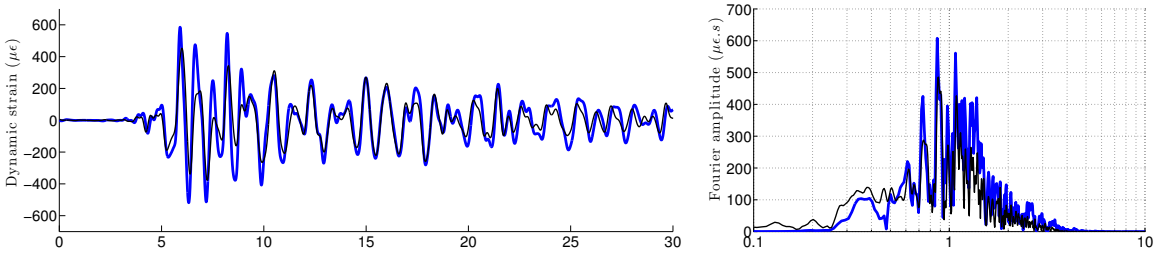

(c) T-Flexible-AH

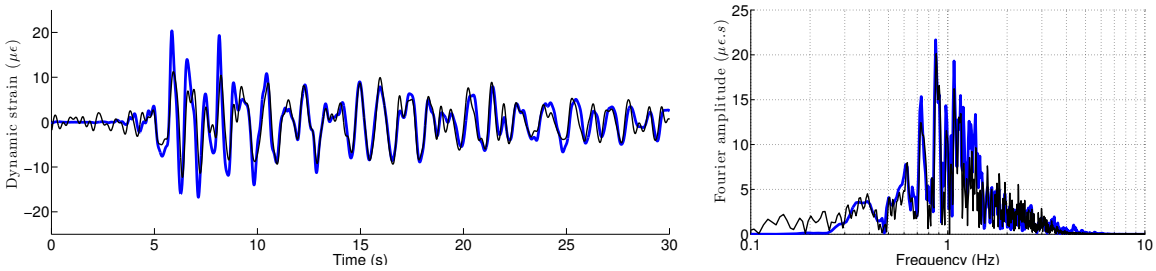

(d) T-Stiff-AH

Figure 7.12: Time-series and Fourier amplitude of the experimentally measured and numerically computed dynamic bending strain of the sensor SG8 at the bottom of the north wall.

Table 7.5, which shows the significant contribution of the first mode in all cases.

$$E_{\lambda_i} = \frac{\lambda_i^2}{\sum_{i=1}^{i=n} \lambda_i^2} \quad \text{for} \quad i = 1, \ldots, n\,. \tag{7.4}$$

Table 7.5: Energy of the first and second proper orthogonal components of numerical and experimental strain data.

	NM 1		Experimental	
Test	$E_{\lambda_1}(\%)$	$E_{\lambda_2}(\%)$	$E_{\lambda_1}(\%)$	$E_{\lambda_2}(\%)$
T-Flexible-AL	99.54	0.34	97.98	1.30
T-Stiff-AL	99.97	0.03	84.07	7.75
T-Flexible-AH	99.58	0.33	98.70	1.00
T-Stiff-AH	99.94	0.05	95.25	2.37

7.3.4 Dynamic lateral earth pressures on the structure walls

Dynamic lateral earth pressures were experimentally measured on the walls of buried structures using tactile pressure sensors (manufactured by Tekscan Inc.) that were statically and dynamically calibrated as detailed by Gillis et al. (2015). Data was averaged over each row of sensels to reduce scatter (Hushmand et al., 2016). Even though significant effort went into the understanding and calibration of tactile sensors by the authors for this particular application, in general, earth pressures in dynamic centrifuge experiments are difficult to measure reliably. Therefore, a degree of uncertainty is embedded in all experimental recordings of earth pressure that should be considered when comparing them with numerical results. To compute dynamic earth pressures numerically, first the normal nodal forces applied on the walls are computed at their interface with soil elements. Then, normal stresses are obtained at the center of the side of each element through dividing the nodal force by the length of the element side.

We use the same procedure, as described in the previous section, to obtain the spatial and temporal variations of the dynamic stresses along the walls of buried structures. Figure 7.14

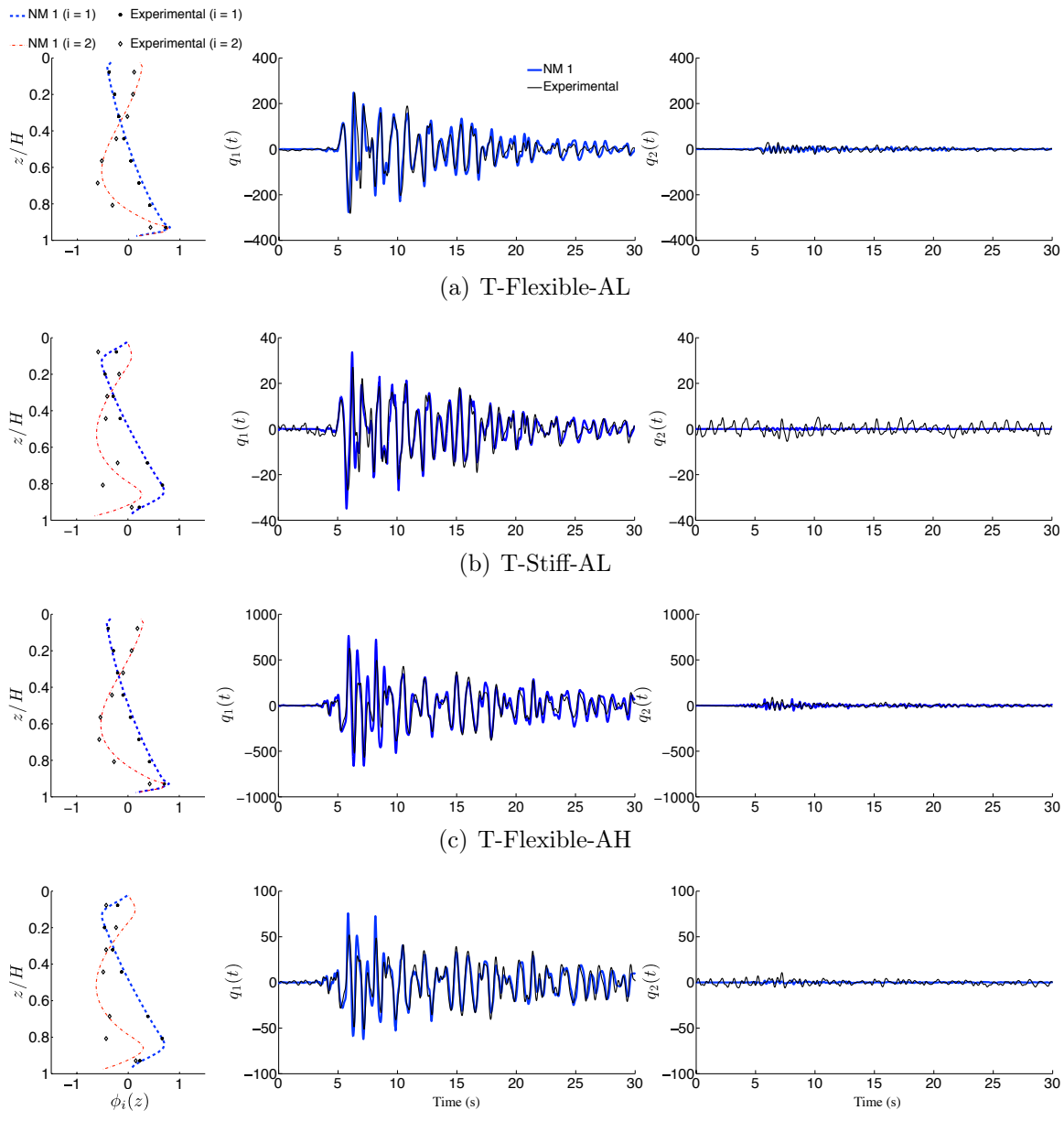

(a) T-Flexible-AL

(b) T-Stiff-AL

(c) T-Flexible-AH

(d) T-Stiff-AH

Figure 7.13: Spatial distribution and temporal variation of the first two proper orthogonal components of the dynamic bending strain along the walls of the structures.

shows the resulting distributions for both experimental and numerical data. As shown, for the flexible structure, even though the temporal variations of the first proper orthogonal component are slightly underestimated, the spatial distributions are captured well. For the stiff structure, on the other hand, capturing the spatial distribution is not as successful as that of the more flexible structure. This may be attributed partially to the perfectly bonded assumption used for soil-structure interface modeling in numerical analyses as well as, to some extent, the uncertainties in experimental recordings (particularly since dynamic strains compared very well).

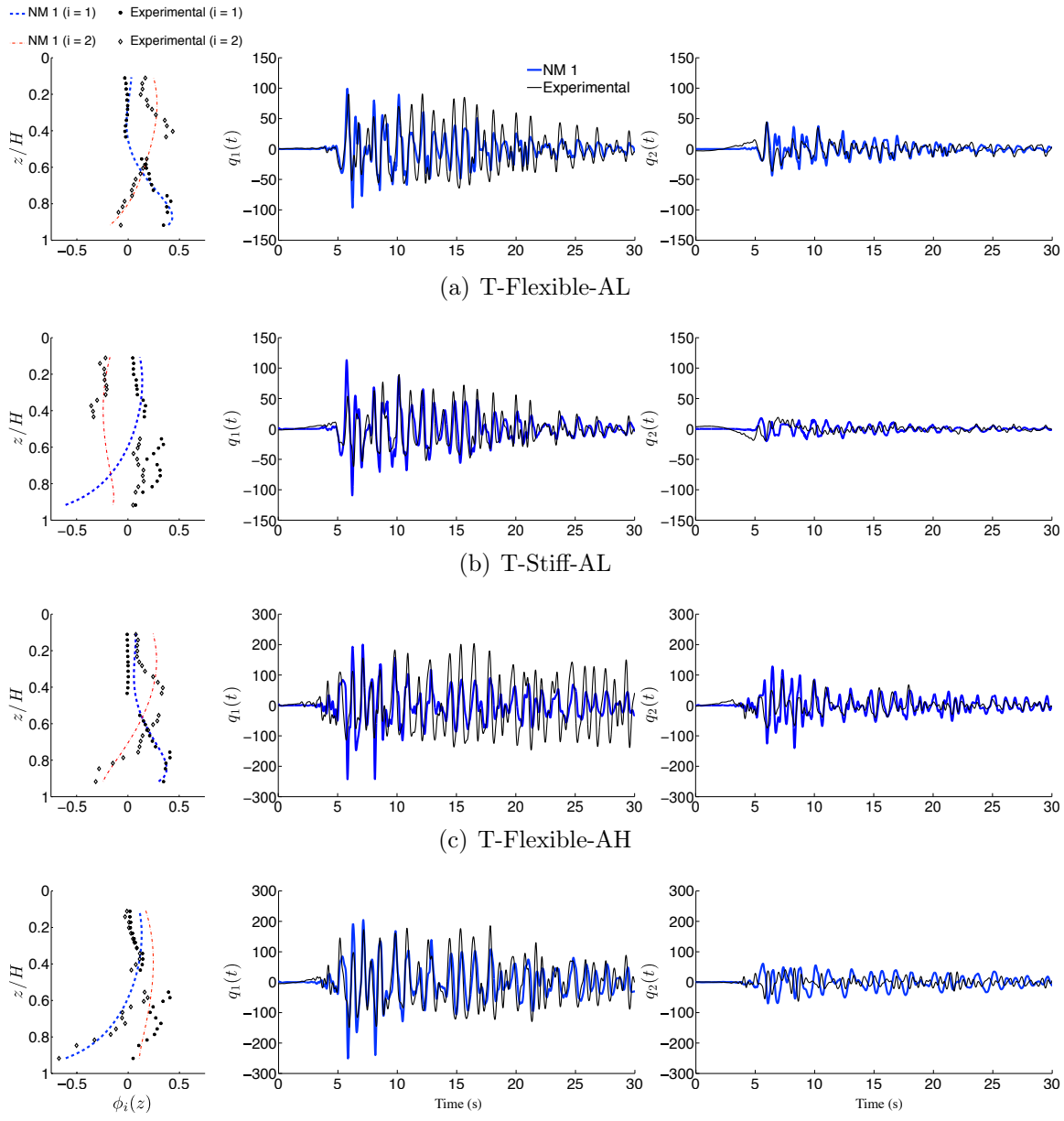

(a) T-Flexible-AL

(b) T-Stiff-AL

(c) T-Flexible-AH

(d) T-Stiff-AH

Figure 7.14: Spatial distribution and temporal variation of the first two proper orthogonal components of the dynamic stresses along the walls of the structures.

CHAPTER 8

Application studies III: Interaction of a pile with layered soil under vertical excitations

Whereas numerical models of manufactured construction materials (e.g., concrete, steel, masonry, wood) are deemed as accurate proxies for their real-life behavior, the same cannot be said for most natural, or even engineered, soils. In fact, accurate prediction of soil behavior still remains a challenge. This is, on one hand, due to the high cost of large-scale field tests that naturally limits the number of such experiments; and on the other hand, due to the lack of adequately validated numerical models specially for dynamic problems. As such, efforts to devise numerical modeling approaches and to validate them with experimental data–to the extent possible—are essential for understanding the in-situ soil behavior, and for setting-up more insightful experiments.

Moreover, despite current advances in computing impedance functions for different types of soil-foundation systems, very few field validation studies of these impedance functions exists in literature, and those that do are only for shallow foundations (e.g., Tileylioglu et al., 2011; Givens, 2013). As such, field measurements of impedance functions and validation of modeling techniques are highly valuable, especially for deep (pile) foundations.

In this work, we explore measurements from a full-scale field test program on soil-pile interaction, which was conducted by Kurtulus (2006) as part of a NEES (Network for Earthquake Engineering Simulation) project (Grant No. CMS-0324326). We use the axisymmetric FE solver formulated in Chapter 3 to compute the vertical impedance function of a drilled shaft. We also attempt to numerically extract the small-strain—i.e., less than $\%10^{-3}$—dynamic properties of the soil by using the results of a steady-state forced-vibration test. In

a previous study (Kurtulus and Stokoe II, 2008), the measured velocities were used to calculate the in-situ shear wave velocity by dividing the distance between the transducers that recorded the responses by the wave travel time. It was assumed that the vertically vibrated drilled shift would produce pure cylindrical shear wave at the depth where measurements were conducted. Moreover, no recipe was provided for measuring the in-situ material damping.

8.1 An overview of the field experiments

Here, only a brief overview of the field experiments is provided. Further details may be found in Kurtulus (2006). The field tests involved axial loading of a 12 ft-long (3.7 m) and 15 in-diameter (381 mm) drilled concrete shaft using a variety of excitation sources. Two of these dynamic sources, of which the test results will be used in the present study, were (i) a hand-held instrumented hammer that was used to generate small impulses with varying frequency contents, and (ii) a vibroseis shaker (a.k.a. the NEES "Thumper") that generated steady-state single-frequency dynamic loadings.

The drilled shaft was reinforced with a steel cage and was constructed using concrete that had a compressive strength of approximately 4800 psi (33 MPa). Prior to construction, the rebar cage of the shaft was instrumented with vertical velocity transducers at two depths within the shaft. Based on modal hammer tests performed in the field, and laboratory tests conducted on concrete cylinder samples, the shaft had an unconstrained compression wave velocity of approximately 12,700 fps (3870 m/s), and a unit weight of approximately 130 pcf (20 kN/m^3). The shaft was extended about 6 inches (152 mm) above the ground surface to allow the loading system to be mounted.

Several small-diameter—as small as 2 in. (or 51 mm)—boreholes were installed in the soil adjacent to the shaft at successively larger radial distances. The distance from the edge of the drilled shaft to the nearest borehole was about 5 in. (127 mm). The boreholes were instrumented with geophones at two depths, which are approximately 12 in. (305 mm) apart.

Each sensor was 1.5 in. (38 mm) in diameter and 2.3 in. (58 mm) in length and consisted of a single 14-Hz geophone oriented in the vertical direction. The unit weight of the sensors was approximately 135 pcf (21 kN/m^3) while the unit weight of the surrounding soil at the time of testing was around 110 pcf (17 kN/m^3). A schematic illustration of the field test configuration is shown in Figure 8.1. The exact locations of the sensors were obtained by excavating the test area after completion of all field tests (Figure 8.1c).

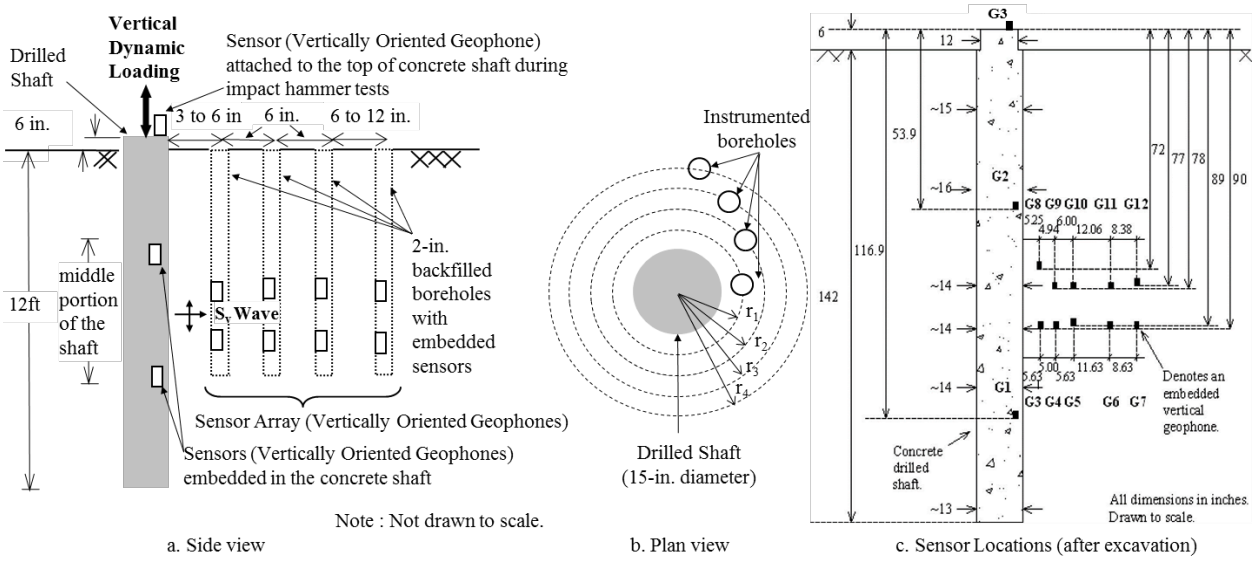

Figure 8.1: The field test configuration (Kurtulus, 2006).

In the first stage of the dynamic testing, an instrumented hand-held hammer was used to perform tests in the small-strain range (less than $\%10^{-3}$) by generating small impacts at the top of the shaft. During these tests a 14-Hz geophone was also attached to the top surface of the shaft. In the second stage, Thumper was mounted on top of the shaft and was operated in the vertical direction to apply 15 cycles of sinusoidal loading of 180 lb. (0.8 kN) at a selected frequency of 55 Hz. This frequency was selected because the frequency response curve measured in the field had a resonance around this frequency, so that "large" motions could be excited at the shaft (Kurtulus, 2006). A static vertical hold-down load of 2000 lb. (8.9 kN) was also exerted on the shaft in order to apply dynamic loading. A sampling rate of 200 samples/sec was used to simultaneously record the response of all embedded geophones to the applied loading.

The calculated strains in the aforementioned tests—i.e. the hammer test and the lowest amplitude dynamic loading from the Thumper tests—were in the order of $\%10^{-4}$ (Kurtulus, 2006). Moreover, these small-strain tests were performed prior to any high-amplitude testing. Prior to any testing, Spectral-Analysis-of-Surface-Waves (SASW) tests were conducted to estimate the shear wave velocity profile of the natural soil in the test area (Kurtulus, 2006). Figure 8.2 shows the average property of each layer as well as properties of the shaft. This soil profile is used in subsequent numerical simulations to extract the pile impedance function.

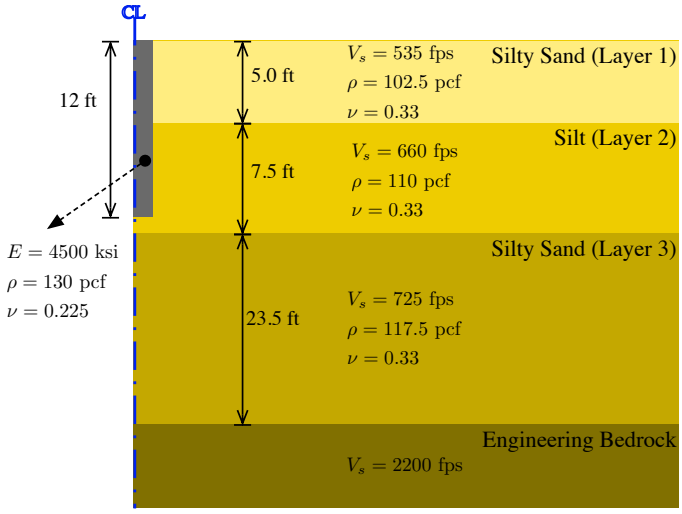

Figure 8.2: Average properties of in-situ soil layers extracted from SASW test.

8.2 Numerical simulation of the soil-pile interaction problem

As mentioned in §8.1, the circular drilled shaft was loaded vertically in all tests. The soil medium is assumed to be horizontally layered, and thus, the problem at hand is treated as an axisymmetric elastodynamics problem. In order to obtain a realistic representation of the in-site soil's dynamic behavior, it is important to accurately model the effects of radiation and material dampings in numerical simulations. This is because an inaccurate accounting of the former will yield inaccurate estimates of the latter.

To take the effects of semi-infinite extent of soil into account accurately and efficiently, we use the hybrid PML formulation for axisymmetric problems as already discussed in Chap-

ter 3. We repeat the resulting semi-discrete form of the system of equations (Eq. (3.38)) here, as in:

$$\mathbf{M}\dddot{\mathbf{d}} + \mathbf{C}\ddot{\mathbf{d}} + \mathbf{K}\dot{\mathbf{d}} + \mathbf{G}\mathbf{d} = \dot{\mathbf{f}}. \tag{8.1}$$

We are concerned about small-strain dynamic properties of the soil-pile system, and we expect the system to behave linearly. This allows us to solve the frequency domain counterpart of Eq. (8.1). To wit,

$$\left[(i\omega)^3\mathbf{M} + (i\omega)^2\mathbf{C} + (i\omega)\mathbf{K} + \mathbf{G}\right]\hat{\mathbf{d}}(\omega) = (i\omega)\hat{\mathbf{f}}(\omega) \tag{8.2}$$

Detailed description of all the parameters in Eq. (8.2) can be found in Chapter 3 and Appendix A.

8.2.1 Modeling material damping

Experimental evidence indicate that small-strain behavior of soil can be represented through linear viscoelastic models (Ishihara, 1996), which can be easily handled in the frequency domain by introducing complex-valued moduli. In a rigorous form, the complex-valued velocity V_i^* can be defined as (Lai and Rix, 2002):

$$V_i^*(\omega) = \frac{V_i(\omega)}{\sqrt{1+4\xi_i^2(\omega)}}\left[\frac{1+\sqrt{1+4\xi_i^2(\omega)}}{2} + i\xi_i(\omega)\right] \tag{8.3}$$

where $i \in \{s, p, r\}$ denotes shear, pressure and Rayleigh waves, respectively. For weakly dissipative media (i.e., small material damping values), Eq. (8.3) may be simplified by only retaining the first-order terms (Rix et al., 2000). Moreover, based on several experimental data sets, it is usually assumed that the small-strain material damping is approximately frequency independent over the seismic bandwidth ranging from 0.001 to 10 Hz (Lai and

Rix, 2002). As a result, the complex-valued velocity may be re-stated as,

$$V_i^* = V_i(1 + i\xi_i) \tag{8.4}$$

where it is also assumed that the variation of $V_i(\omega)$ with respect to frequency is negligible. This form is usually used for linear SSI analyses (as already shown in §4.3.2 for computing the impedance functions of viscoelastic two-layered soil) and frequency domain site response analyses (Kramer, 1996; Ostadan et al., 2004).

Since we solve the governing equations in the frequency domain, the shear wave velocity definition in Eq. (8.4) can be modified to incorporate hysteretic small-strain damping ξ in our wave propagation analyses. This will result in the modification of Lamè constants μ and λ that are used to form the system matrices.

8.3 Vertical impedance function of the drilled shaft

In order to obtain the dynamic stiffness of a pile at each frequency ω,numerically, we follow the same procedure provided in Chapter 4 to compute the impedances of soil-structure interfaces in a plane-strain setting. We prescribe a known vertical displacement along its top surface to compute the reaction forces along the same surface. This calls for solving a complex-valued system of linear equations as in Eq. (8.2). Summing up the reaction forces and dividing the resultant by the prescribed displacement will then yield the impedance function of the pile at the selected frequency ω. Repeating this procedure for different frequencies will result in the following function:

$$\hat{S}_V(\omega) = K_0 \left[K_V(\omega) + i\, a_0\, C_V(\omega)\right] \tag{8.5}$$

where $S_V(\omega)$ is the vertical impedance function of the pile; K_0 is a normalization factor, which may be chosen as the static stiffness, if exists; $a_0 = \omega D/V_s$ is the dimensionless frequency; D is the diameter (characteristic length) of the pile; and K_V and C_V are the

normalized real and imaginary parts of the impedance function.

8.3.1 Verification studies

Using the above procedure, we compute the impedance function of a single pile in homogeneous viscoelastic half-space with $L/D = 15$, $\rho_s/\rho_p = 0.7$, $\nu_s = 0.4$, and $\nu_p = 0.25$—where D and L denote the pile diameter and length, respectively; E_p, ρ_p and ν_p denote the elastic modulus, mass density and Poisson's ratio of the elastic pile, and E_s, ρ_s and ν_s are elastic modulus, mass density and Poisson's ratio of the soil half-space, respectively. The soil damping is $\xi = 0.05$, and $E_p/E_s = 1000$, which represents a soft soil condition. Figure 8.3 displays the real and imaginary parts of the numerically computed impedance function normalized by K_0, which are in excellent agreement with the analytical solutions provided by Miura et al. (1994).

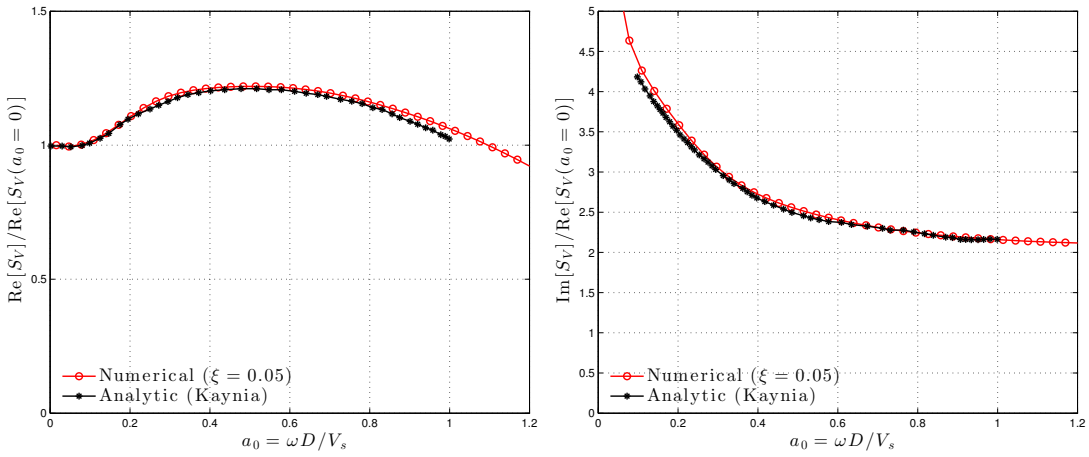

(a) (b)

Figure 8.3: Dynamic stiffness of a single pile embedded in a homogeneous viscoelastic half-space.

8.3.2 Validation studies against in-situ measurements

In order to investigate the capability of the FE solver in replicating the field conditions, the impedance of the drilled shaft with specifications provided in Figure 8.2 is computed

numerically. The recorded data of the hammer test are used to extract the "field" impedance function of the shaft. It should be noted here that in order to compute the field impedance function, the applied force as well as the top surface response of the shaft must be recorded synchronously. Five successive hammer tests are analyzed here. Figure 8.4 shows the frequency content—i.e., amplitude and phase angle—of the hammer-induced vertical force $f_H(t)$ for one of the tests. V_{s1} in the horizontal axis label of Figure 8.4 is the shear wave velocity of the first layer (see Figure 8.2).

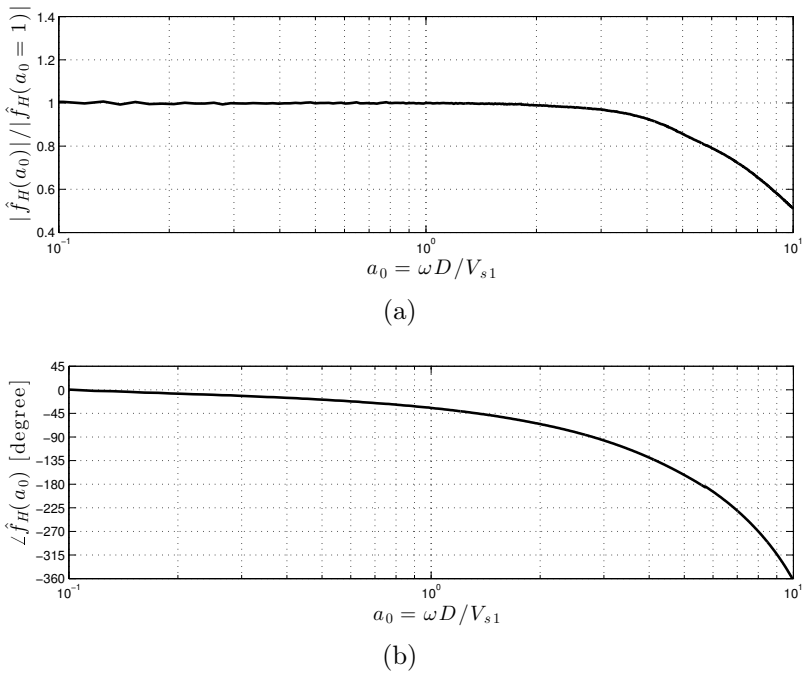

Figure 8.4: (a) The normalized Fourier amplitude and (b) phase angle of the hammer-induced force $f_H(t)$.

Both homogeneous and layered soil profiles are considered in the numerical simulations. First, the soil is considered as a homogeneous half-space with soil properties of the first layer shown in Figure 8.2. For the layered configuration, soil properties are taken to be the same as those provided for the first three layers in Figure 8.2. Since the bedrock is at a depth of three times the pile length—and thus adequately far away from the source of dynamic loading—, only the first three layers are modeled. It should be noted here that the motivation for modeling the one-layered/homogenous case is to assess the capability (or lack

thereof) of the hammer tests in capturing the layering effects at higher frequencies. Because the wavelength of the outgoing waves traveling at a specified velocity becomes shorter as the excitation frequency increases, these waves will not have enough time to reach the underlying layers and reflect back during the tests' observation windows. Also, it is assumed here that the soil material damping is the same for all layers.

Figure 8.5 displays the real and imaginary parts of the numerically computed impedances versus the field results obtained from each hammer test. Here, 5% material damping is assumed for numerical analyses. As mentioned earlier, the resonant frequency of the site is around 55 Hz, for which the dimensionless frequency a_0 is approximately equal to 0.65. As shown in Figure 8.5, numerically computed and field measured damping coefficients are in a very good agreement except for $a_0 \leq 0.2$. On the other hand, the field stiffness coefficients start to deviate from the numerically computed coefficients when $a_0 \leq 0.2$ and $a_0 \geq 1.4$. Therefore, only the mid-range frequencies with $0.2 \leq a_0 \leq 1.4$ is considered for further investigations.

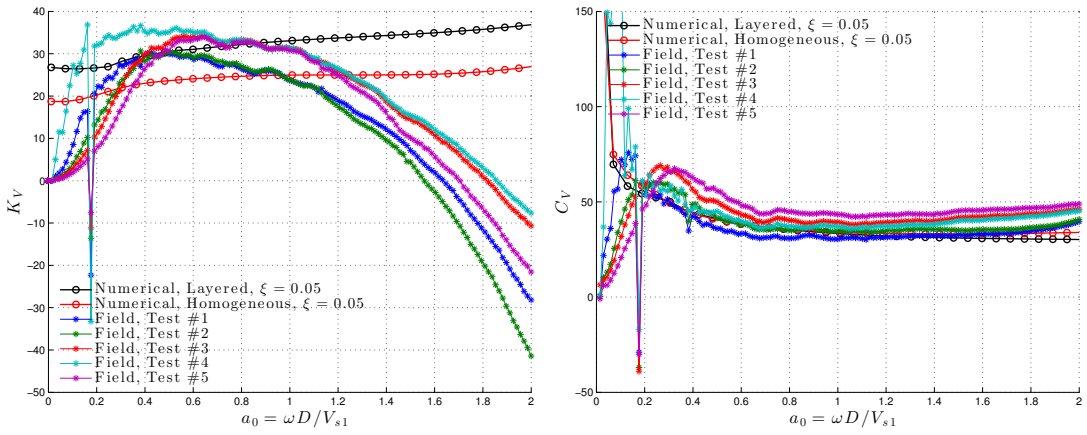

(a) Real part (b) imaginary part

Figure 8.5: Field impedance function of the drilled shaft from different hammer tests.

Figure 8.6 shows the mean ± one standard deviation of the real and imaginary parts of the field vertical impedance. In numerical simulations, since the level of damping is unknown, different values ranging from zero to 10% are considered. Numerically computed

impedance functions for different values of material damping ξ are plotted in the same figure for the two aforementioned cases of homogeneous and layered soils. Figures 8.6a and 8.6b indicate that, as the frequency increases, the average field stiffness coefficients make a gradual transition from the *numerically computed layered* to *numerically computed homogeneous* soil stiffnesses. On the other hand, Figures 8.6c and 8.6d indicate that the average field damping coefficient exhibits the same trend as the numerical damping coefficients. For frequencies close to resonant frequency, it lies within the numerically obtained curves with $\xi = 0.04$ and $\xi = 0.06$; and for other frequencies it follows curves with $\xi = 0.08$ and $\xi = 0.1$.

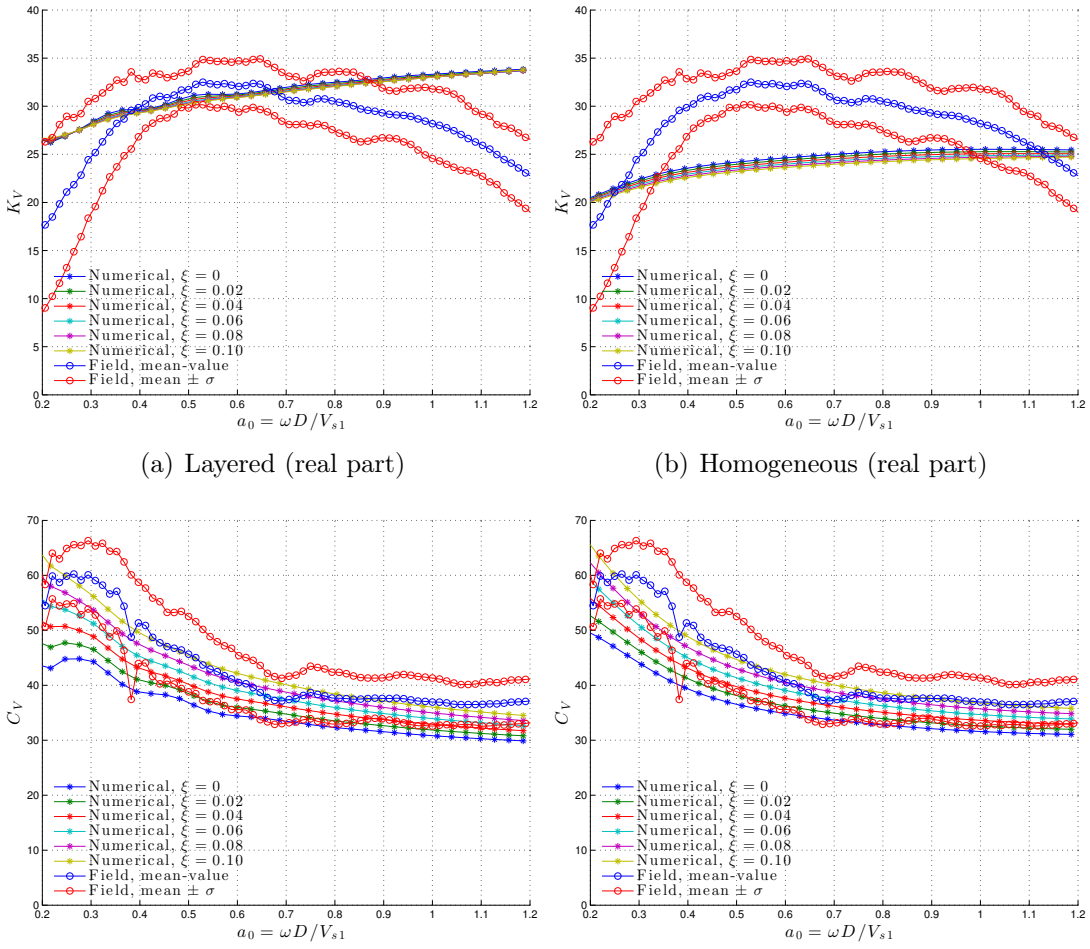

(a) Layered (real part)

(b) Homogeneous (real part)

(c) Layered (imaginary part)

(d) Homogeneous (imaginary part)

Figure 8.6: Real and imaginary parts of the vertical impedance function for homogenous and layered soils.

It is expedient to note here that Kurtulus (2006) used a combined resonant column and torsional shear device for determining the variation of shear modulus and material damping with strain and excitation frequency. Small-strain damping values measured for the undisturbed silty sand and silt samples were approximately 0.015 and 0.03, respectively. Moreover (as also mentioned earlier), the average soil properties used for computing the numerical impedance functions were obtained from the SASW tests at the natural soil area, which were carried out prior to any testing/construction activity at the site. Therefore, the actual site properties during the hammer tests may have been different. Moreover, unlike the numerical model, the pile-soil interface is not perfectly bonded. Nevertheless, the obtained results show that the numerically computed impedances capture the experimentally computed impedances reasonably well, despite these inherent uncertainties.

8.4 Small-strain dynamic properties of the in-situ soil

8.4.1 On the validity of purely cylindrical shear wave propagation assumption

In the previous experimental study conducted by Kurtulus (2006); Kurtulus and Stokoe II (2008), the measured responses of the Thumper test were used to extract the shear wave velocity of the soil. It was expected that the vertically loaded drilled shaft would behave as a line source creating cylindrical shear waves within the soil domain, especially at horizontal planes that lie within the mid-depth of the pile where the geophones rested. With this assumption, the shear wave velocity was computed by dividing the horizontal distance of the sensors by the time interval it took for the waves to travel that distance. However, the plausibility of this assumption was not further investigated.

In order to have a better insight regarding the displacement envelope of the waves emanating from the shaft, the aforementioned Thumper test is simulated numerically here. A vertical sinusoidal force of 180 lb. (0.8 kN) is applied at $(r, z) = (0, 0)$. Two different frequencies are studied—i.e., $f = 5$ and 55 Hz. The latter is the frequency that was used in the actual Thumper test (Kurtulus, 2006). The soil material damping is assumed to be 5%.

Figures 8.7a and 8.7b display the spatial variations of the amplitude of the resulting steady-state vertical displacement $U_z(r, z, \omega)$, normalized by the maximum displacement amplitude U_z^{max}, for $f = 5$ and 55 Hz, respectively. $U_z(r, z, \omega)$ is computed using the following equation:

$$U_z(r, z, \omega) = \sqrt{\{\mathrm{Re}[\hat{u}_z(r, z, \omega)]\}^2 + \{\mathrm{Im}[\hat{u}_z(r, z, \omega)]\}^2}\,. \tag{8.6}$$

The sensors' positions used for recording responses in the Thumper test are shown in the same figure as black squares. As seen, the spatial variation of the amplitude of the vertical displacement field is not purely cylindrical and depends highly on the frequency of the applied loading.

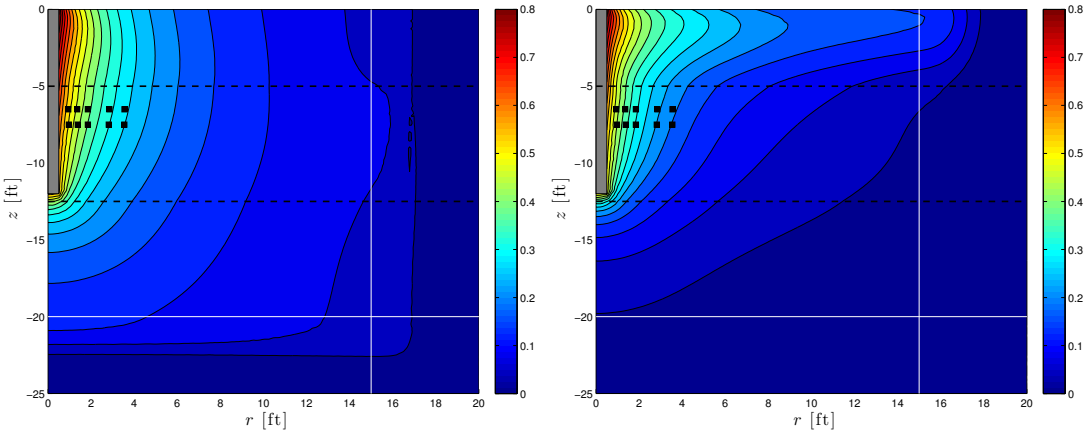

(a) (b)

Figure 8.7: Spatial variation of the normalized amplitude of the vertical displacement field within the soil domain for (a) $f = 5$ Hz and (b) $f = 55$ Hz.

For further investigation, the phase velocity in horizontal direction V_p^h at each point (r_i, z_i) is computed within the regular soil domain as follows:

$$V_p^h(r_i, z_i) = \omega \frac{\Delta r}{\Delta \phi} \tag{8.7}$$

where ω is the frequency in which the steady-state response is measured; $\Delta r = |r_{i+1} - r_i|$; $\Delta \phi = |\phi_{i+1} - \phi_i|$; r_{i+1} and r_i are radial distances between adjacent points $i + 1$ and i, respectively; ϕ_{i+1} and ϕ_i are the corresponding phase angles of the steady-state vertical

displacement response, which can be computed as follows:

$$\phi_i = \arctan\left(\frac{\mathrm{Im}[\hat{u}_z(\omega, r_i, z_i)]}{\mathrm{Re}[\hat{u}_z(\omega, r_i, z_i)]}\right) . \tag{8.8}$$

Figure 8.8 shows the spatial variation of the computed phase velocity within the regular domain for the numerically simulated Thumper test. Again, soil material damping is 5%. As r goes to zero (i.e., as locations become closer to the shaft), the irregularities in the phase velocity field increases. Also, it is seen that the phase velocity is not constant within the second layer and its value varies between 580 fps (177 m/s) and 660 fps (201 m/s) within the area that the sensors are located. This all but ascertains that the test conditions will not produce purely cylindrical wave fronts within the soil, and longitudinal and Rayleigh waves may also contribute to the responses measured in the field.

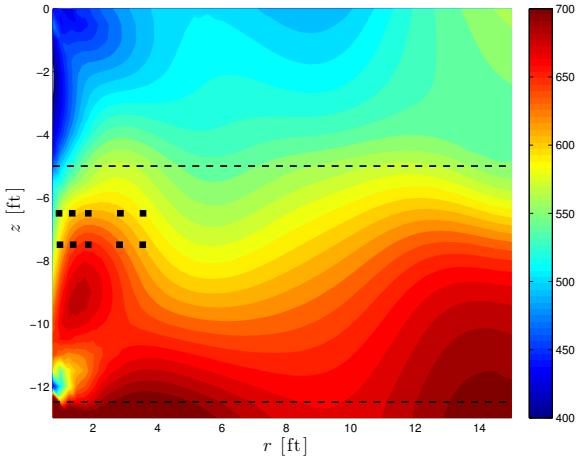

Figure 8.8: Spatial variation of the horizontal phase velocity within the soil domain for $f = 55$ Hz.

8.4.2 Numerical approximations of equivalent small-strain dynamic properties of the in-situ soil

As mentioned earlier, extracting soil material damping from experimental data is a challenging task. This is mainly because the measurements necessarily include radiation (as well as geometric) damping. Here, we use the data from the steady-state tests to estimate field val-

ues of equivalent shear wave velocity and material damping at depth. In total, velocity data for 10 points (sensor locations) are available, as shown in Figure 8.1. However, only 6 data points—i.e., G3, G4, G5, G8, G9 and G10—are used here to determine equivalent dynamic properties due to the complexities found in the measured responses at the remaining data points (for details, see Kurtulus, 2006).

For the present investigation, the actual soil profile is replaced by a homogeneous half-space with a shear wave velocity V_s^{eq} and material damping ξ^{eq}, and each of these parameters were varied over reasonable ranges of values. The soil density and Poisson's ratio are selected to be the same as those in the second layer of the actual test[1]. As noted above, the effects of radiation damping are taken into account through the use of PMLs, and thus, the approximated damping ξ^{eq} would be representative of the average material damping within the soil domain tested in the field.

For each test case, displacement responses are recorded at sensor locations. Then, the following error function is defined,

$$E(V_s^{eq}, \xi^{eq}) = \sum_{i=\{3,4,5,8,9,10\}} \left| \frac{U^i_{z,fld} - U^i_{z,num}}{U^i_{z,fld}} \right| + \sum_{i=\{4,5,9,10\}} \left| \frac{\phi^i_{fld} - \phi^i_{num}}{\phi^i_{fld}} \right| \tag{8.9}$$

where $U_{z,fld}$ and $U_{z,num}$ are the vertical displacement amplitudes obtained from field data and numerical simulations, respectively; ϕ_{fld} and ϕ_{num} are the corresponding phase angles. The minimization of this function with respect to the updating parameters (V_s^{eq} and ξ^{eq}) will yield the best agreement between measured and numerically obtained response quantities.

In order to compute the error function, we need to obtain the amplitude and phase angle of the vertical displacement at each point. In our frequency domain analyses, we use Eqs. (8.6) and (8.8) to compute these parameters. For processing the field measurements, which are originally in the time domain, an appropriate procedure should be used. Figure 8.9a shows displacement responses obtained by post-processing the recorded velocity data,

[1]This is because all sensors are almost in the mid-depth of the second layer and it is expected that properties of this layer dominantly control the measured responses.

which involves (i) removing the linear trend in the data, (ii) transforming data to the frequency domain via Fourier transforms, (iii) calibrating the data using amplitude and phase calibration curves of the 14-Hz geophone, (iv) dividing the calibrated data by $i\omega$ to convert it to displacement data, and (v) transforming the displacement data back to the time domain using inverse Fourier transforms. After this 5-step procedure, a sinusoidal function is fitted to the steady-state part of the response at each sensor location in order to obtain the amplitude of the displacement history. Figure 8.9b displays an example of the fitted functions at locations G3, G4, and G5. The time delay Δt is calculated by obtaining the lags that produce a maximum cross-correlation between each recorded displacement history and its counterpart at the reference point—i.e., G3 for G4 and G5, and G8 for G9 and G10. Then, the phase angle at any point i with respect to its reference point is computed as

$$\phi^i_{fld} = \omega \Delta t \,. \tag{8.10}$$

In subsequent analyses, first, the viability of the approach described above for extracting equivalent dynamic properties is investigated by studying two synthetic examples. These numerical experiments do not bear the adverse effects of modeling and measurement errors that naturally exist in field experiments, and thus they will only provide an understanding the general topology of the objective function described in Eq. (8.9). The information gleaned from the said numerical experiments will then be used to estimate the field shear wave velocity and damping values from the test data.

Two-layered half-space: Here, in order to create a "pseudo-reference" solution, the problem of a soil layer over half-space is solved numerically and displacement responses are recorded at the same locations where the actual sensors are located (6 points). These results are used in lieu of the field data (denoted with subscripts "fld" in Eq. (8.9)). The thickness of the first layer is 12.5 ft (3.8 m). The properties of the first layer and the underlying half-space are respectively the same as properties of the second and third layers of the field (see Figure 8.2). The soil material damping is assumed to be 5% in both layers. Then,

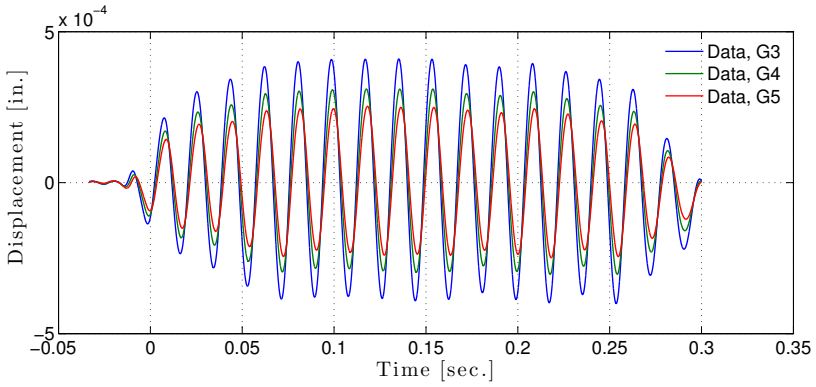

(a)

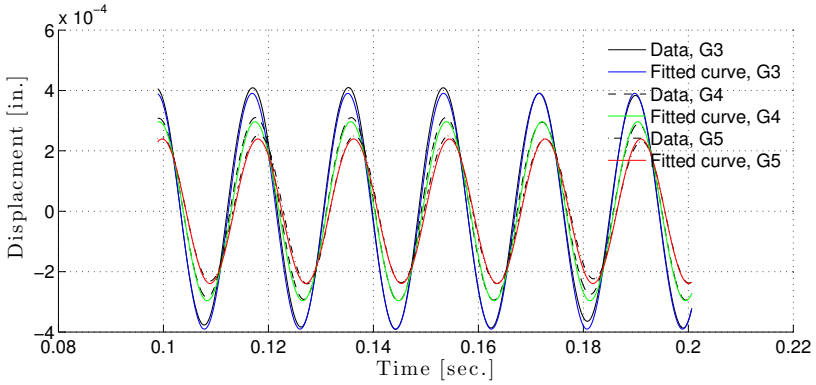

(b)

Figure 8.9: (a) Displacement responses and (b) sinusoidal fitted curves at sensors G3, G4, and G5.

the analyses are repeated to test different equivalent parameters. A total of 1890 cases are simulated with 400 fps$\leq V_s^{eq} \leq$845 fps (121 m/s$\leq V_s^{eq} \leq$ 258 m/s) at 5 fps (1.5 m/s) increments and $0 \leq \xi^{eq} \leq 0.2$ at 0.01 increments. Then, the corresponding error functions are obtained using Eq. (8.9).

Figure 8.10a shows the variation of error with V_s^{eq} and ξ^{eq}. The optimal updating parameter values—i.e., V_s^{opt} and ξ^{opt}—are shown as well. The dashed line shows the line of minimum variations in error, which lies along the major axis of the ellipsoidal contour lines. In order to obtain this line, the V_s^{eq} values are varied within the lowest error function contour for each equivalent damping ξ^{eq} value, and the locations of the minimizers for each of those specific optimization sub-problems are obtained. Then, a linear function is fitted through the said minimizers. As seen, by only using the information of 6 points, we are able to approximate the dynamic properties of the first layer with sufficient accuracy. However, the results have only a small sensitivity along the line of minimum errors. Substituting $\xi^{eq} = 0.05$ in the equation given for the dashed line results in $V_s^{eq} = 662.75$ fps (202 m/s), which is close to the value set for the first layer. This observation also suggests that the properties of the underlying half-space do not affect the results.

Three-layered half-space: The same study is repeated for the case of approximating equivalent dynamic properties of the three-layered half-space soil profile. The layer properties are the same as those given in Figure 8.2. The soil damping for all layers is 5%. Figure 8.10b shows the resulting error contours along with the optimal point and the line of minimum variation in error. Using the information of six data points, the best approximation is attained with $V_s^{opt} = 610$ fps (186 m/s) and $\xi^{opt} = 0.02$. However, If we substitute $\xi^{eq} = 0.05$ in the given equation for the line of minimum error, then the equivalent shear velocity will be $V_s^{eq} = 598$ fps (182 m/s). It is useful to note that the average shear wave velocity of the first two layers is $(5 \times 535 + 7.5 \times 660)/(5 + 7.5) = 610$ fps (186 m/s) based on a one-dimensional wave propagation assumption.

The parametric studies (on two- and three-layered half spaces) described above suggest that the method devised around the error function described in Eq. (8.9) can be used to

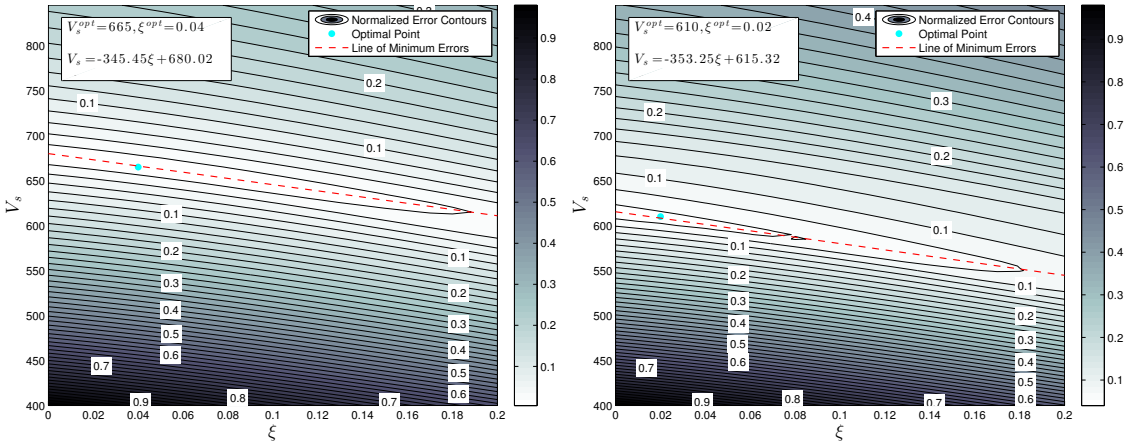

Figure 8.10: Error analysis of (a) two-layered and (b) three-layered half-space pseudo examples.

produce reasonable approximations of field equivalent dynamic properties. The trend of the minimum error line in Figure 8.10 indicates that, as expected, the estimation of the damping ratio is coupled with the estimation of the shear wave velocity. In other words, the overestimation of damping ratio will result in an underestimation of shear wave velocity and vice versa (e.g. Esmaeilzadeh Seylabi et al., 2012). Therefore, *a priori* information regarding one of these parameters can help significantly improve the accuracy in the estimation of the other parameter. A similar observation was also reported by Ahn (2007) who opted to use pre-defined damping curves for more accurate estimation of shear modulus reduction curves.

The same procedure employed in the parametric studies above is used now to approximate equivalent dynamic properties of the in-situ soil by using the *actual* field measurements when computing the error/objective function values. Figure 8.11 displays the error contours for the case of a vertical load applied at 55 Hz with amplitude of 180 lb. (0.8 kN). Again, it is seen that the error contours are inclined and indicate sensitivity to material damping. Moreover, picking any (V_s^{eq}, ξ^{eq}) combination along the indicated line of minimum error will not significantly change the objective function value. The topography of the objective function value can thus be used in understanding and quantifying the sensitivity of the estimates obtained for (V_s^{eq}, and ξ^{eq}).

Table 8.1 shows the values of field shear wave velocity obtained from extracting the phase differences using the procedure described earlier in §8.4, which is based on Eq. (8.7). As seen, the shear wave velocity ranges from 758 fps to 886 fps depending on the location of the sensors. These values, which are the representative of localized shear wave velocity field, differ from those obtained from the aforementioned minimization procedure that is based on Eq. (8.9), which yields the representative of average shear wave velocity for the first two layers. This comparison indicates that using the phase difference to approximate shear wave velocities may not always be a reliable approach, because the wave field may become complex (as opposed to cylindrical, for example) depending on the setting of the field test. As a result, it appears that obtaining in-situ dynamic soil properties through an optimization method that uses an appropriate numerical model as its computational engine is a better approach (Ahn et al., 2009) compared to simplified approaches based on time-of-arrival and/or phase differences.

Table 8.1: Local shear wave velocity obtained from using the field data using Eq. (8.7).

Sensor	Distance (in.)	Phase difference	Excitation frequency (Hz)	Shear wave velocity (fps)
G3-G4	5.00	0.18983	55	758.52
G4-G5	5.63	0.19862	55	816.29
G8-G9	4.94	0.16698	55	851.97
G9-G10	6.00	0.19510	55	885.64

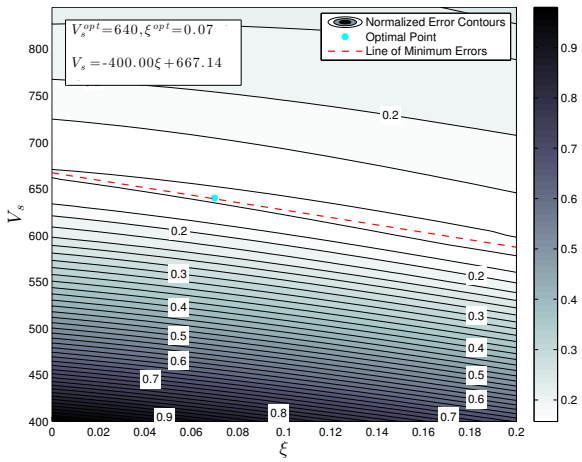

Figure 8.11: Error analysis for approximating equivalent dynamic properties of the in-situ soil.

CHAPTER 9

Summary and Conclusions

The main objective of this work has been the development of a numerical platform for reduced order modeling of SSI problems in a two-dimensional setting. In the following sections, we provide a summary of the steps we took to achieve this goal as well as the core findings from this study.

9.1 Chapters 1-3: Introduction, background, and simulation of wave propagation in a PML-truncated heterogeneous half-space

After providing a synopsis on different aspects of the SSI problem and the existing modeling techniques, we presented a detailed description of the formulations we used to develop a finite element code for direct modeling of SSI problems with high fidelity. A standard hybrid symmetric PML formulation was used to truncate the semi-infinite extent of soil, and the DRM was used to translate the seismic excitation within the PML-truncated model.

9.2 Chapter 4: Computing the soil impedance functions

We presented a numerical approach that was devised to compute the soil impedance functions for rigid and flexible soil-structure interfaces. The conducted numerical experiments showed that it was indeed feasible to evaluate impedance functions of foundation systems resting on (or embedded in) heterogeneous soils by using both time- and frequency-domain FEM-PML wave solvers. While it was simpler to implement the soil material damping in the

frequency-domain solver, inverting the large complex-valued system matrices arising in a frequency-domain solver requires larger computational costs than solving its real-numbered counterpart in the time-domain. This issue would be even more crucial in a three-dimensional setting. Moreover, the temporal characteristics of the input signal would not affect the quality of the numerically computed impedance functions, as long as the frequencies in which the impedance values were computed lay within the frequency-band of both the input and output spectra.

9.3 Chapter 5: Computing the kinematic interaction transfer functions

We described a numerical method to compute the response of a soil-structure interface embedded in a heterogeneous soil deposit on an elastic bedrock and subjected to vertically propagating shear waves. The presented numerical experiments showed that the implemented approach was successful both in recovering the free-field soil response when there was no scatterer, and in capturing the kinematic responses of an embedded rigid scatterer.

9.4 Chapter 6: Application studies I – Reduced order modeling of buried structures

We solved different types of problems to demonstrate the direct application of the developed framework. First, we computed the impedance functions and KITFs for different types of rigid buried structures to show how the spectra of these functions could be influenced by wave reflections, refractions, and interferences induced by the soil heterogeneity as well as interface geometry.

Second, we provided a step-wised procedure to construct a reduced order model of a non-rigid buried structure in an elastic half-space, including detailed description of the method we used for time-domain representation of the numerically computed impedance functions as

a discrete-time filter. We showed that the portrayed approach could accurately capture the response of the studied cases while other simplified approaches that were previously proposed by other researchers might result in erroneous outcomes. We also showed the importance of exploring the stability of the models used for time-domain representations of the soil subsystem as they interact with the structure.

9.5 Chapter 7: Application studies II – Numerical simulation of centrifuge experiments on underground structures

We used the developed FE solver for numerical simulations of a series of centrifuge experiments conducted on buried reservoir structures. Due to inherent complexities of nonlinear soil models, we examined the capabilities of the equivalent linear soil model in capturing experimentally measured responses. We used an optimization based method to calibrate the shear wave velocity profile and the Rayleigh damping model of a soil column using the available far-field acceleration data. We showed that the numerical simulations with the calibrated equivalent linear dynamic soil properties could capture the measured accelerations, racking, bending strains as well as dynamic earth pressures with acceptable accuracy even for the high amplitude base motion case. Therefore, for the soil and structural properties evaluated in this study, one can use the results of nonlinear site response analyses of a soil column to calibrate the equivalent linear soil model properties. Then, 2D linear wave propagation analyses can be conducted for the numerical simulations of a buried structure.

Due to the limited width and height of the centrifuge containers, it may not be possible to study the behavior of deep soil deposits with large lateral extents resting on elastic bedrocks purely by experimental means. We showed that the centrifuge container boundaries affect the measured responses significantly, especially closer to the soil surface. Moreover, the scattering effects of the centrifuge container were influenced by the specimen structures' stiffnesses. The proposed numerical modeling methodology therefore enables the exploration of more realistic site conditions when designing underground reservoir structures for seismic

loading.

9.6 Chapter 8: Application studies III – Interaction of a pile with layered soil under vertical excitations

Finally, we used the developed FE solver to simulate experimental data from dynamic field testing of a drilled shaft for model validation. The study showed that the devised numerical tool is capable of extracting in-situ foundation and soil properties of the instrumented drilled shaft-soil system from measured data. The field impedance function was calculated directly using data from a set of small-strain impact hammer tests that were carried out at the top of the shaft. The numerically extracted frequency-dependent vertical impedance function—which was first verified against a simpler analytical solution for a pile in homogenous half-space–, compared well with the said field impedance function obtained directly from data for a certain range of frequencies, including the resonant frequency of the soil-pile system.

The developed numerical tool was also able to simulate the small-strain field response of the soil layers as excited by steady-state dynamic loading. Successful extraction of in-situ material damping ratio of soils at depth requires explicit delineation between the radiation- and material-based constituents of the overall soil damping. The numerical model devised in the present study took advantage of the PML-truncated boundaries in order to handle the radiation damping correctly. It was shown that small-strain shear stiffness and material damping ratio of soil layers could be extracted using this numerical tool by solving an optimization problem. We also quantified the degree of coupling between the estimates of equivalent shear wave velocity and material damping values, and highlighted that simplified approaches based on localized calculations may bear significant estimation errors of dynamic soil properties.

Appendix A

Ingredients of system matrices: the axisymmetric setting

$$\mathbf{M} = \begin{bmatrix} \mathbf{M}_{u_r u_r} & \mathbf{0} & \mathbf{0} & \mathbf{0} & \mathbf{0} & \mathbf{0} \\ & \mathbf{M}_{u_z u_z} & \mathbf{0} & \mathbf{0} & \mathbf{0} & \mathbf{0} \\ & & \mathbf{M}_{\mathcal{S}_{rr}\mathcal{S}_{rr}} & \mathbf{M}_{\mathcal{S}_{rr}\mathcal{S}_{\theta\theta}} & \mathbf{M}_{\mathcal{S}_{rr}\mathcal{S}_{zz}} & \mathbf{0} \\ & & & \mathbf{M}_{\mathcal{S}_{\theta\theta}\mathcal{S}_{\theta\theta}} & \mathbf{M}_{\mathcal{S}_{\theta\theta}\mathcal{S}_{zz}} & \mathbf{0} \\ & & & & \mathbf{M}_{\mathcal{S}_{zz}\mathcal{S}_{zz}} & \mathbf{0} \\ & & & & & \mathbf{M}_{\mathcal{S}_{rz}\mathcal{S}_{rz}} \end{bmatrix} \tag{A.1}$$

$$\mathbf{C} = \begin{bmatrix} \mathbf{C}_{u_r u_r} & \mathbf{0} & \mathbf{C}_{u_r \mathcal{S}_{rr}} & \mathbf{C}_{u_r \mathcal{S}_{\theta\theta}} & \mathbf{0} & \mathbf{C}_{u_r \mathcal{S}_{rz}} \\ & \mathbf{C}_{u_z u_z} & \mathbf{0} & \mathbf{0} & \mathbf{C}_{u_z \mathcal{S}_{\theta\theta}} & \mathbf{C}_{u_z \mathcal{S}_{rz}} \\ & & \mathbf{C}_{\mathcal{S}_{rr}\mathcal{S}_{rr}} & \mathbf{C}_{\mathcal{S}_{rr}\mathcal{S}_{\theta\theta}} & \mathbf{C}_{\mathcal{S}_{rr}\mathcal{S}_{zz}} & \mathbf{0} \\ & & & \mathbf{C}_{\mathcal{S}_{\theta\theta}\mathcal{S}_{\theta\theta}} & \mathbf{C}_{\mathcal{S}_{\theta\theta}\mathcal{S}_{zz}} & \mathbf{0} \\ & & & & \mathbf{C}_{\mathcal{S}_{zz}\mathcal{S}_{zz}} & \mathbf{0} \\ & & & & & \mathbf{C}_{\mathcal{S}_{rz}\mathcal{S}_{rz}} \end{bmatrix} \tag{A.2}$$

$$\mathbf{K} = \begin{bmatrix} \mathbf{K}_{u_r u_r} & \mathbf{K}_{u_r u_z} & \mathbf{K}_{u_r \mathcal{S}_{rr}} & \mathbf{K}_{u_r \mathcal{S}_{\theta\theta}} & \mathbf{0} & \mathbf{K}_{u_r \mathcal{S}_{rz}} \\ & \mathbf{K}_{u_z u_z} & \mathbf{0} & \mathbf{0} & \mathbf{K}_{u_z \mathcal{S}_{\theta\theta}} & \mathbf{K}_{u_z \mathcal{S}_{rz}} \\ & & \mathbf{K}_{\mathcal{S}_{rr}\mathcal{S}_{rr}} & \mathbf{K}_{\mathcal{S}_{rr}\mathcal{S}_{\theta\theta}} & \mathbf{K}_{\mathcal{S}_{rr}\mathcal{S}_{zz}} & \mathbf{0} \\ & & & \mathbf{K}_{\mathcal{S}_{\theta\theta}\mathcal{S}_{\theta\theta}} & \mathbf{K}_{\mathcal{S}_{\theta\theta}\mathcal{S}_{zz}} & \mathbf{0} \\ & & & & \mathbf{K}_{\mathcal{S}_{zz}\mathcal{S}_{zz}} & \mathbf{0} \\ & & & & & \mathbf{K}_{\mathcal{S}_{rz}\mathcal{S}_{rz}} \end{bmatrix} \tag{A.3}$$

$$\mathbf{G} = \begin{bmatrix} \mathbf{G}_{u_r u_r} & \mathbf{0} & \mathbf{G}_{u_r \mathcal{S}_{rr}} & \mathbf{G}_{u_r \mathcal{S}_{\theta\theta}} & \mathbf{0} & \mathbf{G}_{u_r \mathcal{S}_{rz}} \\ & \mathbf{G}_{u_z u_z} & \mathbf{0} & \mathbf{0} & \mathbf{G}_{u_z \mathcal{S}_{\theta\theta}} & \mathbf{G}_{u_z \mathcal{S}_{rz}} \\ & & \mathbf{G}_{\mathcal{S}_{rr}\mathcal{S}_{rr}} & \mathbf{G}_{\mathcal{S}_{rr}\mathcal{S}_{\theta\theta}} & \mathbf{G}_{\mathcal{S}_{rr}\mathcal{S}_{zz}} & \mathbf{0} \\ & & & \mathbf{G}_{\mathcal{S}_{\theta\theta}\mathcal{S}_{\theta\theta}} & \mathbf{G}_{\mathcal{S}_{\theta\theta}\mathcal{S}_{zz}} & \mathbf{0} \\ & & & & \mathbf{G}_{\mathcal{S}_{zz}\mathcal{S}_{zz}} & \mathbf{0} \\ & & & & & \mathbf{G}_{\mathcal{S}_{rz}\mathcal{S}_{rz}} \end{bmatrix} \tag{A.4}$$

$$\dot{\mathbf{f}} = \begin{bmatrix} \dot{\mathbf{f}}_r \\ \dot{\mathbf{f}}_z \\ \mathbf{0} \\ \mathbf{0} \\ \mathbf{0} \\ \mathbf{0} \end{bmatrix}, \quad \dot{\mathbf{f}}_r = \int_{\Gamma_{\text{Loaded}}} \mathbf{\Phi} \dot{g}_r d\Gamma, \quad \dot{\mathbf{f}}_z = \int_{\Gamma_{\text{Loaded}}} \mathbf{\Phi} \dot{g}_z d\Gamma \tag{A.5}$$

Each block matrices are defined as:

$$\mathbf{M}_{u_r u_r} = \mathbf{M}_{u_z u_z} = \int_{\Omega_0} \rho \mathbf{\Phi}\mathbf{\Phi}^T d\Omega + \int_{\Omega_{\text{PML}}} a\rho \mathbf{\Phi}\mathbf{\Phi}^T d\Omega \tag{A.6}$$

$$\mathbf{M}_{\mathcal{S}_{rr}\mathcal{S}_{rr}} = \mathbf{M}_{\mathcal{S}_{\theta\theta}\mathcal{S}_{\theta\theta}} = \mathbf{M}_{\mathcal{S}_{zz}\mathcal{S}_{zz}} = -\int_{\Omega_{\text{PML}}} aD_1 \mathbf{\Psi}\mathbf{\Psi}^T d\Omega \tag{A.7}$$

$$\mathbf{M}_{\mathcal{S}_{rr}\mathcal{S}_{\theta\theta}} = \mathbf{M}_{\mathcal{S}_{rr}\mathcal{S}_{zz}} = \mathbf{M}_{\mathcal{S}_{\theta\theta}\mathcal{S}_{zz}} = \int_{\Omega_{\text{PML}}} aD_2 \mathbf{\Psi}\mathbf{\Psi}^T d\Omega \tag{A.8}$$

$$\mathbf{M}_{\mathcal{S}_{rz}\mathcal{S}_{rz}} = -\int_{\Omega_{\mathrm{PML}}} a\frac{1}{\mu}\mathbf{\Psi}\mathbf{\Psi}^T d\Omega \tag{A.9}$$

$$\mathbf{C}_{u_r u_r} = \mathbf{C}_{u_z u_z}\int_{\Omega_{\mathrm{PML}}} b\rho\mathbf{\Phi}\mathbf{\Phi}^T d\Omega \tag{A.10}$$

$$\mathbf{C}_{u_r\mathcal{S}_{rr}} = \mathbf{C}_{u_z\mathcal{S}_{rz}} = \int_{\Omega_{\mathrm{PML}}} \frac{\alpha_z\bar{\alpha}_r}{r}\mathbf{\Phi}_{,r}\mathbf{\Psi}^T d\Omega \tag{A.11}$$

$$\mathbf{C}_{u_r\mathcal{S}_{\theta\theta}} = \int_{\Omega_{\mathrm{PML}}} \frac{\alpha_r\alpha_z}{r}\mathbf{\Phi}\mathbf{\Psi}^T d\Omega \tag{A.12}$$

$$\mathbf{C}_{u_r\mathcal{S}_{rz}} = \mathbf{C}_{u_z\mathcal{S}_{zz}} = \int_{\Omega_{\mathrm{PML}}} \frac{\alpha_r\bar{\alpha}_r}{r}\mathbf{\Phi}_{,z}\mathbf{\Psi}^T d\Omega \tag{A.13}$$

$$\mathbf{C}_{\mathcal{S}_{rr}\mathcal{S}_{rr}} = \mathbf{C}_{\mathcal{S}_{\theta\theta}\mathcal{S}_{\theta\theta}} = \mathbf{C}_{\mathcal{S}_{zz}\mathcal{S}_{zz}} = -\int_{\Omega_{\mathrm{PML}}} bD_1\mathbf{\Psi}\mathbf{\Psi}^T d\Omega \tag{A.14}$$

$$\mathbf{C}_{\mathcal{S}_{rr}\mathcal{S}_{\theta\theta}} = \mathbf{C}_{\mathcal{S}_{rr}\mathcal{S}_{zz}} = \mathbf{C}_{\mathcal{S}_{\theta\theta}\mathcal{S}_{zz}} = \int_{\Omega_{\mathrm{PML}}} bD_2\mathbf{\Psi}\mathbf{\Psi}^T d\Omega \tag{A.15}$$

$$\mathbf{C}_{\mathcal{S}_{rz}\mathcal{S}_{rz}} = -\int_{\Omega_{\mathrm{PML}}} b\frac{1}{\mu}\mathbf{\Psi}\mathbf{\Psi}^T d\Omega \tag{A.16}$$

$$\tag{A.17}$$

$$\mathbf{K}_{u_r u_r} = \int_{\Omega_0}[(2\mu+\lambda)\mathbf{\Phi}_{,r}\mathbf{\Phi}_{,r}^T + \frac{\lambda}{r}\mathbf{\Phi}_{,r}\mathbf{\Phi}^T + \mu\mathbf{\Phi}_{,z}\mathbf{\Phi}_{,z}^T + \frac{\lambda+2\mu}{r^2}\mathbf{\Phi}\mathbf{\Phi}^T + \frac{\lambda}{r}\mathbf{\Phi}\mathbf{\Phi}_{,r}^T]d\Omega + \int_{\Omega_{\mathrm{PML}}} c\rho\mathbf{\Phi}\mathbf{\Phi}^T d\Omega \tag{A.18}$$

$$\mathbf{K}_{u_r u_z} = \int_{\Omega_0}[\lambda\mathbf{\Phi}_{,r}\mathbf{\Phi}_{,z}^T + \mu\mathbf{\Phi}_{,z}\mathbf{\Phi}_{,r}^T + \frac{\lambda}{r}\mathbf{\Phi}\mathbf{\Phi}_{,z}^T]d\Omega \tag{A.19}$$

$$\mathbf{K}_{u_r\mathcal{S}_{rr}} = \mathbf{K}_{u_z\mathcal{S}_{rz}} = \int_{\Omega_{\mathrm{PML}}} \frac{\alpha_z\bar{\beta}_r + \bar{\alpha}_r\beta_z}{r}\mathbf{\Phi}_{,r}\mathbf{\Psi}^T d\Omega \tag{A.20}$$

$$\mathbf{K}_{u_r\mathcal{S}_{\theta\theta}} = \int_{\Omega_{\mathrm{PML}}} \frac{\alpha_r\beta_z + \beta_r\alpha_z}{r}\mathbf{\Phi}\mathbf{\Psi}^T d\Omega \tag{A.21}$$

$$\mathbf{K}_{u_r\mathcal{S}_{rz}} = \mathbf{K}_{u_z\mathcal{S}_{zz}} = \int_{\Omega_{\mathrm{PML}}} \frac{\alpha_r\bar{\beta}_r + \bar{\alpha}_r\beta_r}{r}\mathbf{\Phi}_{,z}\mathbf{\Psi}^T d\Omega \tag{A.22}$$

$$\mathbf{K}_{u_z u_z} = \int_{\Omega_0}[\mu\mathbf{\Phi}_{,r}\mathbf{\Phi}_{,r}^T + (2\mu+\lambda)\mathbf{\Phi}_{,z}\mathbf{\Phi}_{,z}^T]d\Omega + \int_{\Omega_{\mathrm{PML}}} c\rho\mathbf{\Phi}\mathbf{\Phi}^T d\Omega \tag{A.23}$$

$$\mathbf{K}_{\mathcal{S}_{rr}\mathcal{S}_{rr}} = \mathbf{K}_{\mathcal{S}_{\theta\theta}\mathcal{S}_{\theta\theta}} = \mathbf{K}_{\mathcal{S}_{zz}\mathcal{S}_{zz}} = -\int_{\Omega_{\mathrm{PML}}} cD_1\mathbf{\Psi}\mathbf{\Psi}^T d\Omega \tag{A.24}$$

$$\mathbf{K}_{\mathcal{S}_{rr}\mathcal{S}_{\theta\theta}} = \mathbf{K}_{\mathcal{S}_{rr}\mathcal{S}_{zz}} = \mathbf{K}_{\mathcal{S}_{\theta\theta}\mathcal{S}_{zz}} = \int_{\Omega_{\mathrm{PML}}} cD_2 \mathbf{\Psi}\mathbf{\Psi}^T d\Omega \tag{A.25}$$

$$\mathbf{K}_{\mathcal{S}_{rz}\mathcal{S}_{rz}} = -\int_{\Omega_{\mathrm{PML}}} c\frac{1}{\mu}\mathbf{\Psi}\mathbf{\Psi}^T d\Omega \tag{A.26}$$

$$\mathbf{G}_{u_r u_r} = \mathbf{G}_{u_z u_z} = \int_{\Omega_{\mathrm{PML}}} d\rho \mathbf{\Phi}\mathbf{\Phi}^T d\Omega \tag{A.27}$$

$$\mathbf{G}_{u_r \mathcal{S}_{rr}} = \mathbf{G}_{u_r \mathcal{S}_{rz}} = \int_{\Omega_{\mathrm{PML}}} \frac{\beta_z \bar{\beta}_r}{r} \mathbf{\Phi}_{,r} \mathbf{\Psi}^T d\Omega \tag{A.28}$$

$$\mathbf{G}_{u_r \mathcal{S}_{\theta\theta}} = \int_{\Omega_{\mathrm{PML}}} \frac{\beta_r \beta_z}{r} \mathbf{\Phi}\mathbf{\Psi}^T d\Omega \tag{A.29}$$

$$\mathbf{G}_{u_r \mathcal{S}_{rz}} = \mathbf{G}_{u_z \mathcal{S}_{zz}} = \int_{\Omega_{\mathrm{PML}}} \frac{\beta_r \bar{\beta}_r}{r} \mathbf{\Phi}_{,z} \mathbf{\Psi}^T d\Omega \tag{A.30}$$

$$\mathbf{G}_{S_{rr}S_{rr}} = \mathbf{G}_{\mathcal{S}_{\theta\theta}\mathcal{S}_{\theta\theta}} = \mathbf{G}_{\mathcal{S}_{zz}\mathcal{S}_{zz}} = -\int_{\Omega_{\mathrm{PML}}} dD_1 \mathbf{\Psi}\mathbf{\Psi}^T d\Omega \tag{A.31}$$

$$\mathbf{G}_{\mathcal{S}_{rr}\mathcal{S}_{\theta\theta}} = \mathbf{G}_{\mathcal{S}_{rr}\mathcal{S}_{zz}} = \mathbf{G}_{\mathcal{S}_{\theta\theta}\mathcal{S}_{zz}} = \int_{\Omega_{\mathrm{PML}}} dD_2 \mathbf{\Psi}\mathbf{\Psi}^T d\Omega \tag{A.32}$$

$$\mathbf{G}_{\mathcal{S}_{rz}\mathcal{S}_{rz}} = -\int_{\Omega_{\mathrm{PML}}} d\frac{1}{\mu}\mathbf{\Psi}\mathbf{\Psi}^T d\Omega \tag{A.33}$$

Bibliography

S. Ahmad and A. Bharadwaj. Horizontal impedance of embedded strip foundations in layered soil. *Journal of Geotechnical Engineering*, 117:1021–1041, 1991.

J. Ahn. *In situ determination of dynamic soil properties under an excited surface foundation*. PhD thesis, Texas A&M University, 2007.

J. Ahn, G. Biscontin, and J. M. Roesset. Wave propagation velocity under a vetically vibrated surface foundation. *International Journal for Numerical and Analytical Methods in Geomechanics*, 33:1153–1167, 2009.

D. Baffet, J. Bielak, D. Givoli, T. Hagstrom, and D. Rabinovich. Long-time stable high-order absorbing boundary conditions for elastodynamics. *Computational Methods in Applied Mechanics and Engineering*, 241(244):20–37, 2012.

S. Balay, W. D. Gropp, L. C. McInnes, and B. F. Smith. Efficient management of parallelism in object oriented numerical software libraries. In E. Arge, A. M. Bruaset, and H. P. Langtangen, editors, *Modern Software Tools in Scientific Computing*, pages 163–202. Birkhäuser Press, 1997.

S. Balay, S. Abhyankar, M. F. Adams, J. Brown, P. Brune, K. Buschelman, L. Dalcin, V. Eijkhout, W. D. Gropp, D. Kaushik, M. G. Knepley, L. C. McInnes, K. Rupp, B. F. Smith, S. Zampini, H. Zhang, and H. Zhang. PETSc users manual. Technical Report ANL-95/11 - Revision 3.7, Argonne National Laboratory, 2016b. URL `http://www.mcs.anl.gov/petsc`.

S. Balay, S. Abhyankar, M. F. Adams, J. Brown, P. Brune, K. Buschelman, L. Dalcin, V. Eijkhout, W. D. Gropp, D. Kaushik, M. G. Knepley, L. C. McInnes, K. Rupp, B. F. Smith, S. Zampini, H. Zhang, and H. Zhang. PETSc Web page. `http://www.mcs.anl.gov/petsc`, 2016a. URL `http://www.mcs.anl.gov/petsc`.

H. Bao, J. Bielak, O. Ghattas, L. F. Kallivokas, D. R. O'Hallaron, J. R. Shewchuk, and J. Xu. Large-scale simulation of elastic wave propagation in heterogeneous media on parallel computers. *Computer methods in applied mechanics and engineering*, 152(1):85–102, 1998.

U. Basu and A. K. Chopra. Perfectly matched layers for time-harmonic elastodynamics of unbounded domains: theory and finite-element implementation. *Computer Methods in Applied Mechanics and Engineering*, 192(11–12):1337–1375, 2003.

J. P. Berenger. A perfectly matched layer for the absorption of electromagnetic waves. *Journal of Computational Physics*, 114:185–200, 1994.

J. P. Berenger. Numerical reflection from fdtd-pmls: a comparison of the split pml with the unsplit and cfs pmls. *IEEE Transactions on Antennas and Propagation*, 50:258–265, 2002a.

J. P. Berenger. Application of the cfs pml to the absorption of evanescent waves in waveguides. *IEEE Microwave Wireless Components Letters*, 12:218–220, 2002b.

A. Bharadwaj and S. Ahmad. Rocking impedance of embedded strip foundations in layered soil. *Journal of Geotechnical Engineering*, 118:796–813, 1992.

J. Bielak and P. Christiano. On the effective seismic input for non-linear soil-structure interaction systems. *Earthquake Engineering and Structural Dynamics*, 12:107–119, 1984.

J. Bielak, K. Loukakis, Y. Hisada, and C. Yoshimura. Domain reduction method for three-dimensional earthquake modeling in localized regions, part i: theory. *Bulletin of the Seismological Society of America*, 93:817–824, 2003.

S. J. Brandenberg, G. Mylonakis, and J. P. Stewart. Kinematic Framework for Evaluating Seismic Earth Pressures on Retaining Walls. *Journal of Geotechnical and Geoenvironmental Engineering*, 141(7):1–10, 2015.

S. Carbonari, F. Dezi, and G. Leoni. Linear soil-structure interaction of coupled wall-frame structures on pile foundations. *Soil Dynamics and Earthquake Engineering*, 31:1296–1309, 2011.

K. M. Carpenter. Note on 'radiation conditions for lateral boundaries of limited-are numerical models' by m. j. miller and a. j. thorpe. *Quarterly Journal of the Royal Meteorological Society*, 108:711–719, 1982.

A. Cazzani and P. Ruge. Numerical aspects of coupling strongly frequency-dependent soil-foundation models with structural finite elements in the time-domain. *Soil Dynamics and Earthquake Engineering*, 37:56–72, 2012.

S. Chen and J. Hou. Modal analysis of circular flexible foundations under vertical vibration. *Soil Dynamics and Earthquake Engineering*, 29:898–908, 2009.

F. Collino. High order absorbing boundary conditions for wave propagation models. straight line boundaries and corner cases. In *R. Kleinman et al. (Eds.), Proceedings of the Second International Conferenceon Mathematical and Numerical Aspects of Wave Propagation, SIAM*, pages 161–171, Delaware, 1993.

D. Correia and J. M. Jin. On the development of a higher order pml. *IEEE Transactions on Antennas and Propagation*, 53:4157–4163, 2005.

R. R. Craig and A. J. Kurdila. *Fundamentals of structural dynamics*. Wiley & Sons, Hoboken, New Jersey, 2006.

S. M. Day. *Finite element analysis of seismic scattering problems*. PhD thesis, University of California, San Diego, 1977.

S. M. Day and G. A. Frazier. Seismic response of hemispherical foundation. *Journal of the Engineering Mechanics Division*, 105(1):29–41, 1979.

F. C. P. de Barros and J. E. Luco. Identification of foundation impedance functions and soil properties from vibration tests of the hualien containment model. *Soil Dynamics and Earthquake Engineering*, 14(4):229–248, 1995.

D. de Klerk, D. J. Rixen, and S. N. Voormeeren. Genral framework for dynamic substructuring: history, review, and classification of techniques. *AIAA Journal*, 46(5):1169–1181, 2008.

Y. H. Deng, S. Dashti, A. Hushmand, C. Davis, and B. Hushmand. Seismic response of underground reservoir structures in sand: evaluation of class-c and c1 numerical simulations using centrifuge experiments. *Soil Dynamics and Earthquake Engineering*, 85:202–216, 2016.

J. Dominguez. Response of embedded foundations to travelling waves. Technical report, Massachusetts Institute of Technology, 1978.

X. Du and M. Zhao. A local time-domain transmitting boundary for simulating cylindrical elastic wave propagation in infinite media. *Soil Dynamics and Earthquake Engineering*, 30:937–946, 2010.

F. Elsabee and J. P. Morray. Dynamic behavior of embedded foundations. Technical report, Massachusetts Institute of Technology, 1977.

E. Esmaeilzadeh Seylabi, H. Jahankhah, and M. A. Ghannad. Equivalent linearization of non-linear soil-structure systems. *Earthquake Engineering ans Structural Dynamics*, 41: 1775–1792, 2012.

A. Fathi. *Full-waveform inversion in three-dimensional PML-truncated elastic media : theory , computations , and field experiments.* PhD thesis, University of Texas at Austin, 2015.

R. Gash, E. Esmaeilzadeh Seylabi, and E. Taciroglu. Frequency dependent effects of soil-structure interaction on inelastic behavior of superstructures. *ACI Special Publication*, 2016.

R. J. H. Gash. *On the implementation and applications of discrete-time filters for soil-structure interaction analyses*. PhD thesis, University of California, Los Angeles, 2015.

G. Gazetas. Static and dynamic displacements of foundations on heterogeneous multilayered soils. *Geotechnique*, 30:159–177, 1980.

G. Gazetas. Strip foundations on a cross-anisotropic soil layer subjected to dynamic loading. *Geotechnique*, 31:161–179, 1981.

G. Gazetas. Analysis of machine foundation vibrations: state of the art. *Soil Dynamics and Earthquake Engineering*, 2(1):2–42, 1983.

ACS SASSI NQA VErsion 2.3.3 User Manuals. Ghiocel Predictive Technologies, Inc., USA, 2010.

K. Gillis, S. Dashti, and Y. Hashash. Dynamic calibration of tactile sensors for measurement of soil pressure in centrifuge. *ASTM Geotechnical Testing Journal*, 38:261–274, 2015.

M. J. Givens. *Dynamic soil-structure interaction of instrumented buildings and test structures*. PhD thesis, Universtiy of California, Los Angeles, 2013.

D. Givoli. High-order local non-reflecting boundary conditions: a review. *Wave Motion*, 39: 319–326, 2004.

L. Grigori, J. W. Demmel, and X. S. Li. Parallel symbolic factorization for sparse LU with static pivoting. *SIAM J. Scientific Computing*, 29(3):1289–1314, 2007.

N. Gucunski. Rocking response of flexible circular foundations on layered media. *Soil Dynamics and Earthquake Engineering*, 15:485–497, 1996.

N. Gucunski and R. Peek. Vertical vibration of circular flexible foundations on layered media. *Earthquake Engineering and Structural Dynamics*, 12:183–192, 1993.

T. Hagstrom and T. Warburton. A new auxiliary variable formulation of high-order local radiation boundary conditions: corner compatibility conditions and extensions to first order systems. *Wave Motion*, 39:327–338, 2004.

Y. Hashash, D. R. Groholski, and C. Phillips. Recent advances in nonlinear site response analysis. In *5th International Conference on Recent Advances in Geotechnical Earthquake Engineering*, 2010.

N. A. Haskell. Radiation pattern of surface waves from point sources in a multi-layered medium. *Bulletin of the Seismological Society of America*, 54(1):377–393, 1964.

R. L. Higdon. Radiation boundary conditions for the scalar wave equation. *SIAM Journal on Numerical Analysis*, 27(4):831–870, 1990.

Y. Hisada. An efficient method for computing green's functions for a layered half-space with sources and receivers at close depths. *Bulletin of Seismological Society of America*, 84: 1456–1472, 1994.

Z. Hryniewicz. Dynamic response of a rigid strip on an elastic half-space. *Computer Methods in Applied Mechanics and Engineering*, 25:355–364, 1981.

A. Hushmand, S. Dashti, C. Davis, B. Hushmand, M. Zhang, M. Ghayoomi, J. S. McCartney, Y. Lee, and J. Hu. Seismic performance of underground reservoir structures: insight from centrifuge modeling on the influence of structure stiffness. *Journal of Geotechnical and Geoenvironmental Engineering*, 142(7):04016020, 2016.

M. Iguchi. An approximate analysis of input motions for rigid embedded foundations. *Transactions of Architectural Institute of Japan*, 57(315):61–75, 1982.

M. Iguchi and J. E. Luco. Dynamic response of flexible rectangular foundations on an elastic half-space. *Earthquake Engineering and Structural Dynamics*, 9:239–249, 1981.

K. Ishihara. *Soil behavior in earthquake geotechnics*. Oxford Science Publications, 1996.

A. Israil and S. Ahmad. Dynamic vertical compliance of strip foundations in layered soils. *Earthquake engineering & structural dynamics*, 18(7):933–950, 1989.

C.-G. Jeong. Verification of seismic motion input into the finite element models. Master's thesis, University of California, Davis, 2013.

B. Jeremic, S. Kunnath, and F. Xiong. Influence of soil-foundation-structure interaction on seismic response of the i-880 viaduct. *Engineering Structures*, 26:391–402, 2004.

P. Joly and C. Tsogka. Higher order absorbing boundary conditions for elastodynamics. In *4th European Conference on Computational Mechanics (ECCM-2010)*, Paris, May 2010.

W. B. Joyner. Method for calculating nonlinear seismic response in 2-dimensions. *Bulletin of the Seismological Society of America*, 65:1337–1357, 1975.

D. L. Karabalis and D. E. Beskos. Dynamic response of 3-d flexible foundations by time domain bem and fem. *Soil Dynamics and Earthquake Engineering*, 4:91–101, 1985.

P. Karasudhi, L. M. Keer, and S. L. Lee. Vibratory motion of a body on an elastic half plane. *Journal of Applied Mechanics*, 35:697, 1968.

E. Kausel. Early history of soil-structure interaction. *Soil Dynamics and Earthquake Engineering*, 30:822–832, 2010.

E. Kausel and J. M. Roesset. Stiffness matrices for layered soil. *Bulletin of the Seismological Society of America*, 71(6):1743–1761, 1981.

G. Kerschen, J. C. Golinval, A. F. Vakakis, and L. A. Bergman. The method of proper orthogonal decomposition for dynamical characterization and order reduction of mechanical systems: and overview. *Nonlinear Dynamics*, 41:147–169, 2005.

F. T. Kokkinos and C. C. Spyrakos. Dynamic analysis of flexible strip-foundations in the frequency domain. *Computers and Structures*, 39:473–482, 1991.

S. K. Kramer. *Geotechnical earthquake engineering.* Prentice Hall, New Jersey, 1996.

S. Kucukcoban. *The inverse medium problem in PML-truncated elastic media.* Doctoral dissertation, The University of Texas at Austin, 2010.

S. Kucukcoban and L. Kallivokas. A symmetric hybrid formulation for transient wave simulations in pml-truncated heterogeneous media. *Wave Motion*, 50(1):57–79, 2013.

S. Kucukcoban and L. F. Kallivokas. A mixed perfectly-matched-layer for transient wave simulations in axisymmetric elastic media. *Computer Modeling in Engineering and Sciences*, 64:109–146, 2010.

S. Kucukcoban and L. F. Kallivokas. Mixed perfectly-matched-layers for direct transient analysis in 2D elastic heterogeneous media. *Computer Methods in Applied Mechanics and Engineering*, 200:57–76, 2011.

A. Kurtulus. *Field measurements of the linear and nonlinear shear moduli of soils using drilled shafts as dynamic cylindrical sources.* PhD thesis, University of Texas at Austin, 2006.

A. Kurtulus and K. H. Stokoe II. In situ measurement of nonlinear shear modulus of silty soil. *Journal of Geotechnical and Geoenvironmental Engineering*, 134:1531–1540, 2008.

M. Kuzuoglu and R. Mittra. Frequency dependence of the constitutive parameters of causal perfectly matched anisotropic absorbers. *IEEE Microwave Guided Wave Letters*, 6:447–449, 1996.

C. B. Lai and G. J. Rix. Solution of the rayleigh eigenproblem in viscoelastic media. *Bulletin of the Seismological Society of America*, 92:2297–2309, 2002.

A. D. Laudon, O.-S. Kwon, and A. Ghaemmaghami. Stability of the time-domain analysis method including a frequency-dependent soil-foundation system. *Earthquake Engineering & Structural Dynamics*, 44:2737–2754, 2015.

N. Lesgidis, O.-S. Kwon, and A. Sextos. A time-domain seismic ssi analysis method for inelastic bridge structures through the use of a frequency-dependent lumped parameter model. *Earthquake Engineering & Structural Dynamics*, 44:2137–2156, 2015.

X. S. Li and J. W. Demmel. SuperLU_DIST: A Scalable Distributed-Memory Sparse Direct Solver for Unsymmetric Linear Systems_DIST: A scalable distributed-memory sparse direct solver for unsymmetric linear systems. *ACM Trans. Mathematical Software*, 29(2): 110–140, June 2003.

G. Liou and P. Huang. Effect of flexibility on impedance functions for circular foundation. *Journal of Engineering Mechanics*, 120:1429–1446, 1994.

J. E. Luco. On the relation between radiation and scattering problems for foundations embedded in an elastic half-space. *Soil Dynamics and Earthquake Engineering*, 5(2):97–101, 1986.

J. E. Luco and R. A. Westmann. Dynamic response of a rigid footing bonded to an elastic half space. *Journal of Applied Mechanics*, 39:527–534, 1972.

J. Lysmer and L. Kuhlemeyer. Finite dynamic model for infinite media. *ASCE Journal of the Engineering Mechanics Division*, 95:859–877, 1969.

A. Mar-Or and D. Givoli. High-order global-regional model interaction: extension of carpenter's scheme. *International Journal for Numerical Methods in Engineering*, 77:50–74, 2009.

A. Maravas, G. Mylonakis, and D. L. Karabalis. Discrete impedance matrix for flexible surface foundations. In *4th ECCOMAS Thematic Conference on Computational Methods in Structural Dynamics and Earthquake Engineering*, 2013.

A. Mikami, J. P. Stewart, and M. Kamiyama. Effects of time series analysis protocols on transfer functions calculated from earthquake accelerograms. *Soil Dynamics and Earthquake Engineering*, 28(9):695–706, 2008.

K. Miura, A. M. Kaynia, K. Masuda, E. Kitamura, and Y. Seto. Dynamic behavior of pile foundations in homogeneous and non-homogeneous media. *Earthquake Engineering ans Structural Dynamics*, 23:183–192, 1994.

N. Muskhelishvili. *Some basic problems of the mathematical theory of elasticity*. Noordhoff, Groningen, 1963.

G. Mylonakis and G. Gazetas. Seismic soil structure interaction: Beneficial or detrimental? *Journal of Earthquake Engineering*, 43:277–301, 2000.

N. C. H. R. P. NCHRP Report 611. *NCHRP Report 611: Seismic analysis and design of retaining walls, buried structures, slopes, and embankments*. Transportation Research Board, Washington, DC, 2008.

N. M. Newmark. A method of computation for structural dynamics. In *Proc. ASCE*, volume 85, pages 67–94, 1959.

N. NIST. *Soil-Structure-Interaction for Building Structures (NIST GCR 12-917-21)*. National Institute of Standards and Technology, Gaithersburg, MD 20899, September 2012.

A. V. Oppenheim, A. S. Willsky, and S. H. Nawab. *Signals and Systems*. Prentice-Hall, Upper Saddle River, NJ, USA, second edition, 1996.

F. Ostadan, N. Deng, and J. M. Roesset. Estimating total system damping for soil-structure interaction systems. In *Third UJNR Workshop on Soil-Structure Interaction, Menlo Park, California*, 2004.

A. L. Pais and E. Kausel. On rigid foundations subjected to seismic waves. *Earthquake Engineering & Structural Dynamics*, 18:475–489, 1989.

D. Park and Y. Hashash. Soil damping formulation in nonlinear time domain site response analysis. *Journal of Earthquake Engineering*, 8:249–274, 2004.

K. Pitilakis and G. Tsinidis. *Earthquake Geotechnical Engineering Design*, volume 28 of *Geotechnical, Geological and Earthquake Engineering*, chapter 11, pages 279–340. Springer, 2014.

M. Preisig. Nonlinear finite element analysis of dynamic soil-foundation-structure interaction. Master's thesis, University of California, Davis, 2005.

D. Rabinovich, D. Givoli, and E. Becache. Comparison of high-order absorbing boundary conditions and perfectly matched layers in the frequency domain. *International Journal for Numerical Methods in Biomedical Engineering*, 26:1351–1369, 2010.

D. Rabinovich, D. Givoli, J. Bielak, and T. Hagstrom. A finite element scheme with a high order absorbing boundary condition for elastodynamics. *Computational Methods in Applied Mechanics and Engineering*, 200:2048–2066, 2011.

R. K. N. D. Rajapakse and A. H. Shah. Impedance of embedded rigid strip foundations. *Earthquake Engineering and Structural Dynamics*, 16:255–273, 1988.

E. M. Rathje, N. A. Abrahamson, and J. D. Bray. Simplified frequency content estimates of earthquake ground motions. *Journal of Geotechnical and Geoenvironmental Engineering*, 124:150–159, 1998.

C. S. Rha and E. Taciroglu. Coupled macroelement model of soil-structure interaction in deep foundations. *ASCE Journal of Engineering Mechanics*, 133(12):1326–1340, 2007.

H. R. Riggs and G. Waas. Influence of foundation flexibility on soil-structure interaction. *Earthquake Engineering and Structural Dynamics*, 13:597–615, 1985.

G. J. Rix, C. G. Lai, and A. W. Spang. In situ measurement of damping ratio using surface waves. *Journal of Geotechnical and Geoenvironmental Engineering*, 126:472–480, 2000.

J. A. Roden and S. D. Gedney. Convolutional pml (cpml): an efficient fdtd implementation of the cs-pml for arbitrary media. *Microwave and Optiacal Technology Letters*, 27:334–339, 2000.

E. N. Rovithis, H. Parashakis, and G. E. Mylonakis. 1d harmonic response of layered inhomogeneous soil:analytical investigation. *Soil Dynamics and Earthquake Engineering*, 31:879–890, 2011.

P. Ruge, C. Trinks, and S. Witte. Time-domain analysis of unbounded media using mixed-variable formulations. *Earthquake Engineering and Structural Dynamics*, 30:899–925, 2001.

E. Safak. Time-domain representation of frequency-dependent foundation impedance functions. *Soil Dynamics and Earthquake Engineering*, 26:65—70, 2006.

M. Saitoh. Simple model of frequency-depenent impedance functions in soil-structure interaction using frequency-independent elements. *Journal of Engineering Mechanics ASCE*, pages 1101–1113, October 2007.

M. Saitoh and H. Watanabe. Effects of flexibility on rocking impedance of deeply embedded foundation. *Journal of Geotechnical and Geoenvironmental Engineering*, 130:438–445, 2004.

S. A. Savidis and A. T. Richter. Dynamic response of elastic plates on the surface of the half-space. *International Journal for Numerical and Analytical Methods in Geomechanics*, 3:245–254, 1979.

H. B. Seed and R. V. Whitman. Design of earth retaining structures for dynamic loads. In *ASCE Specialty Conference, Lateral Stresses in the Ground and Design of Earth Retaining Structures*, pages 103–147, 1970.

J. M. Solberg, Q. Hossain, J. A. Blink, S. R. Bohlen, G. Mseis, and H. Greenberg. Development of a generalized methodology for soil-structure interaction analysis using nonlinear time-domain techniques. Technical Report LLNL-TR-635762, NEAMS Program, DOE Office of Nuclear Energy (NE-41), April 2013.

C. C. Spyrakos and D. E. Beskos. Dynamic response of flexible strip-foundations by boundary and finite elements. *Soil Dynamics and Earthquake Engineering*, 5:84–96, 1986.

C. C. Spyrakos and C. Xu. Dynamic analysis of flexible massive strip-foundations embedded in layered soils by hybrid bem-fem. *Computers and Structures*, 82:2541–2550, 2004.

J. P. Stewart and S. Tileylioglu. Input ground motions for tall buildings with subterranean levels. *The Structural Design of Tall and Special Buildings*, 16:543–557, 2007.

S. Tileylioglu, J. P. Stewart, and R. L. Nigbor. Dynamic stiffness and damping of a shallow foundation from forced vibration of a field test structure. *ASCE Journal of Geotechnical and Geoenvironmental Engineering*, 137(4):344–353, 2011.

R. Tokmashev, A. Tixier, and B. B. Guzina. Experimental validation of the topological sensitivity approach to elastic-wave imaging. *Inverse Problems*, 29(12):125005, 2013.

A. S. Veletsos, A. M. Prasad, and W. H. Wu. Transfer functions for rigid rectangular foundations. *Earthquake Engineering and Structural Dynamics*, 26(1):5–17, 1997.

C. Y. Wang and R. B. Herrmann. A Numerical Study Of P-, SV-, And SH-Wave Generation In A Plane Layered Medium. *Bulletin of the Seismological Society of America*, 70(4): 1015–1036, 1980.

Y. Wang and R. K. N. D. Rajapakse. Dynamics of rigid strip foundations embedded in orthotropic elastic soils. *Earthquake Engineering and Structural Dynamics*, 20(10):927–947, 1991.

Y.-C. Wang, V. Murti, and S. Valliappan. Assessment of the accuracy of the newmark method in transient analysis of wave propagation problems. *Earthquake engineering & structural dynamics*, 21(11):987–1004, 1992.

J. P. Wolf. *Dynamic soil-structure interaction*. Prentice-Hall, Englewood Cliffs, N.J. 07632, 1985.

J. P. Wolf. Consistent lumped-parameter models for unbounded soil: physical representation. *Earthquake Engineering and Structural Dynamics*, 20:11–32, 1991.

J. P. Wolf. *Foundation Vibration Analysis Using Simple Physical Models*. Prentice Hall, Upper Saddle River, NJ 07458, 1994.

J. P. Wolf and M. Motosaka. Recursive evaluation of interaction forces of unbounded soil in the time domain from dynamic-stiffness coefficients in the frequency domain. *Earthquake Engineering and Structural Dynamics*, 18:365–376, 1989.

J. H. Wood. *Earthquake induced soil pressures on structures*. PhD thesis, California Institute of Technology, 1973.

W. Wu and W. Lee. Systematic lumped-parameter models for foundations based on polynomila-fraction expansion. *Earthquake Engineering and Structural Dynamics*, 31: 1383–1412, 2002.

W. Wu and W. Lee. Nested lumped-parameter models for foundation vibrations. *Earthquake Engineering and Structural Dynamics*, 33:1051–1058, 2004.

D. Xiuli and M. Zhao. Stability and identification for rational approximation of frequency response function of unbounded soil. *Earthquake Engineering & Structural Dynamics*, 39 (2):165–186, 2010.

Y. Zhang, Z. Yang, J. Bielak, J. P. Conte, and A. Elgamal. Treatment of seismic input and boundary conditions in nonlinear sesimic analysis of bridge ground system. In *16th ASCE Engineering Mechanics Conference*, University of Washington, Seattle, July 16-18 2003.

Y. Zhang, J. P. Conte, Z. Yang, A. Elgamal, J. Bielak, and G. Acero. Two-dimensional nonlinear earthquake response analysis of a bridge-foundation-ground system. *Earthquake Spectra*, 24(2):343–386, 2008.

L. Zhu and L. A. Rivera. A note on the dynamic and static displacements from a point source in multilayered media. *Geophysical Journal International*, 148(3):619–627, 2002.